Asteroseismic inferences from red-giant stars

Dissertation
zur Erlangung des mathematisch-naturwissenschaftlichen Doktorgrades

"Doctor rerum naturalium"

der Georg-August-Universität Göttingen

im Promotionsprogramm PROPHYS
der Georg-August University School of Science (GAUSS)

vorgelegt von

Nathalie Themeßl

aus Winklern, Österreich

Göttingen, 2019

Betreuungsausschuss

Dr. ir. Saskia Hekker
Max-Planck-Institut für Sonnensystemforschung, Göttingen, Deutschland
Stellar Astrophysics Centre, Aarhus University, Denmark

Prof. Dr. Stefan Dreizler
Institut für Astrophysik, Georg-August-Universität Göttingen, Deutschland

Prof. Dr. Laurent Gizon
Max-Planck-Institut für Sonnensystemforschung, Göttingen, Deutschland
Institut für Astrophysik, Georg-August-Universität Göttingen, Deutschland

Mitglieder der Prüfungskommission

Referent: **Dr. ir. Saskia Hekker**
Max-Planck-Institut für Sonnensystemforschung, Göttingen, Deutschland
Stellar Astrophysics Centre, Aarhus University, Denmark

Korreferent: **Prof. Dr. Stefan Dreizler**
Institut für Astrophysik, Georg-August-Universität Göttingen, Deutschland

Weitere Mitglieder der Prüfungskommission:

Prof. Dr. Laurent Gizon
Max-Planck-Institut für Sonnensystemforschung, Göttingen, Deutschland
Institut für Astrophysik, Georg-August-Universität Göttingen, Deutschland

Prof. Dr. Ansgar Reiners
Institut für Astrophysik, Georg-August-Universität Göttingen, Deutschland

Prof. Dr. Hardi Peter
Max-Planck-Institut für Sonnensystemforschung, Göttingen, Deutschland

Prof. Dr. Andreas Tilgner
Institut für Geophysik, Georg-August-Universität Göttingen, Deutschland

Tag der mündlichen Prüfung: 28.09.2018

Bibliografische Information der Deutschen Nationalbibliothek

Die Deutsche Nationalbibliothek verzeichnet diese Publikation in der Deutschen Nationalbibliografie; detaillierte bibliografische Daten sind im Internet über `http://dnb.d-nb.de` abrufbar.

About the cover

The cover was designed for use in this thesis by Nathalie Themeßl.

ISBN 978-3-944072-66-1

uni-edition GmbH 2019
http://www.uni-edition.de
© Nathalie Themeßl

This work is distributed under a
Creative Commons Attribution 3.0 License

Printed in Germany

Summary

The analysis of high-precision long-term photometric time-series of data from the NASA *Kepler* space mission (2008 – 2012) has revolutionized the field of red-giant seismology. Solar-like oscillations could be detected in several thousands of pulsating red-giant stars that cover a wide range of stellar properties and different evolutionary stages. This thesis presents a dedicated study of oscillating red giants that belong to eclipsing binary systems (EBs) and open clusters. Through the study of stellar oscillation modes it is possible to draw inferences on the interior structure and evolution of stars, which is called asteroseismology. In the case of oscillating binary and cluster stars, the stellar parameters can be determined either by analysing the asteroseismic signal or through orbital analysis (EBs), and through stellar isochrones (clusters). The comparison between stellar parameters derived from independent analyses provides the means to test the reliability and accuracy of asteroseismic methods. The research presented in this thesis provides improvements to already existing asteroseismic concepts to allow high-precision asteroseismology.

The first part of this thesis focuses on three oscillating red-giant components in EBs. Consistencies between the asteroseismic and dynamical stellar parameters using Kepler's laws were found in cases where the asteroseismic methods accounted for the stellar mass, temperature, and metallicity dependence, as well as the so-called surface effect. The second part of this thesis discusses an asteroseismic ensemble study with the main objective of determining asteroseismic age estimates of about 60 oscillating red-giant stars that are members of the open clusters NGC 6791 and NGC 6819. Individual age determinations for the cluster giants led to a fairly large age span, although stars in open clusters are assumed to be coeval. The spread in the asteroseismic ages could be reduced by using the clusters' metallicity from isochrone fitting as constraints for the asteroseismic modelling of the observed cluster giants. The global metallicity of the stars was shown to have a large impact on the age determinations. Improving the accuracy of this parameter would be helpful in obtaining more accurate asteroseismic ages. Among the stars that were targeted by *Kepler* for open cluster studies was a rare case of a Fourier power density spectrum showing solar-like oscillations of two red giants. The similar asteroseismic ages and masses of the two stars provided indications that they could be physically bound into a rare case of a multiple star system, while different distance estimates could point to an even rarer case of a chance alignment. This study is presented in the third part of this thesis.

Zusammenfassung

Die NASA *Kepler* Weltraummission (2008 – 2012) konnte sonnenähnliche Oszillationen in Tausenden von Roten Riesensternen nachweisen, die verschiedene physikalische Eigenschaften besitzen, und sich in unterschiedlichen Entwicklungsstadien befinden. Die Zeitreihenanalyse der photometrischen Daten von *Kepler* führte zu grundlegenden neuen Erkenntnissen auf dem Gebiet der "Roten Riesen Asteroseismologie". Diese Dissertation widmet sich der Untersuchung von Roten Riesen, die sich in Doppelsternsystemen oder offenen Sternhaufen befinden. Es werden physikalische Zustandsgrößen wie Masse, Radius, mittlere Dichte und Oberflächenschwerkraft ermittelt, die einen Einblick in den inneren Aufbau dieser Sterne und in ihre Entwicklung geben. Um die Eigenschaften der Sterne zu bestimmen, können einerseits asteroseismologische Methoden verwendet werden, andererseits können Doppelsternsysteme mithilfe der Keplergesetze untersucht oder offene Sternhaufen mit sogenannten Isochronen (Evolutionsmodelle für Sterne mit einem bestimmten Alter und einer bestimmten Metallizität) erforscht werden. Diese Arbeit stellt Verbesserungen von bereits existierenden asteroseismologischen Konzepten vor und ermöglicht damit eine bessere Charakterisierung der Roten Riesensterne.

Zunächst wurden drei Sterne auf dem Roten Riesenast untersucht, die Komponenten von bedeckungsveränderlichen Doppelsternsystemen sind. Für diese Sterne wurden verschiedene physikalische Zustandsgrößen bestimmt, die anschließend mit den Ergebnissen der Doppelsternsystemanalysen verglichen wurden. Die Resultate beider Verfahren stimmten nur überein, wenn die Masse, Temperatur und chemische Zusammensetzung der Sterne, sowie der sogenannte "Oberflächeneffekt", in den asteroseismologischen Methoden berücksichtigt wurde. Darüberhinaus wurden ungefähr 60 Rote Riesen analysiert, die sich in den offenen Sternhaufen NGC 6791 and NGC 6819 befinden. Das Alter der beobachteten Haufensterne wurde mithilfe der Asteroseismologie ermittelt und mit Stern-Isochronen verglichen, die das Alter und die Metallizität des jeweiligen Sternhaufens repräsentierten. Durch Miteinbeziehung der chemischen Zusammensetzung der Sternhaufen in die Sternmodelle konnte die Altersspanne der Roten Riesensterne verringert werden. Bei der Altersbestimmung spielte die Metallizität der einzelnen Sterne eine sehr wichtige Rolle. Je präziser diese bekannt war, desto genauer konnte das Alter der Sterne bestimmt werden. Um die Arbeit abzurunden, wurde eine ausführliche Untersuchung von zwei Roten Riesen durchgeführt, die sich eine gemeinsame *Kepler* Lichtkurve teilen. Ihr ähnliches Alter und ihre ähnlichen Massen könnten ein Hinweis darauf sein, dass sie sich in einem Mehrfachsternsystem befinden. Anhand der beobachteten Helligkeiten beider Sterne wurden jedoch unterschiedliche Entfernungen festgestellt, was auch auf ein optisches Doppelsternsystem hindeuten könnte, dass sich gravitativ nicht beinflusst.

We are All made of Stardust

- Anonymous

1 Introduction

In the introductory chapter, key aspects of this thesis are outlined that are dedicated to draw inferences from red-giant stars through asteroseismology. After a preface on the evolution of low-mass stars and stellar oscillations, I describe how stellar parameters can be determined for oscillating red-giant stars. In addition, I introduce the crucial role of eclipsing binary systems as well as open clusters for this research.

1.1 Stellar evolution (in a nutshell)

Stars live for some ten millions to billions of years. Their lifetime and end-product are strongly linked to their initial mass. Lower mass stars consume their energy slower and thus live longer, while higher mass stars burn their fuel faster and have a shorter lifetime. In the classical picture, star formation takes place in dense giant molecular clouds of gas and dust with masses between 10^3 and 10^7 $M_\odot$ (Murray 2011). The Jeans criterion describes the conditions for a cloud to undergo gravitational collapse and, as it collapses, breaks into smaller and smaller fragments. These fragments further collapse releasing gravitational energy and increasing their temperature and pressure, until they reach a state of hydrostatic equilibrium and rotating spheres of hot gas are formed. These objects, known as protostars, are fully convective with core temperatures of a few thousand degrees and high opacities in their interiors. After reaching hydrostatic equilibrium, the protostar begins its pre-main-sequence phase, which is characterized by slow contraction. When the internal temperature is high enough, the protostar starts converting hydrogen into deuterium, and then to helium. At this point the nuclear reactions are very sensitive to temperature, which causes a convective core to develop. While stars with masses $\lesssim 1.1$ $M_\odot$ loose the convective core again, more massive stars retain it. Finally, the star reaches the zero-age main sequence (ZAMS), when hydrogen burning in the core becomes the dominant source of energy production. From this stage onward, stars are powered by nuclear fusion reactions that occur deep in their interiors. The life cycle of a star after leaving the main sequence consists of different evolutionary phases, which depend on the initial mass. When stars die, they enrich the surrounding interstellar medium with elements heavier than helium and hence provide the basic component for the creation of new stars and planets. The full complexity of the process of star formation is demonstrated in recent three-dimensional hydrodynamical simulations (e.g. Bate et al. 2014, Wurster et al. 2018).

During stellar evolution, the inner structure (e.g. chemical composition, temperature, and pressure stratification) varies, causing the stellar characteristics to change. As the physical changes occur slowly during the life cycle of a star and mostly in sequences over very

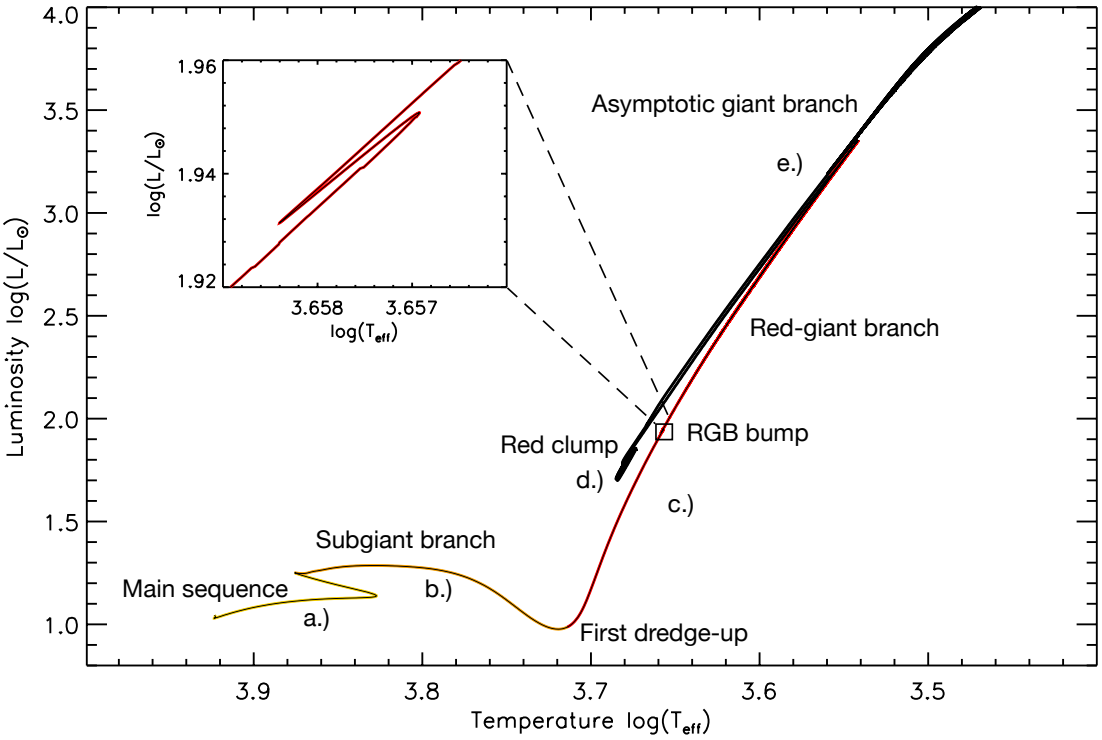

Figure 1.1: Hertzsprung-Russell diagram showing the evolution of a star with $M = 1.8\ \mathrm{M}_\odot$. The evolutionary track was computed with MESA (e.g. Paxton et al. 2018) by using an initial heavy-element and helium abundance of $Z_0 = 0.02$ and $Y_0 = 0.28$, respectively (see Sec. 1.1.3). The colours represent different phases of stellar evolution, i.e. main-sequence, subgiant, red-giant-branch, and asymptotic giant branch phase, which are described in Section 1.1.1 for low-mass stars.

long timescales, it is difficult to probe stellar evolution on a single star. Stellar clusters are helpful in this context, since they contain many stars of different masses that can be observed at different evolutionary stages. Stellar evolution can be studied through simulations of the stellar structure and computations of the evolutionary path of stars. Through comparison with observations it is possible to improve our understanding of stars.

1.1.1 Evolution of low-mass stars

One of the most important charts in stellar astrophysics is the Hertzsprung-Russell diagram (HRD), which shows the relation between a star's brightness (luminosity) and its color (temperature). Throughout their lives, stars change their positions in this diagram. Figure 1.1 shows the evolutionary path of a star with $M = 1.8\ \mathrm{M}_\odot$ from the ZAMS to the asymptotic giant branch (AGB) in the HRD. Stars spend about 90 % of their lifetime on the main sequence (MS), while later stages of stellar evolution proceed faster with stars relatively rapidly reaching their end-products.

After settling on the MS low-mass stars ($0.48 \lesssim \mathrm{M}_\odot \lesssim 2$) pass through the following stages of stellar evolution:

a.) On the **main sequence** low-mass stars can have radiative (below about $1 - 1.2$ $M_\odot$) or convective cores (above $\sim$ 1.2 $M_\odot$), which affect their interior structure and evolution. For stars with radiative cores, the energy production is dominated by the proton-proton (p-p) chain, which slowly fuses hydrogen to helium in the stellar core and the energy transport is carried out by radiation. Stars with convective cores, like the one in Figure 1.1, have a more centrally concentrated carbon-nitrogen-oxygen (CNO) burning region as their dominating energy source. This set of fusion reactions operates at higher temperatures than the p-p chain. In these stars, overshooting of material beyond the formal convective boundary, a process called convective-core overshoot, can extend the main-sequence lifetime by mixing additional hydrogen into the burning regions.

As the star evolves on the main sequence, hydrogen is gradually depleted from the growing inert helium core. The nuclear burning in the centre increases the mean molecular weight, which consequently decreases the ideal gas pressure affecting the hydrostatic equilibrium of the star. To compensate for this, the central density and temperature rise by means of core contraction in order to maintain the support for the overlying stellar layers. The higher efficiency of the burning causes the luminosity to increase. At the point when complete hydrogen depletion in the core occurs, the star has reached the terminal-age main sequence and begins its **subgiant** phase. For a 1.8 $M_\odot$ star with a convective core this event is visible as a 'hook' feature in the HRD (see Fig. 1.1).

b.) After the cease of nuclear reactions in the stellar core, the star requires a new source of energy generation. The central density in stars with $M \lesssim 1.1$ $M_\odot$ is high enough for electron degeneracy to occur. Due to the pressure support that is provided, a low-mass star with a degenerate isothermal helium core remains in thermal and hydrostatic equilibrium, while it gradually transitions to hydrogen-shell burning. With the beginning of shell burning, the degenerate helium core slowly increases in mass, while the envelope of the star expands. The boundary between contraction and expansion lies near the hydrogen-burning shell, where the CNO cycle becomes the dominating energy source. When the star moves from the main sequence to the red-giant branch, the stellar envelope expands and cools down. At a specific point, i.e. the Hayashi line, the temperature cannot be decreased any further, otherwise the star would not be able to remain in hydrostatic equilibrium. Thus, a further increase of the radius leads to a rise in the stellar luminosity. The transition is the so-called bottom of the **red-giant branch** (RGB).

c.) On the RGB, the hydrogen-burning shell continues to move outwards, while the bottom of the convective envelope moves inwards. In the deep interior the ashes of the hydrogen-burning shell are deposited on the degenerate helium core, which continues to grow in mass. The increasing temperature in the contracting core heats up the hydrogen-burning shell which, due to compression, enhances the energy production. Inevitable, the shrinking stellar core becomes effectively decoupled from the expanding stellar envelope.

When the star ascends the RGB the inward moving convective envelope transports material from the deep interior processed by nuclear reactions during the main-

sequence phase to the surface. This is the so-called **first dredge-up** event. At this point, the convective envelope extends deep into the star and is forced to retreat by the hydrogen-burning shell moving outwards. Since convection is an efficient form of mixing that homogenized the chemical composition in the star, all that remains is a chemical mean molecular weight discontinuity. Convection is also an efficient means of energy transport. The shell becomes less blanketed and energy is efficiently transported to the surface. This causes the stellar luminosity to rise dramatically during the RGB phase of stellar evolution and the stellar radius to expand greatly. Once the stellar surface is cooled, the star proceeds nearly vertically in the HRD.

The degenerate helium core grows in mass and the hydrogen-burning shell moves further outwards. When the shell encounters the chemical composition discontinuity, the stellar luminosity first decreases due to the reduced mean molecular weight and then increases again, when the helium core continues to grow in mass at a constant mean molecular weight. In simple terms, the star readjusts itself and reverses its direction of evolution before continuing on the RGB. This feature is observable as the so-called **RGB bump**.

In the final stages of the RGB phase, the temperature in the degenerate core is eventually high enough ($T \sim 10^8$ K) to ignite helium fusion via the triple-alpha process. The onset of helium fusion causes a short-lived thermal runaway process, in which enormous amounts of energy are produced. Due to efficient neutrino cooling and losses in the inner centre, the helium-burning is first initiated in a shell off centre, where the temperature is at its maximum. The resulting energy release occurs explosively in one or more so-called helium flashes. In order for them to stop, the degeneracy in the helium-rich core has to be lifted by the energy generated during these flashes. Since most of the energy is absorbed by the overlying layers without reaching the surface, the stellar luminosity remains very similar during this process.

d.) At this point, the star has two energy sources, i.e. helium-burning in a convective core that produces predominantly carbon and oxygen, and hydrogen-burning in a shell, which is the dominant source of energy. After the helium flash, the energy production in the hydrogen-burning shell is less efficient due to its expansion and, thus, has a lower temperature and density. Hence, the stellar luminosity decreases and the star ends up in the **red clump**. As a further note, stars that are massive enough to slowly start the ignition of helium under non-degenerate core conditions, form the population of secondary clump stars.

e.) Once the helium is exhausted in the core, the star rapidly ascends the **asymptotic giant branch**. Now, the star has an inert carbon and oxygen core, a helium-burning shell, which is thermally unstable, and a hydrogen-burning shell further out. When the star climbs up the AGB, the stellar luminosity and radius increase. The shells become thinner and alternate in being the most efficient energy source. This is caused by thermal instabilities due to the extinction and reignition of the helium-burning shell. Since nuclear reactions are highly temperature-dependent, thermal pulses are created when the regions between the nuclear-burning shells become very narrow. This phase of stellar evolution is very important for the chemical

enrichment of the universe. The star produces large amounts of carbon and through several mass loss processes and dredge-up events, the galaxy gets enriched with heavier elements.

The final stages of stellar evolution depend primarily on the initial mass of the star and the amount of mass loss that occurred during the star's lifetime. Helium fusion generates a carbon-oxygen core, which in the case of a low-mass star will never ignite carbon fusion. Most of the star's mass is lost due to dust-driven winds. At some point, its envelope starts to contract and shell-burning is ceased. The outer stellar layers are ejected by radiation and a planetary nebula is formed. Finally, the star becomes a white dwarf.

As the described sequence only tells part of the story of the life of a star, I refer the interested reader to e.g. Kippenhahn and Weigert (1990), Maeder and Renzini (1984), Lattanzio (1986), Salaris and Cassisi (2005), Aerts et al. (2010), Iben (2013), Hekker and Christensen-Dalsgaard (2017) as well as the lecture notes[1] on stellar structure and evolution by Christensen-Dalsgaard (2008), which give an elaborate description of different evolutionary phases for low-, intermediate-, and high-mass stars.

1.1.2 Overview of stellar structure

In a stellar model, a star is defined as a spherical symmetric fluid that is in hydrostatic equilibrium without any rotation or magnetic fields (e.g. Basu and Chaplin 2017). In this 'standard theory', the influence of these more complex processes is usually neglected. Also, if hydrodynamic effects, e.g. convection, convective overshoot, and chemical mixing between radiative and convective zones, are included in the model, they are treated in a simplified manner. The stellar structure can be described by a set of non-linear equations under the assumption that radius $r(m)$, gas pressure $P(m)$, temperature $T(m)$, density $\rho(m)$, luminosity $L(m)$ and chemical composition $X_i(m)$ vary only in the radial direction $r(m)$ at a point in time and where m is the mass of the star enclosed within the radius r from the stellar centre. Hence, when the star evolves, its mass remains constant, while its radius changes considerably. This assumption holds for many evolutionary stages, even though mass loss plays an important role in very early and late stages of stellar evolution. The conditions in the stellar interior can be characterized by means of four stellar structure equations that are based on the conservation of mass, momentum, and energy, as well

[1] http://astro.phys.au.dk/~jcd/evolnotes/LN_stellar_structure

as the descriptions for energy transport and nucleosynthesis:

$$\frac{\partial r}{\partial m} = \frac{1}{4\pi r^2 \rho}, \tag{1.1}$$

$$\frac{\partial P}{\partial m} = -\frac{Gm}{4\pi r^4}, \tag{1.2}$$

$$\frac{\partial L}{\partial m} = \epsilon_{\mathrm{n}} - \epsilon_{\nu} - \epsilon_{\mathrm{g}}, \tag{1.3}$$

$$\frac{\partial T}{\partial m} = -\frac{GmT}{4\pi r^4 P}\nabla, \tag{1.4}$$

$$\frac{\partial X_i}{\partial t} = \frac{m_i}{\rho}\left(\sum_j r_{ji} - \sum_k r_{ik}\right), i = 1, ..., I. \tag{1.5}$$

Eq. 1.1: In the conservation of mass equation, the star is described by a number of spherical mass shells with ∂m representing the mass of a shell at a radius r and thickness ∂r. Eq. 1.2: The conservation of momentum defines the balance between the downward force of gravity and upward pressure, with G as the gravitational constant and m as the fractional mass (hydrostatic equilibrium). Eq. 1.3: In the conservation of energy equation, ϵ_{n}, ϵ_{ν}, and ϵ_{g} represent the energy release through nuclear reactions, the energy loss due to neutrinos, and the gravitational energy release, respectively. On this basis, the inflow and outflow of energy are in balance. Eq. 1.4: The equation defines the temperature stratification in the stellar interior. Here, ∇ is the dimensionless temperature gradient, which depends on the mechanism of energy transport inside the star that is, radiation and convection. Eq. 1.5: The composition inside the star changes with time and position. The parameter X_i is the mass fraction of the element i, m_i is the mass of the nucleus of the isotope i, r_{ji} is the energy generation rate for the formation of the isotope i from the isotope j, and r_{ik} is the rate at which the isotope i is lost when transforming into the isotope k.

1.1.3 Stellar modelling

A stellar model can be computed by solving the stellar structure equations 1.1 – 1.5 with the addition of some external physics and boundary conditions. The properties of stellar matter are given by the equation of state, radiative opacities (interactions between radiation and matter), nuclear reaction rates (e.g. energy generation, neutrino fluxes, composition changes), diffusion coefficients (e.g. transport processes in the matter) and element settling (e.g. collisions and interactions between gas components). An atmospheric model serves as an external constraint to set the outer boundary conditions of the star. Based on these inputs one obtains a classical stellar model that can be computed in a reasonable amount of time. Another major issue in stellar modelling is the incorporation of heat transport in convective stellar layers. The standard approach is based on mixing-length theory (Böhm-Vitense 1958), which describes how far a convective element rises before it merges with its environment, thus providing information about the efficiency of energy transport from the deep interior to the stellar surface. In a general manner, the complex concept of convection is parametrized with a single mixing-length parameter that is commonly set to a solar-calibrated value. This approximation is used due to the computation

cost of the process with very different timescales.

Models of stars can be obtained by using stellar evolution codes, e.g. the PAdova and TRieste Stellar Evolution Code[2] (PARSEC; e.g. Bressan et al. 2012, Marigo et al. 2017) or the Modules for Experiments in Stellar Astrophysics[3] (MESA; e.g. Paxton et al. 2011, 2018), as well as databases such as the Bag of Stellar Tracks and Isochrones database[4] (BASTI; e.g. Pietrinferni et al. 2004, 2014). All these stellar modelling codes use slightly different input physics and approximations to create their grids of stellar models.

Stellar evolutionary tracks: Starting from some basic conditions, i.e. initial mass M_0, initial heavy-element abundance Z_0, and initial helium abundance Y_0, the stellar model can be evolved in time until it satisfies some observed surface properties (e.g. effective temperature and luminosity). The initial input values for M_0, Y_0, and Z_0 affect the structure and evolution of the model, which becomes the proxy of an observed star. Figure 1.2 shows evolutionary tracks for modelled stars with initial masses between 0.6 $M_\odot$ and 1.4 $M_\odot$ as a function of age from the zero-age main sequence up to the red-giant branch. In case of the 1 $M_\odot$ model, the variations due to different heavy-element abundances are shown as well. Stars with lower initial Z_0 are generally hotter.

Isochrones: Stellar isochrones for any given choice of age and metallicity can be derived from stellar evolutionary tracks that were calculated for a range of different M_0, Y_0 and Z_0. An isochrone is a curve, which represents a population of stars with the same age and metallicity as a function of mass. Figure 1.3 presents a selection of isochrones for varying metallicities and ages that extend from the MS to the AGB. Along these isochrones, important stellar parameters such as the luminosity, effective temperature, radius, and evolutionary phase can be retrieved for any given stellar model. In combination with bolometric corrections, the theoretical luminosities and effective temperatures can be transformed into several photometric systems in order to provide magnitudes and colours.

By comparing stellar models with observational data it is possible to improve the understanding of stellar physics and test theoretical stellar evolution calculations. This opens up new possibilities to refine theoretical assumptions and it helps to analyze and predict future observations. Even if a stellar model is able to reproduce the global properties of an observed star, the age and internal structure of the best-fitting model can still be different from the observed star. One way to improve the model fitting is to use additional information from individual frequencies of oscillation modes (see Sec. 1.3.6) that can be measured for stars that show oscillations.

1.2 Stellar oscillations

Acoustic stellar oscillations are a common feature among stars with a large range of stellar properties and different evolutionary stages. In the following, I provide a brief

[2] http://stev.oapd.inaf.it/cgi-bin/cmd
[3] http://mesa.sourceforge.net
[4] http://www.te.astro.it/BASTI/index.php

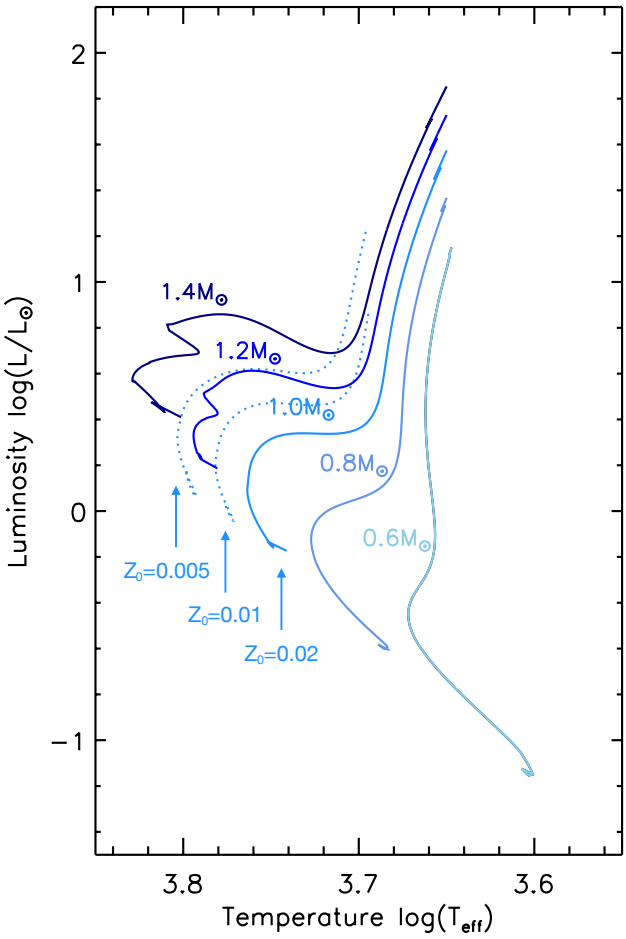

Figure 1.2: Examples of MESA model tracks (e.g. Paxton et al. 2011) in the Hertzsprung-Russell diagram with different initial masses M_0 (solid lines) at given heavy-element abundance $Z_0 = 0.02$. For the 1 $M_\odot$ model the impact of different Z_0 values are shown (dotted lines). Models with lower initial heavy-element abundance are shifted towards higher temperatures and larger luminosities.

overview of why, how, and which types of stars pulsate, and what methods are used to analyze them. More information about the theory of stellar oscillations is available in Cox (1980), Aerts et al. (2010), Hekker and Christensen-Dalsgaard (2017), Basu and Chaplin (2017), amongst others, as well as the lecture notes[5] on stellar oscillations provided by Christensen-Dalsgaard (2014).

1.2.1 A description of oscillations in stars

Low-amplitude acoustic oscillations arise from small perturbations to the equilibrium structure of a star, which are generated in the stellar interior, and then propagate as acoustic waves inside the star. They can be described as acoustic oscillations on the basis of the general equations of hydrodynamics in the presence of a gravitational field and under the

[5] http://users-phys.au.dk/jcd/oscilnotes/

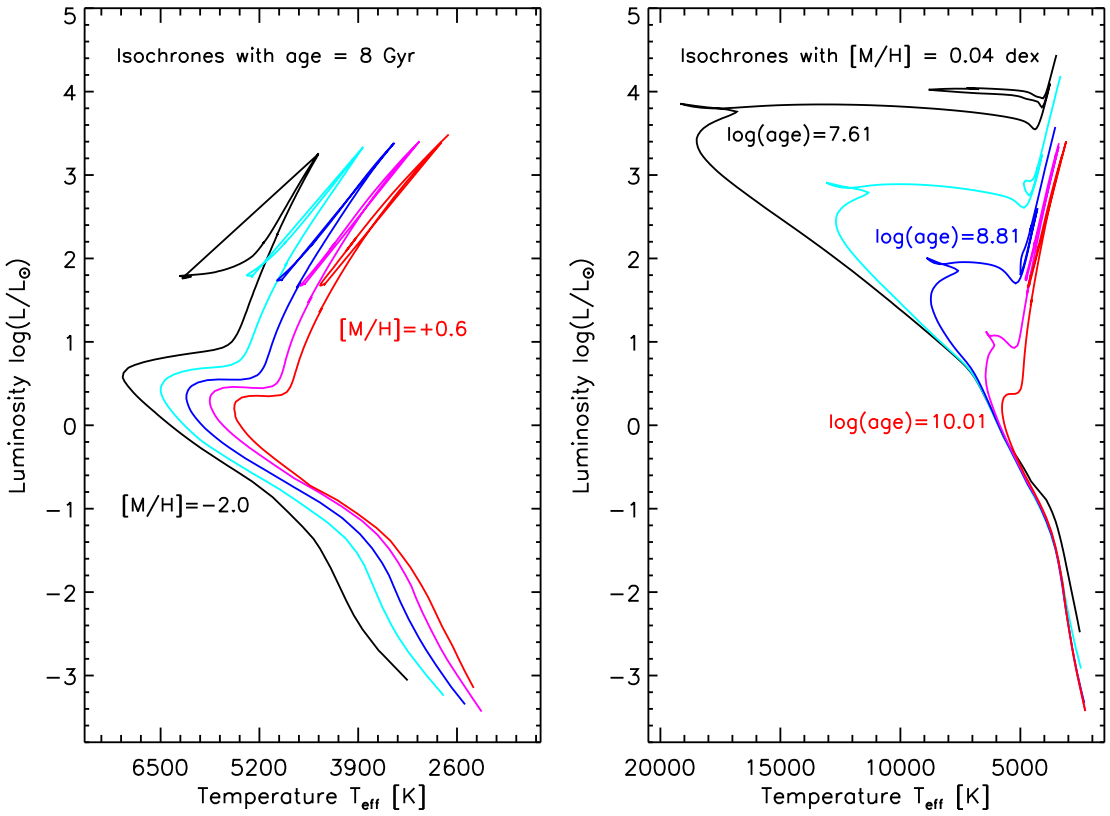

Figure 1.3: Examples of PARSEC (e.g. Bressan et al. 2012) isochrones. Left: A set of isochrones for a fixed age ($\log \tau = 9.91$) and varying metallicities of [M/H] = $-2.0, -1.0, -0.4, +0.1$, and $+0.6$ dex from left to right. Right: A set of isochrones with different ages between about 41 Myr and about 10 Gyr ($\log \mathrm{age} = 7.61, 8.21, 8.81, 9.4$, and 10.01 (dex) from top to bottom) at a fixed metallicity of [M/H] = 0.04 dex.

assumption that oscillations are adiabatic linear perturbations to a spherically symmetric stellar model. The use of the linear approximation is justified, since velocity amplitudes of oscillations are in most cases much smaller than the sound speed in the region where they propagate. For example the velocity perturbations at the surface of the Sun are smaller than $20\,\mathrm{cm\,s^{-1}}$ (Libbrecht 1988), i.e. roughly 10^4 times smaller than the local sound speed at the solar photosphere. The use of the adiabatic approximation is also justified, since the oscillations operate on much shorter timescales than the heat transport timescale in the corresponding layer.

Based on these assumptions, it is possible to write the linearised equation of continuity and momentum, and the linearised Poisson equation for gravity, which represent the set of so-called stellar adiabatic oscillation equations. These equations, complemented with a set of boundary conditions at the surface and at the centre of the star, constitute an eigenvalue problem, whose eigenmode solutions give the resonant oscillations of the star. Each eigenmode can be completely described by its eigenfrequency $\omega_{n\ell}$ and its displacement

vector $\delta\mathbf{r}_{n\ell m}$, which in spherical coordinates can be written in the form:

$$\delta\mathbf{r}_{n\ell m}(r,\theta,\phi,t) = \mathrm{Re}\left\{\left[\xi_r(r)Y_\ell^m(\theta,\phi)\mathbf{a_r} + \xi_h(r)\left(\frac{\partial Y_\ell^m(\theta,\phi)}{\partial\theta}\mathbf{a}_\theta + \frac{1}{\sin\theta}\frac{\partial Y_\ell^m(\theta,\phi)}{\partial\phi}\mathbf{a}_\phi\right)\right]e^{-i\omega_{n\ell}t}\right\}, \tag{1.6}$$

where r is the radial distance from the centre of the star, θ is the colatitude, and ϕ is the longitude. This vector is split in a radial (ξ_r) and horizontal (ξ_h) component with Re representing the real part. Here $\mathbf{a_r}$, $\mathbf{a}_\theta$, and $\mathbf{a}_\phi$ denote the unit vectors in the spherical coordinate system. Moreover, spherical harmonics $Y_\ell^m(\theta,\phi)$ are used to define the geometrical properties of the oscillation modes of a spherically symmetric star. They are characterized by two integer numbers, the angular degree ℓ, with $\ell \geq 0$, and the azimuthal order m, with $-\ell \leq m \leq \ell$:

$$Y_\ell^m(\theta,\phi) = (-1)^m\sqrt{\frac{2\ell+1}{4\pi}\frac{(\ell-m)!}{(\ell+m!)}}P_\ell^m(\cos\theta)e^{im\phi}, \tag{1.7}$$

where $P_\ell^m(\cos\theta)$ are the associated Legendre polynomials.

The eigenmode solution is uniquely determined by three integer numbers n, ℓ, m. For any given value of ℓ, we obtain different eigenfrequencies $\omega_{n\ell}$ that are indicated by the radial order n, i.e. the overtone of the mode, which represents the number of node surfaces between the centre and the surface of the star. Positive (negative) values of n are used to indicate acoustic (gravity) modes. For $\ell > 0$ and for each n, there are $2\ell + 1$ eigenmodes of different azimuthal order m. In presence of rotation these modes may have different frequencies. However, in a non-rotating spherically symmetric star, as is assumed here, eigenmodes are degenerate in m, and therefore all the modes with the same values of n and ℓ have the same eigenfrequency $\omega_{n\ell}$. The eigenfrequency is further related to the cyclic oscillation frequency according to $\nu_{n\ell} = \omega_{n\ell}/2\pi$. We can directly measure $\nu_{n\ell}$ from the observations.

Radial and non-radial modes of oscillation: Many stars show pulsations in both radial ($\ell = 0$) and non-radial modes ($\ell \geq 1$ and $n \geq 1$). A star with $\ell = 0$ oscillates in the radial direction only and thus remains spherically symmetric. These modes appear as pure pressure modes (see Sec. 1.2.4). Non-radial modes have both horizontal and vertical displacements. In Figure 1.4 we show a graphical visualization of non-radial modes in stars with a viewing angle of 60°. Adjacent surface elements move in opposite directions with different colours indicating contracting (i.e. heating) and expanding (i.e. cooling) parts. These parts are separated by nodal lines. The angular degree ℓ represents the total number of nodal lines on the stellar surface, and the azimuthal order m is the number of meridional node lines. As distant stars are observed as point sources, one measures the integrated brightness or velocity in the line-of-sight over the visible disk of the star. This causes partial cancellation of modes, where the intensity variations of the surface elements of high-degree modes with $\ell > 3$ cancel each other out. According to theoretical predictions, the visibility of $\ell = 3$ modes in intensity observations is already only about one tenths compared to radial $\ell = 0$ modes (Aerts et al. 2010).

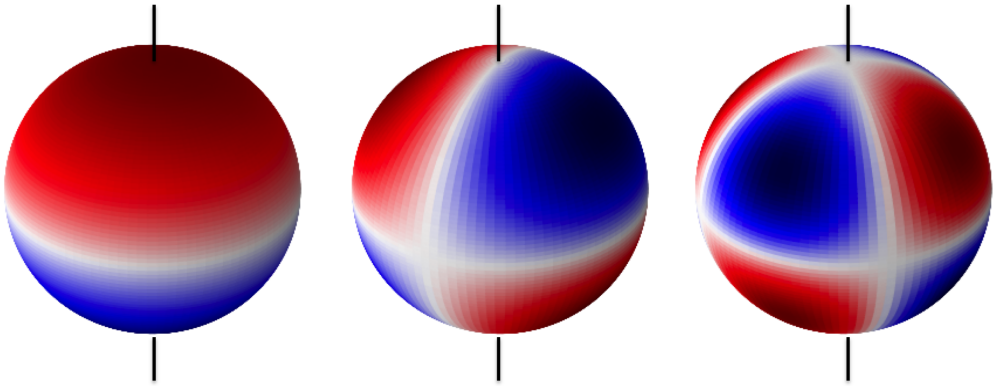

Figure 1.4: Graphical illustration of different oscillation modes as seen from an inclination angle of 60°. Black lines show the axis of rotation. The angular degree ℓ and azimuthal order m are increasing from left to right with $(\ell, m) = (1, 0), (2, 1)$, and $(3, 2)$.

1.2.2 Driving mechanisms

Small perturbations to the stars equilibrium structure do not generate enough energy to preserve stellar oscillations over time. Most of the energy is lost throughout the star, where layers damp the oscillations, because the star attempts to recede into hydrostatic equilibrium. Therefore, stars require efficient driving mechanisms in order to excite oscillation modes globally and to reach amplitudes that can be detected.

κ mechanism: Many stars have forced self-excited oscillations, where radial stellar layers act as heat engines by converting thermal energy into mechanical energy. The temperature plays an important role for this mechanism. Thus, the layer where the modes are excited must be located at a certain depth. In classical pulsators (see Fig. 1.5 and Sec. 1.2.3), oscillations are predominantly driven in the first partial ionization zones of hydrogen and helium (Mira stars, semiregular variables) and the second partial ionization zone of helium (rapidly oscillating Ap stars, δ Scuti, RR Lyrae, Cepheids and pre-main-sequence stars). In more massive stars, such as β Cepheids, slowly pulsating B stars, B supergiants, and subdwarf B stars, the κ mechanism acts in iron partial ionization zones. In these ionized stellar layers, the radiation is blocked by opacity. Due to increasing pressure and heat of the gas, the star surpasses its equilibrium point. With increasing ionization of the gas, the layer becomes less opaque and the radiation passes through. Then, the gas cools down and the overlying layers can no longer be supported. Compression takes place, which causes the layer to gain heat again.

Only modes that are in resonance with the forcing can be excited by the κ mechanism. They usually have large amplitudes and therefore they have been studied by means of ground- and space-based data for several decades. The 'classical' instability strip shown in the HRD in Figure 1.5, is occupied by classical pulsators with oscillations driven by the heat engine mechanism.

Stochastic excitation: In solar-type main-sequence, subgiant and red-giant stars, modes are stochastically excited and damped through turbulence in convection zones near the stellar surface.

In contrast to classical pulsators, all modes can be excited. These small-amplitude oscillations were first detected in the Sun (Sec. 1.3.2), hence they are called solar-like oscillations. Long-term space-based observations were necessary to study them in detail in many stars with different evolutionary stages. In the HRD, the solar-like oscillators are situated on and near the main sequence (Fig. 1.5).

ϵ mechanism: According to theoretical considerations, global oscillations could possibly be driven by variations in the energy rate produced in the stellar core of very massive and evolved stars, which have yet to be observed.

Convective blocking: Convective blocking is another mechanism that is capable of driving oscillations. At the base of the convection zone, the radiative flux can be effectively blocked by convection. This causes the heating of the star to be in phase with its compression, which then leads to the excitation of modes. This driving mechanism has been found to excite g modes in γ Doradus stars.

Tidally induced oscillations: Global oscillations in close binary systems can be triggered by tidal actions, which force resonantly excited oscillation modes. Theoretical studies imply that the period and eccentricity of the binary orbit, masses and radii of the components, as well as the properties of the oscillation modes strongly influence the driving of these oscillations. The modes can be excited through resonances between forced frequencies from dynamic tides and free oscillation modes of one of the binary components. Observationally, they are detectable for spherical degree $\ell = 2$, which is the dominant degree for dynamic tides. They appear as g modes, since their frequencies are similar to the orbital frequencies of binary systems. Solid detections, however, are hampered by the presence of multiples of the orbital frequency, which can be falsely interpreted as resonantly excited modes.

1.2.3 Stellar oscillations across the Hertzsprung-Russell diagram

Pulsating stars occupy certain regions in the HRD. Due to different physical mechanisms (Sec. 1.2.2) their brightness varies periodically, semi-periodically, or irregularly as a function of time. According to common characteristics, pulsating stars are grouped together in several classes and subclasses. Besides some hybrid pulsators that have both p- and g-mode oscillations, each group exhibits one dominating mode type. The asteroseismic HRD shows that oscillations can be excited in almost all types of stars and in many different stages of stellar evolution. In the following, the main characteristics of the oscillations of different classes of pulsating stars are introduced, which are shown in the HRD in Figure 1.5.

Near the main sequence

- ⋆ *Slowly pulsating B stars*: The SPB stars are multiperiodic g-mode pulsators with amplitudes smaller than 50 mmag and periods between 0.5 and 5 days.

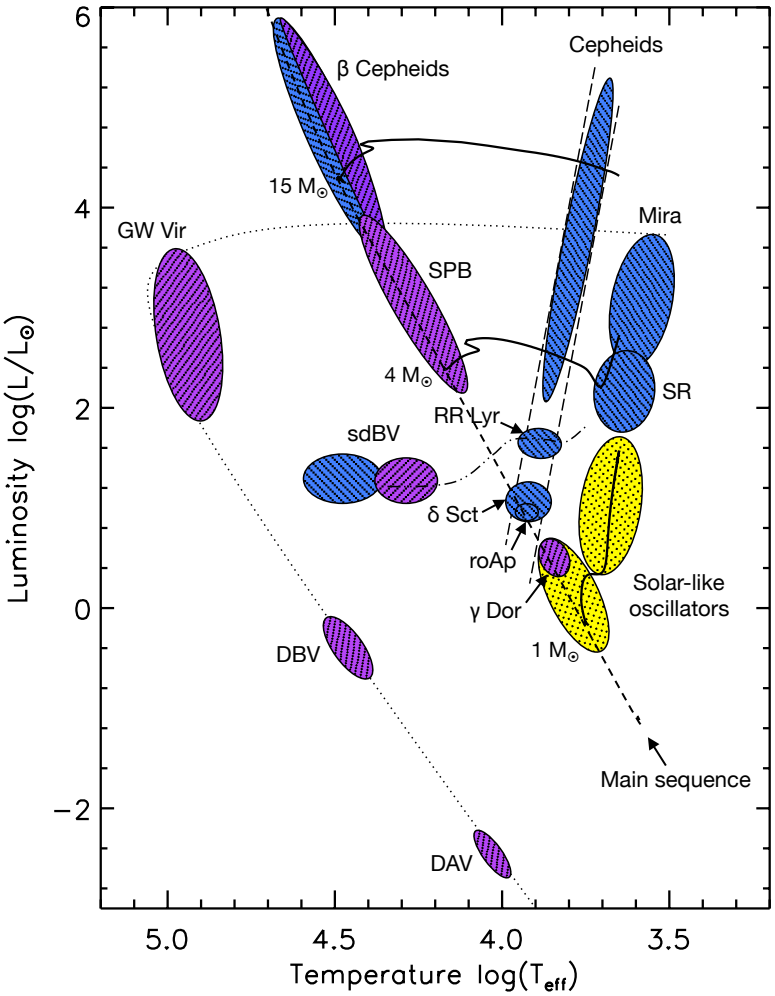

Figure 1.5: Theoretical asteroseismic HRD showing different groups of pulsating stars (see Sec. 1.2.3). Black solid lines show evolutionary tracks of model stars with different initial masses (1 $M_\odot$, 4 $M_\odot$, and 15 $M_\odot$). The dashed line represents the main sequence and the instability strip is indicated by the two nearly vertically long dashed lines. The dotted line shows the path from the AGB to the white-dwarf stage and the double-dotted-dashed line marks the horizontal branch. The main mode type of oscillations, i.e. p modes and g modes through the heat engine mechanism, are emphasized by blue and purple colours. Solar-like oscillations occur in main-sequence, subgiant and red-giant stars, which are highlighted in yellow.

- ⋆ *β Cepheids*: Members of this group range from dwarfs to giants. They can be multiperiodic p- and g-type pulsators with short periods from 2 to 8 hours (p modes with < 0.1 mag) and of a few days (g modes with < 0.01 mag).
- ⋆ *Pulsating Be stars*: This class comprises fast rotating population I stars that show Balmer-like emission lines due to the presence of circumstellar discs. They usually oscillate with one dominant mode, even though multiperiodicity is possible. Oscillation periods range from 0.1 to 5 days with amplitudes < 20 mmag. Many pulsating Be stars are members of close binary systems.
- ⋆ *δ Scuti stars*: The population I stars of this group have radial and non-radial low-order p modes with short periods of 18 minutes to 8 hours. The observed amplitudes range from one mmag to tenths of a magnitude. Some stars show amplitude variability over years and even decades, as well as non-linear resonant mode coupling. In more evolved stars mixed modes can appear. The population II (SX Phe) stars of this group have a generally lower metallicity and high amplitudes. Usually, they are members of globular clusters and some of them may even be blue stragglers.
- ⋆ *roAp stars*: The rapidly oscillating A-type pulsators are highly-magnetic population I stars with peculiar chemical surface compositions. They show multiperiodic low-degree p-mode oscillations of high radial order with periods between 5 and 20 min, and amplitudes < 10 mmag. Moreover, rotational amplitude modulations occur, when the axis of pulsation is aligned with stellar magnetic fields. This is the so-called oblique pulsator model (Kurtz 1982).
- ⋆ *γ Doradus stars*: This group of multiperiodic stars exhibits non-radial g modes of high order and low degree with periods of 0.3 – 3 days and amplitudes < 50 mmag.
- ⋆ *Solar-like oscillating stars*: On the main sequence, solar-like oscillating stars show multiperiodic p modes with low amplitudes of a few ppm and periods of minutes to tens of minutes.

Evolved stars

- ⋆ *RR Lyræ stars*: They are low-mass population II stars burning helium in their cores. RR Lyræ stars mostly pulsate mono-periodically or additionally in the first overtone of the mode. Special characteristics of this class of stars are amplitude and phase modulations that are caused by the Blazhko effect, strong atmospheric shocks, and many overtones in the frequency spectrum. They have radial modes with periods in the range between 0.3 and 0.5 days and their amplitudes reach up to about 1.5 mag. RR Lyræ stars are divided into three sub-classes (RRab, RRc, and RRd) based on the skewness of their light curve and their oscillation period and amplitude.
- ⋆ *Cepheids*: This group comprises stars with high masses that are in the core-helium burning phase. Due to their brightness, Cepheids are commonly used as standard candles to determine distances through the period-luminosity relation. Population I classical Cepheids are giants or supergiants with periods ranging from 1 to 50 days and with amplitudes < 1 mag. Their light curves are extremely periodic. They can oscillate in both the fundamental and the first overtone, or the first and second overtone of the mode. The population II Cepheids exhibit periods from one day to

one month with amplitudes < 1 mag. These stars cross the instability strip when moving away from the horizontal branch or during the AGB phase and are divided into groups according to their period. Among the short-period pulsators are the BL Her class with periods from 1 to 5 days and the W Virginis class with periods between 10 and 20 days. Longer pulsation periods belong to the RV Tauri class, which are F to K supergiants with radial pulsations that have periods between 30 and 150 days. They show regularly alternating deep and less deep minima in their light curves. Many of them are long-period binaries.

- ⋆ *Semiregular variables*: The SR stars are giants and supergiants that pulsate in an overtone with periods from about 20 days to longer than 2 000 days. Strong periodicities and irregularities are present in their light curves.
- ⋆ *Mira stars*: They represent the long-period pulsators near the tip of the red-giant branch. Mira stars oscillate in the radial fundamental mode ($\ell = 0$) with long periods (> 80 days to years) and amplitudes up to 8 mag.
- ⋆ *Solar-like oscillating stars*: The more evolved solar-like oscillators (subgiants, red giants) have multiperiodic low-spherical degree p modes in the range of minutes to hours as well as mixed pressure-gravity modes (Sec. 1.2.4).

Compact pulsators

- ⋆ *Variable subdwarf B stars*: This group of old low-mass population I stars is located on the extreme horizontal branch with members having masses less than $\sim 0.5\,M_\odot$ due to extreme mass loss. They are multiperiodic pulsators that show p modes with periods of the order of ~ 1 to 5 min with amplitudes < 0.1 mag as well as g modes with periods of ~ 0.5 to 3 hours with amplitudes < 0.01 mag.
- ⋆ *White dwarfs*: There are three distinct types of white dwarf pulsators, which all have multiperiodic g modes of low degree and high order with amplitudes < 0.2 mag. Strong mode trapping occurs because of the stratification in their envelope layers. The first group are the GW Vir stars, which are among the DO variable dwarfs. These stars have periods between 7 and 30 min, and their spectra show a deficiency in hydrogen and large abundances of helium, carbon, and oxygen. The second group are the DB type stars (V777 Her) with periods of the order of ~ 4 to 12 min with amplitudes < 0.2 mag. The DA type stars (ZZ Ceti stars) constitute the third group, which exhibit periods from less than 100 s to longer than 1 000 s. These variable dwarfs have hydrogen atmospheres with strong Balmer lines visible in the spectrum and a frequency spectrum that contains multiplets.

A complete picture and more information about different types of pulsating stars is provided by Aerts et al. (2010) and references therein.

1.2.4 Asteroseismology of red-giant stars

Asteroseismology is an observational method to analyze pulsating stars. This technique is based on the study of global stellar oscillations through the measurement of mode frequencies, when they reach observable amplitudes at the surface of stars. Asteroseismology provides a unique view into the deep stellar interior. Other 'classical' photometric

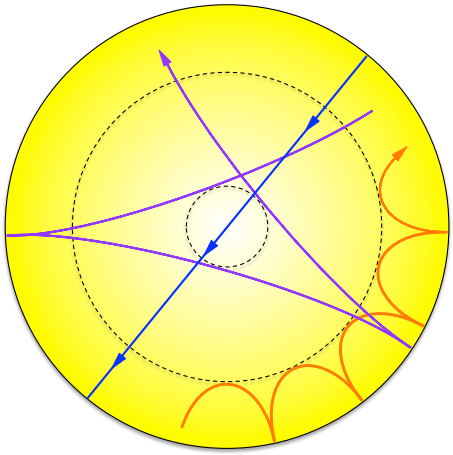

Figure 1.6: Graphical visualization of pressure (acoustic) waves propagating as rays through the star. Higher angular degree ℓ modes have more nodes on the stellar surface (e.g. orange ray), while lower angular degrees penetrate deeper inside the star (e.g. purple ray) with the $\ell = 0$ mode (in blue) propagating through the stellar core.

and spectroscopic methods are mostly useful for exploring stellar surfaces, since distant stars are very opaque and can only be observed as point sources.

Over the past two decades, asteroseismology has shown its great astrophysical potential (e.g. Aerts et al. 2010, Hekker and Christensen-Dalsgaard 2017, Basu and Chaplin 2017). The advent of continuous long-term high-precision space observations and high-resolution spectroscopic ground-based campaigns have introduced, what is sometimes referred to as, a 'golden era of stellar variability'. The quantity and quality of photometric time series data and radial velocity measurements have reached a level to perform in-depth analyses for hundreds of thousands of oscillating stars. By using different asteroseismic methods combined with spectroscopy it is possible to derive several stellar properties, including mass and radius, age, luminosity and thus distance, temperature, chemical composition, and evolutionary stage. In addition, physical processes can be studied through stellar modelling in order to advance the understanding of the internal stellar structure, evolution, rotation, diffusion, convection, and excitation mechanisms. Some of this information cannot be retrieved by any other method, which makes asteroseismology a very powerful analysis tool.

Asymptotic theory for solar-like oscillators: Solar-like oscillators show pressure (p) modes with pressure acting as their primary restoring force. Modes with different degrees are sensitive to different regions inside the star with low-degree p modes reaching the deeper layers. Figure 1.6 illustrates pressure waves as rays travelling through the star. As the wave moves towards the centre, the sound speed increases, which causes the wave to travel faster in the deeper interior and to be refracted until it reaches an inner turning point. There, the wave is reflected back to the surface, where the drop in pressure prevents it from leaving the star and the wave is reflected again. The observational signature that can be measured are the frequency, amplitude, and phase of the pressure wave, which provide valuable information about the stellar regions that the wave penetrated through.

In solar-like oscillators, gravity (g) modes are mostly trapped in the deep stellar interior. Their primary restoring force is buoyancy.

Deriving the properties of the oscillations from the linear and adiabatic stellar oscillation equations is a complicated task and oscillatory solutions can only be obtained for the eigenfrequencies of the star (Sec. 1.2.1). To mitigate this difficulty, it is possible to use some approximations. One of the basic assumptions is to neglect the perturbation to the gravitational potential by using the Cowling approximation (Cowling 1941). This principle holds for modes of high radial order and is applicable to many stars that show oscillations, among which are the red-giant stars and the Sun. After reducing the adiabatic stellar oscillation equations to a second-order system, three characteristic frequencies can be derived that are important for describing the behaviour of the oscillations (e.g. Hekker and Christensen-Dalsgaard 2017, Basu and Chaplin 2017). The Lamb frequency is a characteristic frequency for pressure (acoustic) waves, the Brunt-Väisälä frequency represents a characteristic frequency of internal gravity waves, and the acoustic cut-off frequency marks the frequency below which waves are reflected. These frequencies determine regions, so-called cavities, inside the star where p and g modes propagate. The boundaries of the trapping regions are called turning points. G modes have their turning point below the base of the convection zone, which is defined by the location where the Brunt-Vaisälä frequency matches the frequency of a g mode. The Lamb frequency identifies the lower turning point for a p mode, while the acoustic cut-off frequency is the upper turning point beyond which a p mode is damped. As the star evolves, the locations of the p- and g-mode cavities change and the frequencies of the modes can overlap. When a g-mode frequency gets close to a non-radial p-mode frequency with the same spherical degree, coupling takes place and mixed p-g modes can appear. Due to their mixed character, they behave like p modes in the stellar envelope and like g modes in the deep interior of the star. The observed oscillation spectrum is different for a main-sequence and a more evolved red-giant star, which can show many mixed p-g modes. Due to their very low amplitudes, mixed modes are mainly observed for $\ell = 1$ modes. For these modes the coupling between the cavities is strongest and the modes are better resolved.

1.3 Accurate stellar parameters of red-giant stars

The focus of this thesis is the determination of stellar parameters of oscillating red-giant stars, which can be determined from measurements of their observed asteroseismic signals. The target stars were monitored by the *Kepler* space mission (Sec. 1.3.3) and they belong to eclipsing binary systems or open clusters. Stars in these associations benefit from the fact that their stellar parameters can also be determined independently of asteroseismology, either from the eclipsing binary analysis or from isochrone fitting to clusters (Sec. 1.3.9). They are perfect candidates for testing the accuracy and reliability of asteroseismic methods, and for validating asteroseismically derived stellar parameters.

1.3.1 Motivation

The Sun is the only star for which the stellar properties are known to high accuracy and precision due to the fact that the solar surface can be resolved. The situation is different

for stars that are located at far distances and, which can only be observed as point sources. Obtaining reliable estimates of their stellar parameters requires different measures and the results typically have larger uncertainties. A good example is the age of the Sun, which can be determined to better than 1 %, while ages for field stars can only be derived with an accuracy of up to 30 – 40 % (e.g. Soderblom 2010).

One way to improve the accuracy of stellar parameter measurements is to use stars that are associated in binary systems and/or stellar clusters. The basic assumption that stars are formed at approximately the same time and from the same molecular cloud puts useful constraints on the stars' age, chemical composition, and distance. This thesis focuses on oscillating red-giant stars in these associations. Their stellar parameters can be computed based on the analysis of the observed asteroseismic signal. Complementary to asteroseismology, the binary nature can be used to derive stellar masses and radii in a model-independent way by using Kepler's laws, if radial velocity measurements are available, and if the system is eclipsing. For an ensemble of stars in a cluster sufficient constraints are available to find a matching cluster isochrone, which provides the cluster's global age and metallicity. If the same stellar parameters are determined from different methods, they are expected to be consistent to a certain level and hence, they can be used to validate asteroseismic results. Moreover, the impact of different choices of constraints on stellar parameter determinations can be investigated as well as the accuracy, with which the initial input parameters need to be known. One of the essential requirements for studying stellar parameters of a sample of stars are homogeneously determined quantities in order to avoid systematics and biases in the results. With a dedicated approach the reliability of asteroseismic methods can be tested, which is very important for the future analysis of asteroseismic data that will become available for an unprecedented number of stars thanks to the K2, TESS and PLATO missions (Sec. 5.1). In the wider context, accurate stellar parameters play a role for the study of extrasolar planetary systems, because their understanding depends on accurate descriptions of their host stars. Additionally, detailed characterizations of the properties of stellar populations add to the current knowledge of the Milky Way.

1.3.2 From helio- to asteroseismology

Solar-like oscillations were first detected for the Sun in the early 1960s and were confirmed as global oscillations in the late 1970s, when the Sun was first observed as a star. Dedicated ground-based multi-site campaigns and long-term space-based observations followed this discovery, which revolutionized the field of helioseismology. The left panel of Figure 1.7 shows a smoothed version of the Fourier power density spectrum of the Sun, which was computed based on a 4-year long photometric time series with one data point taken every minute. The data were provided by the VIRGO experiment (Variability of solar IRradiance and Gravity Oscillations) on board SOHO (Solar and Heliospheric Observatory) by using three Sun photometers (e.g. Fröhlich et al. 1995, 1997, Jiménez et al. 2002). The right panel of Figure 1.7 shows the frequency range of the observed oscillations for the Sun. Many individual frequencies of oscillation modes with different spherical degrees and radial orders were detected in 'Sun-as-a-star' data.

The first indications of low-amplitude solar-like oscillations in stars other than the Sun

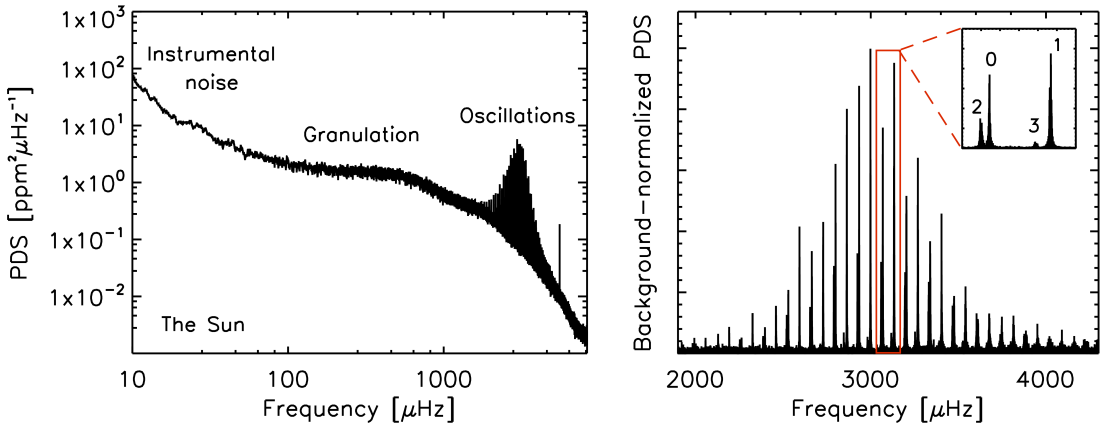

Figure 1.7: Left: Fourier power density spectrum (smoothed with 50 μHz) of the Sun based on 4 years of SOHO Virgo SPM observations. The main components of the spectrum are granulation, oscillations, and instrumental noise. Right: Background-normalized spectrum (Sec. 1.3.5) centred on the oscillation modes. The inset shows a small excerpt with different spherical degrees ℓ indicated by numbers.

were based on radial velocity and photometric studies from the ground in the early 1990s for a few bright main-sequence and subgiant stars. Extensive observing efforts were necessary to detect their small brightness variations, since ground-based observations suffer from bad weather conditions, turbulent seeing, and incomplete datasets due to the day-night rhythm, which introduces large gaps in the time series data. Arcturus (Smith et al. 1987) and Procyon (Brown et al. 1991) were among the first stars, where the typical power excess due to solar-like oscillations were detected based on spectroscopic one-site campaigns. Using ground-based datasets for the detection of many individual frequencies of oscillation modes was challenging and due to extensive observing efforts (e.g. observations over many months, multi-site campaigns) not practicable for a large number of solar-like oscillators (e.g. Bedding and Kjeldsen 2008). This difficulty could be overcome with observations from space.

While earlier photometric space surveys, such as the Wide Field Infrared Explorer (WIRE; e.g. Buzasi et al. 2000), the Hubble Space Telescope (HST; e.g. Edmonds and Gilliland 1996) and the Microvariability and Oscillations of STars (MOST; e.g. Matthews et al. 2000) detected solar-like oscillations in single stars, the breakthrough for red-giant asteroseismology could be achieved by the Convection, Rotation and planetary Transits (CoRoT; e.g. Baglin et al. 2006) and *Kepler* (e.g. Borucki et al. 2008) missions. The nearly continuous long-term high-precision photometric observations from CoRoT and *Kepler* provided the accuracy necessary for asteroseismic studies with unambiguous detections of frequencies in an unprecedented number of stars. The analysis of these data have shown the potential of asteroseismic methods to characterize the interior properties of many main-sequence, subgiant and red-giant stars. An overview of the groundbreaking results for solar-like oscillators can be found in Chaplin and Miglio (2013), Hekker (2013), Hekker and Christensen-Dalsgaard (2017), Basu and Chaplin (2017), and references therein.

1.3.3 The *Kepler* space mission

The photometric time series of data used in this thesis were obtained by the *Kepler* space mission (e.g. Koch et al. 2010), which was launched on May 13, 2009. The mission was dedicated to search for transits of extrasolar planets, in particular terrestrial planets, around Sun-like stars. From 2009 to 2013, *Kepler* monitored more than 190 000 stars in a 115 deg^2 field in the constellations of Cygnus and Lyra. With about 30 min and 1 min cadences for the brightness measurements, the datasets were of great interest for asteroseismic studies (e.g. Blomme et al. 2010). The data were collected during operational quarters Q0 to Q17. After the commissioning quarter Q0 ($\sim$ 10 days) and the start of the science program in Q1 ($\sim$ 1 month), all the consecutive quarters lasted for an average of about 3 months each. In addition to advances in the field of asteroseismology, *Kepler* has discovered thousands of transiting exoplanets by the end of its mission. More than 100 of them are located in the habitable zone with many more exoplanet candidates identified, which require further investigations (e.g. Batalha 2014, Mullally et al. 2015, Kane et al. 2016).

1.3.4 Stellar intensity observations

Time series observations can be used to detect variations of the stellar signal, e.g. brightness, or radial velocity, over time. Most of the data used in this thesis are stellar intensity observations, which form the basis of asteroseismic studies of oscillating red-giant stars. The top panel of Figure 1.8 shows the *Kepler* photometric time series data for KIC 8410637. This light curve consists of more than 66 000 data points that were obtained during 4 years of observations with one measurement taken every $\sim$ 29.4 min (long-cadence mode). Important parameters of the time series are the total time span ($T = N \times \delta t$) of the observations and the cadence (δt) of the data. The latter is a measure of the typical sampling time of the total number of flux measurements (N).

Most asteroseismic diagnostics are determined from the Fourier transform of the photometric time series, which converts the data from the time-domain into the frequency-domain. Due to discrete-time datasets with real values, a single-side calibration of the discrete Fourier transform can be adopted, where the positive-frequency transform yields all the power from the time-domain. Parseval's theorem is commonly applied to calibrate the power in the discrete Fourier transform in order for the total power in the transform to be equal to the mean-squared power of the flux data in the time-domain. The power can be calculated per frequency unit, which provides a Fourier power density spectrum (PDS). The computed PDS in the bottom panel of Figure 1.8 shows the behaviour, frequency range and amplitudes of the solar-like oscillations of a red-giant star. In Fourier space, the observational time span and the sampling of the time series data are related to the frequency resolution ($\delta\nu = 1/T$) and the Nyquist frequency ($\nu_{\rm nyq} = 1/(2\,\delta t)$), which is the highest frequency that can be resolved in the transform. For *Kepler* long-cadence observations $\nu_{\rm nyq}$ is about 283 μHz.

An important aspect of time series analysis is the window function, which shows the effect of gaps in the observations by providing the times when data were stored. Gaps create significant artefacts, i.e. alias peaks, in the frequency-domain that hamper the analysis of the oscillations. In contrast to ground-based single-site campaigns, observations from

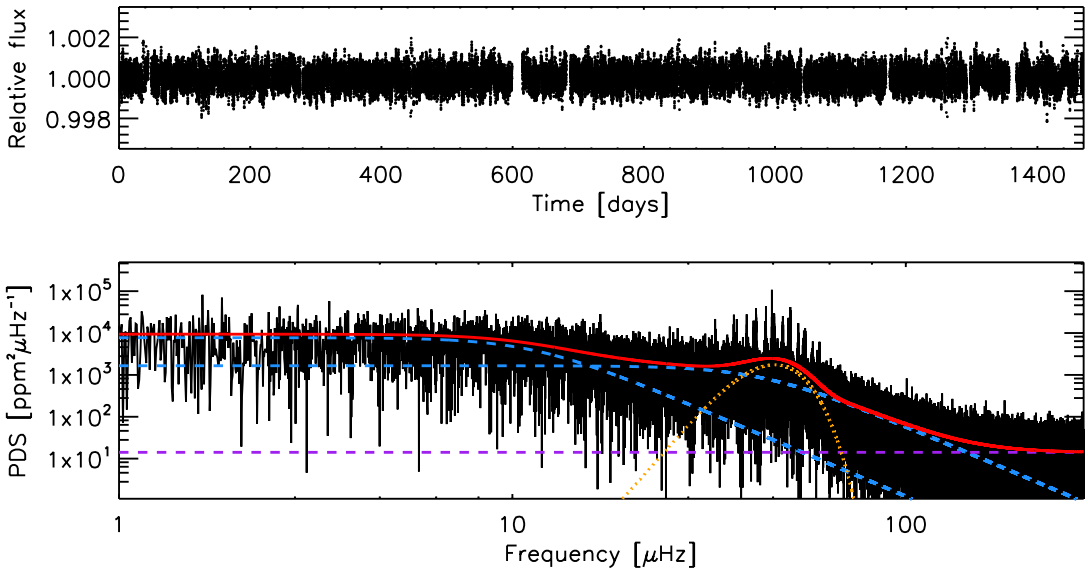

Figure 1.8: Top: The *Kepler* light curve for the red-giant star KIC 8410637. Bottom: Computed Fourier power density spectrum (in black) derived from 4 years of *Kepler* long-cadence observations. The global fit (eq. 1.9) to the power density spectrum is shown in red. Blue dashed lines represent the granulation background components (eq. 1.10), the violet dashed line shows the white noise component, and the orange dotted line is the Gaussian fit to the power excess (eq. 1.11).

space are usually not prone to many gaps. The former are in particular affected by diurnal gaps causing additional peaks (and sidelobes) that surround the true signal frequencies. Their regular occurrence leads to one-day aliasing effects in the Fourier spectrum. Due to the stochastic nature of solar-like oscillations where the phase information is lost, large gaps can be removed by stitching the datasets together, which provides a cleaner PDS (Hekker et al. 2010a).

The intrinsic stellar signal is also influenced by the integration time of the photon measurements from the star. This causes apodization η with the largest effect on the power of frequencies close to the Nyquist frequency (e.g. Kallinger et al. 2014):

$$\eta = \mathrm{sinc}\left(\frac{\pi}{2}\frac{\nu}{\nu_{\mathrm{nyq}}}\right) \quad \text{with} \quad \mathrm{sinc} = \frac{\sin \mathrm{x}}{\mathrm{x}}. \tag{1.8}$$

More information about the fundamentals of observational light curve data, their statistics and the analysis of the data in the frequency-domain are provided in Chapters 4 and 5 by Basu and Chaplin (2017).

1.3.5 Characteristics of the red-giant power density spectrum

In the PDS of a red-giant star, the oscillations are superimposed on a global background signal that comprises a number of other stellar intrinsic features, as well as photon-counting ('white') noise, and instrumental effects (Figs. 1.7 and 1.8). The low-frequency

regime in the PDS is dominated by signatures of the visible surface patterns of convection, i.e. granulation, magnetic activity, spots and flares, and instrumental noise (e.g. telescope drifts and jitter). White noise is predominant in the high-frequency regime. Other harmonic signatures that can be detected in the PDS are the signals of stellar rotation, binary companions, or exoplanets. Their contributions are usually removed with filters before asteroseismic analyses are performed.

The PDS of an oscillating red-giant star shows contributions from the following components:

$$P_{\rm PDS}(\nu) = n_{\rm w} + \eta^2 \left[P_{\rm gran}(\nu) + P_{\rm gauss}(\nu) \right]. \tag{1.9}$$

Here, $n_{\rm w}$ describes the white noise that is used to model the photon-shot noise. This parameter can be estimated from the apparent magnitude of the target star and the performance of the instrument. The global granulation background is represented by $P_{\rm gran}(\nu)$. The third contribution are the oscillations, which are embedded in a power envelope $P_{\rm gauss}(\nu)$. The stellar granulation and oscillation signals are both influenced by the apodization defined in equation 1.8.

Global granulation background: The number of granulation components for describing the global background over the range of observed frequencies (ν) depends on the presence of features such as activity, (meso-) and (super-)granulation, or faculae. Usually, one to three components are used, which can have different functional forms. The formulations are all based on the 'classical Harvey model' that was introduced for fitting the solar background signal (Harvey 1985). Kallinger et al. (2014) have shown that for most red-giant stars, observed with *Kepler*, a two-granulation component fit is suitable for studying the global properties of the oscillations that is given by:

$$P_{\rm gran}(\nu) = \sum_{\rm i=1}^{2} \frac{A_{\rm i}}{1 + (\nu / b_{\rm i})^{c_{\rm i}}}. \tag{1.10}$$

Each granulation background component is characterized by an amplitude $A_{\rm i}$ and characteristic frequency $b_{\rm i}$. This frequency is further related to the characteristic timescale ($\tau_{\rm i}$) of granulation with $b_{\rm i} = (2\pi\tau)^{-1}$, which depends on the properties of the outer layers of the star. The exponent $c_{\rm i}$ describes the decay of the power with increasing frequency for the granulation component. While Harvey (1985) originally adopted a value of two for the slope of the decay, it was found that a value of 4 is more appropriate for fitting red-giant stars (e.g. Kallinger et al. 2014). In the bottom panel of Figure 1.8, a two-granulation component fit to the PDS of a red-giant star is shown.

1.3.6 Global asteroseismic diagnostics from the oscillation spectrum

The most distinct feature in the PDS of a red-giant star is the power excess due to solar-like oscillations. The bottom panel of Figure 1.8 shows excess power at about 45 μHz for KIC 8410637. From the PDS it is possible to derive a number of global oscillation parameters that provide information about the physical properties of red giants.

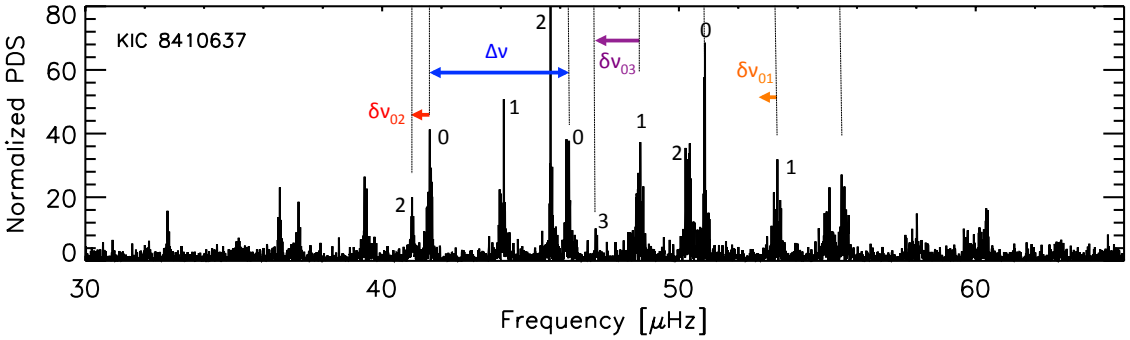

Figure 1.9: Background-normalized power density spectrum over the range of observed frequencies for KIC 8410637. The large and small frequency separations are indicated with arrows and for some peaks the spherical degree is shown with numbers 0, 1, 2, or 3.

The frequency of maximum oscillation power: Solar-like oscillations observed in red-giant stars are acoustic modes of low-spherical degree (ℓ) and radial overtones $n > \ell$. The oscillation modes form a power envelope that has a Gaussian-like shape. The specific frequency of the oscillations at the centre of the power excess is the frequency of maximum oscillation power $\nu_{\rm max}$. This global oscillation parameter can be determined from a Gaussian fit to the power excess:

$$P_{\rm gauss}(\nu) = \Lambda_{\rm g} \exp\left(\frac{-(\nu - \nu_{\rm max})^2}{2\sigma_{\rm g}^2}\right), \tag{1.11}$$

where $\Lambda_{\rm g}$ and $\sigma_{\rm g}$ represent the height and the width (i.e. standard deviation) of the Gaussian function. When red giants evolve, $\nu_{\rm max}$ shifts to lower frequencies and the observed power excess becomes narrower (e.g. Stello et al. 2010).

P-mode frequency pattern: Figure 1.9 provides a closer look at the oscillation modes. The significant peaks form a near-regular pattern of frequencies in the PDS, which reveals the structure of the radial ($\ell = 0$) and non-radial ($\ell = 1, 2, 3$) modes. In evolved stars, non-radial modes have a mixed character. Their diagnostic potential is larger, because they are not restricted to the stellar envelope as is the case for pure p non-radial modes. Observationally, the pattern of p-mode frequencies is defined by the asymptotic approximation (e.g. Tassoul 1980, Mosser et al. 2011):

$$\nu_{n,\ell} \simeq \Delta\nu\left(n + \frac{\ell}{2} + \epsilon\right) - \delta\nu_{0,\ell}, \tag{1.12}$$

where $\nu_{n,\ell}$ is the frequency of an oscillation mode with radial order n and spherical degree ℓ. The parameter $\Delta\nu$ represents the mean large frequency separation and ϵ is the frequency-dependent phase term, i.e. the offset of the radial $\ell = 0$ modes. Here, $\delta\nu_{0,\ell}$ denotes the small frequency separations of non-radial modes relative to radial modes. An observable feature is that red giants with low-radial ($n \sim \ell$) order modes show a triplet structure of $\ell = 1, 2, 0$ modes (top panel in Fig. 1.12) instead of the $\ell = 0, 2$ duplet with $\ell = 1$ modes at half $\Delta\nu$-spacing between consecutive radial modes (second panel in

Fig. 1.12). The asymptotic approximation (eq. 1.12) is useful for identifying the spherical degree and for estimating the radial order of the mode.

The global mean large frequency separation: The global oscillation parameter $\Delta\nu_{n,\ell}$ is the difference between frequencies of consecutive radial orders (n) and the same spherical degree (ℓ), as shown in Figure 1.9:

$$\Delta\nu_{n,\ell} = \nu_{n+1,\ell} - \nu_{n,\ell}. \tag{1.13}$$

Both global asteroseismic parameters ($\nu_{\rm max}$ and $\Delta\nu$) are related according to $\Delta\nu \sim \nu_{\rm max}^{\rm exp}$ (e.g. Hekker et al. 2009, Stello et al. 2009, Mosser et al. 2010) with the exponent (exp) depending on mass and to a lesser extent on metallicity (Hekker et al. 2011a). Different methods can be employed to determine the global mean large frequency separation, for example the power spectrum of the power spectrum (e.g. Hekker et al. 2010b), the autocorrelation of the time series (e.g. Mosser and Appourchaux 2009), or the frequency differences between radial modes with consecutive orders, i.e. 'peakbagging analysis' (e.g. Kallinger et al. 2010).

The local large frequency separation: When the large frequency separation is derived as a central value based on the three innermost $\ell = 0$ modes around $\nu_{\rm max}$, it can be used as an indicator for the evolutionary stage of red-giant stars (Kallinger et al. 2012). For radial modes, the asymptotic relation can be expressed as:

$$\nu_{\rm c,0} = \Delta\nu_{\rm c}(n + \epsilon_{\rm c}') \;\text{ with }\; \epsilon_{\rm c}' = \frac{\nu_{\rm c,0}}{\Delta\nu_{\rm c}} \text{ modulo } 1, \tag{1.14}$$

where $\epsilon_{\rm c} = \epsilon_{\rm c}' + 1$ if $\epsilon_{\rm c}' < 0.5$ and $\Delta\nu > 3\ \mu$Hz, otherwise $\epsilon_{\rm c} = \epsilon_{\rm c}'$. The local large frequency separation $\Delta\nu_{\rm c}$ together with the local phase term ϵ_c provides a means to differentiate between hydrogen-shell burning stars on the red-giant branch and more evolved core-helium burning stars. Figure 1.10 shows that red-giant-branch stars have a larger value of $\epsilon_{\rm c}$ than more evolved red clump, secondary clump, and asymptotic giant branch stars with $\Delta\nu_{\rm c}$ of the same value. One of the drawbacks of this method is the lack of a clear separation between stars of different evolutionary stages.

The mean small frequency separations: In addition to the large frequency separation, there are three characteristic small frequency separations between $\ell = 0$ and 2 modes ($\delta\nu_{02}$), between $\ell = 0$ and 1 modes ($\delta\nu_{01}$), and between $\ell = 0$ and 3 modes ($\delta\nu_{03}$), which are shown in Figure 1.9. They can be defined according to:

$$\delta\nu_{02}(n) = \nu_{n,0} - \nu_{\rm n-1,2}, \tag{1.15}$$

$$\delta\nu_{01}(n) = \frac{1}{2}(\nu_{n,0} + \nu_{n+1,0}) - \nu_{n,1}, \tag{1.16}$$

$$\delta\nu_{03}(n) = \frac{1}{2}(\nu_{\rm n,0} + \nu_{\rm n+1,0}) - \nu_{\rm n,3}. \tag{1.17}$$

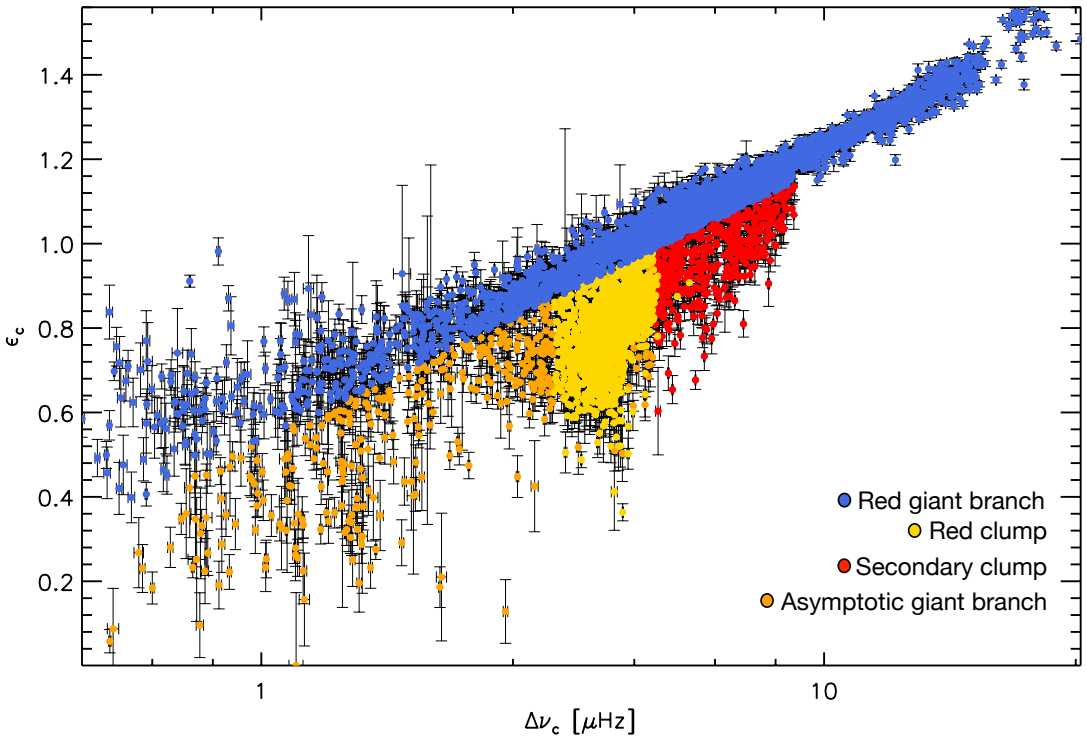

Figure 1.10: The central values for the phase term (ϵ_c) as a function of the central values for the mean large frequency separation ($\Delta\nu_c$) for about 6600 red-giant stars observed with *Kepler*. The colours represent stars with different evolutionary stages. Data courtesy of Dr. Thomas Kallinger.

For main-sequence stars, the small frequency separations are a diagnostic for age, because they are related to the gradient of the sound speed in the stellar interior (Christensen-Dalsgaard 1984, Ulrich 1986), which is sensitive to the chemical composition and hence to the evolutionary stage of the star. As structural changes occur when the star evolves, the small separations cannot be used as an age diagnostic for red-giant stars, because they are no longer sensitive to the density gradient due to their compact cores and expanded envelopes. The mean small frequency separations are usually derived from the individual frequencies of the observed oscillation modes.

Period spacing: Similar to the asymptotic relation for p modes, g modes are equally spaced in period and follow an asymptotic approximation in period. The periods of the g modes ($\Pi_{n,\ell}$) of a given spherical degree ℓ and radial order n satisfy the following asymptotic approximation in the period PDS:

$$\Pi_{n,\ell} = \Delta\Pi_\ell(n + \epsilon_g + \frac{1}{2}) \text{ with } \Delta\Pi_\ell = \frac{\Pi_0}{\sqrt{\ell(\ell+1)}}. \tag{1.18}$$

Here, $\Delta\Pi_\ell$ is the asymptotic period spacing and ϵ_g is the phase term for g modes. Pure g modes are not observable in red-giant stars. Instead, $\ell = 1$ modes with a mixed p and g

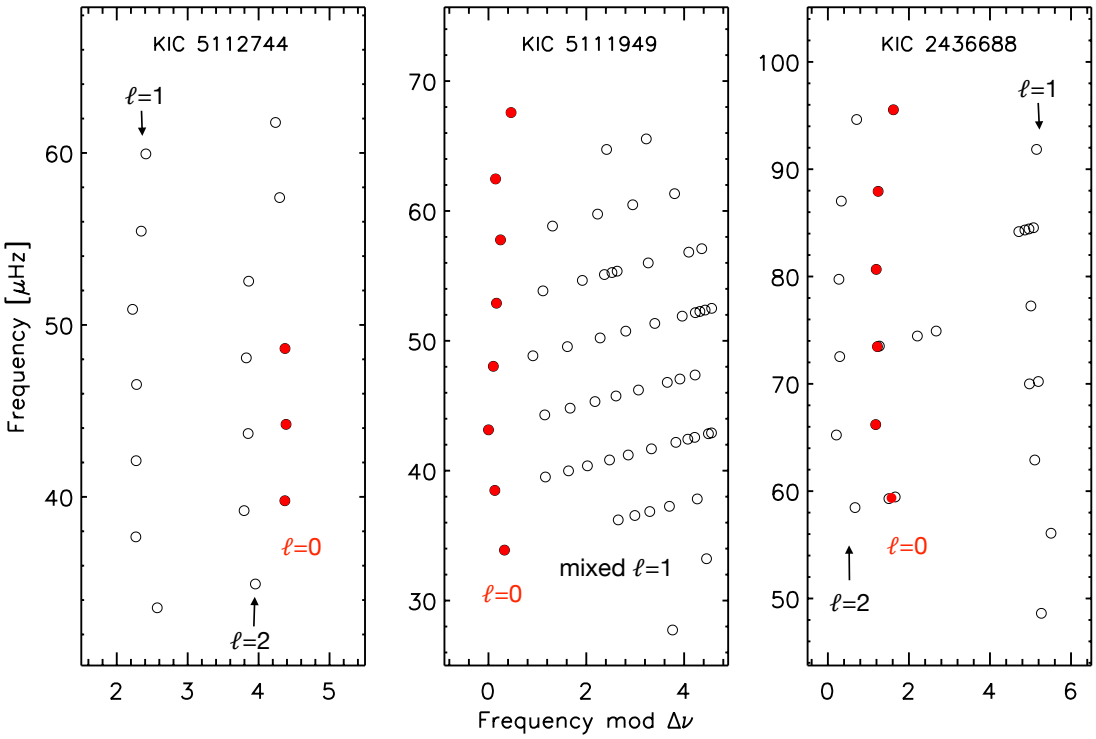

Figure 1.11: Échelle diagrams for three red-giant stars. Left: For KIC 5112744 three ridges of spherical degree $\ell = 1, 2$, and 0 (from left to right) are visible. Middle: KIC 5111949 is a clump star, which shows many mixed modes. Right: KIC 2436688 shows three distinct ridges of $\ell = 2, 0$, and 1 modes (from left to right).

character can be detected and analyzed (Sec. 1.2.4). Common methods for determining the period spacing include period échelle diagrams (e.g. Bedding et al. 2011, Mosser et al. 2012b, Datta et al. 2015, Hekker et al. 2018), inertia ratio of dipole and radial modes (Benomar et al. 2014), and analysis of stretched period power density spectrum (e.g. Mosser et al. 2015, Vrard et al. 2016). Since the observed period spacing is measured based on mixed modes (not on pure g modes), its value is different from the asymptotic period spacing. Mixed modes have a strong diagnostic power for the central regions of the star. Therefore, the (observed) period spacing can be used to differentiate between different evolutionary stages of red-giant stars (e.g. Bedding et al. 2011, Mosser et al. 2012b, 2014).

Peakbagging: Due to the high quality of space data, it is possible to extract a set of individual frequencies of oscillation modes for a large number of observed red-giant stars. This procedure is called 'peakbagging analysis'. The region around $\nu_{\max}$ in the PDS contains many peaks. At the side of $\nu_{\max}$ towards higher frequencies, the peaks are broadened due to short mode lifetimes. Towards lower frequencies the peaks are more narrow due to increased damping rates (e.g. Basu and Chaplin 2017).

The significant peaks in the PDS can be described with a set of Lorentzian functions of

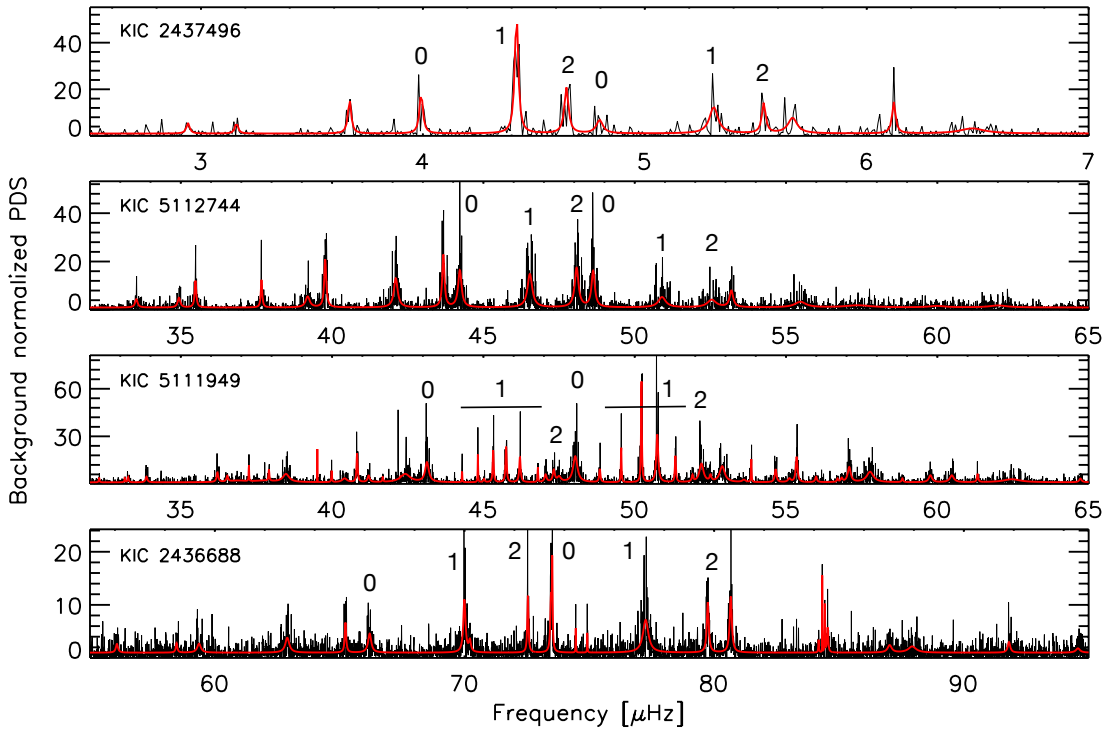

Figure 1.12: Background-normalized power density spectra (in black) showing the frequency range of the oscillations for four red-giant stars with KIC numbers indicated in each panel. The red solid lines represent the peakbagging fits. Although $\nu_{\max}$ values are similar for KIC 5112744 and KIC 5111949, they show different mixed-mode patterns, because they are in different evolutionary stages. For KIC 5111949 many mixed modes are present, which is typical for a red-clump star.

the form (e.g. Anderson et al. 1990, Corsaro et al. 2015a):

$$P_{\text{peaks}}(\nu) = \sum_{\text{j}} \frac{H_{\text{j}}}{1 + 4\left(\frac{\nu - \nu_{\text{j}}}{\Gamma_{\text{j}}}\right)^2}. \tag{1.19}$$

Each Lorentzian function j is defined by a mode frequency ν_{j}, mode height H_{j} and mode linewidth Γ_{j}. While the height relates to the amplitude of the mode with $A_{\text{j}} = \sqrt{\pi H_{\text{j}} \Gamma_{\text{j}}/2}$, the width is related to the mode lifetime τ_{j} according to $\Gamma_{\text{j}} = (\pi\tau_{\text{j}})^{-1}$ (Chaplin et al. 2005). If unresolved oscillation peaks are present in the PDS, they can be fitted with sinc functions that are described by two parameters, i.e. a frequency and a height (or amplitude).

The extracted set of frequencies can be used to generate an échelle diagram (Grec et al. 1983), which shows segments of the Fourier spectrum of equal lengths $\Delta\nu$ stacked on top of each other (see Fig. 1.11). The observed oscillation modes form near-vertical ridges in this diagram, which are representative of the spherical degrees. Individual frequencies provide additional constraints to find best-fitting models for the observed star, which are usually constrained by using the global oscillation parameters and some spectroscopic ob-

servables. However, if frequencies are included in stellar modelling, one needs to account for the so-called surface effect (Sec. 1.3.8).

1.3.7 Parameter estimation in the Fourier power density spectrum

For the interpretation of the asteroseismic signal it is important to obtain reliable estimates of the parameters that describe the global granulation background (eq. 1.10), the Gaussian fit to the power excess (eq. 1.11), and the Lorentzian functions for peakbagging (eq. 1.19). Maximum likelihood estimation techniques are commonly used to fit a model to the data. These fitting procedures require a likelihood function to define the probability of a dataset given the model parameters and they have to include the correct noise statistics of the data. Boundaries are set for the model parameters by using some prior distributions that are based on previous knowledge. In the case of a solar-like oscillating star, the Fourier power density spectrum can be modelled by a mean spectrum profile $\mathcal{M}(\nu_k;\theta)$ that is characterized by a number of free parameters θ, which is multiplied by random noise that has a χ^2 distribution with two degrees of freedom (e.g. Duvall and Harvey 1986, Appourchaux 2003). The relation between the mean spectrum profile and the observed Fourier power density spectrum (D_k) at a frequency bin (k) can be expressed by the following probability density (e.g. Handberg and Campante 2011):

$$f(D_k) = \frac{1}{\mathcal{M}(\nu_k;\theta)} \exp\left(-\frac{D_k}{\mathcal{M}(\nu_k;\theta)}\right). \tag{1.20}$$

Under the assumption of uncorrelated frequency bins, the joint probability density function for the data sample can be obtained from the product over the frequency interval k:

$$L(\theta) = \prod_k f(D_k;\theta). \tag{1.21}$$

Estimates of the model parameters can be derived by maximizing the likelihood function (e.g. Toutain and Appourchaux 1994):

$$\mathcal{L}(\theta) \equiv \ln L(\theta) = -\sum_k \left\{\ln \mathcal{M}(\nu_k;\theta) + \frac{D_k}{\mathcal{M}(\nu_k;\theta)}\right\}. \tag{1.22}$$

Due to improved numerical stability, the log-likelihood is preferred for the computations.

Metropolis-Hastings Markov Chain Monte Carlo method: Markov Chain Monte Carlo (MCMC) methods are commonly used for fitting Bayesian statistical models (e.g. Metropolis et al. 1953, Hastings 1970, Robert 2015). The Metropolis-Hastings algorithm is a sampling technique based on MCMC that performs a quasi random walk through a predefined parameter space by using a probability density distribution. While at the beginning the sampling area is large, with increasing number of iterations the size decreases and the probability to reach the global minimum is enhanced. The idea behind this method is to obtain the posterior probability density function for the model parameters, and to estimate their median values, and credible intervals.

The algorithm generates a sequence of random samples with stationary distributions that

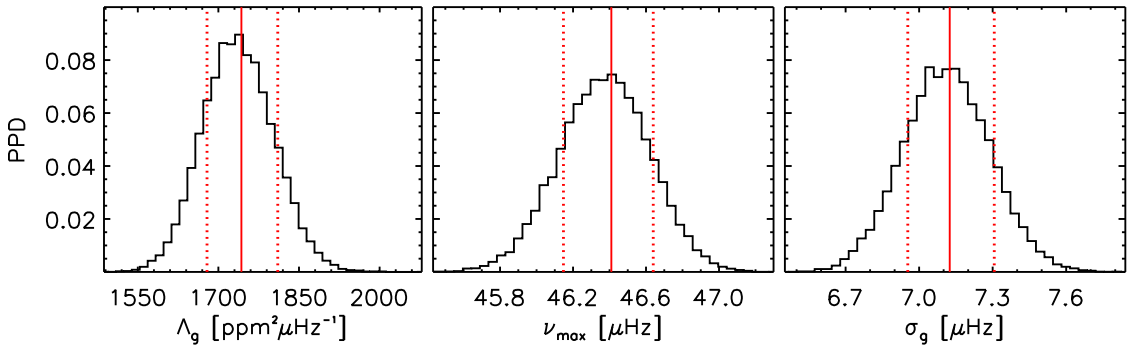

Figure 1.13: Posterior probability distributions (PPD) of the parameters Λ_g, ν_{max}, and σ_g computed by means of the MCMC algorithm. The vertical red solid lines represent median values of the parameters of the Gaussian fit (eq. 1.11) to the oscillation power excess of KIC 8410637. The vertical red dotted lines indicate the boundaries of the 68 % credible intervals.

lie within the prior parameter space. At each iteration, a parameter is randomly changed by a small value within an arbitrary range to ensure that the new parameter space is close to the previous point. While at the beginning the amount of change can be large, it should decrease when the search algorithm approaches the true value towards the end of the total number of iterations. Based on the proposed value, the likelihood is re-evaluated. If a higher likelihood is achieved, the new value is accepted and the so-called Markov chain moves to this position in the parameter space. Otherwise, the proposed value is rejected and the parameter remains the same in the next iteration. With each iteration the chain is extended and after a sufficient number of samples are drawn, a random walk through the prior parameter space is accomplished. To avoid local minima, the algorithm accepts certain bad samples in proportion to the evaluated likelihood. In addition, multiple chains are generated, which start at random places within the prior parameter space. In the end, the chain with the best likelihood is chosen and used to build the posterior probability density function containing all accepted values after an initial 'burn-in' phase. Due to the burn-in period, the influence of random starting values of the chain is minimized, since a certain fraction of earlier parameter samples is discarded. The posterior probability density function of the sample can be used to compute the best parameter set and its credible intervals.

It is important to check the mixing and the convergence of the chains, because MCMC algorithms stop after a number of iterations when a certain sample size is reached. The MCMC sample can be examined graphically by means of trace plots, histograms and density plots.

The parameter estimations in Chapter 2 were carried out by using the Metropolis-Hastings MCMC method. Figure 1.13 shows the posterior parameter distributions normalized by the frequency of the counts (probability) of the Gaussian parameters for KIC 8410637, which was one of the stars under study. The most likely parameter values are located in the high-probability regions.

1.3.8 Determination of asteroseismic stellar parameters

The stellar parameters of oscillating red-giant stars can be determined by using different asteroseismic methods. The two global oscillation parameters ($\nu_{\rm max}$ and $\Delta\nu$) together with spectroscopic effective temperatures and global metallicities are most frequently used as input parameters for deriving asteroseismic mean densities and surface gravities. Based on these fundamentals it is possible to infer stellar masses and radii, luminosities, and ages.

Direct method through asteroseismic scaling relations: While the mean density ($\bar{\rho}$) can be computed based on $\Delta\nu$ alone, $\nu_{\rm max}$ and effective temperature ($T_{\rm eff}$) are required for the calculation of the surface gravity ($\log g$) from the asteroseismic scaling relations.

The parameter $\nu_{\rm max}$ can be defined as the observed frequency where the oscillations reach a maximum amplitude. This observable can be further related to the physical properties in the near-surface layers of the star, where the acoustic cut-off frequency ($\nu_{\rm ac}$) affects the modes of oscillations. Since both frequencies could be linked empirically, and because $\nu_{\rm ac}$ is proportional to g and T (Lamb 1932):

$$\nu_{\rm ac} \propto gT^{-1/2} \quad \text{and} \quad g \propto \frac{M}{R^2}, \tag{1.23}$$

$\nu_{\rm max}$ can be used to obtain g, M, and R, if $T_{\rm eff}$ of the star is known (e.g. Brown et al. 1991, Kjeldsen and Bedding 1995):

$$\nu_{\rm max} = \nu_{\rm max\odot} \frac{M/{\rm M}_\odot}{(R/{\rm R}_\odot)^2} \sqrt{\frac{T_{\rm eff,\odot}}{T_{\rm eff}}}. \tag{1.24}$$

A theoretical explanation for the $\nu_{\rm max}$ scaling relation does not exist. A first step towards exploring equation 1.24 from the theoretical point of view is provided by Belkacem et al. (2011).

The observed mean large frequency separation $\Delta\nu$ is proportional to the inverse of the sound-travel time in the star. The parameter is further related to the stellar mean density $\bar{\rho}$ according to:

$$\Delta\nu \simeq \left(2\int_0^R \frac{1}{c}dr\right)^{-1} \propto \sqrt{\bar{\rho}}, \tag{1.25}$$

where c is the sound speed and r is the distance to the stellar centre, and thus (Ulrich 1986):

$$\Delta\nu = \Delta\nu_\odot \sqrt{\frac{M/{\rm M}_\odot}{(R/{\rm R}_\odot)^3}}. \tag{1.26}$$

The asteroseismic scaling relations are only approximations. By assuming an uncertainty of $\sim 2.5\,\%$ for $\Delta\nu$, of $\sim 5\,\%$ for $\nu_{\rm max}$ and of $\sim 1.5\,\%$ for $T_{\rm eff}$, one obtains an uncertainty of ~ 20 and $\sim 10\,\%$ in stellar mass and radius, when derived from equations 1.24 and 1.26 (Basu and Chaplin 2017). In addition, the $\nu_{\rm max}$ and $\Delta\nu$ scaling relations have to be scaled. Usually, the Sun is adopted as a reference and so inherently it is assumed that the structure of the interior of stars is the same. This assumption does not hold, since both

theoretical predictions and observations show that many structural changes occur during the evolution of a star. Therefore, many studies proposed modifications to the original asteroseismic scaling relations or suitable reference values in order to improve the asteroseismic stellar parameter estimates for stars with different masses, metallicites, temperatures, and evolutionary stages from the main sequence to the red-giant branch (e.g. White et al. 2011, Miglio et al. 2012, Mosser et al. 2013, Hekker et al. 2013b, Guggenberger et al. 2016, Sharma et al. 2016, Rodrigues et al. 2017, Viani et al. 2017, Guggenberger et al. 2017, Themeßl et al. 2018). Chapter 2 presents a dedicated study of three red-giant stars in eclipsing binary systems, where a new reference value for the $\Delta\nu$ scaling relation (eq. 1.26) was found, which takes the mass, effective temperature, and metallicity dependence of the stars, as well as the surface effect into account.

Grid-based modelling: A set of asteroseismic stellar parameters can be derived by using a pre-computed grid of stellar models (e.g. Gai et al. 2011). An advantage of this method is that additional knowledge about the structure and evolution of stars can be included. In order to search for matching stellar models a set of observables is used. The different choices of input parameters include the global oscillation parameters, effective temperatures, global metallicities, period spacings, luminosities, and parallaxes. Usually, the asteroseismic scaling relations are used to calculate $\Delta\nu$ and $\nu_{\rm max}$ for stellar models, although the mean large frequency separation can also be derived from calculations of computed frequencies. An advantage of grid-based modelling is that stellar ages are provided, which is not possible by using the asteroseismic scaling relations. Chapter 3 of this thesis discusses the importance of metallicity for asteroseismic stellar parameter determinations based on grid-based modelling.

One of the issues of this method is that a stellar model can be obtained, which satisfies the global properties of the star, yet it can have a different age and internal structure. Therefore, it would be useful to also add the knowledge from individual oscillation frequencies in the stellar modelling approach. Due to high-precision photometric data from space missions, many individual mode frequencies can be measured for solar-like oscillators. In order to use the information provided by the frequencies, it is important to relate the observed frequencies to those calculated from stellar models. In this regard, the 'surface effect' plays an important role. This effect is caused by improper modelling of the convective near-surface layers of the star. Convective regions in stars are usually approximated by mixing-length theory in stellar models, although the whole process of convection and turbulence is much more complex. As a result, the surface effect causes a systematic shift between modelled and observed frequencies that gets larger with increasing frequency. In addition, p modes of all spherical degrees are affected, which is an indication that this effect is connected to the stellar surface (Ball 2017). Several groups suggested parametric forms for a function to describe the surface effect of mode frequencies in other stars, e.g. a power law (correction) with an index fixed to a solar-calibrated value (Kjeldsen et al. 2008); direct scaling of the solar offset on a suitable frequency scale (Christensen-Dalsgaard 2012); corrections that are based on mode inertia with a cubic and combined term (Ball and Gizon 2014, Ball et al. 2016, Ball and Gizon 2017, Ball et al. 2018), and a modified Lorentzian (Sonoi et al. 2015).

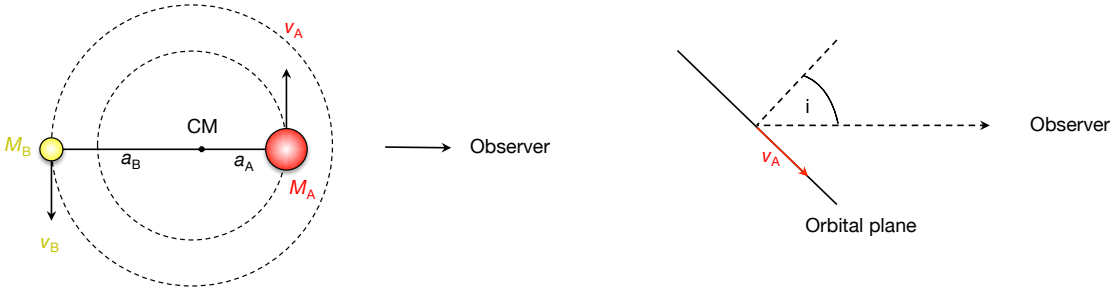

Figure 1.14: Left: Illustration of two stars with masses (M_A, M_B) and relative velocities (v_A, v_B) moving on circular orbits around a common centre of mass (CM) of the system. Parameters a_A and a_B represent semi-major axes. Right: Observable is the velocity along the line of sight of the star, which can be defined as: $v_{r,A} = v_A \sin i$, since the binary system is observed at an angle i with respect to the observer.

1.3.9 Stellar parameters from 'classical' methods

In order to further validate and improve asteroseismic results one can use additional knowledge about the properties of stars under study, when available. For stars in binary systems or open clusters we do have additional knowledge as these stars are assumed to be born at about the same time, from material with the same initial chemical composition, and they are located at about the same distance. These additional constrains can be used to derive stellar parameters with higher accuracy. Hence, binary and cluster stars provide a robust benchmark for testing the asteroseismic stellar parameters and for improving age estimates.

Basic principles of eclipsing binary analysis: Observational studies show that most (nearby) stars are formed in binary ($\geq 50\,\%$) or multiple systems (e.g. Batten 1973, Shu et al. 1987, White and Ghez 2001, Kirk et al. 2016). The study of binaries is very valuable for astrophysics, since the masses in a binary system can be determined both, accurate and precise, by using Kepler's laws. This is not the case for isolated field stars, where the stellar parameters can only be determined with larger uncertainties. The different types of binary stars can be classified according to their appearance on the sky, i.e. optical, visual, astrometric, and spectroscopic binaries, as well as according to the orientation of their orbits with respect to the line of sight, i.e. eclipsing binaries, and according to the level of their physical interaction, i.e. detached, semi-detached and contact systems. In addition, there are also optical (apparent) doubles, which are not gravitationally bound and only appear as companion stars due to projection effects when they lie along the same line of sight. Of particular interest are double-lined eclipsing binary systems (EBs). They have orbital planes lying near the line of sight to the observer ($\approx 90°$) and their spectrum is composed of spectral lines from both binary components. In these systems, the dynamical masses and radii of each individual component can be derived from the combined analysis of radial velocity data (spectroscopy) and light curves (photometry).

The basic concept of binary analysis is build on Kepler's 3rd law, which states that the squares of orbital periods are proportional to the cubes of the semi-major axis. As a basis, one can consider an isolated binary system that comprises two stars with similar

masses M_A and M_B that move on circular orbits around a common centre of mass. The movements of the binary components are influenced by their mutual gravitational forces without any further interactions taking place between them. This constitutes a classical two-body problem, which can be solved in the reference frame of the centre of mass. From the definition of the centre of mass, the ratio of the stellar masses satisfies the condition:

$$\frac{M_A}{M_B} = \frac{a_B}{a_A}, \tag{1.27}$$

where a_A and a_B are the orbital radii (see left panel in Fig. 1.14). After applying Newton's laws of motion and Newton's law of gravity we can express Kepler's 3rd law for circular orbits as:

$$M_A + M_B = \frac{4\pi^2}{G}\frac{a^3}{P_{orb}^2}, \tag{1.28}$$

where G is the gravitational constant, P_{orb} is the orbital period, and a is the semi-major axis of the binary orbit, i.e. the total separation between the stars with $a = a_A + a_B$. As an additional note, equation 1.28 is also valid for elliptical orbits, which will not be described in further detail here. From equation 1.28 follows, that the sum and ratio of masses can be calculated, if the period and semi-major axis of the binary system are known. Since it is particularly difficult to obtain a for distant binary systems, one can derive the velocities of the stars instead in order to substitute a in Kepler's 3rd law. Based on the assumption that the orbits are circular, the relative velocities of the two binary components (v_A, v_B) can be expressed as:

$$v_A = \frac{2\pi a_A}{P_{orb}} \text{ and } v_B = \frac{2\pi a_B}{P_{orb}}. \tag{1.29}$$

These velocities remain constant around the orbit. From this follows:

$$a = a_A + a_B = \frac{P_{orb}}{2\pi}(v_A + v_B), \tag{1.30}$$

which substituted into Kepler's 3rd law provides the relation between the sum of masses and the relative velocities of the stars:

$$M_A + M_B = \frac{P_{orb}}{2\pi G}(v_A + v_B)^3. \tag{1.31}$$

However, due to projection effects only the component of velocity along the line of sight, i.e. the radial velocity (RV), can be observed (see right panel in Fig. 1.14). In practise, RV variations of stars can be measured from spectral lines. The lines in a spectrum are shifted due to the Doppler effect, which describes the relative motion of a star with respect to the observer. For $v_r << c$, the Doppler shift is given by:

$$\frac{\lambda_{obs} - \lambda_{rest}}{\lambda_{rest}} = \frac{\Delta\lambda}{\lambda} = \frac{v_r}{c}, \tag{1.32}$$

where λ_{obs} is the observed wavelength, λ_{rest} is the wavelength one would obtain if the star was at rest, v_r is the radial velocity component along the line of sight, and c is the speed of light. A positive value of v_r indicates that the star is receding from the observer.

Then, the lines are shifted towards redder wavelength (redshift). A negative value of v_r shows that the object is moving towards the observer and the lines are shifted to bluer wavelength (blueshift). When all phases of the binary orbit are well sampled with RVs, it is possible to describe the orientation of the binary system with a number of orbital elements. To determine these variables, the RVs are plotted as a function of time and/or phase. Then, by fitting the RVs to the shape of the velocity curve, one obtains the orbital period, eccentricity, and semi-major axis together with additional parameters that define the binary orbit and its orientation on the sky. The observed radial velocities ($v_{r,A}, v_{r,B}$) are related to the true relative velocities according to:

$$v_{r,A} = v_A \sin i, \tag{1.33}$$

$$v_{r,B} = v_B \sin i, \tag{1.34}$$

where i represents the inclination angle of the orbital plane of the system with respect to the observer. Thus, $v_{r,A}$ and $v_{r,B}$ represent the lower limits to v_A and v_B. By including this, the relation between the ratio of the masses and the observed radial velocities can be expressed as:

$$\frac{M_A}{M_B} = \frac{a_B}{a_A} = \frac{v_B}{v_A} = \frac{v_{r,B}}{v_{r,A}}, \tag{1.35}$$

and by substituting the true relative velocities in Kepler's 3rd law, one obtains:

$$M_A + M_B = \frac{P_{orb}}{2\pi G} \frac{(v_{r,A} + v_{r,B})^3}{\sin^3 i}. \tag{1.36}$$

While the mass ratio can be derived independently of the inclination of the orbit of the binary system, the knowledge of i is necessary for deriving the sum of masses. If i remains unknown, stellar masses have a $\sin i$ ambiguity and only the minimum masses ($M_A \sin^3 i, M_B \sin^3 i$) and the minimum orbital separation ($a \sin i$) can be obtained. In case of EBs, the orbital inclination i can be computed from the light curve data, and thus dynamical stellar masses can be determined for each component in the system.

Another parameter of interest is the stellar radius, which for components in eclipsing binaries can be derived from the analysis of the light curve, which shows the brightness variations of a star over time. A distinct feature of the light curve of EBs are the distinct dips in brightness, when the components periodically eclipse one another. These eclipses can only be observed, when the inclination angle of the systems is close to 90°. Their shape depends on the types of stars that are involved and in particular on their luminosities, radii, and effective temperatures, as well as the inclination of the binary orbit. Figure 1.15 shows part of the *Kepler* light curve of KIC 8410637, which is an eclipsing binary system that consists of an oscillating red-giant component and a main-sequence companion star. The deeper eclipse occurs, when the main-sequence star passes behind the red giant, while the eclipse is shallower when part of the red-giant surface is obscured by the main-sequence star. By fitting a geometrical model to the light curve, it is possible to determine the orbital period of the system from the eclipse period, which defines the radius of the binary orbit. One of the challenges of fitting light curve data is that the surface brightness of the visible disc of a distant star decreases towards the edge. This effect is known as limb darkening and has to be accounted for in the model. Moreover, the depth

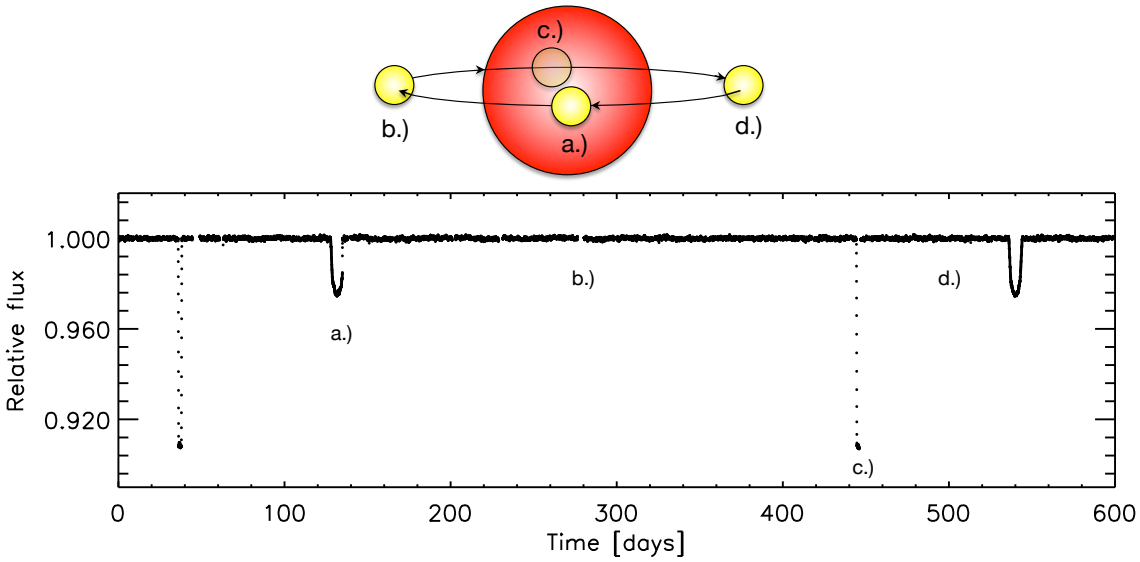

Figure 1.15: Part of the *Kepler* light curve of the eclipsing binary system KIC 8410637. Two primary and two secondary eclipses are shown. Letters a.) - d.) indicate approximate positions of the binary stars with respect to each other during one orbit, which is shown in the graphic above.

of the eclipse minimum is related to the effective temperature of the eclipsed star. Hence, the ratio of the effective temperatures of the binary stars can be derived. Furthermore, from the timing and the duration of eclipses, one can measure the radii of both binary components. The radius of the smaller star (R_A) can be calculated from the time duration from first contact (t_a) to minimum light (t_b) of the eclipse (see right panel in Fig. 1.16):

$$v = \frac{2R_A}{t_b - t_a} \Rightarrow R_A = \frac{v}{2}(t_b - t_a), \tag{1.37}$$

where $v = v_A + v_B$ is the relative velocity of the two stars. Similarly, the time duration from first contact (t_a) to first exposure (t_c) of the eclipse provides the radius of the larger star (R_B):

$$v = \frac{2R_B}{t_c - t_a} \Rightarrow R_B = \frac{v}{2}(t_c - t_a) = R_A + \frac{v}{2}(t_c - t_b). \tag{1.38}$$

If RVs are available, individual stellar radii can be derived for each component of an eclipsing binary system. Without RVs, only the ratio of the radii can be computed.

The light curves and RVs of a binary system can be modelled together by using dedicated analysis codes such as JKTEBOP (Southworth 2013, and references therein). This algorithm provides the physical properties of the eclipsing binary system including the dynamical stellar parameters (e.g. masses, radii, logarithmic surface gravities, mean densities) of its components.

Basic principles of isochrone fitting to star clusters: Star clusters are important stellar laboratories for astrophysical studies due to the wide range of masses, luminosities, effective temperatures, and different evolutionary stages that are found in a cluster. Cluster stars are born from the same molecular cloud at approximately the same time. Thus,

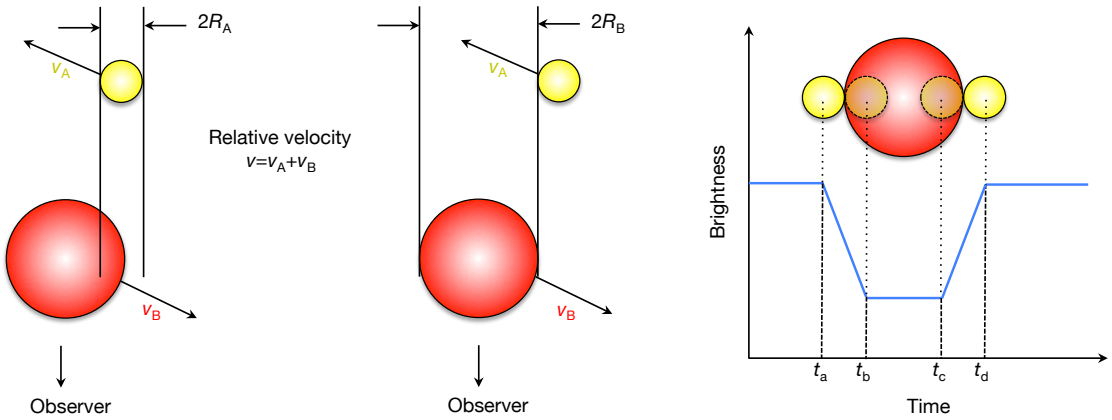

Figure 1.16: Illustration of the determination of individual radii for components of an eclipsing binary system. Left: Radius determination of the smaller star. Middle: Radius determination of the larger star. Right: Relation between radii and timing of eclipse. See text for further details.

one expects a population of stars in a cluster with common properties. Their similar ages, metallicities, and distances make cluster stars ideal test objects for investigating the formation and evolution of stars, the dynamical interactions that take place between them, as well as the formation of our own Galaxy, and its chemical and dynamical evolution.

There are two types of star clusters, i.e. globular and open clusters. Globular clusters resemble tight spherical bundles that contain hundreds of thousands of usually old and metal-poor stars. They are located around the centres of galaxies. Owing to their age, the most massive cluster members have already exploded as supernova. Globular clusters were formed during the early phases of the formation of the Galaxy, thus providing a limit to the age of the universe, since the oldest clusters have to be younger than the universe itself. In contrast, open clusters have an irregular shape and they comprise a more loosely-bound collection of stars. Generally, hundreds to a few thousands of generally young and metal-rich stars are found in these clusters. Open clusters are mostly located in the Galactic plane and they gradually fall apart. When non-cluster-members are passing through, they can disrupt the motion of the cluster stars, which causes members to be ejected during this interaction.

A common way to estimate the age of a cluster is to use brightness and colour measurements of individual cluster stars that can be plotted together in a colour-magnitude diagram (CMD). Figure 1.17 shows the apparent magnitudes V versus colour index $B-V$ for observed stars in the region of NGC 6791, which is an old ($\sim$ 8.5 Gyr) metal-rich ([M/H] $\approx$ +0.35 dex) open cluster that has been extensively studied over decades (e.g. Stetson et al. 2003, 2005). In the CMD of the cluster, the main sequence is densely populated by observed stars and a well defined turn-off is visible. This point in stellar evolution, when stars evolve off the main sequence, is a commonly used indicator for the age of the cluster. By comparing theoretical calculations of mono-age populations, i.e. isochrones, to observed colour-magnitude measurements of cluster stars, it is possible to derive the physical properties of a cluster. This technique is known as isochrone fitting and it requires a suitable grid of models, which can describe the stellar properties of every

star in the cluster population. Each isochrone is characterized by a fixed age and metallicity. Along the isochrone a set of stellar parameters such as mass, luminosity, effective temperature, surface gravity, as well as magnitudes, are provided.

A source of systematic uncertainty in the isochrones is introduced by the conversion from luminosities and temperatures to absolute magnitudes and colours in different photometric systems. This step requires appropriate tabulations of bolometric corrections and colours, which can be obtained from a convolution of spectral energy distributions from spectral libraries with response functions of filters. A necessary input parameter is the total extinction. The interaction of starlight with dust grains along the line of sight prevents some stellar photons from reaching the observer. This effect is called interstellar extinction and reddening. Due to the absorption and scattering of blue light, distant stars appear dimmer and redder in an optical filter. Interstellar reddening ($E_{\mathrm{B-V}}$) can be estimated from the observed colour index $B - V$ of a star by comparing it to its intrinsic value $(B - V)_0$:

$$E_{\mathrm{B-V}} = (B - V) - (B - V)_0. \tag{1.39}$$

The total extinction, i.e. the sum of absorption and scattering of star light, is wavelength dependent and can be derived from the colour excess:

$$E_{\mathrm{B-V}} = \left(\frac{A_{\mathrm{B}}}{A_{\mathrm{V}}} - 1\right) A_{\mathrm{V}} = 0.324\, A_{\mathrm{V}} \Rightarrow A_{\mathrm{V}} = 3.086\, E_{\mathrm{B-V}}, \tag{1.40}$$

where A_{B} and A_{V} are the total extinctions in the photometric bands B and V. The ratio $A_{\mathrm{B}}/A_{\mathrm{V}}$ represents the wavelength dependence of extinction based on the empirically derived Milky Way extinction law with $A_{\mathrm{B}} = 1.324$ and $A_{\mathrm{V}} = 1$. Without correcting the CMD for the effect of interstellar extinction, the age and distance estimates of the cluster from isochrone fitting would be compromised.

Moreover, stellar isochrones provide absolute magnitudes, while apparent magnitudes are observed for the cluster stars. Thus, one needs to apply a conversion before isochrone fitting can be performed. Stellar magnitudes are defined on a logarithmic scale with larger values representing fainter stars. The observed brightness of stars is given in apparent magnitudes, i.e. the appearance of the brightness of the star at its distance from the observer. Absolute magnitudes are a measure of the apparent magnitude of the star if viewed at a distance of 10 pc from the observer. In order to convert between absolute (M) and apparent (m) magnitudes, the distance modulus can be used:

$$m - M = 5 \log\left(\frac{d}{10}\right) + A_{\mathrm{V}}, \tag{1.41}$$

where d is the distance in units of pc. This relation is in particular useful for determining the distance to a star in cases where both, the apparent and absolute, magnitudes are known. From equation 1.41 follows, that one needs to know the distance to a cluster in order to convert the magnitudes.

Once these issues are solved, isochrones can be fitted to the colour-magnitude data of cluster stars. Commonly, the physical properties of clusters are derived from visual fitting of the main sequence and the turn-off point, mostly because there is no parametric form of the isochrones. Instead, each isochrone comprises tabulated points for a set of stellar

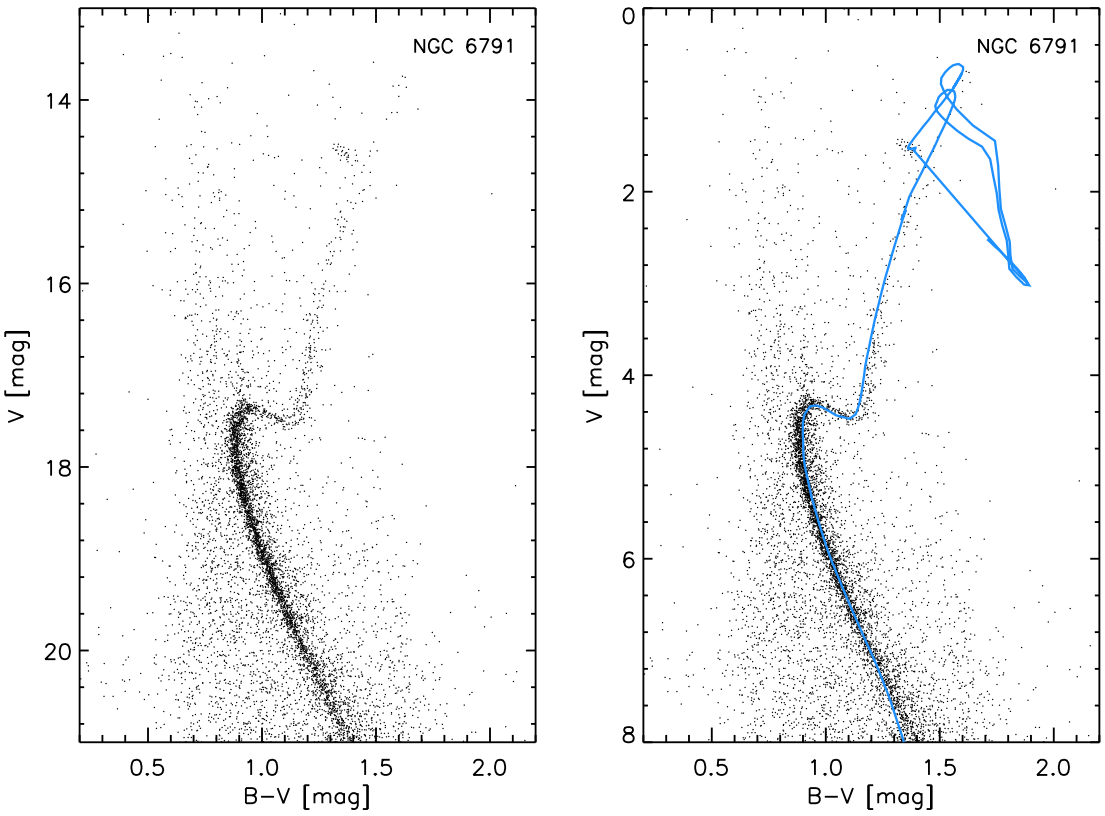

Figure 1.17: Left: The observed colour-magnitude diagram (CMD), i.e. apparent V magnitudes versus colour index $B - V$, of NGC 6791 (Stetson et al. 2003, 2005). Right: An isochrone (in blue) is shown on top of the CMD of NGC 6791. Here, apparent magnitudes of the extinction-corrected isochrones were transformed into absolute magnitudes by using the distance modulus.

parameters (luminosity, effective temperature, surface gravity) with a constant age and metallicity. Using this traditional technique, one first adjusts the ZAMS to the observed CMD of the cluster, which provides an estimate of the interstellar reddening. Then after fixing this parameter, the distance and age can be derived through adjustments of the isochrones to the CMD. Since this approach is based on visual inspections, it is a subjective method that is prone to incorrect results. Frayn and Gilmore (2003) pointed out that similar geometrical properties of isochrones lead to large discrepancies in the age and metallicity estimates from isochrone fitting. Due to the age-metallicity degeneracy, an isochrone with an increased metal abundance is very similar to an isochrone with a higher age. Moreover, the distance-metallicity degeneracy can lead to an underestimate in the true metallicity when stellar magnitudes are overestimated, while the true metallicity can be overestimated in cases where distances are underestimated. These discrepancies can be of the order of 20 %. In addition, the interstellar reddening causes the star to appear dimmer, which can be reflected in a larger distance, while a shift to redder colours results in an increased metallicity. Due to the similarities in the geometry of isochrones with different ages and metallicities, it is better to use a proper statistical framework in order to match isochrones with observed data and to evaluate the goodness of fit.

Among the first statistical approaches that were introduced to perform isochrone fitting was the deterministic 'near point estimator' method, which was described by e.g. Flannery and Johnson (1982). Based on this approach, one uses a statistic to measure the coincidence between isochrones and stars in a CMD through minimization of a χ^2 statistic. Moreover, with this method one assumes that stars are uniformly distributed along the isochrone. The set of observed data (N) is defined as $(x_{i,\mathrm{obs}}, y_{i,\mathrm{obs}})$ with $i = 1, ..., N$, where $(x = B-V)$ and $(y = V)$ are the coordinates in the observed CMD, while individual isochrones consist of a set of coordinates $(x_{\mathrm{mod}}, y_{\mathrm{mod}})$ in the theoretical CMD. It is possible to compute the minimum distance between each pair of $(x_{i,\mathrm{obs}}, y_{i,\mathrm{obs}})$ with each isochrone. The nearest point of the isochrone is then given by:

$$(x_{i,\mathrm{mod}}, y_{i,\mathrm{mod}}) = \min_{(x_{\mathrm{mod}}, y_{\mathrm{mod}})} \{(x_{i,\mathrm{obs}} - x_{\mathrm{mod}})^2 + (y_{i,\mathrm{obs}} - y_{\mathrm{mod}})^2\}. \tag{1.42}$$

Then, the χ^2 statistic of the observed data with respect to that isochrone can be calculated according to:

$$\chi^2 = \sum_{i=1}^{N} \left(\frac{(y_{i,\mathrm{mod}} - y_{i,\mathrm{obs}})^2}{\sigma_{i,\mathrm{y}}^2} + \frac{(x_{i,\mathrm{mod}} - x_{i,\mathrm{obs}})^2}{\sigma_{i,\mathrm{x}}^2} \right), \tag{1.43}$$

where $\sigma_{i,\mathrm{y}}$ and $\sigma_{i,\mathrm{x}}$ are the uncertainties of the observed colour-magnitude measurements. The isochrone with the lowest χ^2 value is considered to be close to the actual age and metallicity of the cluster under study. Uncertainties in the estimated parameters can be derived from the elements of the covariance matrix. The right panel of Figure 1.17 shows an isochrone (in blue) placed on the CMD of NGC 6791, which was obtained through isochrone fitting by using a similar formulation as the near point estimator method introduced by Flannery and Johnson (1982).

Besides using the geometrical shapes of isochrones to find the age and metallicity of a cluster, it can be useful to apply a more elaborate statistical basis that can be described with a Bayesian formalism. A useful feature of Bayesian techniques is that individual probabilities of membership can be assigned to different populations of stars in a cluster. These methods are computationally intensive and it is not easy to include them in the fitting and evaluation process of isochrones. Valls-Gabaud (2014) provides a recent review on Bayesian isochrone fitting and discusses different statistical methods that are commonly used, including some descriptions about the different treatments that can be applied to single objects, binaries, and whole ensembles of stars.

1.3.10 Scope of this thesis

My research is focused on asteroseismic studies of oscillating red-giant stars that are either components of eclipsing binary systems or that are part of open clusters. In addition, I may have found a rare candidate binary system that comprises two oscillating red-giant components.

- ⋆ In **Chapter 2**, I describe the analysis of three eclipsing binary systems that were observed during the nominal *Kepler* space mission with supplementary spectroscopic data available from ground-based observatories. In this study, I investigate consistencies between asteroseismic and dynamical stellar parameters for the oscillating red-giant components in these systems. I found a new reference value for the $\Delta\nu$-scaling relation (eq. 1.26) that takes mass, effective temperature, metallicity, as well as surface effects, for red-giant stars into account. This reference provides parameter estimates that agree when obtained from asteroseismic scaling relations and when obtained from the orbital analysis.

- ⋆ In **Chapter 3**, I present an asteroseismic ensemble analysis of about 60 red giants in the open clusters NGC 6791 and NGC 6819. For the asteroseismic age determinations, I use additional constraints from the physical properties (metallicity) of the open clusters that are derived from isochrone fitting. I show that the accuracy of the obtained metallicity of individual stars is the limiting factor in determining accurate ages.

- ⋆ **Chapter 4** is dedicated to the in-depth study of a rare *Kepler* Fourier power density spectrum, which shows solar-like oscillations of two red-giant stars. Based on the stellar properties (masses, ages, and distances) of both stars, I investigate the probability of this pair of stars being gravitationally bound into a binary star system. Based on the similar asteroseismic ages and masses for both stars this is a rare candidate binary system consisting of either two red-giant-branch stars or a red-giant-branch and asymptotic-giant-branch combination.

- ⋆ Finally, **Chapter 5** provides the final discussion and future prospects concerning asteroseismic inferences of red-giant stars in eclipsing binaries and open clusters.

Chapter 2

2 Red giants in eclipsing binaries

This chapter reproduces the article *Oscillating red giants in eclipsing binary systems: empirical reference value for asteroseismic scaling relation* by N. Themeßl, S. Hekker, J. Southworth, P. G. Beck, K. Pavlovski, A. Tkachenko, G. C. Angelou, W. H. Ball, C. Barban, E. Corsaro, Y. Elsworth, R. Handberg, and T. Kallinger, published in Monthly Notices of the Royal Astronomical Society, Volume 478, Issue 4, p.4669-4696 (2018), DOI: 10.1093/mnras/sty1113. The Author(s) Published by Oxford University Press on behalf of the Royal Astronomical Society[1].

2.1 Summary

The internal structures and properties of oscillating red-giant stars can be accurately inferred through their global oscillation modes (asteroseismology). Based on 1460 days of *Kepler* observations we perform a thorough asteroseismic study to probe the stellar parameters and evolutionary stages of three red giants in eclipsing binary systems. We present the first detailed analysis of individual oscillation modes of the red-giant components of KIC 8410637, KIC 5640750, and KIC 9540226. We obtain estimates of their asteroseismic masses, radii, mean densities, and logarithmic surface gravities by using the asteroseismic scaling relations as well as grid-based modelling. As these red giants are in double-lined eclipsing binaries, it is possible to derive their independent dynamical masses and radii from the orbital solution and compare them with the seismically inferred values. For KIC 5640750 we compute the first spectroscopic orbit based on both components of this system. We use high-resolution spectroscopic data and light curves of the three systems to determine up-to-date values of the dynamical stellar parameters. With our comprehensive set of stellar parameters we explore consistencies between binary analysis and asteroseismic methods, and test the reliability of the well-known scaling relations. For the three red giants under study, we find agreement between dynamical and asteroseismic stellar parameters in cases where the asteroseismic methods account for metallicity, temperature, and mass dependence, as well as surface effects. We are able to attain agreement from the scaling laws in all three systems if we use $\Delta\nu_{\mathrm{ref,emp}} = 130.8 \pm 0.9\,\mu$Hz instead of the usual solar reference value.

[1]Contribution statement: NT and SH designed research. NT performed asteroseismic analysis and wrote the paper. SH carried out grid-based modelling analysis. JS, KP, PGB and AT performed eclipsing binary analysis. CB, EC and TK provided independent background-fitting and peakbagging results for a consistency check. RH contributed corrected *Kepler* light curves. SH, YE, WHB and GCA provided useful advice, comments, and discussions on the paper.

2.2 Introduction

Asteroseismology is the study of stellar oscillations with the aim of unravelling the structure and dynamics of stellar interiors. In-depth asteroseismic studies require either high-precision photometric time series observations or time series of accurate radial velocity measurements (RVs). The former has been obtained by space missions such as MOST (e.g. Barban et al. 2007, Kallinger et al. 2008), CoRoT (e.g. Baglin et al. 2007, De Ridder et al. 2009) and *Kepler* (e.g. Borucki et al. 2010). From 2009 to 2013, the nominal *Kepler* mission provided nearly continuous photometric time series data for more than 100 000 stars. These data are suitable for asteroseismic analyses and led to many discoveries in the field of red-giant seismology: determination of evolutionary stages (e.g. Bedding et al. 2011, Mosser et al. 2014, Elsworth et al. 2017), rotation studies (e.g. Beck et al. 2012, Mosser et al. 2012a), stellar parameter determinations (Kallinger et al. 2010, Huber et al. 2010, Hekker et al. 2013b), ensemble studies and galactic archaeology (e.g. Corsaro et al. 2012, Miglio et al. 2013, Casagrande et al. 2016), amongst others. For recent overviews see Hekker (2013) and Hekker and Christensen-Dalsgaard (2017).

Pulsating red giants exhibit solar-like oscillations that are driven by the turbulent convection in the stellar envelope. The physical properties of red giants, such as mean density and surface gravity and thus stellar mass and radius, can be determined through the study of their oscillations. The most commonly used asteroseismic method is based on scaling relations (e.g. Ulrich 1986, Brown et al. 1991, Kjeldsen and Bedding 1995) that use direct observables from the oscillation spectrum as input. These so-called global oscillation parameters can be measured in a large number of red giants for which high-precision photometric data are available. However, the asteroseismic scaling relations assume that all stars have an internal structure homologous to the Sun (e.g. Belkacem et al. 2013). Since evolved G and K giants span a wide range of masses, metallicities, and evolutionary stages different than that of the Sun, the validity of these scaling relations, based on the principle of homology to the Sun, has to be tested. One possibility is to use eclipsing binary systems with a pulsating red-giant component. For double-lined eclipsing binaries, the stellar mass and radius of the red-giant component can be derived independently of asteroseismology through the binary orbit analysis using Kepler's laws. The binary analysis is limited to the cases in which the orbital parameters can be resolved and require spectra covering the full orbital period of the system.

So far a number of eclipsing binary systems with a red-giant component were detected in *Kepler* data (e.g. Hekker et al. 2010c, Gaulme et al. 2013). The first such system, KIC 8410637, was identified by Hekker et al. (2010c), who carried out a preliminary asteroseismic study based on a month long photometric time series of data in which only one eclipse was detected. The stellar parameters of the red-giant star could be measured from both the solar-like oscillations and from spectroscopy. A detailed comparison between the asteroseismic and dynamical stellar mass and radius of the red giant was performed by Frandsen et al. (2013), who found agreement between the binary and asteroseismic results within uncertainties. When Huber (2014) repeated the asteroseismic analysis of KIC 8410637 with a longer *Kepler* dataset, he contested the findings of Frandsen et al. (2013) and reported large discrepancies between the asteroseismic and dynamical stellar parameters.

Beck et al. (2014) carried out a seismic and binary analysis of 18 red-giant stars among which was KIC 9540226. The red giant was not only found to be in an eccentric eclipsing binary, but also to exhibit an increase in flux during the actual periastron passage (Kumar et al. 1995, Remus et al. 2012). These stars are colloquially referred to as 'heartbeat stars' (Thompson et al. 2012). Beck et al. calculated the orbital parameters of the system from high-resolution spectroscopy and estimated the stellar parameters of the red giant from the asteroseismic scaling relations. In a more recent study, the mass and the radius of the red-giant component of KIC 9540226 could be constrained from two consecutive binary analyses[2] (Brogaard et al. 2016, 2018). Moreover, Brogaard et al. (2018) computed several estimates of its asteroseismic mass and radius based on different methodologies and by using the asteroseismic observables presented by Gaulme et al. (2016).

KIC 8410637, KIC 5640750, and KIC 9540226 were also part of several ensemble studies[3] (Gaulme et al. 2013, 2014, 2016, hereafter G16). In these surveys, eclipse modelling and modelling of the radial velocities were used to derive the orbital and dynamical stellar parameters. In addition, masses and radii of the red-giant components were computed by using the asteroseismic scaling relations. In an extensive comparison between the results from detailed binary modelling and asteroseismology, they showed that the stellar masses and radii are systematically overestimated when the asteroseismic scaling relations are used.

In Table 2.1 we summarize the orbital and stellar parameters for the three red-giant stars (KIC 8410637, KIC 5640750, and KIC 9540226) that are the subject of this study.

For a number of red-giant components in eclipsing binary systems it has been found that the dynamical and asteroseismic stellar parameters differ significantly. This leads us to investigate three such systems in detail, both from the binary point of view including a dedicated spectral disentangling analysis as well as by obtaining individual frequencies. In addition to the observational analysis, we use an asteroseismic grid-based approach to model the three red-giant components. KIC 8410637, KIC 5640750, and KIC 9540226 belong to wide eclipsing binary systems where the components are not expected to be strongly influenced by tidal effects and/or mass transfer. All three systems were observed during the nominal 4-year long *Kepler* mission providing a large photometric dataset of unprecedented accuracy and supplemented with additional high-resolution spectra from ground-based observatories. We analyze these spectroscopic and photometric data and derive up-to-date values of the stellar parameters from both the asteroseismic and orbital analysis. Since the stellar parameters determined using Kepler's laws are considered to be both accurate and precise, they provide a means to test the reliability of the asteroseismic mass and radius from the scaling laws.

For the current in-depth study we obtained orbital solutions and physical properties of three eclipsing binary systems from *Kepler* light curves and phase-resolved spectroscopy (Sec. 2.3). In addition, we analyzed the Fourier spectra of the red-giant components in these systems to derive both global oscillation parameters as well as individual frequen-

[2]Note that we only provide the updated dynamical values of Brogaard et al. (2018) in Tab. 2.1 and Fig. 2.12.

[3]Here we only consider the updated values of Gaulme et al. (2014) and not the results by Gaulme et al. (2013).

cies (Sec. 2.4.3). We studied their asteroseismic stellar parameters and evolutionary states (Sec. 2.4.4). In Section 2.5 we discuss and compare stellar parameters obtained from different asteroseismic methods and from the binary orbit. In the same section we provide an overview of tests that we performed to investigate the importance of different observables that are used for the determination of the asteroseismic stellar parameters and we present the conclusions of our study in Section 2.6.

2.3 Physical properties of the systems from light curves and radial velocity time series

2.3.1 *Kepler* light curves and ground-based spectroscopic data

For the eclipse modelling, we extracted the light curves of each eclipse from the *Kepler* datasets. In this case, we retained all data obtained within three eclipse durations of the eclipse. The data were then converted from flux to magnitude units and a low-order polynomial was fitted to normalize the out-of-transit data to zero relative magnitude. This step removes any slow trends due to instrumental effects and stellar activity. We tested the effects of different treatment of the light curve normalization (e.g. polynomial order), and found that it does not have a significant impact on the best-fitting parameters.

By definition the primary eclipse is deeper than the secondary eclipse, and occurs when the hotter star is eclipsed by the cooler star. For all three objects, the dwarf star is smaller and hotter than the giant, so the primary eclipse is an occultation and the secondary eclipse is a transit. This also means that according to standard terminology (e.g. Hilditch 2001) the dwarf is the primary star and the giant is the secondary star. To avoid possible confusion, we instead refer to the stellar components as the 'dwarf' (denoted as A) and 'giant' (denoted as B).

Complementary to *Kepler* photometry we use spectroscopic data for the binary systems KIC 8410637, KIC 5640750, and KIC 9540226, which were obtained with the HERMES spectrograph (Raskin et al. 2011, Raskin 2011) mounted on the 1.2 m Mercator telescope in La Palma, Canary Islands, Spain. These spectra cover the wavelength range from 3 750 – 9 000 Å with a resolution of $R \simeq 85\,000$. Emission spectra of thorium-argon-neon reference lamps are provided in close proximity to each exposure to allow the most accurate wavelength calibration of the spectra possible. Some HERMES spectra for KIC 8410637 and KIC 9540226 were already used in previous studies by Frandsen et al. (2013) and Beck et al. (2014). Observations were continued to extend the number of spectra and time base of the spectroscopic data. Moreover, the long-period system KIC 5640750 has been monitored spectroscopically by members of our team since its discovery as a binary.

Table 2.1: Stellar and orbital parameters of the red giants studied here obtained from the literature (as per the rightmost column). The orbital periods (P) and eccentricities (e) are determined from orbital analysis of these binary systems. Stellar parameters ($M, R, \log g$) are based on either asteroseismic scaling relations or binary analysis. The latter are indicated with asterisks. Effective temperatures ($T_{\rm eff}$) and logarithmic surface gravities ($\log g$) are mostly derived from spectra within the study referred to. We indicate the cases where they were adopted from the original ([a], Brown et al. 2011) and revised ([b], Huber et al. 2014) *Kepler* input catalogues (KIC).

P [days]	e	R [$R_\odot$]	M [$M_\odot$]	$\log g$	$T_{\rm eff}$ [K]	Evol. phase	Publication
KIC 8410637							
> 75		11.80 ± 0.60	1.70 ± 0.30	2.700 ± 0.150	4650 ± 80		Hekker et al. (2010c)
408.32	0.69	10.74 ± 0.11*	1.56 ± 0.03*	2.569 ± 0.009*	4800 ± 80	RC	Frandsen et al. (2013)
		11.58 ± 0.30	1.83 ± 0.14	2.572 ± 0.011	4800 ± 80		Huber (2014)
408.32	0.69	11.01 ± 0.26	1.61 ± 0.11	2.760 ± 0.400[b]	4872 ± 139[b]	RC	Gaulme et al. (2014)
		11.20 ± 0.20	1.70 ± 0.07	2.569 ± 0.005	4800 ± 100		$G16_{\rm seis}$
		10.75 ± 0.20	1.51 ± 0.07	2.555 ± 0.005	4605 ± 80	RGB	This work$_{\rm seis}$
408.32	0.686	10.60 ± 0.05*	1.47 ± 0.02*	2.556 ± 0.003*	4605 ± 80		This work$_{\rm dyn}$
KIC 5640750							
987.40	0.32	14.27 ± 0.31	1.45 ± 0.09	2.561 ± 0.400[b]	4727 ± 142[b]	RGB/AGB	Gaulme et al. (2014)
		13.08 ± 0.26	1.15 ± 0.06	2.267 ± 0.005	4525 ± 75	RGB	This work$_{\rm seis}$
987.40	0.323	13.12 ± 0.09*	1.16 ± 0.01*	2.266 ± 0.006*	4525 ± 75		This work$_{\rm dyn}$
KIC 9540226							
175.43	0.39	14.10 ± 0.30	1.60 ± 0.10	2.370 ± 0.010	4600 ± 150[a]	RGB	Beck et al. (2014)
175.46	0.39	14.01 ± 0.26	1.59 ± 0.08	2.346 ± 0.030[b]	4761 ± 143[b]	RGB	Gaulme et al. (2014)
		13.60 ± 0.20	1.45 ± 0.05	2.334 ± 0.004	4692 ± 65		$G16_{\rm seis}$
175.44	0.388	12.80 ± 0.10*	1.33 ± 0.05*	2.349 ± 0.008*	4692 ± 65		$G16_{\rm dyn}$
		13.06 ± 0.16*	1.38 ± 0.04*	2.345 ± 0.010*	4680 ± 80		Brogaard et al. (2018)
		12.94 ± 0.25	1.26 ± 0.06	2.314 ± 0.006	4585 ± 75	RGB	This work$_{\rm seis}$
175.44	0.388	13.43 ± 0.17*	1.39 ± 0.03*	2.326 ± 0.010*	4585 ± 75		This work$_{\rm dyn}$

2.3.2 Spectroscopic orbital elements from cross-correlation function and spectral disentangling

2.3.2.1 Cross-correlation function (CCF)

For the three red giants under study we reanalyzed the archived HERMES data and obtained radial velocities by using the cross-correlation method (e.g. Tonry and Davis 1979). Based on this approach each wavelength-calibrated spectrum in the range from 4 780 – 6 530 Å was cross-correlated with a line mask optimized for HERMES spectra (Raskin et al. 2011). In this case a red-giant-star template was used that contains spectral lines corresponding to the spectrum of Arcturus. This method provides excellent precision for deriving the RVs of red-giant stars showing solar-like oscillations (Beck et al. 2014). For KIC 8410637 those RVs with large measurement uncertainties were not included in the further analysis. This leaves 43 RVs for the giant, with a root mean square (*rms*) scatter of 0.23 km s^{-1} around the best fit, and 20 for the dwarf with a scatter of 0.92 km s^{-1} (Tab. 2.11). In the case of KIC 5640750 we only have RV data of the giant star (22 observations with a scatter of 0.08 km s^{-1}, Tab. 2.12), since we were not able to detect the signature of the dwarf component with CCF. As a further attempt to obtain its RVs we applied the least-squares deconvolution (LSD) method developed by Tkachenko et al. (2013). This technique is similar to a cross-correlation with a set of δ functions. It is sensitive to small contributions and thus more suitable for the detection of faint components in double-lined spectroscopic binary systems. Although the overall signal-to-noise ratio (S/N) was high, the contribution from the dwarf star was very weak and therefore difficult to detect. With LSD we were not able to measure sufficiently precise RVs for the dwarf component that could be used to further constrain the orbital parameters for the system KIC 5640750. For KIC 9540226 we derived 32 RVs for the giant with a scatter of 0.33 km s^{-1} that we present in Table 2.13. These were supplemented by RV data for the dwarf star recently published by Gaulme et al. (2016) (7 RVs with a scatter of 0.91 km s^{-1}).

Based on the radial velocities determined for the stars in these binary systems we obtained orbital elements by using Kepler's laws. The lack of RVs for the dwarf star of KIC 5640750 means we cannot measure the masses and radii of the component stars without additional constraints. As these parameters are important for our current study, we extended the spectroscopic analysis to detect the dwarf component of KIC 5640750 by using spectral disentangling.

2.3.2.2 Spectral disentangling (SPD)

The spectra of the binary stars under study are dominated by the spectra of the red-giant components since they contribute the prevailing fraction of the total light of the systems. From the light curve analysis (see light ratio between components in Tab. 2.3, Sec. 2.3.3) it was found that the dwarf companions contribute only about 9.2, 6.5, and 2.0 % to the total light of the system for KIC 8410637, KIC 5640750, and KIC 9540226, respectively. This makes the RVs of the Doppler shifts of the faint companions more difficult to detect, i.e. the *rms* scatter of the dwarfs is about three times more uncertain than for the giants for KIC 8410637 and KIC 9540226, and undetectable for KIC 5640750. The spectral lines of both components are, however, present in the spectra and to extract both we apply spectral

Table 2.2: Spectroscopic orbital elements for KIC 8410637 (columns 2–3), KIC 5640750 (columns 4–6), and KIC 9540226 (columns 7–8) determined using cross-correlation (CCF) and spectral disentangling (SPD). We adopted the solutions based on SPD in the further analysis of these eclipsing binary systems. See Section 2.3.2.3 for parameter definitions. We note that T_0 is given in Heliocentric Julian Date (HJD).

Parameter	KIC 8410637		KIC 5640750			KIC 9540226	
	CCF	SPD	CCF	SPD 1	SPD 2	CCF	SPD
P [d]	408.3248 ± 0.0004	-	987.398 ± 0.006	-	-	175.4438 ± 0.0008	-
T_0 [d]	398.9449 ± 0.0007	403.53 ± 0.06	269.215 ± 0.004	188.7 ± 1.1	188.5 ± 1.1	817.289 ± 0.002	841.71 ± 0.08
e	0.686 ± 0.001	0.694 ± 0.004	0.326 ± 0.002	0.323 ± 0.008	0.322 ± 0.008	0.3877 ± 0.0003	0.387 ± 0.003
ω [deg]	120.9 ± 0.1	120.7 ± 0.2	34.3 ± 0.7	34.0 ± 0.7	33.6 ± 0.7	183.5 ± 0.6	184.2 ± 0.7
K_A [km s^{-1}]	30.33 ± 0.22	29.37 ± 0.12	-	17.21 ± 0.18	15.10 ± 0.19	31.48 ± 0.40	31.94 ± 0.32
K_B [km s^{-1}]	25.76 ± 0.09	26.13 ± 0.08	14.64 ± 0.03	14.68 ± 0.05	14.66 ± 0.06	23.24 ± 0.21	23.33 ± 0.14
q	0.849 ± 0.008	0.890 ± 0.005	-	0.853 ± 0.011	0.971 ± 0.012	0.738 ± 0.016	0.730 ± 0.032

disentangling (SPD).

The method of SPD was developed by Simon and Sturm (1994). In this method, the individual spectra of the components as well as a set of orbital elements can be optimised simultaneously. During this process the fluxes of the observed spectra are effectively co-added. This results in disentangled spectra that have a higher S/N compared to the observed spectra. There is no need for template spectra like in the cross-correlation method. This is highly beneficial in the case of barely visible components' spectrum, like in our case (see Mayer et al. 2013, Torres et al. 2014, Kolbas et al. 2015, for other examples). With the method of SPD the spectra of the faint dwarf companions were successfully reconstructed with the fractional light in the visual spectral region at the extreme values of barely $\sim 1-2\,\%$.

For the present work, we used the spectral disentangling code FDBINARY (Ilijic et al. 2004), which operates in Fourier space based on the prescription of Hadrava (1995) including some numerical improvements. In particular, the Discrete Fourier Transform is implemented in FDBINARY, which gives more flexibility in selecting spectral segments for SPD while still keeping the original spectral resolution. We used the wavelength range of the spectra from $5\,000-6\,000$ Å for both the determination of the orbital elements and the isolation of the individual spectra of the components.

In FDBINARY the optimisation is performed with a simplex routine (cf. Press et al. 1989). We performed 100 runs, each with 1000 iterations, examing a relatively wide parameter space around an initial set of parameters. In most cases of high S/N spectra, that are well distributed in the orbital phases, the convergence is achieved quite fast. The uncertainties in the determination of the orbital elements were then calculated with a novel approach using a bootstrapping method (Pavlovski et al. in prep.). The faint companion's spectra for all three systems were extracted (see Figs. 2.1 and 2.2).

2.3.2.3 Orbital elements

For the three binary systems under study we report the spectroscopic orbital elements obtained from CCF and SPD analysis in Table 2.2. These include the orbital period P, the time of periastron T_0, the eccentricity e, the longitude of periastron ω, the radial velocity semi-amplitudes of the dwarf and giant component $K_{\rm A}$, $K_{\rm B}$, and the mass ratio $q = K_{\rm A}/K_{\rm B}$. The comparison of the results shows agreement between both methods. We note, however, that T_0 is different from SPD and CCF for KIC 5640750 since about one third of the orbital phase is not covered by spectroscopic observations, which results in ambiguities regarding its orbital parameters (Fig. 2.4). From SPD we derived RV semi-amplitudes for all components in the three binary systems making the determination of the dynamical masses for all stars possible. Hence, we adopted these solutions for the further analysis.

KIC 5640750: In the current study we present the first spectroscopic orbit for this binary system based on both components. The CCF nor LSD analysis did reveal the radial velocities of the dwarf spectrum. According to our light curve analysis (Sec. 2.3.3) the companion star contributes only $\sim 6.5\,\%$ to the total light in the visual passband. In addition, the long orbital period of 987 days makes the detection of the dwarf spectrum difficult since for such small Doppler shifts the spectral lines are along the whole cycle close to the prominent lines of the red-giant component. From the SPD analysis we find two

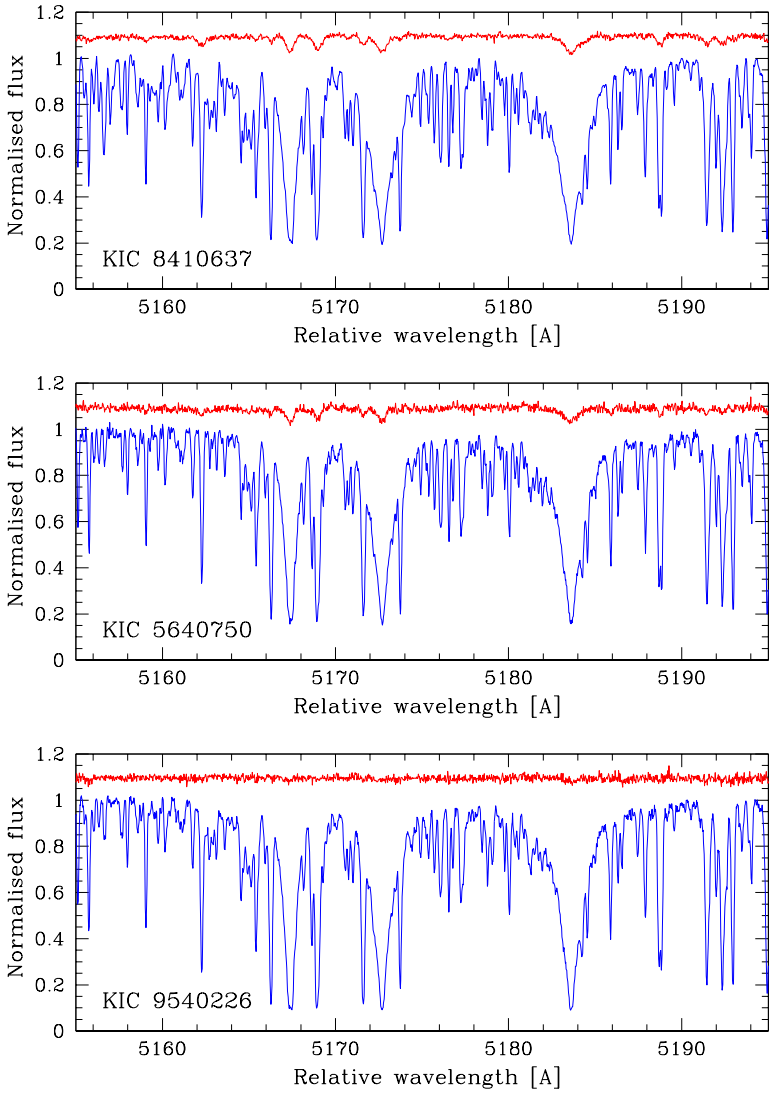

Figure 2.1: Disentangled spectra for the giant (blue) and dwarf (red) component of the eclipsing binary systems KIC 8410637 (top panel), KIC 5640750 (middle), and KIC 9540226 (bottom) centred on Mg I triplet at $\lambda = 5168 - 5185$ Å. The spectra are normalized with respect to the composite continuum and for better visibility we use an arbitrary offset between the individual spectra of the binary components.

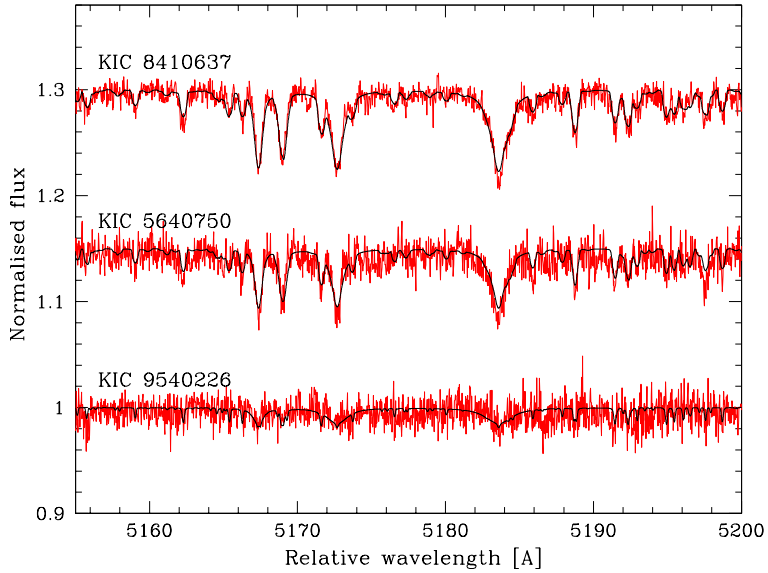

Figure 2.2: Close-ups of the disentangled spectra for the dwarf components (red) of the eclipsing binary systems KIC 8410637 (top panel), KIC 5640750 (middle), and KIC 9540226 (bottom) centred on Mg I triplet at $\lambda = 5168-5185$ Å. Synthetic spectra are overplotted in black. The spectra are normalized with respect to the composite continuum and for better visibility we use an arbitrary offset between the individual spectra of the dwarf components.

statistically significant solutions for this system which are indistinguishable and whose difference is barely visible in the disentangled spectra. This ambiguity arises due to an insufficient coverage of the orbital phase which lacks spectroscopic observations between 0 and 0.35 (see bottom left in Fig. 2.4). Thus, only one extremum in the RV curve is covered by spectroscopic observations. As a result we obtain more than one local minimum in the SPD analysis due to spurious patterns in the reconstructed spectra of the individual components, which can also affect the quality of the orbital solution (Hensberge et al. 2008). As a further attempt to lift the ambiguity between the two orbital solutions, we rerun the SPD with fixed e and ω without success. In any case, follow-up observations would be required to resolve this ambiguity by filling the gap in the orbital phases. In the current study, we use both solutions of this system to infer the stellar parameters of its components and we check these results for consistencies with asteroseismic stellar parameters. It should be noted that the RV semi-amplitudes for the giant are within 1σ confidence level for all solutions.

KIC 8410637: In a comprehensive study by Frandsen et al. (2013) the first spectroscopic orbit was determined for this binary system. Even with about 10 % contribution to the total light, the dwarf companion is barely detectable due to a long orbital period of $P \sim 408$ days. Frandsen et al. used several methods to measure the radial velocities for both components; the line broadening function (Rucinski 2002), the two-dimensional cross-correlation (2D-CCF, Zucker and Mazeh 1994), and the Fourier spectral disentangling (Hadrava 1995). These three sets of measurements gave consistent orbital param-

eters within 1σ errors. Their final orbital solution is a mean of the results determined from the line broadening function and 2D-CCF, and reads, $K_A = 30.17 \pm 0.39$ km s^{-1}, and $K_B = 25.85 \pm 0.07$ km s^{-1}, with the mass ratio, $q = 0.857 \pm 0.011$. Comparing Frandsen et al. spectroscopic solution with our CCF and SPD results, the agreement is only at a 3σ confidence level for the RV semi-amplitudes, and at a 1σ level for the geometric orbital parameters, i.e. the eccentricity, and the longitude of periastron. It is difficult to trace the source of these differences. Some systematics could arise because of the different methodology and different datasets that were used. Frandsen et al. worked with three spectroscopic datasets that were collected with different spectrographs of comparable spectral resolution, FIES at the Nordic Optical Telescope, HERMES at the Mercator Telescope, and CES at the Thüringer Landessternwarte. We used HERMES spectra exclusively, hence our dataset is homogeneous, yet less extensive. Since there is no need for template spectra in the SPD technique, this method is not liable to mismatch problems as the methods used by Frandsen et al. (2013), as shown in numerical experiments by Hensberge and Pavlovski (2007).

KIC 9540226: The first attempt to determine the spectroscopic orbit for this binary system was made by Beck et al. (2014). The cross-correlation method applied on 31 HERMES spectra did not reveal the dwarf's spectrum. Hence, only the giant's RV semi-amplitude was determined, $K_B = 23.32 \pm 0.04$ km s^{-1}, and the geometric orbital parameters, the eccentricity $e = 0.39 \pm 0.01$, and the longitude of periastron $\omega = 4.0 \pm 0.6$ deg. The *Kepler* light curve solution published by Gaulme et al. (2016) shows that the dwarf component contributes barely ~ 2 % to the total light. Despite the low secondary contribution to the total flux, Gaulme et al. report a detection of the dwarf spectra in 7 out of 12 of their observations by using CCF. They used a new series of spectra secured with the 3.5 m ARC telescope at Apache Point Observatory. It is encouraging that the spectroscopic orbital elements derived by Gaulme et al. (2016) and ours based on SPD (Tab. 2.2) agree within 1σ uncertainties.

2.3.2.4 Individual components' spectra from SPD

Spectral disentangling was performed in pure 'separation' mode (Pavlovski and Hensberge 2010) since the light curves do not show any significant light variations outside the eclipses. This is also true for the eccentric eclipsing binary system KIC 9540226 which shows flux modulations at periastron. However, these so-called heartbeat effects are extremely small amplitude that is why they only became widely known through the *Kepler* mission. Hence it is justified to use the pure separation mode for all three binary systems.

The disentangled spectra of the components still have a common continuum of a binary system. For the renormalization of the separated spectra from a common continuum of the binary system to the components' spectra with their individual continua we followed the prescription by Pavlovski and Hensberge (2005). First, an additive correction was made due to different line-blocking of the components. Then these spectra were multiplied for the dilution factor. This multiplicative factor is determined from the light ratio. Since *Kepler* photometry is very precise, we preferred the light ratio determined in the light curve analysis (Sec. 2.3.3), rather than the spectroscopically determined one. Disentangled spectra of all binary components could be extracted and are shown in Figures 2.1

and 2.2. The latter presents close-ups of the disentangled spectra for the dwarfs with decreasing S/N from top (KIC 8410637) to bottom (KIC 9540226). For the synthetic spectra we used the atmospheric parameters from Table 2.4 and the light ratios from Table 2.3. Since the dwarf component of KIC 5640750 is at the limit of detection, we did not obtain its atmospheric parameters and therefore we adjusted the projected rotational velocity to 10 km s^{-1} for its synthetic spectrum in Figure 2.2.

2.3.3 Eclipse modelling

The available light curves of the three systems were modelled with the JKTEBOP code (Southworth 2013, and references therein) in order to determine their physical properties. JKTEBOP parameterises the light curve using the sum and ratio of the fractional radii of the components, $r_A + r_B$ and $k = r_B/r_A$. The fractional radii are defined as $r_A = R_A/a$ and $r_B = R_B/a$, where R_A and R_B are the true radii of the stars and a is the orbital semimajor axis. The parameters $r_A + r_B$ and k were included as fitted parameters, as was the orbital inclination i. We fitted for the combination terms $e\cos\omega$ and $e\sin\omega$ where e is the orbital eccentricity and ω is the argument of periastron. The orbital period, P, and midpoint of primary eclipse, T_0, were also fitted.

The radiative properties of the stars were modelled using the quadratic limb darkening law (Kopal 1950), with linear coefficients denoted u_A and u_B and quadratic coefficients v_A and v_B. We fitted for u_B, which is well constrained by the shape of the light curve during totality. We fixed v_B to theoretical values interpolated from the tabulations of Sing (2010), as it is strongly correlated with u_A (e.g. Southworth et al. 2007, Carter et al. 2008). Both limb darkening coefficients for the dwarf stars (u_A and v_A) were fixed to theoretical values because they are not well constrained by the available data. We also fitted for the central surface brightness ratio of the two stars, J.

According to the *Kepler* Input Catalog (Brown et al. 2011), all three systems have a small but non-zero flux contamination from nearby stars (0.001 for KIC 8410637, 0.021 for KIC 5640750, and 0.012 for KIC 9540226). We obtained solutions with third light, L_3, as a fitted parameter but found that they were not significantly different from solutions with $L_3 = 0$. In each case, the best-fitting value of L_3 was small and its inclusion had a negligible effect on the other fitted parameters.

We included measured RVs for the stars in the JKTEBOP fit, and fitted for the velocity amplitudes of the two stars, K_A and K_B. This was done to include constraints on $e\cos\omega$ and $e\sin\omega$ provided by the RVs and we found that the measured values of K_A and K_B were in agreement with the input values. However, we did not use them in the subsequent analysis because we prefer the homogeneous set for all dwarfs and giants from SPD (Sec. 2.3.2.2). Note that RVs are not available for the dwarf component of KIC 5640750. We also fitted for the systemic velocities of the stars, γ_A and γ_B, but did not require $\gamma_A = \gamma_B$ because the gravitational redshifts of the giants are significantly different to those of the dwarfs. The systemic velocities are formally measured to high precision, but have significantly larger systematic errors due to the intrinsic uncertainty in the stellar RV scale.

As we analyzed the *Kepler* long-cadence data for each system, the JKTEBOP model was numerically integrated to match the 1765 s sampling rate of these data (Southworth 2012).

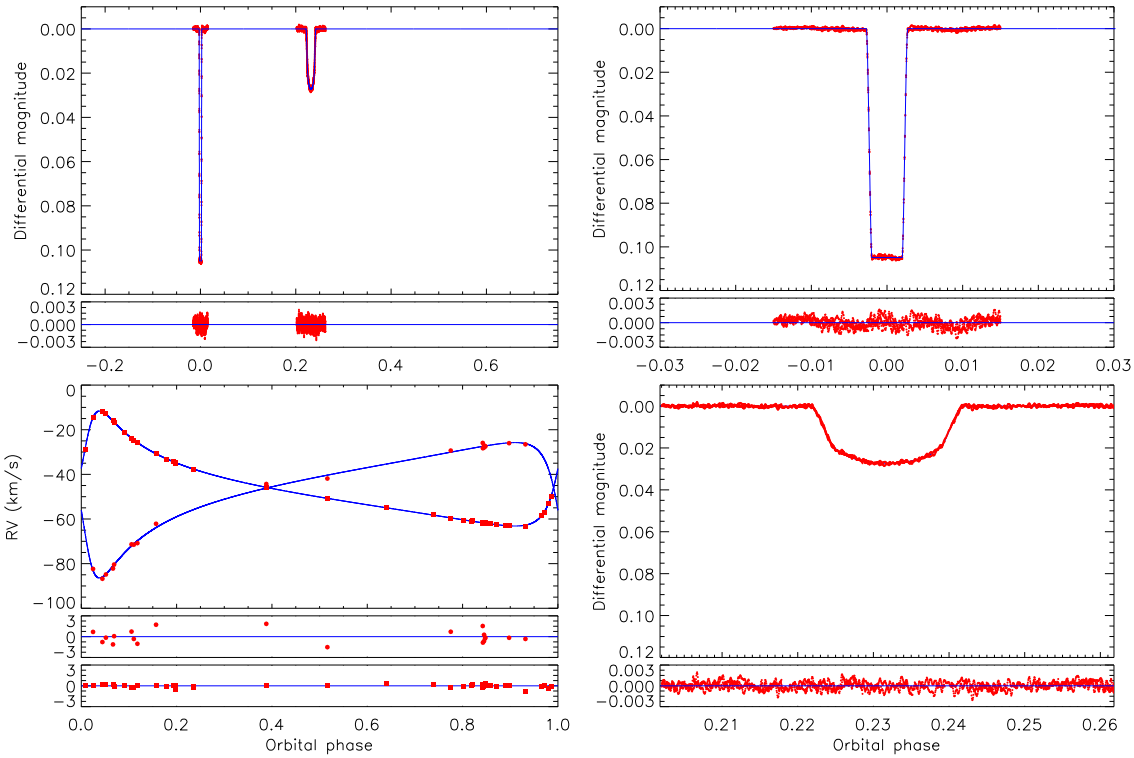

Figure 2.3: Observational data for KIC 8410637 and the best-fitting model from JKTEBOP. The red points give the data and the blue lines the best fits. The four panels show the phase folded light curve (top left), primary eclipse (top right), the RV curve as derived from CCF (left bottom), and secondary eclipse (right bottom). Each panel is accompanied by a plot of the residuals in the lower panel.

This is one point of difference between the current analysis and the study of KIC 8410637 by Frandsen et al. (2013). We note that short-cadence data are available for KIC 9540226 but that we did not use them because the long-cadence data already provide a sufficient sampling rate for both the eclipses and pulsations (Sec. 2.4.1).

The best-fitting values of the fitted parameters for the three systems are listed in Table 2.3, where $M_{\rm A,B}$ are the masses, $R_{\rm A,B}$ the radii, $\log g_{\rm A,B}$ the surface gravities, $L_{\rm A,B}$ the luminosities and a the orbital separation of the two stars. The light ratio $\ell_{\rm B}/\ell_{\rm A}$ of the giant to the dwarf is computed in the *Kepler* passband. The light curves and RV data for the three systems are shown in Figures 2.3, 2.4 and 2.5, superimposed on the best-fitting models from JKTEBOP. Uncertainty estimates for each parameter were obtained via both Monte Carlo and residual-permutation algorithms (see Southworth 2008), and the larger of the two uncertainty estimates is reported for each parameter. In most cases we found that the residual-permutation algorithm yielded uncertainties two to three times larger than those from the Monte Carlo algorithm. This is due to the presence of pulsations, which for the purposes of eclipse modelling are simply a source of correlated (red) noise.

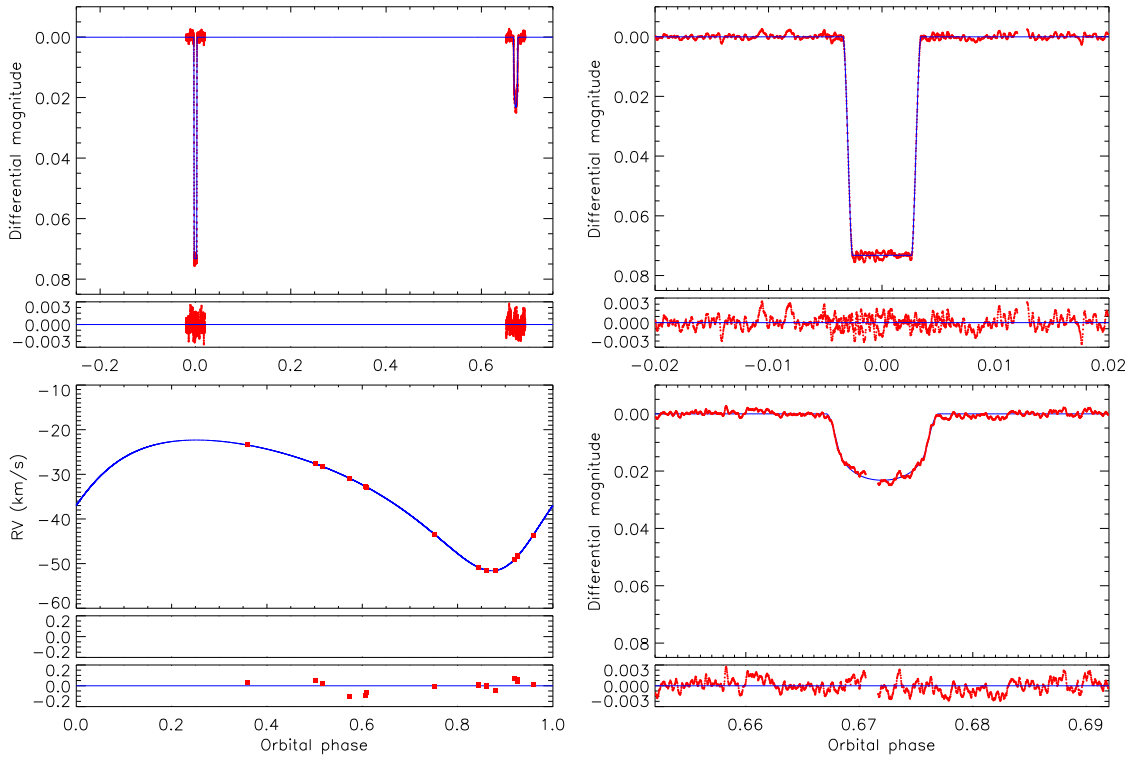

Figure 2.4: Same as Fig. 2.3 now for KIC 5640750.

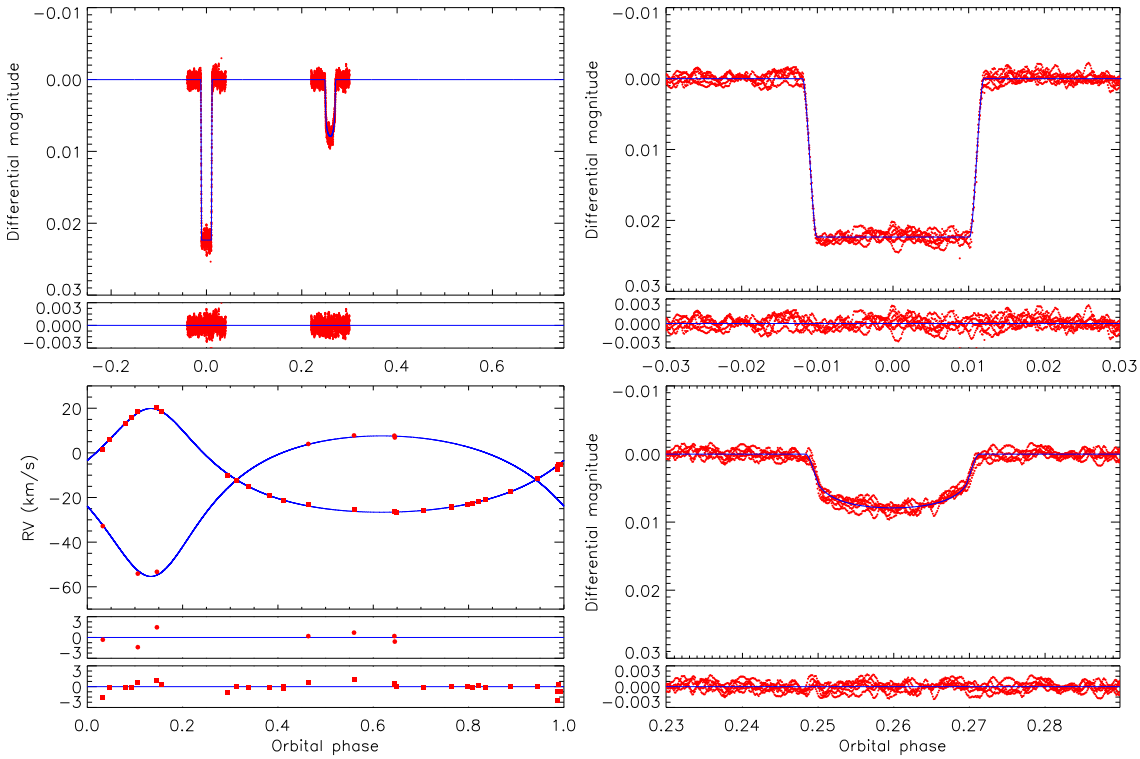

Figure 2.5: Same as Fig. 2.3 now for KIC 9540226.

Table 2.3: Physical properties of the systems measured from the *Kepler* light curves and phase-resolved spectroscopy.

Parameter	KIC 8410637	KIC 5640750			KIC 9540226
Parameters fitted using JKTEBOP:		1st solution		2nd solution	
T_0 [BJD]	2454990.6201 ± 0.0007	2455269.2144	±	0.0042	2455817.2890 ± 0.0024
P [d]	408.32476 ± 0.00035	987.3981	±	0.0060	175.44381 ± 0.00082
$e\cos\omega$	−0.35204 ± 0.00054	0.26916	±	0.00017	−0.38702 ± 0.00011
$e\sin\omega$	0.5884 ± 0.0017	0.1808	±	0.0029	−0.0235 ± 0.0042
$r_A + r_B$	0.03730 ± 0.00012	0.02701	±	0.00016	0.08180 ± 0.00087
k	6.811 ± 0.027	7.584	±	0.066	12.98 ± 0.11
J	0.2556 ± 0.0018	0.2695	±	0.0045	0.2974 ± 0.0046
i [degrees]	89.614 ± 0.032	89.761	±	0.055	88.73 ± 0.19
u_B	0.528 ± 0.024	0.573	±	0.047	0.466 ± 0.058
K_A [km s^{-1}]	30.33 ± 0.22	17.21 ± 0.18		15.098 ± 0.086	31.48 ± 0.40
K_B [km s^{-1}]	25.763 ± 0.090	14.676 ± 0.051		14.664 ± 0.056	23.24 ± 0.21
γ_A [km s^{-1}]	−45.42 ± 0.16				−11.70 ± 0.22
γ_B [km s^{-1}]	−46.445 ± 0.013	−32.993	±	0.013	−12.36 ± 0.11
Derived parameters:					
$T_{\rm eff}$ of dwarf [K]	6066 ± 200	5844	±	200	5822 ± 200
r_A	0.004775 ± 0.000027	0.003147	±	0.000034	0.005850 ± 0.000067
r_B	0.032522 ± 0.000094	0.02387	±	0.00014	0.07595 ± 0.00082
ℓ_B/ℓ_A	9.860 ± 0.017	14.342	±	0.060	48.13 ± 0.16
Mass ratio	1.124 ± 0.006	1.173 ± 0.013		1.030 ± 0.007	1.369 ± 0.016
M_A [$M_\odot$]	1.309 ± 0.014	1.292 ± 0.017		1.125 ± 0.011	1.015 ± 0.016
M_B [$M_\odot$]	1.472 ± 0.017	1.515 ± 0.033		1.158 ± 0.014	1.390 ± 0.031
R_A [$R_\odot$]	1.556 ± 0.010	1.853 ± 0.023		1.730 ± 0.020	1.034 ± 0.014
R_B [$R_\odot$]	10.596 ± 0.049	14.06 ± 0.12		13.12 ± 0.09	13.43 ± 0.17
$\log g_A$ (cgs)	4.171 ± 0.005	4.014 ± 0.010		4.014 ± 0.010	4.416 ± 0.010
$\log g_B$ (cgs)	2.556 ± 0.003	2.323 ± 0.007		2.266 ± 0.006	2.326 ± 0.010
$\log L_A$ [$L_\odot$]	0.468 ± 0.058	0.555 ± 0.060		0.495 ± 0.060	0.042 ± 0.061
$\log L_B$ [$L_\odot$]	1.656 ± 0.030	1.871 ± 0.029		1.811 ± 0.029	1.854 ± 0.030
a [AU]	1.5148 ± 0.0054	2.738 ± 0.016		2.557 ± 0.009	0.8218 ± 0.0052
$E(B-V)$	0.07 ± 0.02	0.16 ± 0.03		0.16 ± 0.03	0.16 ± 0.03
Distance [pc]	1005 ± 29	1569 ± 55		1464 ± 50	1667 ± 63

2.3.3.1 Physical properties of the systems

In Table 2.3 we list the physical properties of the systems derived from the spectral disentangling analysis and the JKTEBOP analyses. These were calculated using the JKTABSDIM code (Southworth et al. 2005), and the uncertainties were propagated via a perturbation approach. We emphasise that the velocity amplitudes from the spectral disentangling analysis were preferred over those from the RV measurements because they are available for all six stars.

We also determined the distances to the systems using published optical and near-IR photometry (Skrutskie et al. 2006, Brown et al. 2011, Henden et al. 2012) and the bolometric corrections provided by Girardi et al. (2002). Values of $E(B-V)$ were obtained by requiring agreement between the distances at optical and near-IR wavelengths, being 0.16 ± 0.03 mag for KIC 5640750, 0.07 ± 0.02 mag for KIC 8410637, and 0.16 ± 0.03 mag for KIC 9540226. We finally quote the distances determined from the 2MASS K-band apparent magnitudes, as these are the least affected by uncertainties in the effective temperatures and $E(B-V)$ values. We conservatively doubled the uncertainties in these measurement to account for some inconsistency in optical apparent magnitudes quoted by different sources. Our distance estimates (see Tab. 2.3) are much more precise than those from *Gaia* Data Release 1 (Gaia Collaboration et al. 2016a); future data releases from the *Gaia* satellite will significantly improve the distance measurements to these three binary systems.

KIC 5640750: We are the first to determine dynamical stellar parameters for this long-period binary system. By using the first set of orbital parameters, denoted as SPD 1 in Table 2.2, we obtained $M_{\rm B} = 1.52 \pm 0.03\,{\rm M}_{\odot}$ and $R_{\rm B} = 14.06 \pm 0.12\,{\rm R}_{\odot}$ for the red-giant component in this system. The second orbital solution (SPD 2) provided significantly lower stellar parameters with $M_{\rm B} = 1.16 \pm 0.01\,{\rm M}_{\odot}$ and $R_{\rm B} = 13.12 \pm 0.09\,{\rm R}_{\odot}$ for the same red-giant star, which results in a relative difference of $\sim 0.4\,{\rm M}_{\odot}$ in stellar mass and $\sim 0.9\,{\rm R}_{\odot}$ in stellar radius, respectively.

KIC 8410637: We found that the velocity amplitudes were different at a 3σ level when measured from the RVs compared to the results from spectral disentangling. Our adoption of the velocity amplitudes from spectral disentangling means that we find significantly lower masses for the two components of this system compared to those found by Frandsen et al. (2013) and Gaulme et al. (2016). However, the discrepancy between the results found by Frandsen et al. (2013) and those from asteroseismic studies led us to investigate this system further. As the dominant source of noise is pulsations in the light curve, we investigated whether the measured radius of the giant was sensitive to which eclipses were included in the analysis. We did this by obtaining eight best fits with each of the eclipses (four primary and four secondary) omitted in turn. The standard deviation of the $R_{\rm B}$ values was 0.047, which is slightly smaller than the error estimate for this quantity in Table 2.3. We therefore conclude that our measured $R_{\rm B}$ is robust against the omission of parts of the input data.

KIC 9540226: For this star our measurements of the system parameters can be compared to those found by Gaulme et al. (2016), who worked with similar data and analysis codes. We find that the agreement between the two sets of results is reasonable but not perfect. Our value of $R_{\rm A}$ and $R_{\rm B}$ are larger by 2σ and 2.6σ, respectively, and the mass measure-

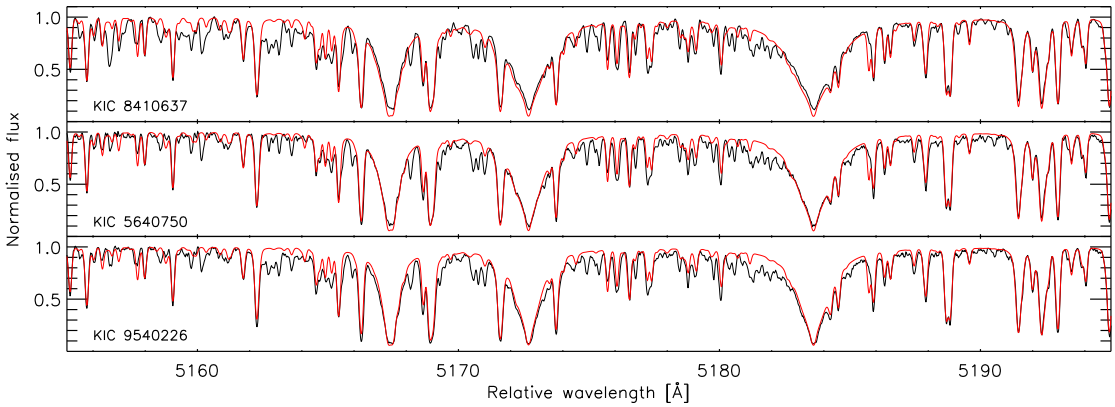

Figure 2.6: Observed (in black) and best-fitting synthetic (in red) spectra for the giant components in the binary systems in the wavelength range between 5 155−5 195 Å around the Mg I triplet.

ments agree to within 1σ. Finally, the mass and the radius of the giant found by Brogaard et al. (2016) are somewhat larger (by 2.4σ and 1.9σ respectively). In their most recent study, Brogaard et al. (2018) re-analyzed this system and obtained considerably lower values for both, the radius and the mass of the red giant. Compared to their latest measurements, our values of $M_{\rm B}$ and $R_{\rm B}$ agree to within 1σ and 2σ respectively.

2.3.4 Atmospheric parameters

For the extraction of the atmospheric parameters we used the Grid Search in Stellar Parameters (GSSP; Tkachenko 2015) software package to analyze the disentangled spectra of the evolved components of each of the eclipsing binary systems. GSSP is a LTE-based software package that uses the SYNTHV (Tsymbal 1996) radiative transfer code to compute grids of synthetic spectra in an arbitrary wavelength range based on a precomputed grid of plane-parallel atmosphere models from the LLMODELS code (Shulyak et al. 2004). The atomic data were retrieved from the Vienna Atomic Lines Database (VALD; Kupka et al. 2000). The optimisation was performed simultaneously for six atmospheric parameters: effective temperature ($T_{\rm eff}$), surface gravity ($\log g$; if not fixed to the value obtained from the light curve solution), micro- and macro-turbulent velocities ($v_{\rm micro}$, $v_{\rm macro}$), projected rotational velocity ($v \sin i$), and global metallicity ([M/H]). The grid of synthetic spectra was built from all possible combinations of the above-mentioned atmospheric parameters and the best-fit solution was obtained by minimising the χ^2 merit function. The 1σ errors were derived from χ^2 statistics taking into account possible correlations between the parameters in question. In general, GSSP allows for the analysis of single and binary star spectra, where both composite and disentangled spectra can be analyzed for atmospheric parameters and elemental abundances of the individual binary components in the latter case. We refer the reader to Tkachenko (2015) for details on the method implemented in GSSP and for several methodology tests on the simulated and real spectra of single and binary stars. In this work, we used the GSSP-SINGLE MODULE, where the spectra were treated as those of single stars. By doing so we take advantage of the fact that the light dilution effect could be corrected for based on the a priori knowledge of light factors from the light

curve solution.

Figure 2.6 shows the best-fitting solutions to a short segment of each observed red-giant spectrum. The atmospheric parameters for KIC 8410637, KIC 5640750, and KIC 9540226 are reported in Table 2.4 except for the dwarf component of KIC 9540226. Due to the high noise level in the disentangled spectrum of this dwarf companion (see bottom panel in Figs. 2.1 and 2.2), we are not able to obtain precise estimates of its atmospheric parameters from spectral fitting. From its mass and by assuming solar metallicity we can only infer that it is a dwarf star of early to intermediate G spectral type.

KIC 5640750: We are the first to determine the atmospheric parameters of the binary components of KIC 5640750. For the red-giant star we derived $T_{\rm eff} = 4525 \pm 75$ K and [M/H] $= -0.29 \pm 0.09$ dex, and for its companion we obtained $T_{\rm eff} = 6050 \pm 350$ K and [M/H] $= 0.08 \pm 0.25$ dex.

KIC 8410637: The atmospheric parameters for the stars in this binary system were also determined by Frandsen et al. (2013) from the disentangled spectra of the components. They used the Versatile Wavelength Analysis (VWA) package (Bruntt et al. 2004). The effective temperatures that they determined for the giant and dwarf component, $T_{\rm eff} = 4800 \pm 80$ K, and $T_{\rm eff} = 6490 \pm 160$ K, respectively, agree with our results (Tab. 2.4) at the 2σ, and 1σ confidence level. The somewhat worse agreement in the effective temperature determinations could be explained as a metallicity effect. Whilst we found almost solar metallicity for the red-giant component, Frandsen et al. determined [Fe/H] $= 0.24 \pm 0.15$ dex, which was based on numerous Fe I lines. Since in this temperature range the metal lines become deeper for lower $T_{\rm eff}$ both results could agree in case the degeneracy between the $T_{\rm eff}$ and metallicity can be lifted. This might also explain a better agreement for the $T_{\rm eff}$ of the dwarf companion. Frandsen et al. fixed the metallicity to [Fe/H] = 0.1 dex, which is closer to the value we derived, although the uncertainties in the determination of the $T_{\rm eff}$ of the dwarf star are considerably larger than in the case of the red-giant component, due to the faintness of the dwarf companion. The fractional light dilution factor for the RG component is $l_{\rm RG} = 0.9085$, and 0.9080, from the light curve analysis in Frandsen et al., and our present study, respectively. The light ratio used in both studies could be another source of slight discrepancies, however it seems unlikely given the small difference between these values.

KIC 9540226: For the red-giant component in this binary system, Gaulme et al. (2016) determined the atmospheric parameters through spectroscopic analysis of Fe I and Fe II lines. They used the MOOG spectral synthesis code (Sneden et al. 2012). It is not clear how they deal with the dilution effect of the secondary component, yet with its contribution of barely ~ 2 % its influence is very small if not negligible. Based on the ARCES spectra they adopted the following principal atmospheric parameters as final results of their work: $T_{\rm eff} = 4692 \pm 65$ K, $\log g = 2.2 \pm 0.2$, and [Fe/H] $= -0.33 \pm 0.04$ dex. It is very encouraging that the result from Gaulme et al. (2016) and the analysis in this work agree within 1σ uncertainties. Brogaard et al. (2016) first announced preliminary spectroscopic analysis results based mostly on previously published data, which was later on followed by a revised analysis of the same system (Brogaard et al. 2018). In both studies, they derived a lower metallicity ([Fe/H] $= -0.21 \pm 0.10$ and $[{\rm Fe/H}]_{\rm rev} = -0.23 \pm 0.10$) for the red-giant component. Moreover, their effective temperature measurements for the giant

are considerably higher than ours with $T_{\rm eff} = 4780 \pm 55$ K and $T_{\rm eff,rev} = 4680 \pm 80$ K. This may again be due to the $T_{\rm eff}$ and metallicity degeneracy mentioned earlier.

The effective temperatures of the dwarf components were barely measurable during the spectroscopic analysis due to the low S/N of the disentangled spectra. Thus as a further test we obtained estimates by interpolating between theoretical spectra from the ATLAS9 model atmosphere code (Kurucz 1993) and using the passband response function of the *Kepler* satellite[4]. We determined the effective temperatures of the synthetic spectra which reproduced the central surface brightness ratios measured using JKTEBOP versus synthetic spectra for the effective temperatures of the giant stars. The formal uncertainties on these parameters are similar to the uncertainties in the effective temperature measurements for the giants. We instead quote a uniform uncertainty of ±200 K to account for systematic errors in this method such as dependence on theoretical calculations, the measured *Kepler* passband response function, and the metallicities of the stars. We report the effective temperatures of each dwarf component of the three eclipsing binary systems in Table 2.3. These results agree with $T_{\rm eff}$ measurements from SPD for the dwarf companions of KIC 8410637 and KIC 5640750 albeit lower by ~ 300 K and ~ 200 K.

2.4 Stellar properties of oscillating red-giant stars from asteroseismology

We complement the binary analysis with a comprehensive study of the stellar oscillations of the systems' red-giant components. For a star showing solar-like oscillations we can infer its asteroseismic mass and radius and thus study consistencies between asteroseismic and dynamical stellar parameters. The asteroseismic approach leads to a more complete description of red giants by revealing their evolutionary stages and ages. In our study, we use well-defined and consistent methods to obtain reliable seismic ($\nu_{\rm max}$ and $\Delta\nu$) and stellar parameters ($M, R, \bar{\rho}$, and $\log g$) for the three stars under study, which we describe here in detail.

2.4.1 *Kepler* corrected time series data

For the asteroseismic analysis we use *Kepler* datasets that have been prepared according to Handberg and Lund (2014). During this procedure long-term variations, outliers, drifts, and jumps were removed together with the primary and secondary eclipses. This is a necessary step as the presence of eclipses would interfere with the study of the global oscillations. Figure 2.7 shows the corrected *Kepler* light curves of KIC 8410637, KIC 5640750, and KIC 9540226. The light curve of KIC 9540226 contains large gaps due to its location on a broken CCD module for three months every year. The Fourier spectra of pulsating red-giant stars reveal a rich set of information consisting of both a granulation as well as an oscillation signal.

[4] https://keplergo.arc.nasa.gov/kepler_response_hires1.txt

Table 2.4: Atmospheric parameters determined with the GSSP code. The stellar surface gravities, $\log g$ were kept fixed to the values coming from the mass and the radius of the stars obtained through the combined photometric-spectroscopic solution (Tab. 2.3).

Parameter	KIC 8410637		KIC 5640750		KIC 9540226
	giant	dwarf	giant	dwarf	giant
$T_{\rm eff}$ [K]	4605 ± 80	6380 ± 250	4525 ± 75	6050 ± 350	4585 ± 75
$\log g$ (cgs)	2.56 [fixed]	4.17 [fixed]	2.32 [fixed]	4.01 [fixed]	2.33 [fixed]
$v_{\rm micro}$ [km s^{-1}]	1.14 ± 0.18	1.95 ± 0.45	1.16 ± 0.17	$0.55\,^{+1.05}_{-0.55}$	1.22 ± 0.17
$v_{\rm macro}$ [km s^{-1}]	5.0 ± 2.5	0.0 [fixed]	4.7 ± 2.5	0.0 [fixed]	5.1 ± 1.5
$v \sin i$ [km s^{-1}]	$2\,^{+3}_{-2}$	17.4 ± 1.2	$2\,^{+3}_{-2}$	13.9 ± 1.8	$1\,^{+3}_{-1}$
[M/H] (dex)	0.02 ± 0.08	0.01 ± 0.14	-0.29 ± 0.09	0.08 ± 0.25	-0.31 ± 0.09

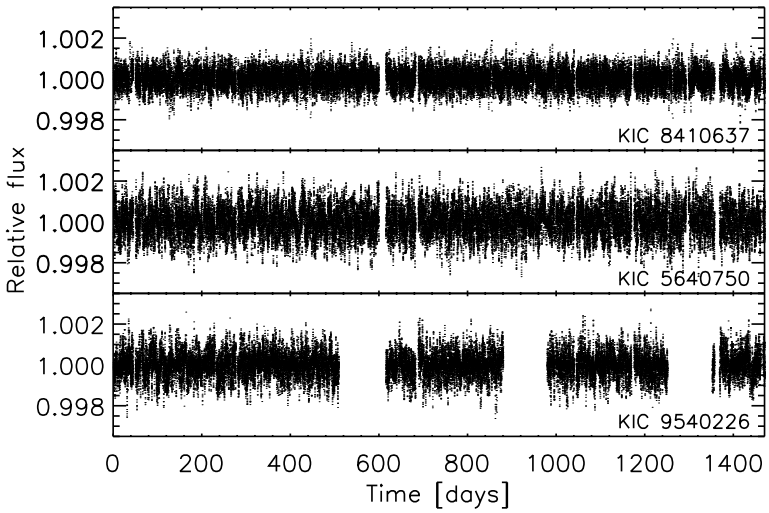

Figure 2.7: Corrected concatenated *Kepler* light curves of the three red-giant stars. The KIC numbers are indicated in each panel. The observations span 1470 days.

2.4.2 The background model

Some power in the red-giant Fourier spectrum originates from sources other than the pulsations, such as activity, granulation, and photon noise. These signals together form a background on which the oscillations are superimposed. In order to fully exploit the oscillations, we first need to assemble a background model consisting of a constant white noise level and granulation components. Here we use two granulation components with different timescales and a fixed exponent of four. This was shown to be appropriate for describing the granulation background of red-giant stars and provides a global background fit similar to model F proposed by Kallinger et al. (2014):

$$P_{\rm bg}(\nu) = w_{\rm noise} + \eta(\nu)^2 \left[\sum_{\rm i=1}^{2} \frac{\frac{2\sqrt{2}}{\pi} \frac{a_{\rm i}^2}{b_{\rm i}}}{1 + (\nu/b_{\rm i})^4} \right]. \tag{2.1}$$

Here, $w_{\rm noise}$ describes the white noise contribution to model the photon noise, $a_{\rm i}$ and $b_{\rm i}$ correspond to the root-mean-square (*rms*) amplitude and characteristic frequency of the granulation background component. The stellar granulation and oscillation signals are also influenced by an attenuation $\eta = \mathrm{sinc}\left(\frac{\pi}{2}\frac{\nu}{\nu_{\rm nyq}}\right)$ due to the integration of the intrinsic signal over discrete time stamps, which increases with higher frequencies approaching the Nyquist frequency $\nu_{\rm nyq}$.

We fitted the background model over a frequency range from 1 μHz up to 283 μHz, which is the Nyquist frequency for *Kepler* long-cadence data. To avoid influences of the oscillation modes, we excluded the frequency range of the oscillations during this procedure. We note here that we also checked the background fit by taking the oscillations into account simultaneously with a Gaussian-shaped envelope, for which we found agreeing results. To sample the parameter space of the variables given by equation 2.1 we used our own implementation of a Bayesian Markov Chain Monte Carlo (MCMC) framework (e.g. Handberg and Campante 2011, Davies et al. 2016, and references therein) that employs a

Table 2.5: Ranges of uniform prior distributions used for the global background and Gaussian parameters.

Parameter	Ranges of the uniform priors
Noise $w_{\rm noise}$	$< 10 \times$ mean power$(0.75 \times \nu_{\rm nyq}$ to $\nu_{\rm nyq})$
Rms amplitude a_1, a_2	$< \sqrt{\text{maximum power}}$
Frequency b_1, b_2	1 to $\nu_{\rm nyq}$ with $b_1 < b_2$
Height of Gaussian $\Lambda_{\rm g}$	$<$ maximum power
Frequency $\nu_{\rm max}$	$\nu_{\rm max,guess} \pm 1.5 \times \Delta\nu_{\rm guess}$
Standard deviation $\sigma_{\rm g}$	$0.05 \times \nu_{\rm max,guess}$ to $0.5 \times \nu_{\rm max,guess}$

Metropolis-Hastings algorithm. In this approach we draw random samples from a probabilistic distribution by using a likelihood function and a proposal distribution (priors) for each of the parameters of interest. We used the exponential log-likelihood introduced by Duvall and Harvey (1986) that is suitable for describing the Fourier power density spectrum (PDS) of a solar-like oscillator that has a χ^2 distribution with two degrees of freedom (Appourchaux 2003). As priors we considered uniform distributions for the global background parameters that are given in the top part of Table 2.5. The Metropolis-Hastings MCMC algorithm was run with multiple chains from different initial conditions. From trace plots we assessed the initial burn-in period and we checked that the chains are well mixed and that they explore the relevant parameter space. The initial values of the burn-in phase were then discarded and we ran the algorithm for another 150 000 iterations before we assessed the convergence of the chains to the posterior distributions. For each distribution we adopted the median as the best-fit parameter value and calculated its 68 % credible interval (Tab. 2.6).

Figure 2.8 shows the global background fits to the Fourier power density spectra. The oscillation power excesses, distinct for pulsating red-giant stars, are clearly visible in each spectrum. For illustrative purposes, we also present the background normalized spectra in the lower panels, which reveal that after correcting for the background only the oscillations are left in the spectra.

2.4.3 Solar-like oscillations

The Fourier spectrum of solar-like oscillators consists of several overtones of radial order (n) and spherical degree (ℓ) modes. A zoom of the individual oscillation modes is shown in Figure 2.9. The dominant peaks are arranged in a well-defined sequence, which forms in an asymptotic approximation a so-called universal pattern (Tassoul 1980, Mosser et al. 2011). This pattern reveals the structure of the radial and non-radial modes. In stellar time series observations only low spherical degree modes ($\ell \leq 3$) are observable. Due to cancellation effects higher degree modes are not visible in observations of the whole stellar disk.

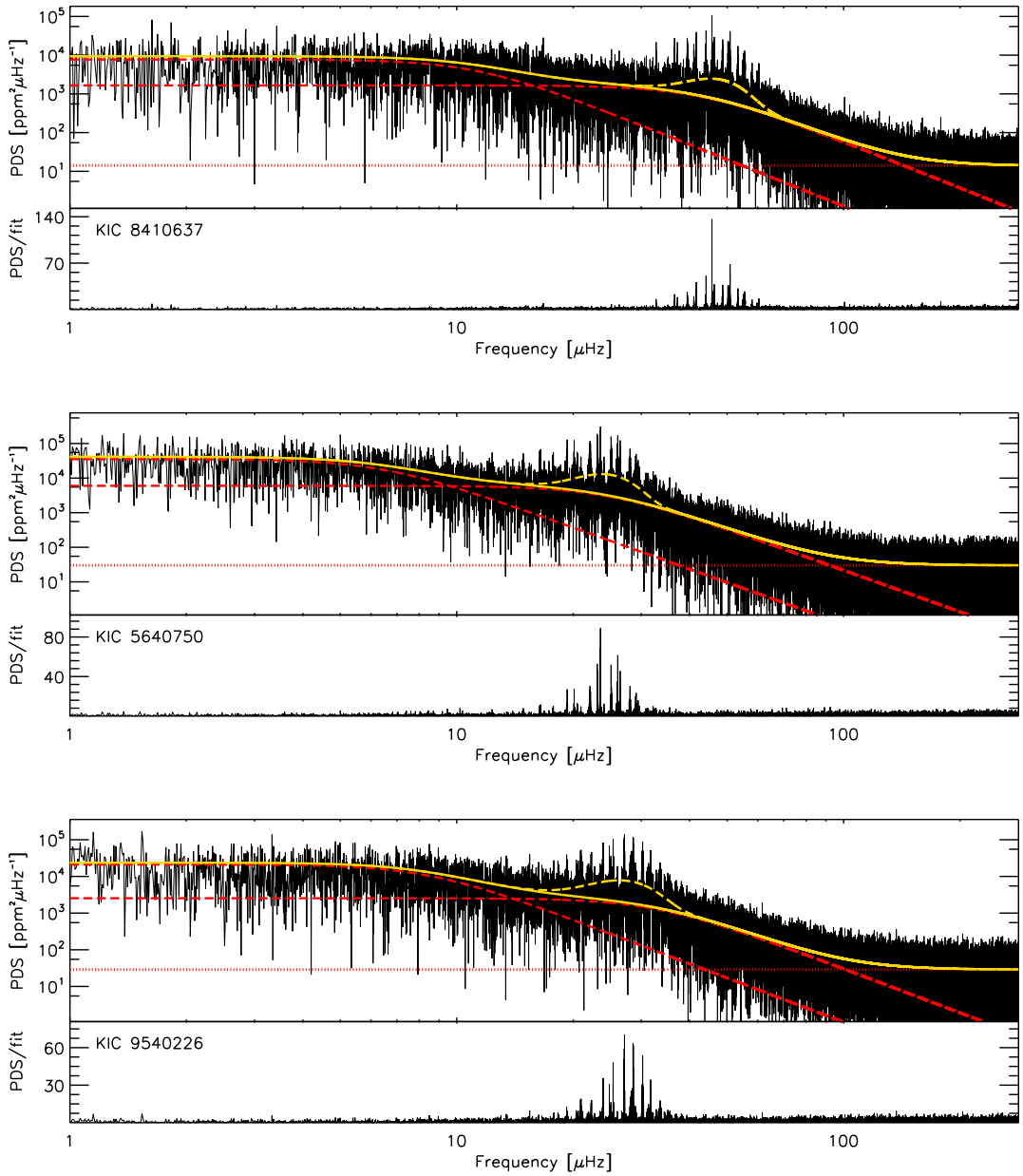

Figure 2.8: Fourier power density spectra of KIC 8410637 (top), KIC 5640750 (middle), and KIC 9540226 (bottom) in black. The yellow solid lines represent the best global background fits to the data. The granulation background components are indicated by the red dashed lines, while the red horizontal dotted lines depict the constant white noise components. The oscillation excesses are modelled by Gaussians (yellow dashed lines, see eq. 2.2, Sec. 2.4.3). The smaller panels below each power density spectrum show the background normalized spectra.

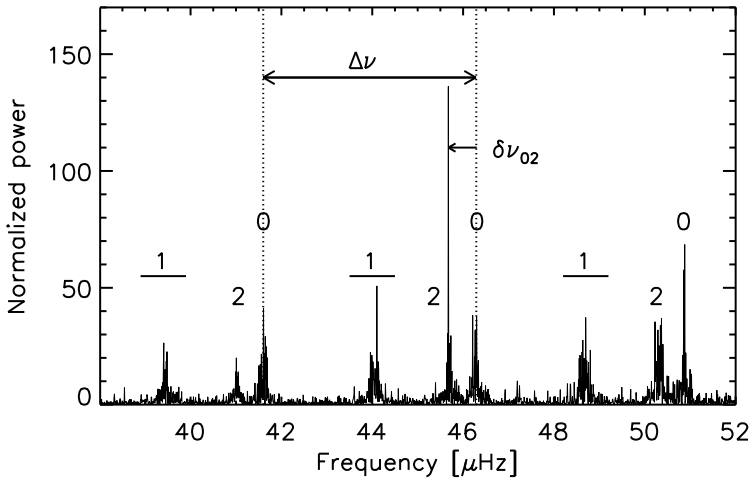

Figure 2.9: Normalized (by background, see Sec. 2.4.2) Fourier power density spectrum of KIC 8410637 centred around the frequency of maximum oscillation power. The large frequency separation $\Delta\nu$ and the small frequency separation $\delta\nu_{02}$ are indicated for some modes only. The dominant peaks represent modes of spherical degree $\ell = 0, 1$, and 2, as indicated.

2.4.3.1 The frequency of maximum oscillation power $\nu_{\rm max}$

The oscillation region of red giants is visible as excess power in the PDS (e.g. for KIC 8410637 at $\sim 45\,\mu$Hz as shown in the top panel of Fig. 2.8). The centre of this power excess is known as the frequency of maximum oscillation power $\nu_{\rm max}$. This global seismic parameter is one of the direct observables used for deriving the asteroseismic mean density, mass, radius and surface gravity of the red giants that we study and thus has to be obtained accurately. We derived $\nu_{\rm max}$ from a Gaussian fit to the power excess according to:

$$P_{\rm g}(\nu) = P_{\rm bg}(\nu) + \eta(\nu)^2 \left[\Lambda_{\rm g} \exp\left(\frac{-(\nu - \nu_{\rm max})^2}{2\sigma_{\rm g}^2}\right)\right]. \tag{2.2}$$

Here, $\Lambda_{\rm g}$ and $\sigma_{\rm g}$ indicate the height and the standard deviation of the Gaussian. To estimate the free parameters we applied the same Bayesian MCMC method including Metropolis-Hastings sampling which we described before in Section 2.4.2. The ranges for the uniform prior distributions of the Gaussian parameters are defined in the bottom part of Table 2.5. We used the frequency peak with the highest amplitude in the oscillation region as an initial guess for $\nu_{\rm max}$ ($\nu_{\rm max,guess}$) and we computed a first estimate of the large frequency separation ($\Delta\nu_{\rm guess}$, see Sec. 2.4.3.3) from the relation between the frequency of maximum oscillation power and the large frequency spacing (Hekker et al. 2009, Stello et al. 2009, Mosser et al. 2010). Since the global background was determined in a preceding step, we kept the parameters of $P_{\rm bg}(\nu)$ (eq. 2.1) in the Gaussian model (eq. 2.2) fixed. The Gaussian fits to the power excesses of KIC 8410637, KIC 5640750, and KIC 9540226 are shown in Figure 2.8. These are based on the model parameters that are reported in Table 2.6, as computed from the MCMC algorithm.

Table 2.6: Median values and corresponding 68 % credible interval for the global background (eq. 2.1) and Gaussian (eq. 2.2) parameters for the three red giants investigated here.

a_1 [ppm]	b_1 [μHz]	a_2 [ppm]	b_2 [μHz]	Λ_g [ppm$^2\mu$Hz^{-1}]	ν_{max} [μHz]	σ_g [μHz]
KIC 8410637						
295 ± 6	11.3 ± 0.4	269 ± 7	43.5 ± 0.9	1743 ± 67	46.4 ± 0.3	7.1 ± 0.2
KIC 5640750						
477 ± 22	6.5 ± 0.4	380 ± 36	24.7 ± 1.5	9732 ± 483	24.1 ± 0.2	3.6 ± 0.1
KIC 9540226						
416 ± 17	8.2 ± 0.5	303 ± 30	32.1 ± 2.3	5806 ± 257	26.7 ± 0.2	4.6 ± 0.1

2.4.3.2 Determination of individual frequencies

Individual frequencies of oscillation modes contain valuable information about the stellar properties and provide essential constraints for detailed stellar modelling. In asteroseismology, the extraction of frequencies is often referred to as 'peakbagging' analysis. Our aim is to extract all significant oscillation modes from the power density spectrum to calculate the mean large frequency spacing, which in combination with ν_{max} and T_{eff} provides access to the stellar parameters of red-giant stars through so-called scaling relations (Ulrich 1986, Brown et al. 1991, Kjeldsen and Bedding 1995). Since frequencies with large power are found around the frequency of maximum oscillation power, we restricted the peakbagging analysis to the frequency range covering $\nu_{max} \pm 4\,\Delta\nu$. In this region, we used the asymptotic relation (Tassoul 1980, Mosser et al. 2011) to obtain the spherical degree and initial frequencies of the modes. We only included the dominant peak of each degree per (acoustic) radial order without incorporating mixed or rotationally-split modes explicitly. These p-dominated mode frequencies are necessary to compute the mean large and small frequency separations. The resulting set of modes were simultaneously fit with Lorentzian profiles (e.g. Anderson et al. 1990, Corsaro et al. 2015a):

$$P_{peaks}(\nu) = P_{bg}(\nu) + \eta(\nu)^2 \left[\sum_{i=1}^{n} \frac{A_i^2/(\pi\Gamma_i)}{1 + 4(\frac{\nu-\nu_i}{\Gamma_i})^2} \right]. \tag{2.3}$$

Each Lorentzian i consists of a central mode frequency ν_i, mode amplitude A_i and mode linewidth Γ_i. For the peakbagging we kept the global background parameters (eq. 2.1) fixed and considered uniform prior distributions for the variables representing the Lorentzian profiles. By using Metropolis-Hastings sampling in our framework of a MCMC simulation (see Sec. 2.4.2 for more details), we explored the parameter space of about 54 free parameters on average per star. Figure 2.10 shows the global peakbagging fits to the frequency range of the oscillations as well as the spectral window functions and the residuals of the fits. Unresolved frequency peaks were also excluded from this analysis since Lorentzian profiles are not appropriate for fitting them. Due to low S/N, we also omitted some of the outermost modes which achieved poor fits and ambiguous posterior probability distributions for the sampled parameters. Median values for all significant mode frequencies, mode widths and mode amplitudes (eq. 2.3) that were computed with our fitting method are listed in Tables 2.14, 2.15, and 2.16 for the three red giants studied here.

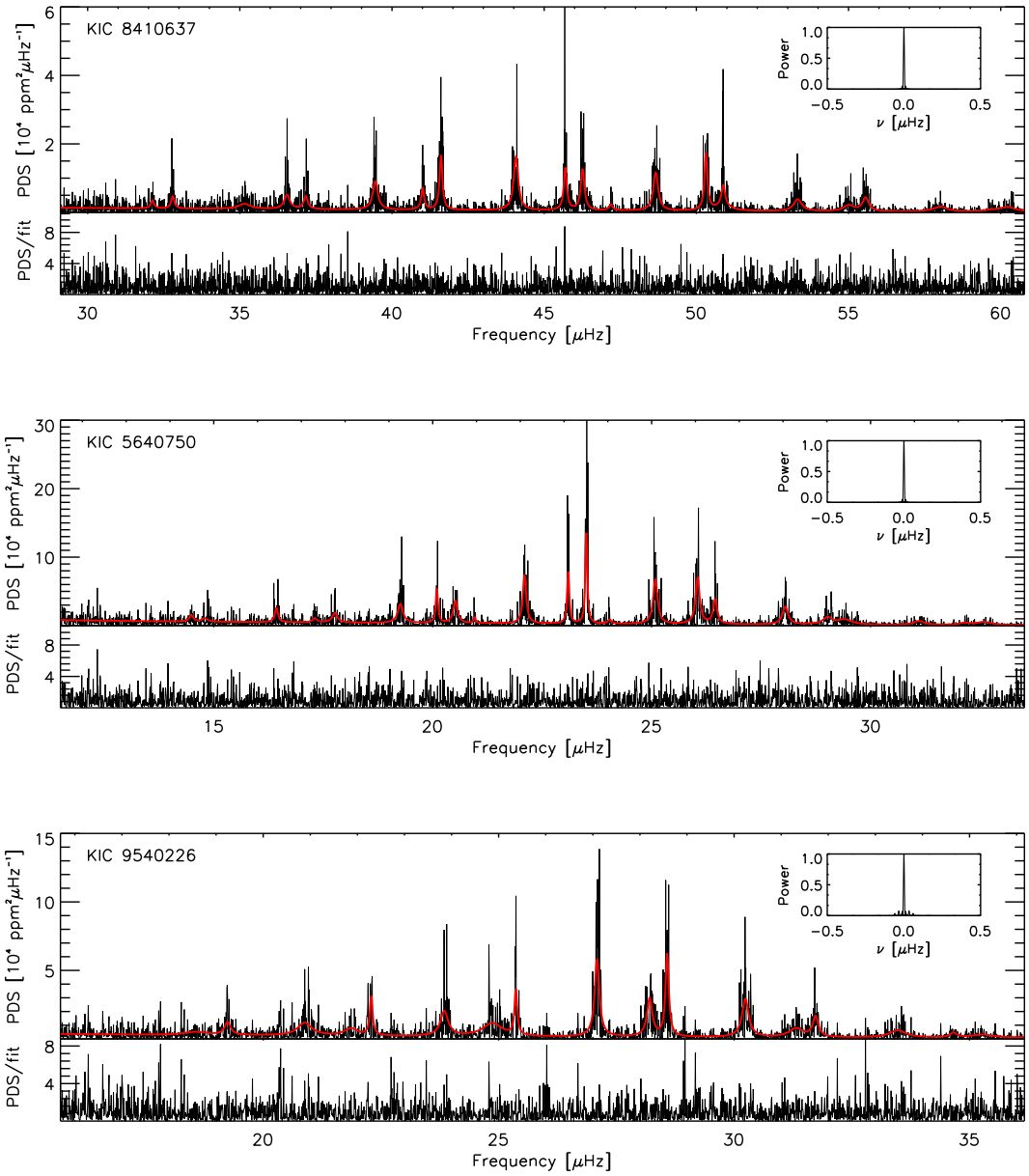

Figure 2.10: Fourier power density spectra (in black) of KIC 8410637 (top), KIC 5640750 (middle), and KIC 9540226 (bottom) in the frequency range of the oscillations. The red solid lines represent the fits to the modes. The spectral window functions are shown in the insets in each panel. The smaller panels below each spectrum show the residuals of the peakbagging fits.

2.4.3.3 Signatures derived from individual frequencies

In the current study, we use the individual mode frequencies to derive the mean large and small frequency separations. The large frequency separation $\Delta\nu_{n,\ell}$ is the spacing between oscillation modes of the same spherical degree (ℓ) and consecutive radial order (n). The large frequency spacing is related to the sound travel time across the stellar diameter and thus to the mean density of the star. We computed the global mean large frequency separation ($\Delta\nu$) from a linear weighted fit to the frequencies of all fitted $\ell = 0$ modes versus radial order that are reported in Tables 2.14, 2.15, and 2.16. Each fit was weighted according to the uncertainties of the individual frequencies as derived from the peakbagging analysis. The slope of this linear fit corresponds to $\Delta\nu$ and the intercept refers to the offset ϵ in the asymptotic relation (Tassoul 1980) multiplied with $\Delta\nu$. Based on the central three radial $\ell = 0$ modes we also calculated local values of $\Delta\nu_c$ and ϵ_c that can be used as an indicator for the evolutionary stage of red-giant stars (see Sec. 2.4.4.1).

Other parameters of interest are the mean small frequency separations $\delta\nu_{02}$, i.e. the frequency difference between $\ell = 0$ and $\ell = 2$ modes, and $\delta\nu_{01}$, i.e. the offset of the $\ell = 1$ modes from the midpoint between consecutive $\ell = 0$ modes. The small frequency spacings have some sensitivity in the stellar core of main-sequence stars and possibly for red giants they provide some information about their evolutionary state (e.g. Corsaro et al. 2012, Handberg et al. 2017). For each couple of modes we obtained estimates of these frequency spacings by using all significant frequencies and we adopted the weighted mean of these measurements as mean small frequency separations $\delta\nu_{02}$ and $\delta\nu_{01}$.

The large and small frequency separations change with evolution and can be used to infer stellar properties of stars showing solar-like oscillations. We report the global seismic parameters for KIC 8410637, KIC 5640750, and KIC 9540226 in Table 2.7. We note that radial and non-radial modes are used to compute the small frequency separations, hence these measurements can also be perturbed by mixed modes. With $\Delta\nu$ known, we constructed so-called échelle diagrams (Grec et al. 1983), in which we detect three clear ridges of $\ell = 0, 1, 2$ modes and several detections of $\ell = 3$ modes (see Appendix 2.8.2 and Fig. 2.15). These diagrams are consistent with the mode identification of the asymptotic relation.

In addition to the large frequency separation, which represents the first frequency difference, we also investigated the second frequency difference for acoustic glitch signatures (see Appendix 2.8.3.1).

In Figure 2.11 we show the comparison between ν_{max} and $\Delta\nu$ derived from our analysis procedures with the results from previous asteroseismic studies. For all three red giants we observe small variations of the order of a few per cent in the derived parameter estimates, which are partly caused by different analysis procedures and different datasets. We find the local mean large frequency separations ($\Delta\nu_c$) to have a larger value than the global mean large frequency separations ($\Delta\nu$). The difference in their computations is the frequency range that is used, which can cause a change in the $\Delta\nu$ value and can be linked to stellar structure changes that occur over longer scales (Hekker and Christensen-Dalsgaard 2017). In Figure 2.11 we also show different $\Delta\nu - \nu_{max}$ relations that were observed for field and cluster giants (Hekker et al. 2011a). KIC 8410637, KIC 5640750, and KIC 9540226 follow such relations and their stellar parameters are in line with the

Table 2.7: Weighted mean $\Delta\nu$ (global and local), small frequency separations, $\delta\nu_{02}$ and $\delta\nu_{01}$, and local offset ϵ_c computed from the frequencies obtained from the peakbagging analysis (see Sec. 2.4.3.2).

KIC	$\Delta\nu_{\ell=0}$ [μHz]	$\delta\nu_{02}$ [μHz]	$\delta\nu_{01}$ [μHz]	$\Delta\nu_c$ [μHz]	ϵ_c
8410637	4.564 ± 0.004	0.583 ± 0.014	-0.109 ± 0.016	4.620 ± 0.008	1.02 ± 0.02
5640750	2.969 ± 0.006	0.429 ± 0.013	-0.098 ± 0.016	2.978 ± 0.015	0.90 ± 0.02
9540226	3.153 ± 0.006	0.517 ± 0.019	-0.095 ± 0.014	3.192 ± 0.010	1.01 ± 0.02

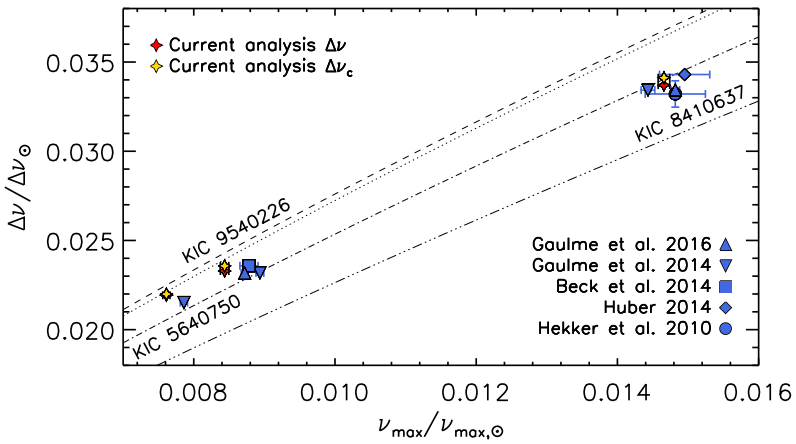

Figure 2.11: Global oscillation parameters ν_{max} and $\Delta\nu$ for KIC 8410637, KIC 5640750, and KIC 9540226. Different symbols correspond to different asteroseismic studies that were performed (see legend). The red and gold symbols correspond to estimates of the global ($\Delta\nu$) and local ($\Delta\nu_c$) large frequency separation that we discuss in Section 2.4.3.3. Different linestyles indicate the $\Delta\nu - \nu_{max}$ relations derived by Hekker et al. (2011a) for three open clusters with different masses (NGC 6791: dash, NGC 6819: dash dot, NGC 6811: dash triple dot) and field stars (dotted line).

mass ranges observed for the cluster stars.

2.4.3.4 Comparison with other asteroseismic fitting methods

To check for consistency with other analysis methods, the three red giants under study were independently fit by several co-authors and their respective methods. Since these methods have been thoroughly tested on red-giant stars, they provide the means to probe the fitting procedures that we used (see Sec. 2.4.3 for more details). The comparison between the global seismic parameters reported in Tables 2.6 and 2.7 with those calculated from the methods developed by Mosser and Appourchaux (2009), Kallinger et al. (2014), Corsaro and De Ridder (2014), Corsaro et al. (2015a) are presented in Appendix 2.8.3 and Figure 2.16. In this Figure we show that the derived ν_{max} and $\Delta\nu$ values from different methods are in line for the three red giants investigated here. In addition, we checked the individual frequencies of oscillation modes (Tab. 2.14 – 2.16) that we obtained based on the fitting algorithm described in Section 2.4.3.2 with independent sets of frequencies that were extracted according to the methods developed by Kallinger et al. (2014), Corsaro

and De Ridder (2014), Corsaro et al. (2015a). For each red-giant star we only report frequencies that were independently detected by different analysis methods.

2.4.4 Derivation of the stellar parameters

2.4.4.1 Evolutionary state of red giants

Asteroseismology allows us to differentiate between red-giant branch and red-clump stars by using different oscillation features (e.g. Mosser et al. 2011, Bedding et al. 2011, Kallinger et al. 2012, Mosser et al. 2014, Elsworth et al. 2017) that are discussed here.

All non-radial modes in red giants are mixed pressure-gravity modes, which carry information of the outer layers of the star as well as from the core (e.g. Beck et al. 2011, Mosser et al. 2012b). These mixed modes can be used to distinguish between less evolved red-giant branch and more evolved red-clump stars through a study of their period spacings. Mosser et al. (2011) and Bedding et al. (2011) considered observed (bumped) period spacings of mixed dipole ($\ell = 1$) modes which give an estimate of the spacings of the g-dominated modes. For hydrogen-shell burning stars on the red-giant branch they observed period spacings of the order of about 50 s, while typical spacings of red-clump stars reached values around 100 to 300 s. The observed period spacing is generally smaller than the so-called asymptotic period spacing which is directly related to the core size of the star. In more recent studies, Mosser et al. (2014, 2015) and Vrard et al. (2016) developed a method to measure this asymptotic period spacing and they found values of about 40 to 100 s for red-giant branch stars and of roughly 200 to 350 s for more evolved stars in the red clump. Based on the technique described by Mosser et al. (2015) and implemented by Vrard et al. (2016), we derived asymptotic period spacings of 58 ± 3 s and 55 ± 5 s for two of the red giants under study, KIC 5640750 and KIC 9540226, which suggests that these stars belong to the red-giant branch.

A clear advantage of this method is that it does not require individual frequencies of g-dominated mixed modes. For the three red giants investigated here only the p-dominated non-radial modes are pronounced. Gaulme et al. (2014) found red-giant components in close binary systems where tidal interactions caused extra mode damping and even complete mode suppression. In our red giants, the lack of distinct mixed modes can also be an indication for some binary influence. In a preliminary study we investigated the presence of only p-dominated mixed modes in a small number of known red giants in binary systems as well as in a larger number of stars from the APOKASC (Pinsonneault et al. 2014) sample. We observed mainly p-dominated mixed modes in a large fraction of known binaries, while we detected the same feature in a significantly smaller fraction of red giants in the APOKASC sample (Themeßl et al. 2017).

For stars without distinct g-dominated mixed modes, Kallinger et al. (2012) proposed another method to determine their evolutionary stage, which is based on the local offset (ϵ_c) of the asymptotic relation. By plotting the local large frequency separation ($\Delta\nu_c$) against this offset, non-helium (red-giant branch) and helium-burning (clump) stellar populations occupy two different parts in this $\Delta\nu_c$ versus ϵ_c space as shown in Figure 4 of Kallinger et al. (2012). The theoretical explanation for this relation was provided by Christensen-Dalsgaard et al. (2014) and additional observational evidence was found by Vrard et al.

Table 2.8: Stellar parameters obtained from asteroseismic scaling relations. Whenever the solar symbol is shown, we used solar values derived in this work and presented in Section 2.4.4.2.

KIC	M [$M_\odot$]	R [$R_\odot$]	$\bar{\rho}$ [$\bar{\rho}_\odot \times 10^{-3}$]	$\log g$ (cgs)
Scaling relations (SR) + $\nu_{\rm max,ref} = \nu_{\rm max,\odot}$ and $\Delta\nu_{\rm ref} = \Delta\nu_\odot$ ($\rm SR_a$)				
8410637	1.74 ± 0.06	11.53 ± 0.15	1.136 ± 0.006	2.555 ± 0.005
5640750	1.33 ± 0.05	14.02 ± 0.20	0.481 ± 0.003	2.267 ± 0.005
9540226	1.45 ± 0.06	13.87 ± 0.20	0.542 ± 0.003	2.314 ± 0.006
SR + $\nu_{\rm max,ref} = \nu_{\rm max,\odot}$ and $\Delta\nu_{\rm ref}$ from Gug16 ($\rm SR_b$)				
8410637	1.62 ± 0.06	11.12 ± 0.13	1.178 ± 0.002	2.555 ± 0.005
5640750	1.19 ± 0.05	13.31 ± 0.17	0.506 ± 0.002	2.267 ± 0.005
9540226	1.31 ± 0.05	13.22 ± 0.18	0.569 ± 0.002	2.314 ± 0.006
SR + $\nu_{\rm max,ref} = \nu_{\rm max,\odot}$ and $\Delta\nu_{\rm ref}$ from Gug17 ($\rm SR_c$)				
8410637	1.61 ± 0.06	11.08 ± 0.13	1.182 ± 0.002	2.555 ± 0.005
5640750	1.17 ± 0.04	13.20 ± 0.17	0.511 ± 0.002	2.267 ± 0.005
9540226	1.30 ± 0.05	13.14 ± 0.17	0.572 ± 0.002	2.314 ± 0.006
SR + $\nu_{\rm max,ref} = \nu_{\rm max,\odot}$ and $\Delta\nu_{\rm ref} = \Delta\nu_{\rm ref,emp} \sim 131\,\mu$Hz ($\rm SR_{emp}$, Sec. 2.5.2)				
8410637	1.51 ± 0.07	10.75 ± 0.20	1.218 ± 0.018	2.555 ± 0.005
5640750	1.15 ± 0.06	13.08 ± 0.26	0.515 ± 0.008	2.267 ± 0.005
9540226	1.26 ± 0.06	12.94 ± 0.25	0.581 ± 0.009	2.314 ± 0.006

(2015) based on the study of the acoustic glitches due to the second-helium ionization. They both note that the separation between red-giant branch and red-clump stars does not only relate to the different structures in their cores. The differences in the cores also cause a change in the outer stellar layers. The observed effect of this is a shift in the acoustic glitch of the helium second ionization zone that affects the oscillations. According to the $\Delta\nu_{\rm c} - \epsilon_{\rm c}$ diagram, the three red-giant stars KIC 8410637, KIC 5640750, and KIC 9540226 are located on the red-giant branch. For KIC 9540226, the identification of the evolutionary state, from both mixed modes and the local offset of the asymptotic relation, agrees with the findings of Beck et al. (2014). They found that nearly all heartbeat stars in their sample are unambiguously hydrogen-shell burning stars. Therefore they identified this as a selection effect through stellar evolution as those systems are likely to undergo a common-envelope phase and eventually eject the outer envelope before they can reach the tip of the red-giant branch.

2.4.4.2 Asteroseismology: Direct method

To apply asteroseismic methods to calculate the stellar parameters of a solar-like oscillating star, we need to know the star's effective temperature and metallicity. In Section 2.3.4 we accurately estimated these parameters from the analysis of the disentangled spectra. The effective temperatures and metallicities for the red-giant components are summarized in Table 2.4.

The frequency of maximum oscillation power is proportional to the acoustic cut-off fre-

quency with $\nu_{\rm max}$ defined as (Brown et al. 1991, Kjeldsen and Bedding 1995):

$$\begin{aligned}\nu_{\rm max} &\simeq \frac{M/{\rm M}_\odot}{(R/{\rm R}_\odot)^2\sqrt{T_{\rm eff}/T_{\rm eff,ref}}}\nu_{\rm max,ref}\\ &\simeq \frac{g/{\rm g}_\odot}{\sqrt{T_{\rm eff}/T_{\rm eff,ref}}}\nu_{\rm max,ref}.\end{aligned} \tag{2.4}$$

The large frequency separation scales with the sound travel time across the stellar diameter and is therefore a measure of the mean density of the star (Ulrich 1986):

$$\begin{aligned}\Delta\nu &\simeq \left(\frac{M}{{\rm M}_\odot}\right)^{0.5}\left(\frac{R}{{\rm R}_\odot}\right)^{-1.5}\Delta\nu_{\rm ref}\\ &\simeq \sqrt{\bar\rho/\bar\rho_\odot}\Delta\nu_{\rm ref}.\end{aligned} \tag{2.5}$$

These equations represent the well-known asteroseismic scaling relations. Parameters M, R, g, and $\bar\rho$ are given in solar units and 'ref' refers to a reference value. By combining these two relations (eq. 2.4 and 2.5) we can compute an estimate of the asteroseismic stellar parameters:

$$\begin{aligned}\left(\frac{\bar\rho}{\bar\rho_\odot}\right) &\simeq \left(\frac{\Delta\nu}{\Delta\nu_{\rm ref}}\right)^2,\\ \left(\frac{g}{{\rm g}_\odot}\right) &\simeq \left(\frac{\nu_{\rm max}}{\nu_{\rm max,ref}}\right)\left(\frac{T_{\rm eff}}{T_{\rm eff,ref}}\right)^{0.5},\\ \left(\frac{R}{{\rm R}_\odot}\right) &\simeq \left(\frac{\nu_{\rm max}}{\nu_{\rm max,ref}}\right)\left(\frac{\Delta\nu}{\Delta\nu_{\rm ref}}\right)^{-2}\left(\frac{T_{\rm eff}}{T_{\rm eff,ref}}\right)^{0.5},\\ \left(\frac{M}{{\rm M}_\odot}\right) &\simeq \left(\frac{\nu_{\rm max}}{\nu_{\rm max,ref}}\right)^3\left(\frac{\Delta\nu}{\Delta\nu_{\rm ref}}\right)^{-4}\left(\frac{T_{\rm eff}}{T_{\rm eff,ref}}\right)^{1.5}.\end{aligned} \tag{2.6}$$

For these relations the Sun is often used as reference star. To obtain solar values in a consistent way we determined the global seismic parameters of the Sun with the same procedures as applied to the stellar data (see Sec. 2.4.2 and 2.4.3). The only difference was the number of granulation background components that were used for the solar background model. We find a better fit to the Fourier spectrum of the Sun if we include a third granulation component. We used full-disk integrated light measurements of the Sun from the VIRGO experiment (Fröhlich et al. 1995) onboard the ESA/NASA Solar and Heliospheric Observatory (SOHO). To analyze the oscillations of the Sun, we used red and green data from 12 years of continuous solar observations with a cadence of one minute. The time span of these observations covers a whole solar cycle during which the p-mode parameters are known to vary with the solar activity (e.g. Libbrecht and Woodard 1990, Jiménez et al. 2002). We divided the data into subsets of four years with a one year step to mimic the observation time span of the nominal *Kepler* mission. Then, we analyzed each subset separately. From the results of all subsets we computed the following mean solar values of $\nu_{\rm max,\odot} = 3166 \pm 6\,\mu$Hz and $\Delta\nu_\odot = 135.4 \pm 0.3\,\mu$Hz. In terms of spectroscopic measurements of the Sun, we make use of the nominal solar effective temperature of $\mathcal{T}^{\rm N}_{\rm eff,\odot} = 5771.8 \pm 0.7$ K (Mamajek et al. 2015, Prša et al. 2016). Using these solar values as a reference, we directly determined the stellar parameters of our three red-giant stars

(eq. 2.6, SR_a in Tab. 2.8). By using a single star as a reference it is implicitly assumed that the internal properties of stars change in a homologous way with stellar evolution for all stars of different masses and metallicities (Belkacem et al. 2011, 2013). However, from theoretical predictions and observations we know that many structural changes occur in stars when they pass through different evolutionary stages during their lives and hence the assumption of homology does not strictly hold. Due to these known difficulties connected with the asteroseismic scaling relations, many studies (e.g. White et al. 2011, Miglio et al. 2012, Mosser et al. 2013, Hekker et al. 2013b, Guggenberger et al. 2016, Sharma et al. 2016, Rodrigues et al. 2017, Viani et al. 2017, Guggenberger et al. 2017) tried to improve the results obtained from these relations. Gaulme et al. (2016) tested different scaling-relation corrections for their study of 10 red-giant stars in eclipsing binary systems and found that they lead to similar results. Guggenberger et al. (2016, hereafter Gug16) derived a metallicity and effective temperature dependent reference function applicable to red-giant branch stars in the mass and ν_{max} range that we are investigating here. They showed that their reference improves the precision of mass and radius estimates by a factor of two, which translates to an accuracy of 5 % in mass and 2 % in radius. In Guggenberger et al. (2017, hereafter Gug17), they expanded their method by including a mass dependence in their formulation of the $\Delta\nu$ reference. We adopted both of their methods to calculate the stellar parameters for KIC 8410637, KIC 5640750, and KIC 9540226, which we present in Table 2.8 (SR_b and SR_c).

2.4.4.3 Asteroseismology: Grid-based modelling

Interpolation through a precomputed grid of stellar models and finding the best fit to the observational data is another method by which stellar parameters can be determined (grid-based modelling, see Gai et al. 2011). For the grid-based modelling (GBM) we used the canonical BASTI grid[5] (Pietrinferni et al. 2004), which spans masses from 0.5 $M_\odot$ to 3.5 $M_\odot$ in steps of 0.05 $M_\odot$ and metallicities of Z = 0.0001, 0.0003, 0.0006, 0.001, 0.002, 0.004, 0.008, 0.01, 0.0198, 0.03, and 0.04. (The corresponding helium abundances are Y = 0.245, 0.245, 0.246, 0.246, 0.248, 0.251, 0.256, 0.259, 0.2734, 0.288, and 0.303.) The BASTI grid includes models from the zero-age main sequence all the way to the asymptotic giant branch phase. The models were computed using an updated version of the code described by Cassisi and Salaris (1997) and Salaris and Cassisi (1998).

We extracted stellar parameters for the stars under study from this grid using an independent implementation of the likelihood method described by Basu et al. (2010). In short, the likelihood of each model was computed given the values of some chosen set of observed parameters, in this case ν_{max}, $\Delta\nu$, T_{eff}, and [M/H]. To obtain a reliable uncertainty for the derived parameters a Monte Carlo analysis was performed, in which the observed values were perturbed within their uncertainties and a new likelihood was determined. The final answer was derived from the centre and width of a Gaussian fit through the total likelihood distribution of 1 000 perturbations. Furthermore, we used the temperature and metallicity dependent reference function developed by Gug16 for the $\Delta\nu$ scaling relation (eq. 2.5). Additionally, we included the fractional solar uncertainties on $\Delta\nu$ and ν_{max} in the uncertainties of the $\Delta\nu$ and ν_{max} values derived for the three giants investigated here to

[5] http://albione.oa-teramo.inaf.it/

Table 2.9: Asteroseismic stellar parameters obtained from grid-based modelling. Whenever the solar symbol is shown, we used solar values derived in this work and presented in Section 2.4.4.2.

KIC	M [$M_\odot$]	R [$R_\odot$]	$\bar{\rho}$ [$\bar{\rho}_\odot \times 10^{-3}$]	log g (cgs)	age [Gyr]
Grid-based modelling + $\nu_{\rm max,ref} = \nu_{\rm max,\odot}$ and $\Delta\nu_{\rm ref}$ from Gug16 (GBM)					
8410637	1.91 ± 0.06	11.83 ± 0.19	1.148 ± 0.003	2.571 ± 0.003	1.2 ± 0.6
5640750	1.39 ± 0.05	14.10 ± 0.53	0.496 ± 0.005	2.282 ± 0.005	2.8 ± 0.8
9540226	1.52 ± 0.06	14.03 ± 0.42	0.557 ± 0.006	2.329 ± 0.005	2.1 ± 0.8
Grid-based modelling + $\nu_{\rm max,ref} = \nu_{\rm max,\odot}$ & $\Delta\nu_{\rm ref} = \Delta\nu_{\rm ref,emp} \sim 131\,\mu$Hz ($GBM_{emp}$, Sec. 2.5.2)					
8410637	1.48 ± 0.06	10.65 ± 0.52	1.223 ± 0.035	2.555 ± 0.010	2.8 ± 1.2
5640750	1.22 ± 0.10	13.31 ± 0.85	0.515 ± 0.016	2.274 ± 0.011	4.6 ± 1.9
9540226	1.32 ± 0.10	13.14 ± 0.88	0.581 ± 0.017	2.321 ± 0.011	3.5 ± 1.6

account for uncertainties in the reference values. The grid-based modelling was carried out twice once using only models on the red-giant branch and once using models in the helium-core burning phase. We only report here the results from the red-giant branch models as this is the evolutionary stage of the stars according to the present asteroseismic analysis (see Sec. 2.4.4.1).

For the grid-based modelling we used the effective temperatures given in Table 2.4, which were derived from the atmospheric analysis of the disentangled spectra. The resulting stellar parameters are listed in Table 2.9 and shown in Figure 2.12. One advantage of grid-based modelling is that it also provides age estimates for the stars. According to our grid-based analysis KIC 8410637, KIC 5640750, and KIC 9540226 have approximate ages of 1.2 ± 0.6, 2.8 ± 0.8, and 2.1 ± 0.8 Gyr, respectively.

2.5 Comparison between asteroseismic and dynamical stellar parameters

The aim of this complementary study is to explore consistencies between stellar parameters derived from asteroseismology, i.e. the asteroseismic scaling relations and grid-based modelling, and from binary analyses.

2.5.1 Comparison

We first consider the mass, radius, mean density, and logarithmic surface gravity values obtained from the binary analyses. The results are shown as the shaded boxes in Figure 2.12. The size of the box is given by the 1σ uncertainties of the individual parameters. For KIC 8410637 we note agreement between the different estimates with the exception of the mass and the mean density from the current study which is lower than the other values. As previously indicated, for KIC 5640750 there are two possible binary solutions at inconsistent values of the parameters. This ambiguity can be attributed to insufficient phase coverage of the spectroscopic observations (Sec. 2.3.2.3). We will shortly use the asteroseismic values to guide us in making a choice between these two options. For KIC 9540226 there is agreement within 1σ for the stellar masses and within 2σ for

the stellar radii. Differences in these results can partly be attributed to the use of different datasets, analysis methods and possibly some signal that is still left in the orbital phase.

We now consider the asteroseismic results that are shown as the open boxes in Figure 2.12. Results from grid-based modelling (GBM) and the application of scaling laws (SR) are shown. Because of underlying physical principles used to compute asteroseismic estimates of mass and radius, mass and radius are correlated and the use of different $\Delta\nu$ values naturally leads to the obvious trends seen in the left panels of Figure 2.12. We note that the uncertainties in $\bar{\rho}$ and $\log g$ for the asteroseismic results are smaller than the corresponding uncertainties of the values that are computed directly from the derived dynamical masses and radii.

From GBM we obtained larger values for the stellar masses and radii than the parameter estimates calculated from the asteroseismic scaling relations. Tayar et al. (2017) pointed out that GBM may modify the inferred effective temperatures in order to find a better match between observed parameters and stellar models. This is the case here. We were not able to find a matching model for the $T_{\rm eff}$ derived from the binary analyses (Tab. 2.4). Instead, GBM favoured models with $\sim$ 200 K higher effective temperatures. As a consequence, we find larger values for the logarithmic surface gravities as well as stellar masses and radii from GBM. We note that these results have relatively large uncertainties, because their computations also take metallicities with uncertainties into account. Furthermore, we obtained lower stellar masses and radii and larger mean densities when using asteroseismic scaling relations that also take the metallicity, temperature and mass dependence of the stars into account ($\mathrm{SR_c}$).

For KIC 5640750 we now compare the dynamical stellar parameters from both orbital solutions with the asteroseismic values. We see that the second option (denoted as $\mathrm{BA_2}$) with $M_{\rm B} = 1.158 \pm 0.014\,\mathrm{M_\odot}$, $R_{\rm B} = 13.119 \pm 0.090\,\mathrm{R_\odot}$ and $\log g_{\rm B} = 2.266 \pm 0.006$ (cgs) is in line with what we observe for the other two red giants where the dynamical masses and radii are lower than the asteroseismic values. Despite the fact that the statistical significance of both binary solutions is almost the same, we can now give more weight to the second option which suits the overall picture of the three red giants studied here. In the further analysis, we consider only the second set of dynamical stellar parameters for KIC 5640750.

In Figure 2.12, in addition to the metallicity-independent mass-radius correlation already alluded to, we see that there is a lack of agreement between the asteroseismic and dynamical stellar parameters for the three red giants under study. To investigate these discrepancies further, we examine the influence of different asteroseismic observables and the asteroseismic scaling relations since these are important for inferring the stellar properties. Among the parameters of interest are the global seismic parameters ($\nu_{\rm max}$, $\Delta\nu$) as well as the reference values ($\nu_{\rm max,ref}$, $\Delta\nu_{\rm ref}$).

2.5.2 Empirically derived $\Delta\nu_{\rm ref,emp}$

Following the determination of the asteroseismic stellar parameters in Section 2.4.4.2, we now reverse the scaling relations (eq. 2.4–2.5) to obtain estimates for the global seismic parameters ($\nu_{\rm max}, \Delta\nu$) and for the reference values ($\nu_{\rm max,ref}, \Delta\nu_{\rm ref}$) to check for coherency.

In both cases we use the dynamical stellar masses and radii and the spectroscopic effective temperatures as input.

In combination with the observed reference values, i.e. from the Sun, we calculated the global seismic parameters, which for all three red-giant stars agree with the observed values within uncertainties. We subsequently computed the reference values by using the observed global seismic parameters of the red-giant stars together with the dynamical M, R, and $T_{\rm eff}$. We obtained consistent reference values for the frequency of maximum oscillation power with a mean value of $3137 \pm 45\,\mu$Hz which agrees with the observed solar reference reported in Section 2.4.4.2.

Based on the same approach we calculated $\Delta\nu_{\rm ref}$ for the three red giants investigated here. We consistently derived lower values around a mean value of $\Delta\nu_{\rm ref,emp} = 130.8 \pm 0.9\,\mu$Hz, which is inconsistent with the observed solar value of $135.4 \pm 0.3\,\mu$Hz (Sec. 2.4.4.2).

We now consider the different $\Delta\nu_{\rm ref}$ references that we used throughout our asteroseismic analysis. We adopted either the observed solar value of $\sim 135\,\mu$Hz or we included the temperature, mass, and metallicity dependence of the stars using corrections based on models. This latter approach led to a $\Delta\nu_{\rm ref} \sim 132\,\mu$Hz based on the formulations provided by Guggenberger et al. (2017). In the latter reference, the so-called surface effect (e.g. Ball and Gizon 2017) is not included, yet it is present in the models on which the $\Delta\nu_{\rm ref}$ is based. This effect arises due to improper modelling of the near surface layers and it causes a shift in the p-mode frequencies which then also changes the value of the mean large frequency separation.

In short, if we consider a star with one solar mass, an effective temperature of 5772 K and [Fe/H] = 0.0, i.e. the Sun, we would derive a large frequency separation of about $136\,\mu$Hz from a solar model. The reason why this is different from the observed solar value of about $135\,\mu$Hz is due to the surface effect. Thus, we may still have to decrease $\Delta\nu_{\rm ref}$ from Gug17 by $\sim 1\,\mu$Hz, i.e. $\sim 1\,\%$, because we would expect a shift of this magnitude for the reference value. This would then be very close to our empirically determined $\Delta\nu_{\rm ref,emp}$ value. A detailed analysis of the scale of the surface effect in KIC 8410637, KIC 5640750, and KIC 9540226 is presented in Ball et al. (2018). It is worth noting that due to the surface effect a shift in frequency between ~ 0.1 and $0.3\,\mu$Hz at $\nu_{\rm max}$ is observed for the three red-giant stars studied here, which show oscillations in the range between ~ 24 and $46\,\mu$Hz. The magnitude of these frequency differences is similar to the 1 % that was found for the model of the Sun.

Most recently, Brogaard et al. (2018) also reported consistencies between asteroseismic and dynamical stellar parameters when using a model-dependent theoretical correction factor that was proposed by Rodrigues et al. (2017) instead of the usual solar reference values. Their correction of $\Delta\nu_{\rm ref}$ is of the same order of magnitude as the one that we present in the current study.

From the combined asteroseismic and binary analysis we derived an empirical $\Delta\nu_{\rm ref,emp}$ reference that seems to be more appropriate for these three specific red-giant stars instead of the commonly used solar reference. We used this in the asteroseismic scaling relations (eq. 2.6) and determined revised stellar parameters for KIC 8410637, KIC 5640750, and KIC 9540226. The asteroseismic stellar masses and radii from both the scaling relations

Table 2.10: Relative differences in per cent of the asteroseismic stellar parameters (Sec. 2.4.4.2 and 2.4.4.3) with respect to the binary solution (Sec. 2.3.3). In the case of KIC 5640750 we compare the dynamical stellar parameters that are based on the second binary solution.

Method	KIC 8410637				KIC 5640750				KIC 9540226			
	M [%]	R [%]	$\bar{\rho}$ [%]	$\log g$ [%]	M [%]	R [%]	$\bar{\rho}$ [%]	$\log g$ [%]	M [%]	R [%]	$\bar{\rho}$ [%]	$\log g$ [%]
SR_a	18	9	8	< 1	15	7	6	< 1	4	3	6	< 1
SR_b	10	5	5	< 1	3	2	1	< 1	6	2	< 1	< 1
SR_c	9	5	4	< 1	1	< 1	< 1	< 1	7	2	< 1	< 1
SR_{emp}	3	2	2	< 1	< 1	< 1	< 1	< 1	9	4	1	< 1
GBM	30	12	7	< 1	20	8	3	1	9	5	3	< 1
GBM_{emp}	< 1	< 1	1	< 1	5	2	< 1	< 1	5	2	1	< 1

and GBM are lower and they are now in line with the dynamical stellar parameters. We show the revised stellar parameters with dotted boxes in Figure 2.12. The uncertainties for these stellar parameters are larger due to a larger uncertainty in the $\Delta\nu_{ref,emp}$ reference. In the GBM analysis, these lower masses have an impact on the ages of these red-giant stars which are now on average 1.5 Gyr older (Tab. 2.9). In addition we note that our conclusions do not change when using slightly different $\Delta\nu$ values (such as the ones given in Fig. 2.16) for the determination of the stellar parameters of the three red giants studied here.

2.5.2.1 Consistency check with a larger sample of red giants

To further test the empirically derived reference value, we applied it to a number of known oscillating red-giant-branch components in eclipsing binary systems. By using published $\nu_{max}, \Delta\nu$ and T_{eff} we recomputed the asteroseismic stellar parameters for nine stars that show solar-like oscillations in the range between $\sim$ 20 and $\sim$ 77 μHz, i.e. KIC 9540226 (Beck et al. 2014, Gaulme et al. 2016, Brogaard et al. 2018), KIC 8410637 (Frandsen et al. 2013), KIC 4663623, KIC 9970396, KIC 7037405, KIC 5786154, KIC 10001167, KIC 7377422 and KIC 8430105 (Gaulme et al. 2016).

Although we find consistencies between the derived asteroseismic and published dynamical stellar parameters, we see some scatter in the results (see Fig. 2.13). This scatter is partly caused by combining global seismic parameters, effective temperatures, RVs and/or disentangled spectra that were obtained from different methods and specific calibrations. The systematics and biases that are introduced by asteroseismic techniques have been thoroughly discussed in literature (e.g. Hekker et al. 2011b, Verner et al. 2011, Hekker et al. 2012, Kallinger et al. 2014).

The observed scatter in the asteroseismic results is larger than the quoted uncertainties of the dynamical stellar parameters. This shows the importance of a homogeneous analysis for all stars under study, which is expected to increase the consistency between the asteroseismic and dynamical stellar parameters. We note that Kallinger et al. (2018) present a careful study where they test the scaling relations with dynamical stellar parameters of

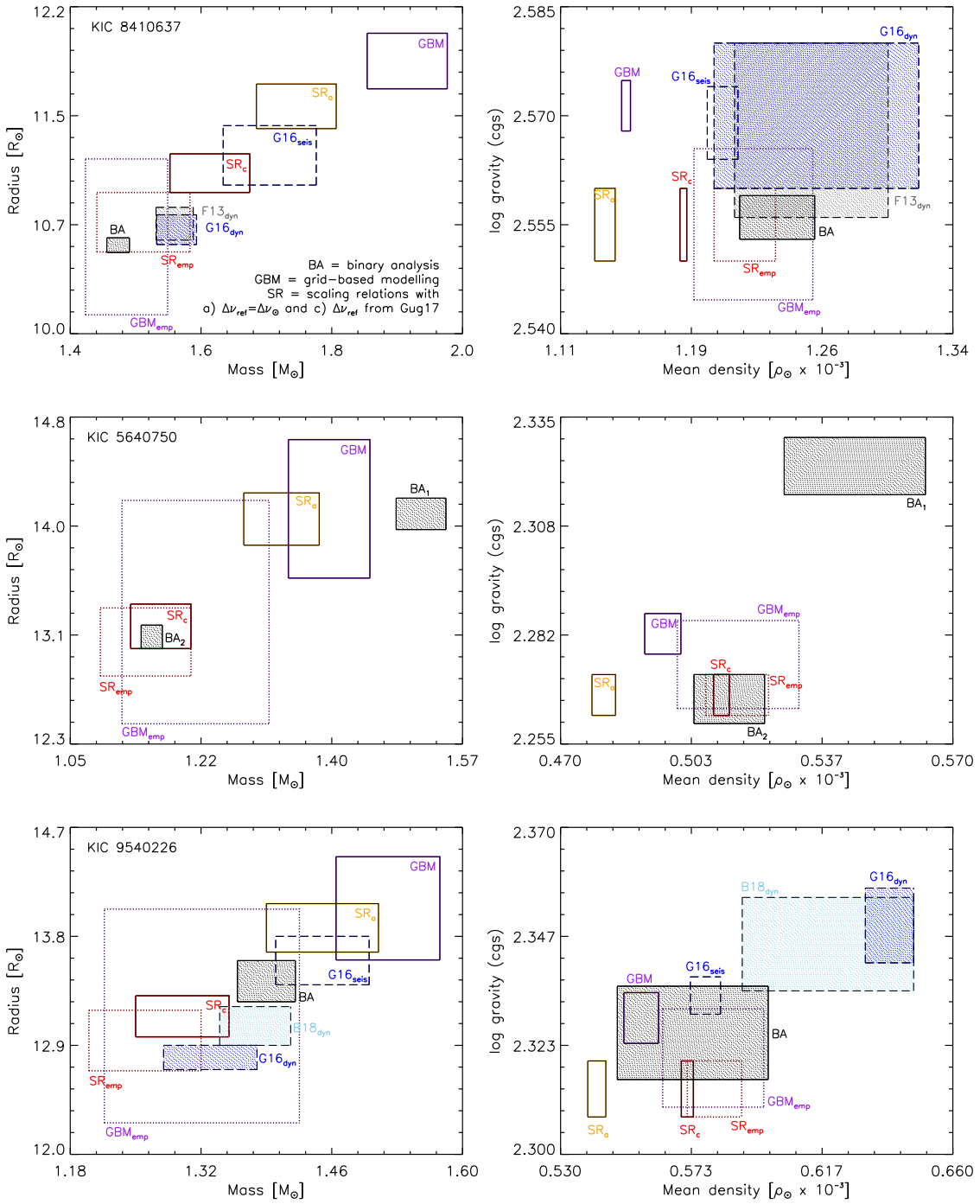

Figure 2.12: Stellar mass versus radius (left) and mean density versus logarithmic surface gravity (right) for KIC 8410637 (top), KIC 5640750 (middle), and KIC 9540226 (bottom) derived from binary orbit analyses (filled boxes) and from asteroseismology (open boxes). Results from the current analysis are shown with solid and dotted lines. The latter refers to stellar parameters determined on the basis of an empirical $\Delta\nu_{\rm ref,emp}$ reference (Sec. 2.5.2). Dashed lines represent already published values of the stellar parameters (Frandsen et al. (2013, $F13_{\rm dyn}$), Gaulme et al. (2016, $G16_{\rm dyn;seis}$), Brogaard et al. (2018, $B18_{\rm dyn}$)). For different colours see legend and Tables 2.3, 2.8, and 2.9.

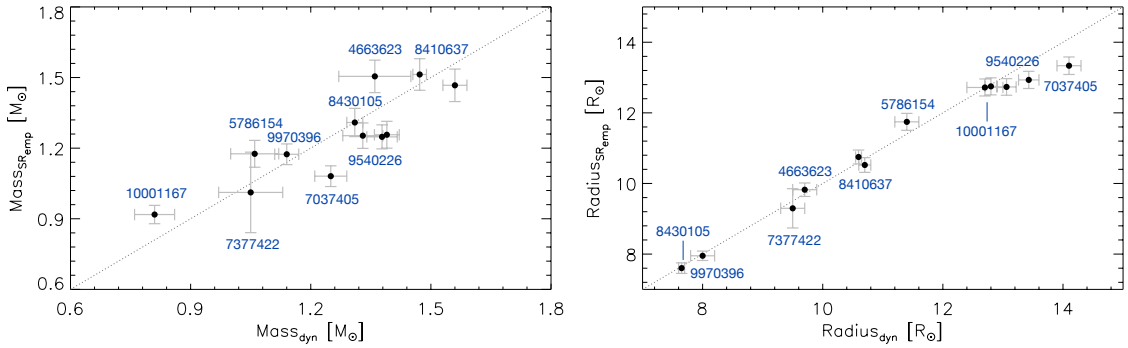

Figure 2.13: Asteroseismic versus dynamical masses (left) and radii (right) for nine RGB components in known eclipsing binary systems with KIC numbers indicated. Asteroseismic stellar parameters (SR_{emp}) were determined by using $\Delta\nu_{ref,emp} \sim 131\,\mu$Hz (Sec. 2.5.2).

eclipsing binary systems and they only found six stars, for which the stellar properties are known with sufficient precision for solid conclusions.

Despite these issues we determined a consistent mean value for the $\Delta\nu$ reference (albeit with large uncertainties) when using the published properties of these nine red-giant branch stars, which cover a larger stellar parameter space than our original sample. This is a further indication that a $\Delta\nu_{ref,emp}$ of about 131 μHz is appropriate for stars on the red-giant branch.

2.6 Conclusions

We find agreement between the stellar parameters determined using asteroseismic scaling relations and eclipse modelling only when using a $\Delta\nu$ reference that we derived empirically and that can be justified by known physical parameters such as mass, effective temperature, metallicity, and the surface effect. In Table 2.10 we show the relative differences of the asteroseismic stellar parameters for the red-giant components of KIC 8410637, KIC 5640750, and KIC 9540226 with respect to the binary solutions. As we look at a small sample of stars here, we cannot investigate the global differences between the asteroseismic scaling relations and orbital parameters. Yet, we performed a careful in-depth observational analysis for each of the red giants and we found consistent results for the three systems.

Calculations of detailed stellar models of the three red giants studied here are on the way. The highly-precise and accurate *Kepler* data can be used to fit oscillation frequencies in a large number of red-giant stars, which provide additional information for stellar models. The oscillation frequencies, however, have to be corrected for surface effects before they can be compared to modelled frequencies (e.g. Ball and Gizon 2017). The surface effects in red giants are not yet fully understood, even though three-dimensional simulations are insightful (Sonoi et al. 2015, for instance). The results from detailed modelling of the surface effects of these three red giants in eclipsing binary systems using individual frequencies is presented in Ball et al. (2018). We note however that for the red giants investigated here we require a lower $\Delta\nu$ reference value of the order of 131 μHz when mass,

temperature, and metallicity dependence, as well as surface effect are taken into account. This supports the idea of using $\Delta\nu_{\rm ref,emp} = 130.8 \pm 0.9\,\mu$Hz which in our case provides consistencies between asteroseismic and dynamical stellar parameters for KIC 8410637, KIC 5640750, and KIC 9540226 which are all located close to the red-giant branch bump.

The current study shows the importance of $\Delta\nu_{\rm ref}$ in the asteroseismic scaling relations. Ideally, we would extend this work to more pulsating red-giant stars in eclipsing binary systems that cover a wide range in stellar parameters. In future, stars with different properties of mass, metallicity, and evolutionary stages (e.g. red-giant components in eclipsing binaries that are in the red clump phase) need to be studied in order to identify appropriate reference values and to investigate the presence of other sources that could influence the stellar parameter measurements.

2.7 Appendix A: RVs for KIC 8410637, KIC 5640750, and KIC 9540226

We applied the CCF method to all available spectra of KIC 8410637, KIC 5640750 and KIC 9540226 to determine the radial velocities of the giants and their corresponding uncertainties, which are given in Tables 2.11, 2.12, and 2.13. For completeness, we also report the RVs for the dwarf components of these systems, which were obtained by previous studies.

Table 2.11: Radial velocity measurements of the two components of KIC 8410637. These are the measurements used in the analysis in Section 2.3.3. They were not used in the determination of the physical properties of the system (which was done with the velocity amplitudes from the spectral disentangling analysis). The RVs in this table are those used by co-author JS in his analysis in Section 2.3.3 and also in Frandsen et al. (2013). However, it was retrospectively discovered that they are not the same as those published in Frandsen et al. (2013), and source of the discrepancy has resisted our attempts to find it (S. Frandsen, 2015, priv. comm.). In future we advise that analyses of this binary system use the results from spectral disentangling, or as a second choice the RVs published in Frandsen et al. (2013). We report the RVs in this table only for completeness.

KIC 8410637			
HJD-2450000	Giant RV [km s^{-1}]	Dwarf RV [km s^{-1}]	Source
5660.7131	-54.69 ± 0.05	-30.68 ± 2.59	FIES
5660.7362	-54.69 ± 0.04	-30.23 ± 2.31	FIES
5733.6205	-60.91 ± 0.05	-27.79 ± 0.76	FIES
5749.5119	-62.18 ± 0.05	-27.39 ± 0.74	FIES
5762.6434	-62.98 ± 0.06	-26.92 ± 0.88	FIES
5795.4991	-56.90 ± 0.05	-29.78 ± 1.04	FIES
5810.4756	-28.70 ± 0.05	-64.60 ± 1.38	FIES
5825.3478	-11.75 ± 0.05	-85.47 ± 1.21	FIES
5828.3417	-12.90 ± 0.05	-84.60 ± 1.30	FIES
5834.4285	-16.01 ± 0.06	-81.75 ± 1.21	FIES

5844.3966	-21.13 ± 0.05	-76.04 ± 1.79	FIES
5855.3398	-25.64 ± 0.05	-68.46 ± 1.59	FIES
5886.3003	-34.33 ± 0.05	-58.98 ± 1.15	FIES
5903.3175	-37.68 ± 0.06	-58.22 ± 1.18	FIES
5903.3444	-37.80 ± 0.07	-57.31 ± 1.55	FIES
5700.4998	-58.00 ± 0.05	-29.28 ± 1.14	CES
5726.4642	-60.47 ± 0.06	-28.01 ± 1.27	CES
5734.4230	-60.87 ± 0.06	-26.41 ± 2.28	CES
5734.5069	-60.84 ± 0.07	-27.56 ± 1.29	CES
5754.4370	-62.55 ± 0.06	-26.19 ± 1.19	CES
5793.3535	-58.62 ± 0.05	-29.30 ± 1.48	CES
5799.4801	-53.04 ± 0.10	-30.89 ± 1.52	CES
5810.4495	-28.76 ± 0.06	-66.44 ± 2.19	CES
5817.3353	-14.40 ± 0.08	-83.10 ± 1.85	CES
5850.3024	-23.98 ± 0.06	-76.39 ± 2.48	CES
5852.2713	-24.85 ± 0.06	-76.17 ± 3.31	CES
5880.2040	-33.14 ± 0.05	-59.91 ± 1.48	CES
5334.5342	-61.94 ± 0.04	-27.85 ± 0.82	HERMES
5334.6737	-61.53 ± 0.05	-27.59 ± 0.84	HERMES
5335.5792	-61.90 ± 0.04	-27.90 ± 0.74	HERMES
5335.6967	-61.58 ± 0.05	-27.48 ± 0.88	HERMES
5336.5676	-61.88 ± 0.05	-27.69 ± 0.78	HERMES
5336.7291	-61.47 ± 0.05	-27.26 ± 1.04	HERMES
5609.7553	-50.64 ± 0.04	-30.81 ± 1.69	HERMES
5715.4610	-59.72 ± 0.05	-28.80 ± 1.68	HERMES
5765.4437	-63.07 ± 0.05	-26.82 ± 0.98	HERMES
5779.4483	-63.58 ± 0.04	-27.28 ± 0.88	HERMES
5801.4416	-49.85 ± 0.05	-41.61 ± 2.13	HERMES
5835.3802	-16.82 ± 0.05	-82.05 ± 1.41	HERMES
5871.3083	-30.75 ± 0.05	-62.92 ± 1.61	HERMES
5888.3093	-35.35 ± 0.05	-58.77 ± 1.00	HERMES
5888.3273	-34.80 ± 0.05	-59.05 ± 1.21	HERMES
5965.7723	-45.72 ± 0.05	-34.82 ± 1.41	HERMES

Table 2.12: Radial velocity measurements of the red-giant component of KIC 5640750 derived with the cross-correlation method (CCF) from HERMES spectra.

KIC 5640750			
HJD-2450000	Giant RV [$\mathrm{km\,s^{-1}}$]	S/N (Mg I triplet)	Source
5623.7602	-23.34 ± 0.04	41.80	HERMES
5765.5211	-27.56 ± 0.03	32.00	HERMES
5778.6673	-28.13 ± 0.03	31.10	HERMES
5835.4160	-30.93 ± 0.03	32.00	HERMES
5867.3840	-32.67 ± 0.03	26.20	HERMES
5870.3324	-32.83 ± 0.03	27.10	HERMES
6011.7324	-43.42 ± 0.04	29.30	HERMES
6101.5477	-50.77 ± 0.03	37.00	HERMES
6101.5691	-50.76 ± 0.03	38.10	HERMES

6119.4962	-51.43 ± 0.04	36.80	HERMES
6119.5199	-51.43 ± 0.04	37.50	HERMES
6138.4671	-51.53 ± 0.03	25.70	HERMES
6138.4908	-51.53 ± 0.04	24.90	HERMES
6176.4195	-49.03 ± 0.03	33.90	HERMES
6182.4333	-48.36 ± 0.03	35.70	HERMES
6183.4953	-48.24 ± 0.03	38.70	HERMES
6183.5190	-48.22 ± 0.04	37.50	HERMES
6196.5769	-46.42 ± 0.03	26.80	HERMES
6215.3964	-43.59 ± 0.04	38.30	HERMES
6479.6168	-22.34 ± 0.03	20.10	HERMES
6484.4643	-22.42 ± 0.04	20.80	HERMES
6488.5134	-22.32 ± 0.04	20.30	HERMES

Table 2.13: Radial velocity measurements of the red-giant component of KIC 9540226 derived with CCF from HERMES spectra.

KIC 9540226			
HJD-2450000	Giant RV [$\mathrm{km\,s^{-1}}$]	S/N (Mg I triplet)	Source
5765.4977	-25.85 ± 0.03	29.60	HERMES
5783.5060	-22.50 ± 0.03	32.80	HERMES
5872.3865	-12.13 ± 0.04	27.10	HERMES
5884.3425	-19.18 ± 0.04	21.80	HERMES
5884.3570	-19.19 ± 0.05	19.90	HERMES
5889.3317	-21.16 ± 0.05	16.70	HERMES
5889.3459	-21.30 ± 0.04	10.90	HERMES
5889.3662	-21.18 ± 0.04	18.40	HERMES
5990.7423	-5.01 ± 0.04	22.90	HERMES
6106.4950	-26.43 ± 0.03	25.40	HERMES
6106.5165	-26.41 ± 0.04	26.90	HERMES
6126.6582	-24.17 ± 0.04	24.40	HERMES
6126.6796	-24.22 ± 0.03	24.10	HERMES
6132.5252	-22.91 ± 0.04	27.60	HERMES
6132.5471	-22.84 ± 0.04	25.60	HERMES
6136.6113	-21.65 ± 0.03	32.20	HERMES
6136.6327	-21.61 ± 0.03	31.70	HERMES
6139.4500	-21.00 ± 0.04	31.50	HERMES
6148.5050	-17.38 ± 0.04	32.10	HERMES
6148.5264	-17.36 ± 0.04	32.10	HERMES
6158.4969	-11.59 ± 0.04	34.20	HERMES
6158.5183	-11.58 ± 0.04	35.00	HERMES
6176.4456	6.03 ± 0.04	30.10	HERMES
6182.4104	13.44 ± 0.04	33.40	HERMES
6184.5669	15.87 ± 0.03	31.40	HERMES
6184.5895	15.92 ± 0.03	29.50	HERMES
6195.5294	18.81 ± 0.04	30.60	HERMES
6506.4110	-13.52 ± 0.03	21.90	HERMES
6506.4324	-13.55 ± 0.04	20.70	HERMES

6510.5030	-10.81 ± 0.03	16.50	HERMES
6518.3925	-4.06 ± 0.04	26.10	HERMES
6519.4668	-2.94 ± 0.04	26.70	HERMES

2.8 Appendix B: Frequencies

2.8.1 Peakbagging results

Based on the methods described in Section 2.4.3.2, we extracted all the significant frequencies from the oscillation spectra of the three stars. The complete list of central mode frequencies, amplitudes, and linewidths are reported in Tables 2.14, 2.15, and 2.16. In addition, we show the linewidths of all significant $\ell = 0$ and $\ell = 2$ modes in Figure 2.14. It is clear that the extracted non-radial modes incorporate contributions from unresolved mixed and rotationally-split modes. For KIC 8410637, KIC 5640750 and KIC 9540226 we derived linewidths of the same order of magnitude as reported by Corsaro et al. (2015a). They performed an extensive peakbagging analysis of 19 red-giant stars and they pointed out a linewidth depression close to the frequency of maximum oscillation power which is also visible in Figure 2.14.

2.8.2 Échelle diagrams

Échelle diagrams (Grec et al. 1983) present an alternative technique to identify modes of different spherical degree ℓ. To construct such a diagram the Fourier power density spectrum is divided into segments of equal lengths ($\Delta\nu$). Then these segments are stacked on top of each other. The modes of the same spherical degree line up as near vertical ridges in the diagram. Figure 2.15 shows the échelle diagrams for KIC 8410637, KIC 5640750, and KIC 9540226. Three ridges are clearly visible, which correspond to spherical degrees $\ell = 0, 1, 2$. The strongest mode frequencies that were extracted through the peakbagging analysis are marked with symbols.

2.8.3 Differences between asteroseismic methods

The global oscillation parameters and frequencies of oscillation modes were derived independently from several co-authors using different approaches. We refer the interested reader to Mosser and Appourchaux (2009) (EACF, hereafter M09), Kallinger et al. (2014) (hereafter K14) and Corsaro and De Ridder (2014), Corsaro et al. (2015a) (DIAMONDS, hereafter C14), for detailed descriptions of these methods. Figure 2.16 shows that the seismic parameter estimates, $\nu_{\rm max}$ and $\Delta\nu$, are of the same order of magnitude and that the use of different procedures does not substantially affect the results. Based on our analysis (Sec. 2.4.3.3) we determined local ($\Delta\nu_{\rm c}$) and global ($\Delta\nu$) mean large frequency separations, which are shown in the same Figure.

Table 2.14: Median values and 68 % confidence interval for central mode frequencies, mode amplitudes, and mode heights for KIC 8410637.

KIC 8410637				
n	ℓ	ν [μHz]	A [ppm]	Γ [μHz]
5	2	32.13±0.05	47.6±6.3	0.43±0.11
6	0	32.79±0.02	40.6±3.6	0.08±0.03
6	1	35.16±0.04	52.1±4.9	0.45±0.11
6	2	36.56±0.03	66.7±7.1	0.38±0.09
7	0	37.18±0.02	46.1±5.4	0.14±0.05
6	3	37.70±0.09	12.3±6.4	0.33±0.13
7	1	39.44±0.02	87.4±6.8	0.23±0.04
7	2	41.02±0.01	62.5±6.2	0.10±0.03
8	0	41.62±0.01	88.0±5.6	0.09±0.02
8	1	44.06±0.02	90.4±6.3	0.26±0.04
8	2	45.69±0.01	87.4±5.0	0.14±0.03
9	0	46.28±0.02	94.5±6.3	0.13±0.03
8	3	47.19±0.01	29.6±4.2	0.07±0.03
9	1	48.70±0.02	93.3±5.7	0.21±0.03
9	2	50.31±0.02	96.4±7.1	0.14±0.03
10	0	50.85±0.01	87.3±5.0	0.11±0.03
9	3	51.71±0.06	37.2±5.1	0.48±0.13
10	1	53.32±0.02	81.4±4.0	0.30±0.04
10	2	55.06±0.04	75.1±8.6	0.48±0.11
11	0	55.54±0.03	61.4±7.7	0.24±0.05
11	1	58.04±0.04	64.5±3.7	0.46±0.04
11	2	59.74±0.05	47.6±8.4	0.44±0.16
12	0	60.28±0.05	62.0±7.0	0.44±0.05
12	1	62.95±0.02	82.7±4.6	0.50±0.01

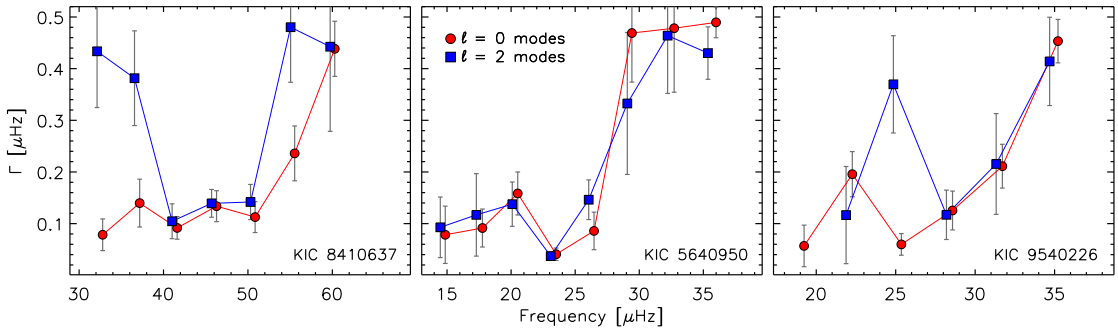

Figure 2.14: Mode linewidths of significant frequencies of KIC 8410637 (left), KIC 5640750 (middle), and KIC 9540226 (right). Red circles and blue squares represent $\ell = 0$ and $\ell = 2$ modes, respectively.

Table 2.15: Same as Table 2.14 for KIC 5640750.

KIC 5640750				
n	ℓ	ν [μHz]	A [ppm]	Γ [μHz]
3	2	14.47±0.06	18.9±17.0	0.09±0.05
4	0	14.86±0.06	48.1±19.1	0.08±0.05
4	1	16.46±0.03	86.2±11.9	0.10±0.06
4	2	17.29±0.03	53.5±11.8	0.12±0.08
5	0	17.76±0.02	75.1±12.7	0.09±0.04
5	1	19.27±0.01	142.2±14.9	0.06±0.03
5	2	20.09±0.01	107.6±11.1	0.14±0.04
6	0	20.52±0.02	99.8±08.4	0.16±0.04
5	3	20.94±0.07	51.8±14.6	0.06±0.02
6	1	22.12±0.01	140.6±12.0	0.12±0.03
6	2	23.09±0.01	141.1±15.7	0.04±0.01
7	0	23.52±0.01	187.4±16.1	0.04±0.01
6	3	24.02±0.02	57.4±10.7	0.13±0.06
7	1	25.09±0.01	182.4±11.7	0.15±0.02
7	2	26.06±0.02	178.5±12.1	0.15±0.04
8	0	26.47±0.02	128.8±13.2	0.09±0.04
8	1	28.02±0.02	147.2±10.3	0.19±0.03
8	2	29.07±0.03	127.2±24.2	0.33±0.14
9	0	29.43±0.08	99.9±23.3	0.47±0.09
9	1	31.08±0.04	93.1±07.1	0.38±0.09
9	2	32.21±0.05	70.0±13.4	0.46±0.11
10	0	32.72±0.06	66.9±12.8	0.48±0.12
10	1	34.23±0.06	58.4±06.7	0.42±0.07
10	2	35.36±0.08	60.3±06.2	0.43±0.05
11	0	35.99±0.05	64.4±11.5	0.49±0.03

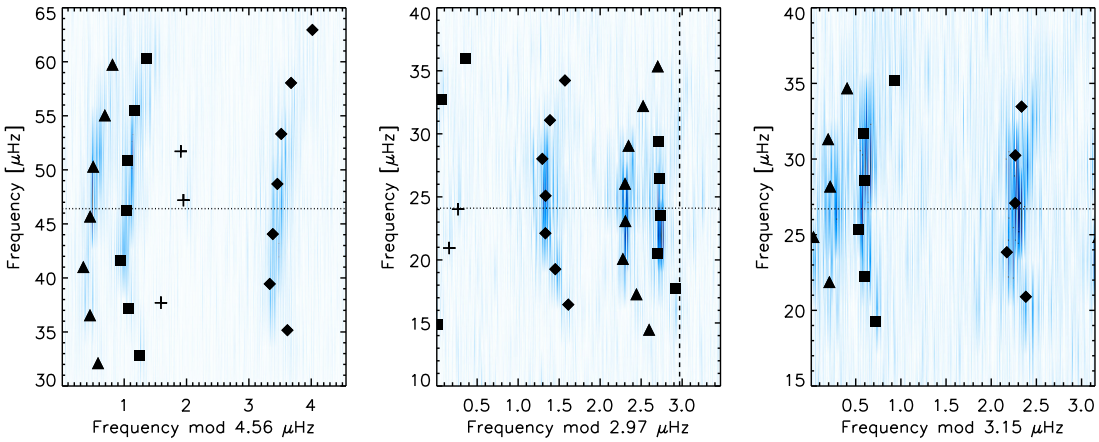

Figure 2.15: Échelle diagrams for KIC 8410637 (left), KIC 5640750 (middle), and KIC 9540226 (right). Darker blue tones correspond to higher power. Extracted mode frequencies are indicated by symbols (square: $\ell = 0$, triangle: $\ell = 2$, diamond: $\ell = 1$, plus: $\ell = 3$) and the horizontal dotted lines show measured $\nu_{\rm max}$ values.

Table 2.16: Same as Table 2.14 for KIC 9540226.

KIC 9540226				
n	ℓ	ν [μHz]	A [ppm]	Γ [μHz]
5	0	19.24±0.02	66.1±10.2	0.06±0.03
5	1	20.90±0.04	140.8±09.0	0.47±0.09
5	2	21.88±0.04	38.3±10.1	0.12±0.09
6	0	22.27±0.02	97.3±09.5	0.20±0.04
6	1	23.84±0.02	130.6±09.1	0.23±0.06
6	2	24.83±0.03	129.7±08.7	0.37±0.09
7	0	25.36±0.01	99.8±11.8	0.06±0.02
7	1	27.09±0.01	172.0±12.2	0.11±0.03
7	2	28.19±0.02	135.6±12.6	0.12±0.05
8	0	28.58±0.01	144.1±13.0	0.13±0.04
8	1	30.24±0.01	154.8±10.9	0.17±0.03
8	2	31.32±0.04	97.2±14.8	0.22±0.10
9	0	31.71±0.02	127.2±13.2	0.21±0.04
9	1	33.46±0.03	111.7±05.9	0.48±0.06
9	2	34.69±0.05	53.4±09.7	0.41±0.08
10	0	35.21±0.04	83.5±10.3	0.45±0.04

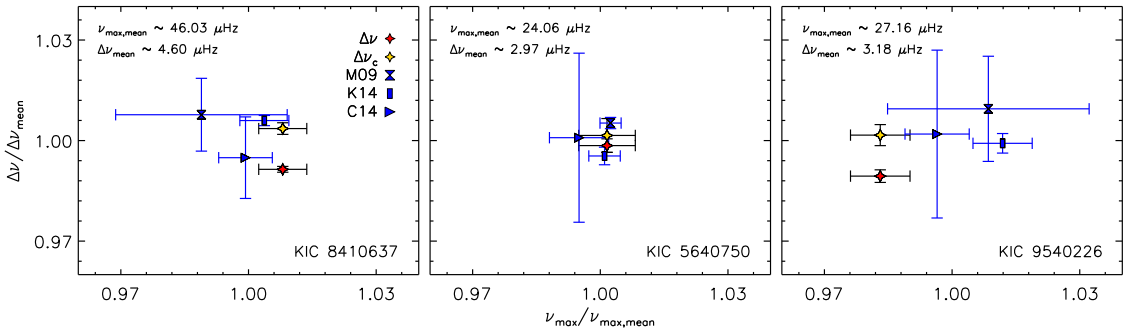

Figure 2.16: Estimates of the global oscillation parameters from different methods for KIC 8410637 (left), KIC 5640750 (middle), and KIC 9540226 (right). The red and gold star symbols represent the global ($\Delta\nu$) and local ($\Delta\nu_c$) mean large frequency separations that were used to determine the stellar parameters and evolutionary stages of the red giants. The KIC number is indicated in each panel.

2.8.3.1 Second frequency differences and acoustic glitches

In addition to the first frequency difference i.e. the large frequency separation $\Delta\nu_{n,\ell}$ which is given by:

$$\Delta\nu_{n,\ell} \equiv \nu_{n+1,\ell} - \nu_{n,\ell}, \tag{2.7}$$

we also computed the second frequency difference $\Delta_2\nu_{n,\ell}$ (Gough 1990):

$$\Delta_2\nu_{n,\ell} \equiv \Delta\nu_{n,\ell} - \Delta\nu_{n-1,\ell} = \nu_{n-1,\ell} - 2\nu_{n,\ell} + \nu_{n+1,\ell}. \tag{2.8}$$

In both equations (2.7–2.8) $\nu_{n,\ell}$ represents the frequency of a mode with given radial order n and spherical degree ℓ. The first and second frequency differences of the radial ($\ell = 0$) modes for KIC 8410637, KIC 5640750, and KIC 9540226 are shown in Figure 2.17. The uncertainties in $\Delta\nu_{n,\ell}$ and $\Delta_2\nu_{n,\ell}$ were derived from a standard error propagation of the uncertainties of the individual mode frequencies. The oscillatory signal which is visible in the second frequency difference is caused by a so-called acoustic glitch. This observable feature appears due to changes in the stellar interior that occur at scales shorter than the local wavelengths of the oscillations. In red giants, such a change is caused by the helium second ionization zone. Recently, acoustic glitch signatures could be examined in modelled and observed oscillation frequencies of stars exhibiting solar-like oscillations (e.g. Miglio et al. 2010, Mazumdar et al. 2014, Broomhall et al. 2014, Corsaro et al. 2015b, Vrard et al. 2015, Pérez Hernández et al. 2016).

In the current analysis we show that it is possible to perform a basic study of the acoustic glitches of two of the red giants (KIC 8410637 and KIC 5640750) for which we have 4 years of nearly uninterrupted *Kepler* data without any larger gaps available. Since this periodic signature caused by the helium second ionization zone is observable in pure p modes (e.g. Vorontsov 1988, Gough 1990), we can measure the acoustic depth and width of the helium second ionization zone (Hekker et al. 2013a) through the analysis of the second frequency differences of $\ell = 0$ modes. The modulation due to the glitch can be described by the following model (Houdek and Gough 2007):

$$\Delta_2\omega_{n,\ell} = A_{\rm osc}\omega_{n,\ell}\exp\left(-2b_{\rm osc}^2\omega_{n,\ell}^2\right)\cos\left[2(\tau_{\rm HeII}\omega_{n,\ell} + \phi)\right] + c, \tag{2.9}$$

where $\omega_{n,\ell}$ and $\Delta_2\omega_{n,\ell}$ define the angular versions of $\nu_{n,\ell}$ and $\Delta_2\nu_{n,\ell}$:

$$\omega_{n,\ell} \equiv 2\pi\nu_{n,\ell}, \Delta_2\omega_{n,\ell} \equiv 2\pi\Delta_2\nu_{n,\ell}. \tag{2.10}$$

This model is composed of a dimensionless amplitude $A_{\rm osc}$, an acoustic depth $\tau_{\rm HeII}$ and characteristic width $b_{\rm osc}$ of the second ionization zone, a constant phase shift ϕ and an offset c. Based on the Bayesian MCMC method with Metropolis-Hastings sampling which is described in more detail in Section 2.4.2, we estimated the model parameters in equation 2.9 and their 68 % credible intervals. In this case we assumed that the parameters follow a Gaussian distribution and therefore used a normal likelihood function. We did not account for correlations between the individual second frequency differences. For the free parameters, we chose uniform priors and a strict constraint on the period $\tau_{\rm HeII}$ with the convention that at least two measurements of the second frequency differences should cover one period of the acoustic glitch. The bottom panels in Figure 2.17 show a fit of the acoustic glitch model to the second frequency differences of KIC 8410637

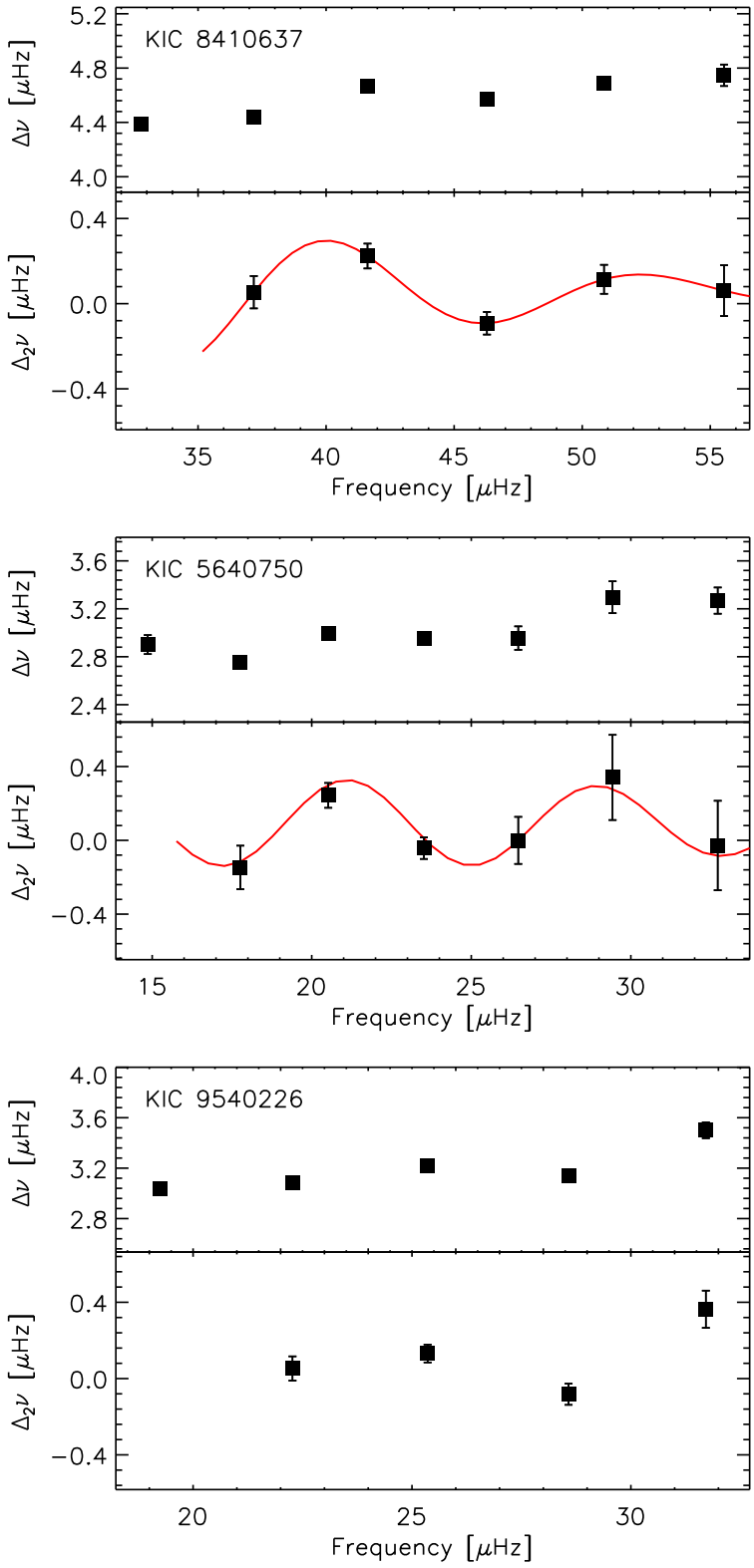

Figure 2.17: First (top panels, eq. 2.7) and second (bottom panels, eq. 2.8) frequency differences for KIC 8410637, KIC 5640750, and KIC 9540226. The red solid lines indicate the fits of the acoustic glitches (eq. 2.9 and Tab. 2.17) to the second differences. Uncertainties are shown on all points. In some cases the error bars are smaller than the symbol size.

Table 2.17: Median values and corresponding 68 % credible interval as derived for the fit parameters of the glitch model (eq. 2.9) using the Metropolis-Hastings MCMC algorithm.

KIC	$A_{\rm osc}$	$\tau_{\rm HeII}$ [s]	$b_{\rm osc}$ [s]	ϕ [rad]	c [μHz]
8410637	0.041 ± 0.003	40437 ± 16	3875 ± 23	2.33 ± 0.01	0.06 ± 0.01
5640750	0.020 ± 0.007	62901 ± 4281	4118 ± 656	1.08 ± 0.67	0.09 ± 0.04

and KIC 5640750, and are based on the best-fit parameters presented in Table 2.17. Due to a low number of available second frequency differences (less than five) we omitted KIC 9540226 (Fig. 2.17) from this part of the analysis.

3 Red giants in open clusters

This chapter reproduces an article in preparation *Ages of oscillating red-giant stars in NGC 6791 and NGC 6819: The impact of stellar physics on asteroseismic age determinations* by N. Themeßl, S. Hekker, A. García Saravia Ortiz de Montellano, A. Mints et al., which will be submitted to a journal in the future.

3.1 Summary

The common formation history puts tight constraints on stars in open clusters. These constraints make oscillating cluster giants excellent test-beds to verify asteroseismic techniques. We tested asteroseismic ages of red-giant stars with cluster isochrones and we explored the influence of metallicity constraints on these age estimates. In addition, we investigated the impact of different mass-loss rates for stellar models on the derived ages. From the oscillation spectra of red-giant stars it is possible to deduce their stellar parameters (asteroseismology), while at the same time these properties can be determined independently through isochrones fitted to all cluster members simultaneously. For the two open clusters, NGC 6791 and NGC 6819, we obtained age and metallicity estimates from isochrone fitting to the clusters' observed colour-magnitude diagrams. We used these global cluster parameters to verify independently determined asteroseismic masses and ages for about 60 oscillating red giants in both clusters. These masses and ages were derived based on *Kepler* long-cadence data and atmospheric parameters ($T_{\rm eff}$,[M/H]) from the SDSS/APOGEE spectrograph using an asteroseismic grid-based modelling approach. For a homogeneous analysis we used the same grids of isochrones for both, the asteroseismic study and the isochrone fitting. For red-giant stars in each cluster, we obtained more consistent results between the asteroseismic ages and isochrones when using the global metallicities of NGC 6791 and NGC 6819 as constraints for grid-based modelling instead of the measured values for individual stars. This shows that the metallicity plays an important role for asteroseismic age determinations. Moreover, we found that using grids of isochrones that incorporate different mass loss rates ($\eta = 0.0, 0.2$ and 0.4) have a small impact on the derived ages.

3.2 Introduction

Galactic open clusters comprise hundreds to a few thousands of stars that are assumed to be born from the same molecular cloud. Their common origin puts tight constraints on the age, metallicity, and distance of cluster stars. Some studies found considerable

discrepancies in the age estimates when derived for individual members in an open cluster. This is in contradiction with a coeval stellar population, which is expected from open cluster formation theories (e.g. Lada and Lada 1991, Friel 1995, Elmegreen et al. 2000, Lada 2010).

In the current study, we investigate consistencies between stellar ages of red-giant stars that belong to the same open cluster. Our aim is to investigate which parameters are important for asteroseismic age determinations and how accurately they need to be determined to obtain consistencies between the asteroseismic ages of individual stars and the global cluster ages from isochrones. Here, we focus on red giants in NGC 6791 and NGC 6819. The global physical properties of both clusters are known due to several surveys and dedicated photometric and spectroscopic campaigns from the ground (e.g. Kinman 1965, Burkhead 1971, Montgomery et al. 1994, Kalirai et al. 2001, Stetson et al. 2003, 2005, Carraro et al. 2006, Grundahl et al. 2008, Hole et al. 2009, Jeffries et al. 2013, An et al. 2015, Ak et al. 2016, and references therein). Different analyses of cluster data have led to a broad range in age, distance, interstellar reddening, and metallicity for each cluster. NGC 6791 is among the oldest galactic open clusters with an age around 7 – 9 Gyr and a global metallicity of about 0.3 – 0.4 dex. NGC 6819 is a younger open cluster with near-solar metallicity and an age of about 2 – 3 Gyr. In Table 3.1 we summarize the global physical properties of NGC 6791 and NGC 6819 that were recently derived by An et al. (2015) and Ak et al. (2016), which are broadly consistent with earlier studies.

For some of the more luminous stars in NGC 6791 and NGC 6819, the nominal *Kepler* space mission (e.g Borucki et al. 2010) provided photometric time series data from 2009 – 2013 that were complemented with spectra from the Apache Point Observatory Galactic Evolution Experiment (APOGEE; Majewski et al. 2017). The observed stars are in the red-giant phase of stellar evolution and they show solar-like oscillations that we can detect. We can probe the interior structure and evolution of red giants through studies of the observed oscillation modes by using an analysis method called asteroseismology. As these stars are members of open clusters, their assumed similar ages and metallicities provide more stringent constraints for testing theories of stellar structure and evolution than field stars. This makes cluster stars very important astrophysical laboratories.

Several studies emerged from the asteroseismic analysis of different subsets of the cluster data of NGC 6791 and NGC 6819, such as the determination of global seismic and stellar parameters (e.g. Stello et al. 2010, Hekker et al. 2011a, Corsaro et al. 2012, Wu et al. 2014b), the asteroseismic cluster membership probability (e.g. Stello et al. 2011), asteroseismic ages for red-giant branch stars in both open cluster (Basu et al. 2011), the analysis of mass loss of cluster stars (e.g. Miglio et al. 2012, Handberg et al. 2017), cluster distance moduli (e.g. Wu et al. 2014a), and the effect of metallicity on the granulation activity in cluster stars (Corsaro et al. 2017). Basu et al. (2011) was first to study individual asteroseismic ages of cluster stars in NGC 6791 and NGC 6819 based on seven months of *Kepler* data. By using asteroseismic constraints, they explored the global astrophysical properties of the two open clusters and computed stellar parameters from stellar models for a sample of stars on the red-giant branch. Basu et al. derived age estimates with relatively large uncertainties due to the length of the datasets present at the time of the study. Since then, the observations of the cluster stars were continued up to the end of the nominal *Kepler* space mission. With more data available at present, we are able to re-

duce the uncertainties in the asteroseismic and stellar parameters. Thus, we can perform a comprehensive investigation of the derived asteroseismic ages of individual cluster giants that are in different evolutionary stages, i.e. on the red-giant branch, in the red clump, and on the asymptotic giant branch. Moreover, Miglio et al. (2012) constrained the red-giant branch (RGB) mass loss for both open clusters through comparisons between the average mass of stars in the red clump with stars on the low-luminosity red-giant branch. For NGC 6791, they found an average mass difference of 0.09 ± 0.03 $M_{\odot}$, which was in line with isochrones that were computed by using a mass-loss efficiency parameter between 0.1 and 0.3. In the case of NGC 6819, Miglio et al. could derive less stringent constraints on the RGB mass-loss rate, because of the lower mass-loss rate for stars in this cluster. In the current study, we used three grids of isochrones that were generated with different mass-loss rates to explore their impact on the resulting age estimates for individual cluster giants.

For about 60 stars in NGC 6791 and NGC 6819 we extracted oscillation frequencies and identified their corresponding spherical degrees. By using published effective temperatures and metallicities from APOGEE, we computed a set of asteroseismic stellar parameters, i.e. masses, ages, radii, mean densities, luminosities, and surface gravities, of the red-giant stars from grid-based modelling by using asteroseismic observables. We studied the age and mass distributions of the red-giant populations in the two open clusters and investigated how different choices of initial constraints such as the metallicity of the cluster affect the asteroseismic age and mass determinations. Although the clusters' ages and metallicities are well constrained from literature studies, we redid the isochrone fitting to the publicly available colour-magnitude data (Stetson et al. 2005, An et al. 2015) to assure a homogeneous analysis by using the same set of stellar isochrones (PARSEC) for the asteroseismic grid-based analyses of individual red-giant stars.

3.3 Isochrone ages and metallicities for NGC 6791 and NGC 6819

Fitting stellar isochrones to the observed colour-magnitude diagram of a cluster is a well-known method to determine the cluster's age and metallicity. This technique requires photometric measurements in different bands for many cluster members as well as a suitable grid of stellar isochrones, i.e. constant age and metallicity tracks, that can describe the stellar properties of the observed stars in the cluster. Although studies in the literature obtained matching isochrones for NGC 6791 and NGC 6819, we reapplied isochrone fitting to both open clusters to avoid biases from models in the comparison with our asteroseismic results.

3.3.1 Ground-based *BVI* photometric data

NGC 6791 and NGC 6819 are among the most-well studied open clusters with absolute magnitudes $V \sim 14 - 17$ mag (e.g. Stetson et al. 2003, 2005) and $V \sim 12 - 14$ mag (e.g. Hole et al. 2009, Ak et al. 2016), respectively.

Table 3.1: Astrophysical parameters of NGC 6791 and NGC 6819 as determined by An et al. (2015) and Ak et al. (2016), respectively.

	NGC 6791	NGC 6819
$E(B-V)$ [mag]	0.105 ± 0.014	0.130 ± 0.035
[Fe/H] (dex)	+0.42 ± 0.07	+0.051 ± 0.020
μ_V [mag]	13.04 ± 0.08	12.22 ± 0.10
d [pc]	6918 ± 240	2309 ± 106
τ [Gyr]	9.5 ± 0.3	2.4 ± 0.2

In the current study, we used broadband BVI photometry[1] for NGC 6791 that were obtained from an extensive campaign including the analysis of 1 764 individual CCD images with additional data obtained more recently (e.g. Stetson et al. 2003, 2005). Furthermore, Platais et al. (2011) determined the membership probability for many stars in the open cluster by using proper motion measurements. Based on the colour-magnitude data provided by Stetson et al. (2005), An et al. (2015) determined the global cluster properties including reddening $E(B-V)$, metallicity [Fe/H], distance modulus μ_V and distance d from main-sequence fitting, and age τ, which we report in Table 3.1.

For NGC 6819 we used UBV measurements[2] from a dedicated ground-based photometric survey by Ak et al. (2016). Based on astrometric measurements, Ak et al. derived the membership probability of the observed stars and obtained a set of astrophysical parameters of the cluster (see Tab. 3.1).

As a further note, Choi et al. (2018) used the recent *Gaia* Data Release 2 (e.g. Gaia Collaboration et al. 2018) to investigate star clusters among which were NGC 6791 and NGC 6819. Choi et al. estimated the distance moduli for both clusters and obtained $\mu_{6791} \approx 13.03 - 13.45$ mag and $\mu_{6819} \approx 12.22$ mag, respectively. These values are consistent with determinations previously presented in the literature.

3.3.2 Stellar isochrones

A further prerequisite for determining cluster ages and metallicities is a homogeneous grid of stellar isochrones that covers the observed stellar properties of the stars in the cluster. Among the modern stellar evolution codes that can be used to generate stellar isochrones, is the PAdova and TRieste Stellar Evolution Code (Bressan et al. 2012). The isochrones extend from the lower main sequence up to the asymptotic giant branch with a mass range $0.1 \leq M \leq 12\,M_\odot$ and metallicities ranging from $-1.49 \leq$ [M/H] $\leq +0.78$ ($0.0005 \leq Z \leq 0.07$). On the red-giant branch mass loss is included in the models by using the empirical formulation by Reimers (1975). Along each isochrone a set of theoretical stellar parameters is provided including mass, effective temperature, luminosity, radius, surface gravity, and evolutionary phase. A description of the input physics of the PARSEC models, such as the solar distribution of heavy elements, opacities, equation of state, nuclear reaction rates, neutrino losses, convective overshoot, and diffusion can be found in Bressan et al. (2012).

[1] http://vizier.cfa.harvard.edu/viz-bin/VizieR?-source=J/PASP/115/413
[2] http://vizier.u-strasbg.fr/viz-bin/VizieR?-source=J/other/ApSS/361.126

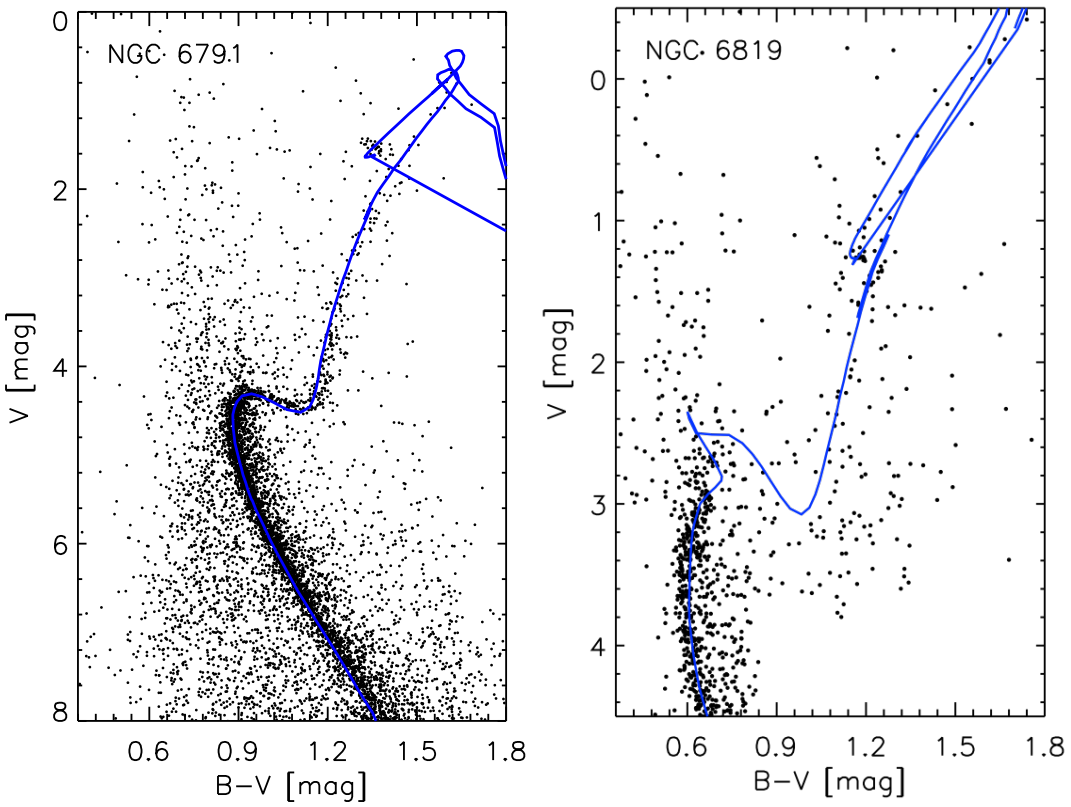

Figure 3.1: Colour-magnitude diagrams of the the open clusters NGC 6791 (left) and NGC 6819 (right) based on data obtained by Stetson et al. (2003, 2005) and Ak et al. (2016). Matching stellar isochrones are shown in blue, which were determined through isochrone fitting by using the grids of models where mass loss was included with an efficiency parameter of $\eta = 0.2$ (see Sec. 3.3 and 3.3.2).

In total, each grid of isochrones comprises 71 unique metallicities with $-1.49 \leq [\mathrm{M/H}] \leq +0.78$ at varying step sizes of 0.026−0.067 dex depending on the metallicity. Due to larger observational uncertainties, we adopted a larger interval for lower metallicites. Stellar ages range from $\sim$ 4 Myr to $\sim$ 12.8 Gyr ($6.61 \leq \log\tau \leq 10.11$), which adds up to 176 unique ages with an average step size of 0.02 dex in $\log\tau$. To include different mass-loss rates on the red-giant branch, we generated three different versions of the grid for each cluster by using efficiency parameters of 0.0, 0.2, and 0.4 in Reimer's empirical law. We obtained our grids of isochrones through the CMD web interface at OAPD[3]. We note that in order to obtain magnitudes and colours in the Johnson photometric system along the isochrones, it is necessary to provide the interstellar extinction of each cluster, which we computed based on the interstellar reddening values given in Table 3.1.

3.3.3 Isochrone fitting

The principle of isochrone fitting is to derive a cluster's age and metallicity by placing all observed stars in a cluster simultaneously on the same isochrone in a colour-magnitude

[3] http://stev.oapd.inaf.it/cgi-bin/cmd_2.7

diagram. Due to the absolute magnitudes (corrected for extinction) provided by the stellar isochrones, we first converted the apparent magnitudes of the observed cluster stars into absolute magnitudes by using the distance modulus. The distances to both clusters are well constrained by several surveys and here we used the values from recent studies as listed in Table 3.1. To find a match between the observed cluster data and our set of stellar isochrones we used a statistical maximum-likelihood approach similar to the near point estimator method, which was first proposed by Flannery and Johnson (1982). In this approach, the likelihood of each isochrone is computed based on the separation between each observed data point to the isochrone through minimization of a χ^2 statistics. So inherently, one of the assumptions of this method is that models are uniformly distributed along the isochrone. In addition, we included Gaussian weighting in the likelihood function in order to take the membership probability of each observed star into account. In the end, we obtained an age and metallicity estimate for the cluster from the isochrone with the lowest χ^2 value and we obtained uncertainties for the derived parameters from the elements of the covariance matrix. In Figure 3.1 we show the colour-magnitude diagrams of NGC 6791 (left) and NGC 6819 (right). For each cluster, we show the isochrone fit (in blue) to the observed data based on the grids of models, in which mass loss was included with an efficiency parameter of $\eta = 0.2$. The cluster isochrones provided $\tau = 8.3 \pm 0.5$ Gyr and [M/H] $= 0.29 \pm 0.03$ dex for NGC 6791, and $\tau = 2.3 \pm 0.2$ Gyr and [M/H] $= 0.07 \pm 0.03$ dex for NGC 6819. These estimates are broadly consistent with values present in the literature.

3.4 Determination of asteroseismic stellar parameters

NGC 6791 and NGC 6819 are both present in the *Kepler* field of view. As both open clusters are rather faint, photometric data could only be obtained for the brightest cluster members. The observed stars are in the red-giant phase of stellar evolution, at which point their luminosities are high and it is easier to observe them than less luminous subgiant and main-sequence stars. Through an analysis of the solar-like oscillations we aim to derive the stellar properties of the cluster giants in NGC 6791 and NGC 6819. We used the asteroseismic observables together with spectroscopic effective temperatures and metallicities from APOGEE in a grid-based approach to model the observed stars.

3.4.1 *Kepler* light curves

We used *Kepler* photometric time series data that were obtained during the 4-year nominal mission with a cadence of about 29.4 min. The concatenated corrected light curves (Handberg and Lund 2014) are available for about 60 cluster giants. It is worth noting that the light curves for stars in the open cluster NGC 6819 contain large gaps every three months per year due to their location on a broken CCD, in which case no data could be stored. We removed all gaps that were longer than ten days in the light curves and merged the datasets together. For a star that shows solar-like oscillations this approach was shown to provide a cleaner Fourier spectrum that is less affected by the window function (Hekker et al. 2010c).

3.4.2 Fourier spectrum analysis

The global asteroseismic parameters that we use in this study are the frequency of maximum oscillation power $\nu_{\rm max}$ and the mean large frequency separation $\Delta\nu$, i.e. the spacing between modes of the same spherical degree (ℓ) and consecutive radial order (n). They can be derived from the Fourier power density spectrum (PDS), which for a pulsating red-giant star consists of a stellar oscillation signal that is superimposed on a global background signal dominated by granulation power. We obtained $\nu_{\rm max}$ from a global model fit to the PDS by using a formulation similar to model F from Kallinger et al. (2014):

$$P_{\rm PDS}(\nu) = n_{\rm wh} + \eta(\nu)^2 \left[\sum_{\rm i=1}^{3} \frac{A_{\rm i}}{1 + (\nu/b_{\rm i})^4} + P_{\rm g}(\nu) \right], \tag{3.1}$$

where:

$$P_{\rm g}(\nu) = \Lambda_{\rm g} \exp\left(\frac{-(\nu - \nu_{\rm max})^2}{2\sigma_{\rm g}^2} \right). \tag{3.2}$$

The global background model comprises a white noise component $n_{\rm wh}$ and three granulation background components where each Lorentzian-like component is defined by an amplitude $A_{\rm i}$ and frequency $b_{\rm i}$. We describe the power envelope with a Gaussian function that is characterized by a height $\Lambda_{\rm g}$, standard deviation $\sigma_{\rm g}$, and $\nu_{\rm max}$. The granulation and oscillation signals are further affected by discrete time-sampling, which is accounted for with $\eta = {\rm sinc}(\pi\nu_{\rm nyq}/2\nu)$, where $\nu_{\rm nyq}$ represents the Nyquist frequency (Kallinger et al. 2014).

To sample the parameter space of equation 3.1, we applied a Bayesian Markov Chain Monte Carlo (MCMC) method with affine invariant sampling, known as the EMCEE algorithm[4]. After an initial burn-in phase and chain convergence, we retained all parameter values in order to generate the posterior probability distributions. From the final distributions we used the medians as expectation parameters and their 16th and 84th percentiles as uncertainties. We report the results from the global model fit (eq. 3.1) for all stars in NGC 6791 and NGC 6819 under study in Table 3.3 in the appendix. Estimates of the frequency of maximum oscillation power $\nu_{\rm max}$ for each red giant are listed in Table 3.2.

3.4.2.1 Frequencies of oscillation modes

After normalizing the PDS by the global background model, we derived an initial set of significant peaks by using the continuous-wavelet pattern-matching algorithm introduced by García Saravia Ortiz de Montellano et al. (2018). This method employs a Mexican hat wavelet that is suitable for the automated detection of resolved modes that can be approximated by Lorentzian functions as well as any unresolved peaks that can be fitted with sinc functions. For the cluster giants, we applied the algorithm and selected signals with a signal-to-noise threshold of 1.5, an Akaike Information Criterion (AIC) above 0, and a number of false-positive peak detections below 1. Each peak is then assigned with a probability of it being due to real signal. Based on these definitions, we obtained an initial set of frequencies including their amplitudes (heights) and linewidths. To obtain reliable

[4] EMCEE: The MCMC Hammer, http://dfm.io/emcee/

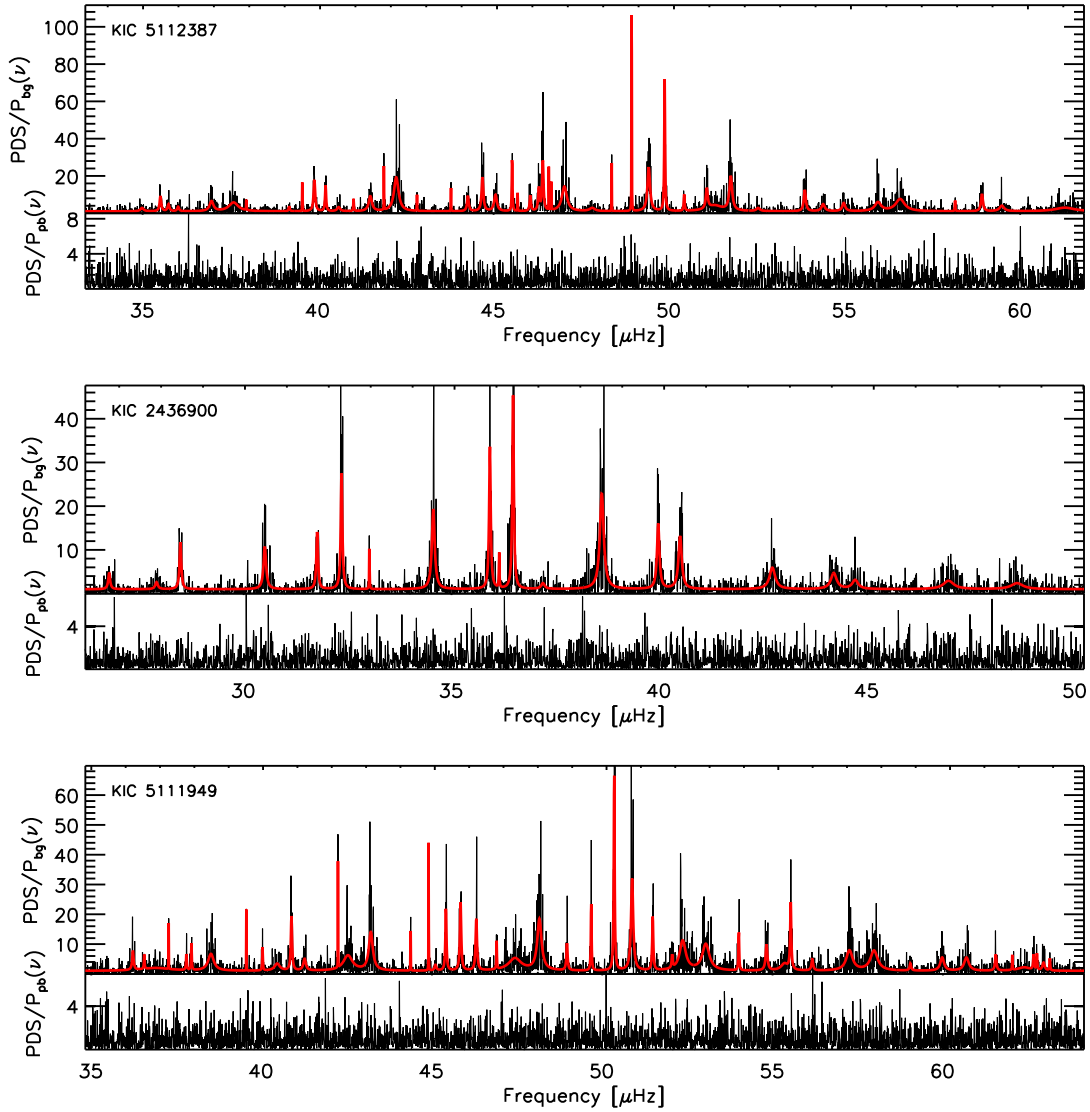

Figure 3.2: Background-removed power density spectrum (in black) including the peak-bagging fits to the oscillation modes (in red) for three red giants in NGC 6791. The lower panels below each fit show the residuals of the fit.

oscillation frequencies, we used a final maximum-likelihood estimation (MLE) fit to optimize all model parameters simultaneously. In Figure 3.2 we show the final peakbagging fits to three red-giant stars over the frequency range of the observed oscillations. Only noise is left in the residuals of the fits that are shown below each PDS.

We applied the asymptotic relation (Tassoul 1980) to our final set of oscillation frequencies to determine the spherical degrees ℓ of the modes. From the pure radial p modes ($\ell = 0$), we calculated the mean large frequency separation $\Delta\nu$ from a linear fit to the frequencies versus radial orders n. In this fit, the slope represents the mean large frequency separation and the intersection is related to the dimensionless phase term ϵ. The derived $\Delta\nu$ values for red giants in NGC 6791 and NGC 6819 are reported in Table 3.2. Moreover, for all stars in our sample we provide the $\ell = 0$ oscillation frequencies, their amplitudes, and linewidths in Tables 3.7 (NGC 6791) and 3.8 (NGC 6819) in the appendix.

3.4.3 Asteroseismic ages and masses from stellar models

We can determine the asteroseismic stellar parameters based on a combination of asteroseismic ($\nu_{\rm max}, \Delta\nu$) and spectroscopic ($T_{\rm eff}$, [M/H]) observables in a grid-based modelling approach.

3.4.3.1 $T_{\rm eff}$ and [M/H] from APOGEE

The asteroseismic data were complemented with spectroscopic parameters derived from high-resolution ($\sim 22\,500$) high signal-to-noise (> 100) near-infrared spectra provided by the Apache Point Observatory Galactic Evolution Experiment (APOGEE; Majewski et al. 2017) as part of the Sloan Digital Sky Survey III (SDSS-III). In Table 3.2 we provide the effective temperatures $T_{\rm eff}$ and metallicities [M/H] for the red giants investigated here.

3.4.3.2 Asteroseismic grid-based modelling

In the asteroseimic grid-based modelling (GBM) approach (Gai et al. 2011) we search for the best match between a precomputed grid of stellar isochrones and the observational data, in this case $\nu_{\rm max}, \Delta\nu, T_{\rm eff}$, and [M/H]. We used the same grid of PARSEC isochrones as for the isochrone fitting (Sec. 3.3.3) in order to ensure a homogeneous comparison. In order to calculate the stellar parameters for the red giants, we used an independent implementation of the likelihood method (Basu et al. 2010) where the likelihood of each model was evaluated based on our set of observed parameters. For the computation of the global seismic parameters of the models, we used the asteroseismic scaling relations (e.g. Ulrich 1986, Brown et al. 1991, Kjeldsen and Bedding 1995) with empirically derived reference values (Themeßl et al. 2018). In addition to stellar masses and ages, the GBM approach provides an indication of the evolutionary stage of the red-giant stars (Hekker et al. 2017).

We performed the GBM analysis six times by applying different constraints to the stellar models and by using grids of isochrones, where different mass-loss rates are included. In the first attempt, we determined the stellar parameters without any further constraints except for the asteroseismic and spectroscopic input parameters. These results are reported in the appendix (Tab. 3.4-3.6) and shown in Figure 3.3. Then, we used additional information about the metallicity of each cluster to further constrain the stellar models.

Table 3.2: Global oscillation parameters ($\nu_{\rm max}$, $\Delta\nu$) and spectroscopic atmospheric parameters ($T_{\rm eff}$, [M/H]), asteroseismic masses, logarithmic ages, and evolutionary stages for oscillating red giants in NGC 6791 and NGC 6819. The last three columns report the results from GBM by using the metallicity as a constraint and grids of models with a mass-loss rate according to $\eta = 0.2$ (Sec. 3.4.3.2). APOGEE does not provide atmospheric parameters for KIC 2436688. Thus, for this star we report $T_{\rm eff}$ and [M/H] from the revised *Kepler* input catalogue (Huber et al. 2014).

KIC	$\nu_{\rm max}$ [μHz]	$\Delta\nu$ [μHz]	$T_{\rm eff}$ [K]	[M/H] (dex)	M [$M_\odot$]	$\log(\tau/{\rm yr})$	Evo. state
			NGC 6791				
2435987	4.215 ± 0.058	0.788 ± 0.008	4399 ± 69	0.355 ± 0.003	1.11 ± 0.02	9.948 ± 0.003	RGB
2436209	31.806 ± 0.453	3.793 ± 0.036	4468 ± 69	0.214 ± 0.003	1.11 ± 0.02	9.966 ± 0.003	RGB
2436688	37.207 ± 0.598	4.135 ± 0.043	4685 ± 155	0.249 ± 0.003	1.13 ± 0.04	9.913 ± 0.003	RGB
2436900	55.863 ± 0.811	5.665 ± 0.054	4362 ± 69	0.214 ± 0.003	1.16 ± 0.02	9.965 ± 0.003	RGB
2437340	28.011 ± 0.419	3.422 ± 0.031	4065 ± 69	0.355 ± 0.003	1.07 ± 0.05	9.948 ± 0.003	AGB
2437353	76.738 ± 1.011	7.162 ± 0.061	4509 ± 69	0.214 ± 0.003	1.05 ± 0.04	9.947 ± 0.052	RC
2437507	35.806 ± 0.379	4.001 ± 0.032	4270 ± 69	0.249 ± 0.003	1.17 ± 0.04	9.869 ± 0.003	RGB
2437804	25.431 ± 0.376	3.064 ± 0.027	4472 ± 69	0.302 ± 0.003	1.04 ± 0.01	9.965 ± 0.003	RC
2437816	8.640 ± 0.142	1.372 ± 0.013	4232 ± 69	0.355 ± 0.003	1.15 ± 0.05	9.942 ± 0.022	RGB
2568654	32.089 ± 0.459	3.798 ± 0.033	4288 ± 69	0.276 ± 0.003	1.13 ± 0.03	9.927 ± 0.021	RGB
2569078	4.547 ± 0.069	0.830 ± 0.009	4392 ± 69	0.329 ± 0.003	1.18 ± 0.02	9.826 ± 0.003	RGB
2569137	20.040 ± 0.226	2.544 ± 0.020	4312 ± 69	0.355 ± 0.003	1.04 ± 0.02	9.948 ± 0.003	AGB
2569360	32.421 ± 0.547	3.806 ± 0.031	4282 ± 69	0.276 ± 0.003	1.16 ± 0.02	9.887 ± 0.003	RGB
2569618	27.376 ± 0.388	3.342 ± 0.028	4437 ± 69	0.355 ± 0.003	1.11 ± 0.02	9.950 ± 0.033	RGB
2570172	17.648 ± 0.179	2.311 ± 0.019	4505 ± 69	0.355 ± 0.003	1.09 ± 0.01	9.965 ± 0.003	RGB
2570214	8.177 ± 0.194	1.317 ± 0.023	4462 ± 69	0.249 ± 0.003	1.06 ± 0.04	9.955 ± 0.072	RC
2436417	30.246 ± 0.630	3.605 ± 0.041	4459 ± 69	0.355 ± 0.003	1.04 ± 0.02	9.966 ± 0.003	RC
2437040	60.303 ± 0.842	5.975 ± 0.059	4297 ± 69	0.355 ± 0.003	1.15 ± 0.04	9.903 ± 0.052	RGB
2437564	15.015 ± 0.187	2.052 ± 0.018	4478 ± 69	0.276 ± 0.003	1.08 ± 0.05	9.908 ± 0.070	RC
2438333	29.585 ± 0.458	3.589 ± 0.034	4487 ± 69	0.214 ± 0.003	1.11 ± 0.02	9.948 ± 0.023	RGB
2569945	24.185 ± 0.221	2.926 ± 0.018	4515 ± 69	0.214 ± 0.003	1.04 ± 0.02	9.965 ± 0.003	RC
2297793	4.755 ± 0.082	0.868 ± 0.025	4081 ± 69	0.214 ± 0.003	1.04 ± 0.01	9.948 ± 0.003	AGB
2297825	21.460 ± 0.229	2.695 ± 0.021	4534 ± 69	0.249 ± 0.003	1.03 ± 0.01	9.966 ± 0.003	RC
2437965	55.104 ± 0.862	5.603 ± 0.052	4122 ± 69	0.214 ± 0.003	1.04 ± 0.02	9.966 ± 0.003	AGB

2569935	5.613 ± 0.107	0.980 ± 0.011	4031 ± 69	0.214 ± 0.003	1.07 ± 0.02	9.929 ± 0.010	AGB
2569055	31.838 ± 0.508	3.781 ± 0.038	4507 ± 69	0.276 ± 0.003	1.03 ± 0.02	9.965 ± 0.003	RC
2437496	75.028 ± 1.008	7.063 ± 0.059	3947 ± 69	0.275 ± 0.003	1.14 ± 0.01	9.965 ± 0.003	AGB
2438051	29.796 ± 0.581	3.570 ± 0.043	4470 ± 69	0.302 ± 0.003	1.07 ± 0.05	9.955 ± 0.101	RC
			NGC 6819				
4937257	35.038 ± 0.277	4.184 ± 0.012	4777 ± 69	0.056 ± 0.025	1.50 ± 0.01	9.467 ± 0.002	RC
4937576	32.284 ± 0.320	3.565 ± 0.005	4641 ± 69	0.012 ± 0.031	1.54 ± 0.03	9.443 ± 0.021	RC
5023732	27.187 ± 0.326	3.095 ± 0.005	4595 ± 69	0.015 ± 0.019	1.59 ± 0.12	9.347 ± 0.019	RGB
5024043	56.145 ± 0.253	5.613 ± 0.007	4786 ± 69	−0.158 ± 0.026	1.47 ± 0.01	9.466 ± 0.002	RGB
5024143	122.008 ± 1.256	9.670 ± 0.006	4916 ± 69	0.035 ± 0.033	1.72 ± 0.03	9.252 ± 0.016	RGB
5024750	13.165 ± 0.297	1.778 ± 0.008	4477 ± 69	0.022 ± 0.026	1.60 ± 0.11	9.440 ± 0.016	AGB
5111949	46.754 ± 0.412	4.794 ± 0.006	4785 ± 69	0.069 ± 0.033	1.64 ± 0.03	9.354 ± 0.024	RC
5112072	125.645 ± 0.582	10.013 ± 0.006	4943 ± 69	0.006 ± 0.033	1.47 ± 0.03	9.446 ± 0.011	RGB
5112288	47.654 ± 0.451	4.753 ± 0.007	4852 ± 69	0.069 ± 0.024	1.65 ± 0.03	9.355 ± 0.026	RC
5112361	69.330 ± 0.398	6.177 ± 0.005	4826 ± 69	−0.029 ± 0.027	1.62 ± 0.10	9.325 ± 0.039	RGB
5112373	44.075 ± 0.331	4.685 ± 0.006	4800 ± 69	0.044 ± 0.032	1.60 ± 0.04	9.381 ± 0.036	RC
5112387	44.905 ± 0.364	4.720 ± 0.007	4817 ± 69	0.048 ± 0.024	1.61 ± 0.03	9.367 ± 0.019	RC
5112401	35.600 ± 0.453	3.991 ± 0.008	4817 ± 69	0.006 ± 0.032	1.52 ± 0.02	9.445 ± 0.011	RC
5112730	43.763 ± 0.389	4.511 ± 0.005	4823 ± 69	0.065 ± 0.023	1.56 ± 0.04	9.423 ± 0.020	RC
5112938	44.765 ± 0.474	4.663 ± 0.005	4830 ± 69	0.057 ± 0.023	1.61 ± 0.04	9.376 ± 0.028	RC
5112948	42.602 ± 0.329	4.262 ± 0.005	4747 ± 69	0.043 ± 0.023	1.54 ± 0.07	9.443 ± 0.019	RC
5112950	41.008 ± 0.612	4.301 ± 0.005	4783 ± 69	0.072 ± 0.020	1.52 ± 0.03	9.443 ± 0.012	RC
5112974	39.976 ± 0.382	4.295 ± 0.005	4816 ± 69	0.032 ± 0.022	1.52 ± 0.02	9.443 ± 0.012	RC
5113041	37.590 ± 0.331	4.001 ± 0.006	4711 ± 69	−0.012 ± 0.027	1.53 ± 0.02	9.445 ± 0.012	RC
5113061	5.303 ± 0.074	0.883 ± 0.016	4173 ± 69	0.078 ± 0.021	1.57 ± 0.07	9.409 ± 0.094	RGB
5023889	54.450 ± 0.293	5.377 ± 0.003	4619 ± 69	0.127 ± 0.023	1.51 ± 0.03	9.442 ± 0.012	RGB
5023953	48.647 ± 0.388	4.768 ± 0.008	4851 ± 69	0.067 ± 0.021	1.66 ± 0.03	9.355 ± 0.013	RC
5112786	7.857 ± 0.161	1.152 ± 0.006	4268 ± 69	0.015 ± 0.027	1.70 ± 0.17	9.269 ± 0.015	AGB
5112481	5.527 ± 0.108	0.919 ± 0.010	4185 ± 69	0.021 ± 0.025	1.54 ± 0.08	9.411 ± 0.050	RGB

We applied a Gaussian weight on the GBM results with the isochrone metallicity as the mean and a width of 3σ uncertainty on the isochrone metallicity. The resulting stellar mass and age estimates for red giants in each cluster are presented in Table 3.2 and in Figure 3.4. Moreover, Figure 3.5 shows the Gaussian distributions of the input metallicities of the stars in each cluster in comparison to the computed metallicity distributions, when the global clusters' metallicities are used as constraints for GBM. For a final consistency check, we used both the global cluster ages and metallicities to constrain the grids of isochrones and obtained similar results (see Fig. 3.6, Tab. 3.4-3.6).

3.5 Results

In the following, we discuss the asteroseismic mass and age estimates that were derived from GBM, and which are shown in Figures 3.3 and 3.4. For both open clusters, we found a slightly younger average age for the red-giant population when models with larger mass-loss rates ($\eta = 0.4$) were used, while the stellar masses remained constant (Figs. 3.8-3.7 and Tab. 3.4-3.6). This is expected, since more mass loss indicates that the stars were more massive and thus they are younger. In the GBM approach, the mass is well-constraint by $\Delta\nu$ and $\nu_{\rm max}$, and these values were not changed. When GBM was carried out without including any constraints from the global cluster properties, we obtained masses between about 0.9 and 1.3 $M_\odot$ and ages ranging $9.70 \leq \log\tau \leq 10.1$ ($\sim 5 - 12$ Gyr) for red giants in NGC 6791 (Fig. 3.3). In NGC 6819 we found red giants with larger masses between about 1.2 and 1.7 $M_\odot$ and younger ages between $9.3 \leq \log\tau \leq 9.8$ ($\sim 2.1 - 6.3$ Gyr). For NGC 6791, we observed that RGB stars were more massive with an average mass around ~ 1.15 $M_\odot$ compared to more evolved red clump and asymptotic giant branch stars, which were lined up around ~ 1.0 $M_\odot$. In the case of NGC 6819, the mass and age estimates for red-giant stars with different evolutionary stages were more scattered without showing a mass difference between red-giant branch and more evolved clump stars independent of the constraints and models with different mass-loss rates that were used.

The current study will be continued with further investigations of different mass-loss rates and the impact of metallicity constraints on the derived asteroseismic ages and masses for the red-giant stars in both open clusters.

3.6 Appendix: Ensemble asteroseismic results

3.6.1 Global granulation background fits

Each red giant was fitted with a global background model comprising three granulation background components, one white noise component, and a Gaussian fit to the power excess. In Table 3.3 we provide the results from the global background fitting of all stars that were investigated here.

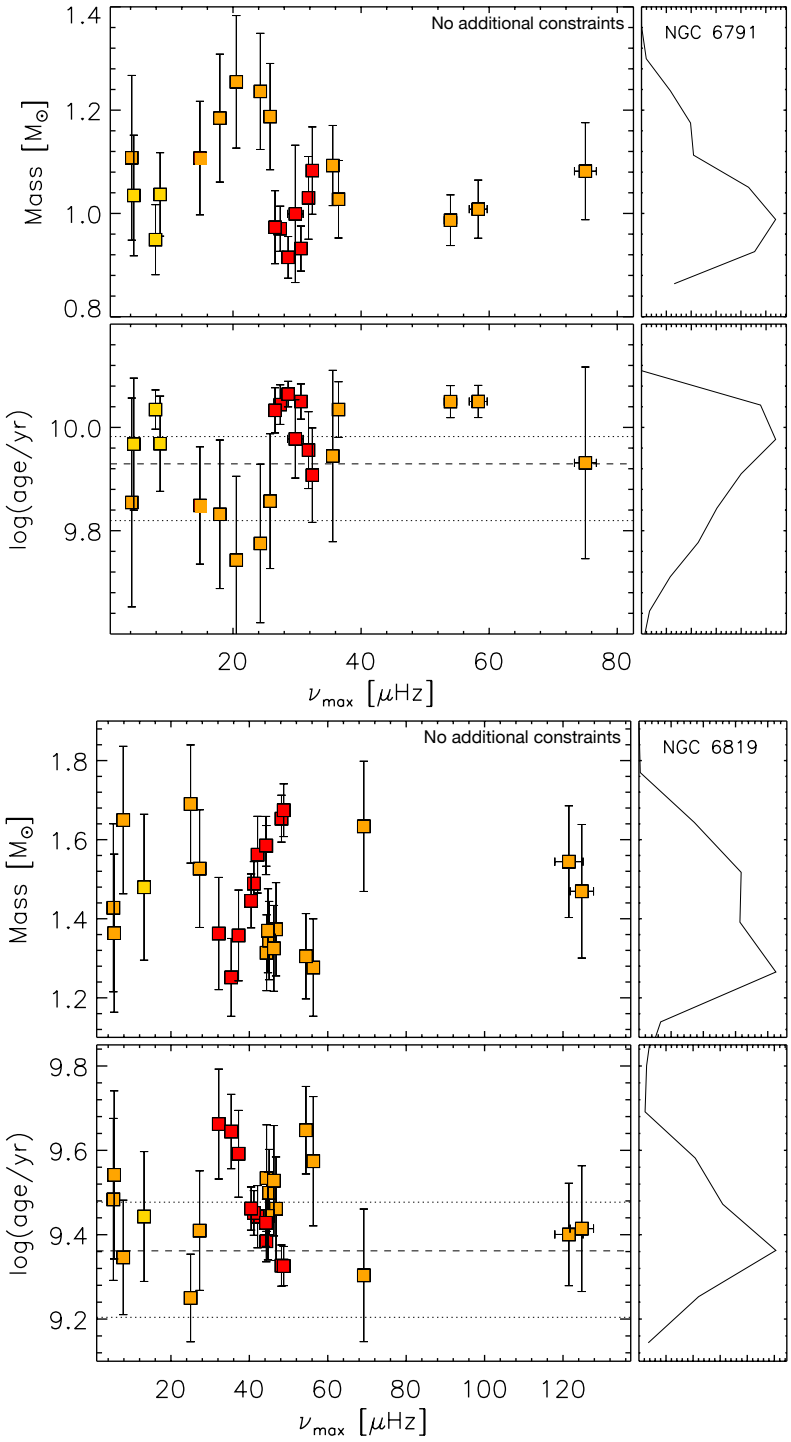

Figure 3.3: Stellar masses and logarithmic ages derived for NGC 6791 (top) and NGC 6819 (bottom) from GBM using $\Delta\nu, \nu_{\rm max}, T_{\rm eff}$, and [M/H] determined for the individual stars, without any additional constraints from the cluster. Here, grids of models with a mass-loss rate according to $\eta = 0.2$ were used. The colours represent different evolutionary stages for the red giants (orange: red-giant branch stars, red: red clump stars, yellow: asymptotic giant branch stars). The dashed lines indicate computed cluster ages from isochrone fitting (including their 3σ uncertainties shown with dotted lines). The right panels provide marginalized distributions of the age and mass estimates based on the results for the red-giant stars that are shown in the left panels.

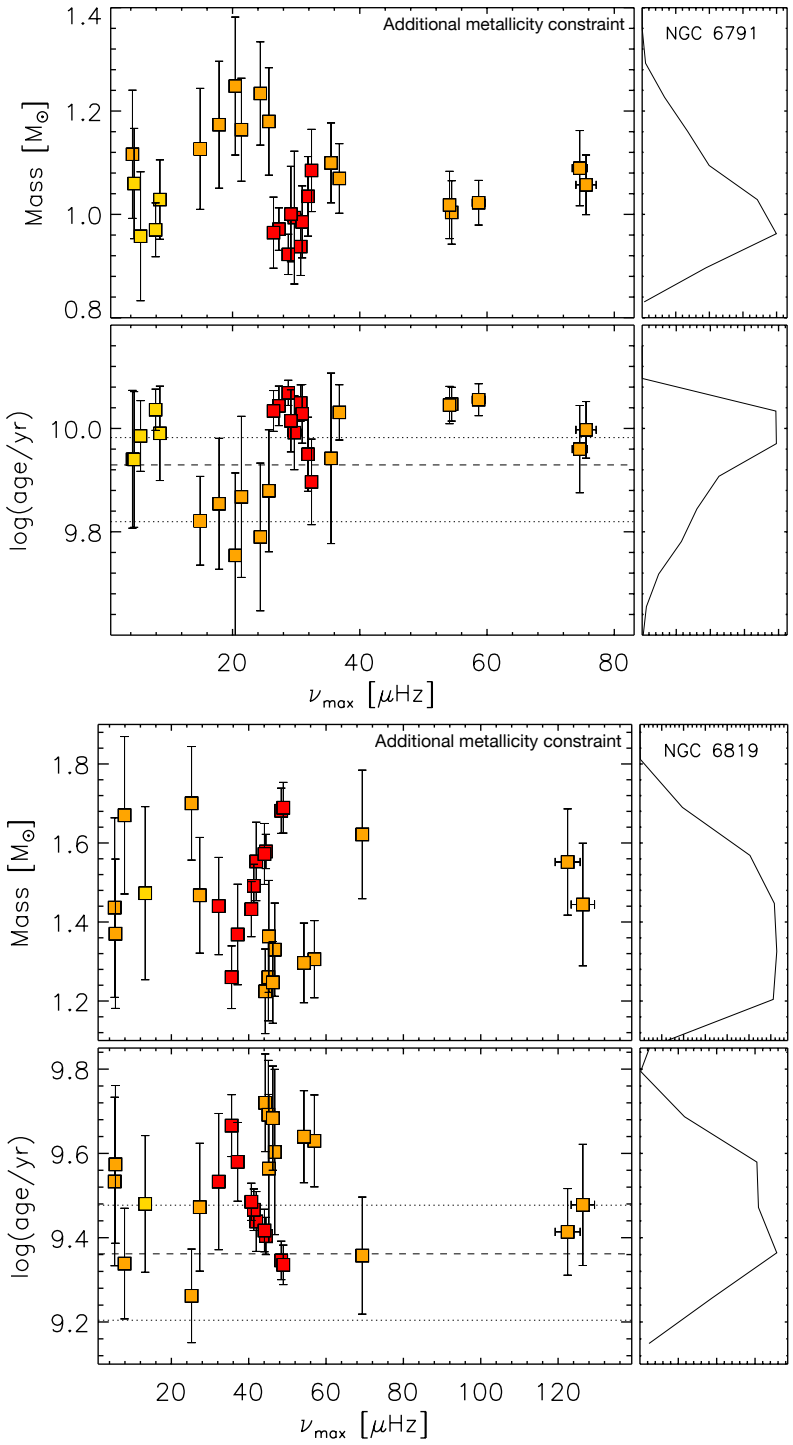

Figure 3.4: Same as Figure 3.3, now with metallicity constraints from the cluster isochrones.

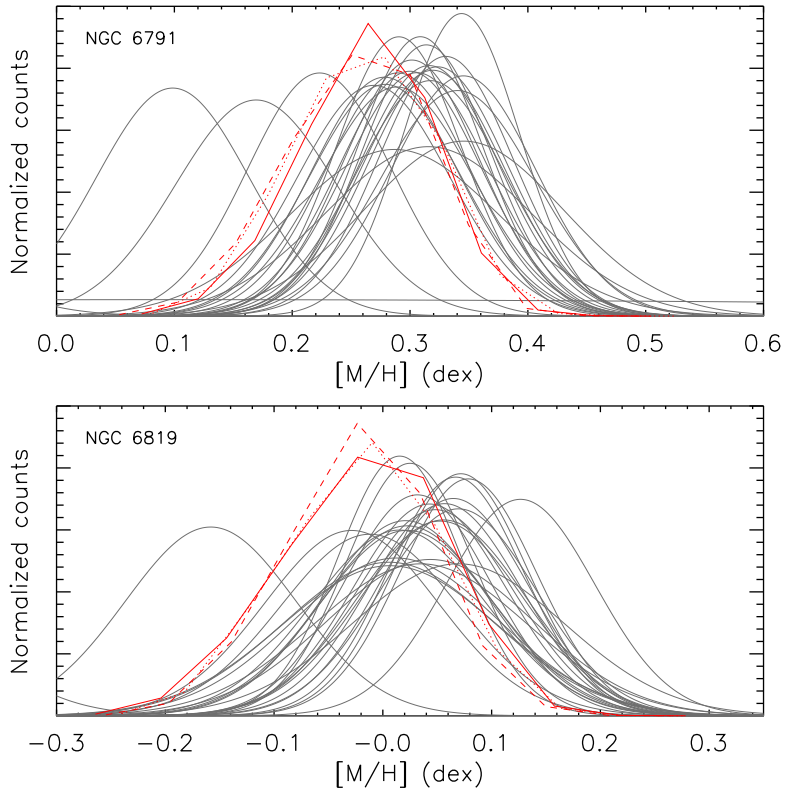

Figure 3.5: Histograms of the individual input and combined output metallicity distributions for red giants in NGC 6791 (top) and NGC 6819 (bottom). Red colours show the computed metallicity distributions when the clusters' metallicities were adopted as constraints for GBM. The line styles represent grids of isochrones with different mass-loss rates (solid: $\eta = 0.0$, dotted: $\eta = 0.2$, dashed: $\eta = 0.4$). The grey Gaussian fits represent the input metallicity distributions for the individual stars in each cluster, which were generated by using [M/H] values (Tab. 3.2) as the mean and their 3σ uncertainties as the width of the Gaussian functions.

3.6.2 Derived asteroseismic masses and ages from different grid-based modelling runs

We provide the results based on different grids of isochrones (mass-loss rates with $\eta = 0.0, 0.2$, and 0.4) and by using different constraints for GBM (Sec. 3.4.3.2, Tab. 3.4-3.6).

3.6.3 Radial ($\ell = 0$) oscillation frequencies

For each red-giant star we extracted the frequencies, amplitudes, and linewidths in the background-normalized PDS by using the method developed by García Saravia Ortiz de Montellano et al. (2018). In addition, we determined the spherical degree ℓ of the oscillation modes by using the asymptotic relation (Tassoul 1980). In Tables 3.7 and 3.8 we provide frequencies that were identified as $\ell = 0$ modes, and which we used for the determination of $\Delta\nu$ in Section 3.4.2.1. A list of all detected frequencies for different spherical degrees ($\ell = 0, 1, 2$, and 3) is available upon request from the first author.

Table 3.3: Global granulation background and Gaussian model parameters from the MCMC fit for the red giants in NGC 6791 and NGC 6819.

KIC	$n_{\rm wh}$ [ppm$^2\mu$Hz^{-1}]	A_1 [ppm$^2\mu$Hz^{-1}]	b_1 [μHz]	A_2 [ppm$^2\mu$Hz^{-1}]	b_2 [μHz]	A_3 [ppm$^2\mu$Hz^{-1}]	b_3 [μHz]	$\Gamma_{\rm g}$ [ppm$^2\mu$Hz^{-1}]	$\sigma_{\rm g}$ [μHz]
NGC 6791									
2297793	$419.3^{+2.9}_{-2.8}$	$1360767^{+254255}_{-900868}$	$1.0^{+0.5}_{-0.3}$	$924705^{+183704}_{-155423}$	$3.8^{+0.1}_{-0.2}$	$431.3^{+9.1}_{-18.8}$	$38.8^{+1.5}_{-1.5}$	$760988^{+94809}_{-106159}$	$0.7^{+0.1}_{-0.1}$
2297825	$412.3^{+2.8}_{-2.7}$	46728^{+7685}_{-8949}	$1.5^{+0.2}_{-0.4}$	30931^{+1804}_{-1820}	$10.7^{+0.6}_{-0.5}$	$3186.8^{+1081.4}_{-1486.1}$	$37.3^{+3.6}_{-4.7}$	9993^{+604}_{-554}	$6.6^{+0.3}_{-0.3}$
2435987	$356.0^{+2.1}_{-2.1}$	33725^{+4361}_{-5550}	$1.7^{+0.2}_{-0.3}$	14449^{+745}_{-740}	$14.0^{+0.5}_{-0.5}$	$357.4^{+2.2}_{-2.4}$	$282.6^{+0.9}_{-0.5}$	4932^{+142}_{-155}	$8.0^{+0.3}_{-0.3}$
2436209	$433.3^{+2.8}_{-2.9}$	15569^{+486}_{-530}	$15.0^{+0.4}_{-0.4}$	435^{+2}_{-2}	$282.5^{+0.7}_{-0.4}$	$434.2^{+2.8}_{-2.7}$	$283.0^{+0.3}_{-0.2}$	2792^{+91}_{-98}	$11.4^{+0.4}_{-0.5}$
2436417	$317.9^{+2.1}_{-2.2}$	25862^{+2901}_{-4235}	$2.2^{+0.8}_{-1.0}$	22056^{+2376}_{-2281}	$10.6^{+1.2}_{-1.0}$	$3591.4^{+1632.2}_{-2017.8}$	$30.6^{+3.2}_{-5.4}$	9515^{+585}_{-631}	$5.1^{+0.3}_{-0.3}$
2436688	$737.3^{+4.9}_{-4.8}$	33561^{+3396}_{-4137}	$1.4^{+0.1}_{-0.1}$	3458^{+142}_{-147}	$23.8^{+0.6}_{-0.7}$	$740.3^{+5.0}_{-5.5}$	$282.5^{+1.3}_{-0.5}$	1169^{+71}_{-74}	$8.5^{+0.6}_{-0.6}$
2436900	$423.2^{+2.8}_{-2.9}$	81453^{+9289}_{-10779}	$1.0^{+0.1}_{-0.1}$	14042^{+838}_{-945}	$8.8^{+0.4}_{-0.4}$	$3481.3^{+218.5}_{-218.8}$	$34.6^{+0.7}_{-0.8}$	4392^{+203}_{-212}	$4.9^{+0.2}_{-0.2}$
2437040	$198.5^{+1.3}_{-1.3}$	34946^{+1883}_{-2119}	$5.8^{+0.3}_{-0.3}$	6956^{+594}_{-601}	$21.1^{+0.5}_{-0.6}$	$199.0^{+1.3}_{-1.4}$	$282.7^{+0.8}_{-0.4}$	8410^{+357}_{-361}	$4.2^{+0.2}_{-0.2}$
2437340	$288.4^{+1.7}_{-1.8}$	345531^{+48810}_{-36708}	$2.9^{+0.3}_{-0.3}$	92555^{+28663}_{-27794}	$8.8^{+2.2}_{-0.6}$	$23563.1^{+20157.3}_{-32325.1}$	$10.3^{+0.8}_{-1.4}$	261970^{+17990}_{-19091}	$1.6^{+0.1}_{-0.1}$
2437353	$251.4^{+1.7}_{-1.8}$	34901^{+4782}_{-5308}	$1.3^{+0.1}_{-0.2}$	13325^{+867}_{-893}	$9.5^{+0.6}_{-0.6}$	$3395.2^{+538.2}_{-475.5}$	$29.9^{+1.0}_{-1.4}$	4286^{+177}_{-190}	$5.7^{+0.2}_{-0.3}$
2437496	$303.3^{+2.0}_{-2.2}$	$979388^{+153596}_{-157503}$	$1.5^{+0.2}_{-0.2}$	$485398^{+118971}_{-110578}$	$4.9^{+0.2}_{-0.4}$	$309.0^{+4.8}_{-9.2}$	$46.4^{+1.6}_{-1.7}$	746410^{+75358}_{-80657}	$0.9^{+0.1}_{-0.1}$
2437507	$332.4^{+2.1}_{-2.1}$	66766^{+9404}_{-5631}	$5.7^{+0.4}_{-0.4}$	13020^{+3209}_{-5508}	$15.1^{+5.6}_{-4.5}$	$4880.5^{+2886.5}_{-4047.9}$	$25.0^{+2.4}_{-3.0}$	27658^{+1393}_{-1459}	$3.4^{+0.1}_{-0.2}$
2437564	$380.1^{+2.4}_{-2.4}$	28286^{+4316}_{-5633}	$1.5^{+0.3}_{-0.4}$	20449^{+1489}_{-1476}	$9.6^{+0.7}_{-0.9}$	$5856.4^{+1055.7}_{-816.5}$	$30.1^{+1.0}_{-1.5}$	6755^{+298}_{-319}	$5.6^{+0.2}_{-0.3}$
2437804	$312.8^{+2.1}_{-2.2}$	47953^{+6926}_{-7480}	$1.6^{+0.2}_{-0.3}$	27082^{+2107}_{-2118}	$9.0^{+0.7}_{-0.6}$	$5776.4^{+1213.1}_{-1428.8}$	$34.3^{+2.0}_{-2.4}$	9542^{+691}_{-704}	$4.9^{+0.3}_{-0.3}$
2437816	$297.9^{+1.9}_{-1.9}$	94937^{+6003}_{-5753}	$5.2^{+0.3}_{-0.3}$	16897^{+4179}_{-4676}	$16.5^{+1.9}_{-1.1}$	$5664.3^{+3744.0}_{-4356.4}$	$19.6^{+1.5}_{-2.1}$	41368^{+1893}_{-2073}	$3.0^{+0.1}_{-0.1}$
2437965	$222.9^{+1.2}_{-1.4}$	518926^{+55884}_{-60778}	$1.9^{+0.2}_{-0.2}$	130630^{+33700}_{-36505}	$6.9^{+3.2}_{-0.5}$	$39657.5^{+34304.7}_{-47156.6}$	$8.4^{+0.7}_{-1.2}$	162336^{+14835}_{-15952}	$1.5^{+0.1}_{-0.1}$
2438051	$323.4^{+2.2}_{-2.2}$	132797^{+15943}_{-19939}	$0.9^{+0.1}_{-0.1}$	27729^{+1621}_{-1604}	$9.8^{+0.5}_{-0.4}$	$2413.0^{+1073.3}_{-1694.1}$	$37.4^{+4.8}_{-6.9}$	5066^{+662}_{-630}	$7.7^{+0.7}_{-0.6}$
2438333	$480.7^{+3.2}_{-3.2}$	13238^{+396}_{-473}	$15.2^{+0.4}_{-0.4}$	483^{+3}_{-3}	$282.4^{+0.8}_{-0.5}$	$481.7^{+3.3}_{-3.2}$	$283.0^{+0.4}_{-0.2}$	2185^{+87}_{-90}	$11.0^{+0.6}_{-0.6}$
2568654	$239.9^{+1.5}_{-1.5}$	210402^{+15376}_{-16475}	$3.7^{+0.3}_{-0.3}$	57070^{+11000}_{-8109}	$13.7^{+0.7}_{-0.6}$	$2642.5^{+2022.4}_{-9995.0}$	$17.1^{+1.9}_{-3.7}$	88081^{+4850}_{-5119}	$2.4^{+0.1}_{-0.1}$
2569055	$387.7^{+2.7}_{-2.7}$	84663^{+11103}_{-12847}	$1.0^{+0.1}_{-0.1}$	33452^{+1542}_{-1627}	$10.1^{+0.3}_{-0.3}$	$1528.6^{+301.3}_{-419.3}$	$45.2^{+3.2}_{-3.3}$	8506^{+331}_{-315}	$7.7^{+0.2}_{-0.2}$
2569078	$212.0^{+1.8}_{-1.8}$	75435^{+13868}_{-16744}	$1.3^{+0.3}_{-0.3}$	34704^{+4398}_{-4929}	$7.2^{+0.7}_{-0.9}$	$10782.9^{+1869.8}_{-1525.9}$	$22.4^{+0.7}_{-1.1}$	18544^{+1076}_{-1084}	$3.3^{+0.2}_{-0.2}$

2569137	$331.1^{+3.1}_{-2.8}$	$644196^{+157510}_{-125414}$	$3.6^{+0.3}_{-0.1}$	$149093^{+120643}_{-173055}$	$4.2^{+0.3}_{-0.7}$	$339.2^{+6.5}_{-13.5}$	$37.3^{+2.1}_{-2.2}$	413795^{+77442}_{-84081}	$0.5^{+0.0}_{-0.1}$
2569360	$299.2^{+1.8}_{-2.0}$	66761^{+11071}_{-35824}	$1.0^{+0.5}_{-0.3}$	51290^{+5154}_{-5550}	$5.8^{+0.4}_{-0.5}$	$13269.3^{+1808.0}_{-1538.0}$	$20.6^{+0.6}_{-0.8}$	20833^{+917}_{-977}	$3.7^{+0.1}_{-0.2}$
2569618	$526.9^{+3.4}_{-3.4}$	37914^{+4497}_{-5185}	$1.2^{+0.1}_{-0.1}$	8273^{+275}_{-300}	$18.6^{+0.5}_{-0.5}$	$528.8^{+3.5}_{-3.8}$	$282.6^{+1.0}_{-0.5}$	2156^{+75}_{-76}	$11.6^{+0.4}_{-0.5}$
2569935	$704.8^{+4.5}_{-4.2}$	$1095738^{+177464}_{-167837}$	$1.7^{+0.2}_{-0.2}$	$325610^{+127430}_{-129892}$	$5.1^{+1.4}_{-0.7}$	$68045.4^{+49551.1}_{-90458.6}$	$7.0^{+0.9}_{-1.1}$	360790^{+49960}_{-55817}	$1.3^{+0.1}_{-0.1}$
2569945	$222.8^{+1.6}_{-1.5}$	83197^{+9139}_{-10160}	$1.2^{+0.1}_{-0.1}$	12418^{+820}_{-824}	$10.8^{+1.0}_{-0.7}$	$1774.6^{+939.1}_{-1096.7}$	$35.3^{+4.0}_{-8.6}$	4140^{+354}_{-406}	$6.6^{+0.4}_{-0.5}$
2570172	$567.1^{+3.6}_{-3.8}$	140490^{+12709}_{-14115}	$1.3^{+0.1}_{-0.1}$	2849^{+124}_{-128}	$23.2^{+0.6}_{-0.7}$	$569.4^{+3.9}_{-4.1}$	$282.6^{+1.0}_{-0.5}$	913^{+59}_{-61}	$6.9^{+0.4}_{-0.5}$
2570214	$407.4^{+2.8}_{-2.8}$	617744^{+60161}_{-71918}	$0.9^{+0.0}_{-0.1}$	30738^{+2432}_{-2579}	$7.5^{+0.6}_{-0.6}$	$7536.7^{+1157.2}_{-950.4}$	$27.7^{+0.8}_{-1.2}$	4915^{+328}_{-369}	$6.2^{+0.4}_{-0.4}$
NGC 6819									
4936335	$109.9^{+0.7}_{-0.7}$	153294^{+33194}_{-37360}	$2.9^{+0.8}_{-0.6}$	76513^{+31878}_{-28380}	$7.3^{+2.6}_{-1.7}$	$23864.4^{+19209.4}_{-26075.2}$	$10.3^{+1.0}_{-1.6}$	98600^{+9794}_{-10240}	$1.6^{+0.1}_{-0.1}$
4937257	$132.5^{+1.0}_{-1.1}$	20787^{+1028}_{-1062}	$8.2^{+0.4}_{-0.4}$	3892^{+387}_{-410}	$30.6^{+0.8}_{-0.9}$	$133.2^{+1.0}_{-1.2}$	$282.3^{+1.5}_{-0.7}$	5207^{+209}_{-223}	$6.2^{+0.2}_{-0.2}$
4937576	$43.1^{+0.4}_{-0.4}$	13330^{+1481}_{-1762}	$5.4^{+1.0}_{-1.2}$	8929^{+2094}_{-1642}	$14.6^{+1.0}_{-1.7}$	$771.2^{+142.1}_{-185.6}$	$46.0^{+2.7}_{-2.7}$	4694^{+178}_{-175}	$6.2^{+0.2}_{-0.2}$
5023732	$35.7^{+0.3}_{-0.3}$	$70228^{+41986}_{-119038}$	$0.3^{+0.1}_{-0.2}$	24095^{+1469}_{-1507}	$8.2^{+0.4}_{-0.4}$	$4475.6^{+804.8}_{-694.9}$	$28.3^{+1.0}_{-1.4}$	6994^{+355}_{-385}	$5.0^{+0.2}_{-0.2}$
5024043	$44.8^{+0.4}_{-0.4}$	5790^{+217}_{-237}	$14.0^{+0.4}_{-0.4}$	833^{+176}_{-175}	$51.1^{+3.1}_{-1.6}$	$297.2^{+177.2}_{-188.5}$	$57.7^{+3.3}_{-5.7}$	1731^{+67}_{-65}	$7.3^{+0.2}_{-0.2}$
5024143	$69.7^{+1.1}_{-1.1}$	5949^{+505}_{-558}	$2.0^{+0.1}_{-0.1}$	337^{+14}_{-14}	$28.4^{+1.0}_{-1.0}$	$76.1^{+4.3}_{-6.0}$	$104.8^{+9.6}_{-8.6}$	45^{+3}_{-4}	$13.2^{+1.9}_{-2.0}$
5024750	$18.5^{+0.1}_{-0.1}$	90244^{+7950}_{-9207}	$3.5^{+0.3}_{-0.3}$	23791^{+6090}_{-5027}	$12.4^{+0.6}_{-0.6}$	$1103.5^{+975.4}_{-5553.2}$	$15.6^{+1.9}_{-5.3}$	21874^{+1740}_{-1977}	$2.6^{+0.2}_{-0.2}$
5111949	$48.4^{+0.5}_{-0.5}$	12487^{+2321}_{-2938}	$1.1^{+0.2}_{-0.2}$	7308^{+322}_{-339}	$14.6^{+0.6}_{-0.7}$	$1157.5^{+215.5}_{-178.3}$	$49.8^{+1.8}_{-2.8}$	2169^{+83}_{-88}	$7.8^{+0.3}_{-0.3}$
5112072	$157.5^{+2.8}_{-2.8}$	9042^{+1099}_{-1230}	$1.4^{+0.1}_{-0.1}$	840^{+30}_{-30}	$32.4^{+1.0}_{-1.0}$	$207.2^{+10.9}_{-10.6}$	$131.4^{+6.9}_{-6.5}$	287^{+14}_{-14}	$11.7^{+0.8}_{-0.9}$
5112288	$46.4^{+0.4}_{-0.4}$	11659^{+1800}_{-1950}	$1.4^{+0.2}_{-0.2}$	6280^{+287}_{-297}	$14.0^{+0.6}_{-0.6}$	$1229.6^{+127.6}_{-121.0}$	$46.6^{+1.1}_{-1.4}$	1178^{+54}_{-56}	$7.4^{+0.3}_{-0.4}$
5112361	$62.3^{+0.6}_{-0.6}$	40684^{+4243}_{-5333}	$1.1^{+0.1}_{-0.1}$	1930^{+79}_{-88}	$19.1^{+0.7}_{-0.8}$	$450.6^{+34.3}_{-32.5}$	$64.3^{+1.6}_{-1.7}$	543^{+20}_{-20}	$10.1^{+0.4}_{-0.4}$
5112373	$47.0^{+0.4}_{-0.4}$	9413^{+1304}_{-1826}	$1.6^{+0.2}_{-0.3}$	7216^{+323}_{-342}	$14.5^{+0.6}_{-0.7}$	$1270.3^{+211.1}_{-199.7}$	$48.0^{+1.8}_{-2.3}$	2603^{+97}_{-103}	$7.2^{+0.3}_{-0.3}$
5112387	$50.3^{+0.5}_{-0.5}$	7674^{+753}_{-1182}	$1.9^{+0.4}_{-0.4}$	6608^{+331}_{-361}	$14.6^{+0.7}_{-0.8}$	$1430.6^{+229.0}_{-208.2}$	$46.9^{+1.6}_{-2.2}$	2482^{+92}_{-101}	$7.5^{+0.3}_{-0.3}$
5112401	$38.2^{+0.4}_{-0.4}$	16960^{+3152}_{-4307}	$1.5^{+0.3}_{-0.5}$	11315^{+668}_{-678}	$13.2^{+0.5}_{-0.5}$	$872.8^{+227.2}_{-412.9}$	$47.9^{+4.8}_{-4.3}$	3214^{+160}_{-149}	$7.3^{+0.4}_{-0.4}$
5112730	$47.2^{+0.4}_{-0.4}$	11222^{+1856}_{-2222}	$1.6^{+0.2}_{-0.3}$	7759^{+389}_{-389}	$13.4^{+0.6}_{-0.6}$	$1537.2^{+218.1}_{-190.5}$	$44.5^{+1.3}_{-1.8}$	2156^{+93}_{-91}	$7.3^{+0.3}_{-0.3}$
5112938	$43.2^{+0.4}_{-0.4}$	37289^{+4275}_{-5082}	$1.1^{+0.1}_{-0.1}$	5481^{+257}_{-272}	$13.9^{+0.7}_{-0.8}$	$1073.9^{+206.3}_{-160.3}$	$47.9^{+1.7}_{-2.8}$	1842^{+78}_{-85}	$7.7^{+0.3}_{-0.4}$
5112948	$48.5^{+0.4}_{-0.4}$	11645^{+2073}_{-2339}	$1.3^{+0.2}_{-0.3}$	7349^{+406}_{-445}	$11.7^{+0.5}_{-0.6}$	$1807.8^{+153.8}_{-145.8}$	$40.3^{+0.8}_{-0.9}$	1800^{+82}_{-87}	$6.5^{+0.3}_{-0.3}$
5112950	$36.9^{+0.3}_{-0.3}$	28433^{+3833}_{-4140}	$1.1^{+0.1}_{-0.1}$	7124^{+332}_{-367}	$12.7^{+0.8}_{-0.9}$	$1293.3^{+353.8}_{-235.1}$	$44.3^{+1.9}_{-4.0}$	2021^{+100}_{-117}	$7.0^{+0.3}_{-0.5}$

5112974	$30.5^{+0.3}_{-0.3}$	14370^{+2014}_{-2355}	$1.2^{+0.1}_{-0.2}$	5057^{+267}_{-263}	$13.2^{+0.6}_{-0.7}$	$1027.0^{+187.0}_{-165.2}$	$42.8^{+1.6}_{-2.3}$	1814^{+79}_{-82}	$6.9^{+0.3}_{-0.3}$
5113041	$50.5^{+0.4}_{-0.4}$	10267^{+1032}_{-1507}	$2.1^{+0.6}_{-0.9}$	9164^{+780}_{-738}	$12.2^{+0.8}_{-1.0}$	$2310.4^{+389.2}_{-324.2}$	$37.7^{+1.2}_{-1.8}$	3360^{+152}_{-158}	$6.0^{+0.3}_{-0.3}$
5113061	$14.9^{+0.2}_{-0.2}$	$524555^{+135706}_{-69598}$	$4.1^{+0.3}_{-0.2}$	$68280^{+54027}_{-150122}$	$5.1^{+0.5}_{-1.6}$	$49.0^{+2.7}_{-2.5}$	$92.5^{+2.5}_{-2.8}$	143376^{+26877}_{-35277}	$0.9^{+0.1}_{-0.1}$
5023889	$20.3^{+0.2}_{-0.2}$	8405^{+490}_{-374}	$14.0^{+0.7}_{-0.6}$	1422^{+314}_{-264}	$45.8^{+12.6}_{-2.6}$	$482.0^{+355.3}_{-443.5}$	$54.3^{+3.1}_{-5.2}$	2261^{+78}_{-89}	$8.0^{+0.2}_{-0.3}$
5023953	$40.4^{+0.4}_{-0.4}$	6568^{+404}_{-281}	$13.1^{+0.7}_{-0.5}$	999^{+232}_{-219}	$42.8^{+14.0}_{-4.8}$	$389.0^{+270.1}_{-244.9}$	$58.0^{+4.6}_{-8.0}$	1741^{+76}_{-77}	$7.9^{+0.3}_{-0.3}$
5112786	$19.3^{+0.2}_{-0.2}$	287117^{+30611}_{-33877}	$2.3^{+0.2}_{-0.2}$	89638^{+18092}_{-19352}	$7.7^{+0.4}_{-0.4}$	$20.3^{+0.8}_{-1.3}$	$101.8^{+4.4}_{-4.5}$	103850^{+10077}_{-10407}	$1.4^{+0.1}_{-0.1}$

Table 3.4: Asteroseismic masses, ages, and evolutionary stages for red giants in NGC 6791 and NGC 6819 from GBM by using models with $\eta = 0.0$.

	Without additional constraints		Metallicity and age constraints		
KIC	M [$M_\odot$]	$\log(\tau/\mathrm{yr})$	M [$M_\odot$]	$\log(\tau/\mathrm{yr})$	Evo.
			NGC 6791		
2297793	1.11 ± 0.15	9.855 ± 0.192	1.13 ± 0.12	9.932 ± 0.126	RGB
2297825	1.00 ± 0.05	10.055 ± 0.029	1.01 ± 0.05	10.054 ± 0.032	RC
2435987	1.03 ± 0.07	10.032 ± 0.074	1.07 ± 0.07	10.032 ± 0.051	RGB
2436209	1.00 ± 0.05	10.045 ± 0.033	1.00 ± 0.05	10.045 ± 0.034	RGB
2436417	1.03 ± 0.04	10.049 ± 0.032	1.03 ± 0.04	10.049 ± 0.034	RC
2436688	1.07 ± 0.09	9.944 ± 0.177	1.06 ± 0.07	9.995 ± 0.055	RGB
2436900	1.09 ± 0.07	9.957 ± 0.163	1.10 ± 0.07	9.940 ± 0.166	RGB
2437040	1.19 ± 0.11	9.867 ± 0.130	1.18 ± 0.10	9.884 ± 0.118	RGB
2437340	1.06 ± 0.05	10.035 ± 0.045	1.06 ± 0.05	10.035 ± 0.043	AGB
2437353	1.05 ± 0.05	10.036 ± 0.054	1.05 ± 0.05	10.035 ± 0.044	RC
2437496	1.10 ± 0.08	10.012 ± 0.064	1.08 ± 0.12	10.000 ± 0.071	AGB
2437507	1.26 ± 0.12	9.746 ± 0.151	1.25 ± 0.13	9.759 ± 0.173	RGB
2437564	1.09 ± 0.06	10.003 ± 0.103	1.09 ± 0.06	10.005 ± 0.097	RC
2437804	1.07 ± 0.04	10.032 ± 0.039	1.07 ± 0.04	10.041 ± 0.037	RC
2437816	1.18 ± 0.12	9.856 ± 0.132	1.17 ± 0.11	9.865 ± 0.115	RGB
2437965	1.02 ± 0.07	10.032 ± 0.039	1.04 ± 0.05	10.034 ± 0.038	AGB
2438051	1.07 ± 0.12	9.990 ± 0.065	1.06 ± 0.11	9.988 ± 0.064	RC
2438333	1.01 ± 0.05	10.050 ± 0.031	1.02 ± 0.04	10.055 ± 0.031	RGB
2568654	1.12 ± 0.08	9.965 ± 0.139	1.16 ± 0.09	9.905 ± 0.149	RC
2569055	0.98 ± 0.04	10.069 ± 0.024	1.01 ± 0.03	10.071 ± 0.023	RC
2569078	1.23 ± 0.11	9.779 ± 0.155	1.24 ± 0.11	9.791 ± 0.130	RGB
			NGC 6819		
4936335	0.91 ± 0.08	10.011 ± 0.060	0.99 ± 0.06	10.025 ± 0.043	AGB
4937257	1.00 ± 0.09	9.904 ± 0.137	0.99 ± 0.07	10.008 ± 0.082	RGB
4937576	1.36 ± 0.15	9.692 ± 0.149	1.42 ± 0.15	9.549 ± 0.191	RC
5023732	1.51 ± 0.15	9.396 ± 0.138	1.47 ± 0.15	9.473 ± 0.154	RGB
5024043	1.27 ± 0.12	9.574 ± 0.152	1.31 ± 0.10	9.629 ± 0.108	RGB
5024143	1.54 ± 0.14	9.398 ± 0.122	1.55 ± 0.13	9.414 ± 0.103	RGB
5024750	1.50 ± 0.16	9.451 ± 0.150	1.49 ± 0.19	9.482 ± 0.158	AGB
5111949	1.38 ± 0.12	9.478 ± 0.125	1.33 ± 0.12	9.606 ± 0.195	RGB
5112072	1.46 ± 0.17	9.418 ± 0.148	1.45 ± 0.15	9.478 ± 0.143	RGB
5112288	1.66 ± 0.06	9.332 ± 0.051	1.69 ± 0.05	9.335 ± 0.042	RC
5112361	1.64 ± 0.16	9.321 ± 0.116	1.62 ± 0.16	9.358 ± 0.139	RGB
5112373	1.31 ± 0.12	9.539 ± 0.131	1.22 ± 0.11	9.722 ± 0.116	RGB
5112387	1.34 ± 0.12	9.493 ± 0.120	1.26 ± 0.11	9.691 ± 0.132	RGB
5112401	1.24 ± 0.10	9.697 ± 0.095	1.25 ± 0.09	9.703 ± 0.087	RC
5112730	1.58 ± 0.05	9.380 ± 0.050	1.58 ± 0.04	9.404 ± 0.043	RC
5112938	1.37 ± 0.11	9.453 ± 0.115	1.36 ± 0.14	9.566 ± 0.177	RGB
5112948	1.56 ± 0.10	9.467 ± 0.072	1.55 ± 0.10	9.461 ± 0.072	RC
5112950	1.49 ± 0.06	9.461 ± 0.048	1.49 ± 0.06	9.474 ± 0.046	RC
5112974	1.44 ± 0.07	9.483 ± 0.063	1.43 ± 0.06	9.498 ± 0.043	RC
5113041	1.38 ± 0.11	9.614 ± 0.115	1.37 ± 0.12	9.614 ± 0.099	RC

5113061	1.42 ± 0.22	9.550 ± 0.190	1.43 ± 0.23	9.561 ± 0.191	AGB
5023889	1.30 ± 0.11	9.649 ± 0.104	1.30 ± 0.10	9.641 ± 0.110	RGB
5023953	1.67 ± 0.08	9.326 ± 0.049	1.69 ± 0.07	9.340 ± 0.048	RC
5112786	1.65 ± 0.21	9.343 ± 0.132	1.67 ± 0.20	9.338 ± 0.131	RGB
5112481	1.36 ± 0.19	9.552 ± 0.199	1.37 ± 0.18	9.578 ± 0.185	RGB
5112880	1.69 ± 0.15	9.247 ± 0.104	1.70 ± 0.14	9.262 ± 0.111	RGB
5112467	1.33 ± 0.11	9.532 ± 0.133	1.25 ± 0.10	9.686 ± 0.124	RGB
5112744	1.59 ± 0.07	9.432 ± 0.053	1.57 ± 0.08	9.419 ± 0.049	RC

Table 3.5: Same as Table 3.4, now for models with $\eta = 0.2$.

	Without additional constraints		Metallicity and age constraints		
KIC	M [$M_\odot$]	$\log(\tau/\mathrm{yr})$	M [$M_\odot$]	$\log(\tau/\mathrm{yr})$	Evo.
			NGC 6791		
2297793	1.11 ± 0.16	9.855 ± 0.202	1.13 ± 0.08	9.918 ± 0.076	RGB
2297825	0.93 ± 0.04	10.050 ± 0.034	1.00 ± 0.06	9.997 ± 0.066	RC
2435987	1.03 ± 0.08	10.035 ± 0.054	1.11 ± 0.05	9.950 ± 0.077	RGB
2436209	0.99 ± 0.05	10.050 ± 0.031	1.07 ± 0.05	9.997 ± 0.066	RGB
2436417	0.97 ± 0.04	10.044 ± 0.038	1.01 ± 0.06	9.987 ± 0.074	RC
2436688	1.08 ± 0.09	9.931 ± 0.186	1.10 ± 0.07	9.976 ± 0.086	RGB
2436900	1.09 ± 0.08	9.945 ± 0.166	1.13 ± 0.07	9.879 ± 0.083	RGB
2437040	1.19 ± 0.10	9.857 ± 0.130	1.15 ± 0.08	9.892 ± 0.071	RGB
2437340	1.04 ± 0.08	9.968 ± 0.092	1.05 ± 0.07	9.941 ± 0.073	AGB
2437353	1.03 ± 0.08	9.956 ± 0.074	1.06 ± 0.06	9.933 ± 0.060	RC
2437496	1.03 ± 0.12	9.968 ± 0.128	1.10 ± 0.08	9.910 ± 0.091	AGB
2437507	1.25 ± 0.13	9.743 ± 0.162	1.19 ± 0.07	9.854 ± 0.088	RGB
2437564	1.08 ± 0.08	9.908 ± 0.091	1.09 ± 0.07	9.909 ± 0.072	RC
2437804	0.97 ± 0.07	10.033 ± 0.044	1.02 ± 0.06	9.988 ± 0.084	RC
2437816	1.18 ± 0.12	9.832 ± 0.144	1.15 ± 0.07	9.885 ± 0.076	RGB
2437965	0.95 ± 0.07	10.035 ± 0.038	1.00 ± 0.08	10.004 ± 0.081	AGB
2438051	1.00 ± 0.13	9.978 ± 0.076	1.07 ± 0.09	9.935 ± 0.101	RC
2438333	1.01 ± 0.06	10.050 ± 0.031	1.07 ± 0.05	10.030 ± 0.079	RGB
2568654	1.11 ± 0.11	9.849 ± 0.114	1.12 ± 0.09	9.838 ± 0.076	RC
2569055	0.91 ± 0.04	10.065 ± 0.025	0.97 ± 0.05	10.039 ± 0.067	RC
2569078	1.24 ± 0.11	9.775 ± 0.154	1.19 ± 0.09	9.849 ± 0.098	RGB
			NGC 6819		
4936335	0.85 ± 0.09	10.009 ± 0.091	1.28 ± 0.07	9.598 ± 0.072	AGB
4937257	1.00 ± 0.09	9.899 ± 0.138	1.29 ± 0.09	9.586 ± 0.074	RGB
4937576	1.36 ± 0.14	9.662 ± 0.130	1.51 ± 0.10	9.438 ± 0.080	RC
5023732	1.53 ± 0.15	9.410 ± 0.142	1.54 ± 0.13	9.398 ± 0.102	RGB
5024043	1.28 ± 0.12	9.574 ± 0.153	1.39 ± 0.07	9.528 ± 0.083	RGB
5024143	1.54 ± 0.14	9.401 ± 0.121	1.57 ± 0.11	9.391 ± 0.085	RGB
5024750	1.48 ± 0.18	9.443 ± 0.154	1.58 ± 0.14	9.404 ± 0.102	AGB
5111949	1.37 ± 0.12	9.462 ± 0.123	1.48 ± 0.13	9.445 ± 0.101	RGB
5112072	1.47 ± 0.17	9.414 ± 0.149	1.52 ± 0.14	9.417 ± 0.115	RGB
5112288	1.65 ± 0.06	9.327 ± 0.049	1.67 ± 0.05	9.352 ± 0.045	RC
5112361	1.63 ± 0.16	9.304 ± 0.157	1.63 ± 0.15	9.353 ± 0.120	RGB

5112373	1.31 ± 0.10	9.534 ± 0.126	1.41 ± 0.10	9.496 ± 0.092	RGB
5112387	1.34 ± 0.10	9.499 ± 0.103	1.43 ± 0.11	9.467 ± 0.086	RGB
5112401	1.25 ± 0.10	9.645 ± 0.088	1.34 ± 0.10	9.553 ± 0.093	RC
5112730	1.58 ± 0.05	9.384 ± 0.049	1.58 ± 0.04	9.403 ± 0.044	RC
5112938	1.37 ± 0.11	9.444 ± 0.104	1.46 ± 0.10	9.448 ± 0.100	RGB
5112948	1.56 ± 0.10	9.443 ± 0.074	1.57 ± 0.10	9.425 ± 0.068	RC
5112950	1.49 ± 0.06	9.452 ± 0.053	1.50 ± 0.06	9.456 ± 0.049	RC
5112974	1.45 ± 0.07	9.462 ± 0.051	1.44 ± 0.08	9.476 ± 0.043	RC
5113041	1.36 ± 0.11	9.592 ± 0.103	1.46 ± 0.11	9.508 ± 0.094	RC
5113061	1.43 ± 0.21	9.484 ± 0.192	1.56 ± 0.18	9.408 ± 0.129	RGB
5023889	1.31 ± 0.11	9.648 ± 0.104	1.43 ± 0.09	9.535 ± 0.103	RGB
5023953	1.67 ± 0.07	9.326 ± 0.046	1.69 ± 0.06	9.340 ± 0.044	RC
5112786	1.65 ± 0.19	9.346 ± 0.136	1.67 ± 0.17	9.334 ± 0.110	RGB
5112481	1.36 ± 0.20	9.542 ± 0.199	1.55 ± 0.15	9.424 ± 0.120	RGB
5112880	1.69 ± 0.15	9.250 ± 0.104	1.69 ± 0.12	9.281 ± 0.105	RGB
5112467	1.33 ± 0.11	9.528 ± 0.131	1.40 ± 0.10	9.526 ± 0.097	RGB
5112744	1.59 ± 0.07	9.428 ± 0.056	1.58 ± 0.08	9.413 ± 0.050	RC

Table 3.6: Same as Table 3.4, now for models with $\eta = 0.4$.

	Without additional constraints		Metallicity and age constraints		
KIC	M [$M_\odot$]	$\log(\tau/\mathrm{yr})$	M [$M_\odot$]	$\log(\tau/\mathrm{yr})$	Evo.
		NGC 6791			
2297793	1.11 ± 0.17	9.853 ± 0.212	1.11 ± 0.14	9.947 ± 0.142	RGB
2297825	0.91 ± 0.08	9.975 ± 0.078	0.92 ± 0.08	9.973 ± 0.075	RC
2435987	1.03 ± 0.05	10.033 ± 0.055	1.06 ± 0.07	10.033 ± 0.052	RGB
2436209	0.99 ± 0.04	10.045 ± 0.033	1.01 ± 0.06	10.047 ± 0.032	RGB
2436417	0.92 ± 0.08	10.001 ± 0.077	0.92 ± 0.08	9.986 ± 0.079	RC
2436688	1.08 ± 0.09	9.930 ± 0.185	1.05 ± 0.07	9.997 ± 0.054	RGB
2436900	1.10 ± 0.08	9.943 ± 0.166	1.10 ± 0.08	9.933 ± 0.159	RGB
2437040	1.19 ± 0.10	9.855 ± 0.130	1.18 ± 0.10	9.862 ± 0.118	RGB
2437340	1.04 ± 0.08	9.884 ± 0.086	1.03 ± 0.08	9.897 ± 0.094	AGB
2437353	1.03 ± 0.08	9.867 ± 0.083	1.04 ± 0.07	9.869 ± 0.068	RC
2437496	1.02 ± 0.14	9.887 ± 0.119	1.03 ± 0.12	9.880 ± 0.101	AGB
2437507	1.26 ± 0.12	9.737 ± 0.161	1.25 ± 0.13	9.746 ± 0.171	RGB
2437564	1.08 ± 0.08	9.821 ± 0.072	1.09 ± 0.08	9.821 ± 0.068	RC
2437804	0.94 ± 0.08	9.988 ± 0.087	0.93 ± 0.08	9.992 ± 0.084	RC
2437816	1.19 ± 0.13	9.843 ± 0.146	1.19 ± 0.12	9.834 ± 0.134	RGB
2437965	0.89 ± 0.08	10.025 ± 0.062	0.90 ± 0.07	10.028 ± 0.057	AGB
2438051	0.97 ± 0.15	9.959 ± 0.122	0.95 ± 0.15	9.975 ± 0.107	RC
2438333	1.01 ± 0.05	10.052 ± 0.030	1.02 ± 0.04	10.057 ± 0.030	RGB
2568654	1.10 ± 0.10	9.919 ± 0.153	1.12 ± 0.09	9.942 ± 0.108	RGB
2569055	0.85 ± 0.04	10.057 ± 0.035	0.85 ± 0.04	10.057 ± 0.031	RC
2569078	1.23 ± 0.11	9.774 ± 0.137	1.24 ± 0.10	9.784 ± 0.124	RGB
		NGC 6819			
4936335	0.85 ± 0.11	9.886 ± 0.138	0.82 ± 0.11	10.008 ± 0.073	AGB
4937257	0.99 ± 0.09	9.917 ± 0.139	0.99 ± 0.06	10.013 ± 0.066	RGB

4937576	1.47 ± 0.12	9.409 ± 0.103	1.48 ± 0.13	9.438 ± 0.144	RGB
5023732	1.50 ± 0.16	9.398 ± 0.137	1.48 ± 0.16	9.466 ± 0.151	RGB
5024043	1.27 ± 0.12	9.568 ± 0.150	1.31 ± 0.10	9.620 ± 0.110	RGB
5024143	1.54 ± 0.14	9.397 ± 0.121	1.56 ± 0.12	9.413 ± 0.104	RGB
5024750	1.49 ± 0.19	9.432 ± 0.140	1.49 ± 0.21	9.439 ± 0.116	AGB
5111949	1.38 ± 0.11	9.462 ± 0.123	1.34 ± 0.12	9.600 ± 0.194	RGB
5112072	1.47 ± 0.17	9.415 ± 0.148	1.47 ± 0.15	9.477 ± 0.145	RGB
5112288	1.66 ± 0.06	9.325 ± 0.047	1.69 ± 0.05	9.346 ± 0.047	RC
5112361	1.63 ± 0.17	9.307 ± 0.148	1.64 ± 0.16	9.348 ± 0.146	RGB
5112373	1.32 ± 0.11	9.523 ± 0.127	1.23 ± 0.10	9.718 ± 0.114	RGB
5112387	1.34 ± 0.10	9.478 ± 0.101	1.25 ± 0.11	9.703 ± 0.120	RGB
5112401	1.25 ± 0.08	9.610 ± 0.101	1.25 ± 0.08	9.649 ± 0.077	RC
5112730	1.59 ± 0.05	9.374 ± 0.047	1.58 ± 0.05	9.391 ± 0.042	RC
5112938	1.37 ± 0.12	9.453 ± 0.114	1.36 ± 0.14	9.585 ± 0.177	RGB
5112948	1.56 ± 0.09	9.448 ± 0.072	1.55 ± 0.10	9.440 ± 0.068	RC
5112950	1.49 ± 0.06	9.438 ± 0.059	1.49 ± 0.06	9.455 ± 0.053	RC
5112974	1.44 ± 0.07	9.435 ± 0.047	1.43 ± 0.07	9.489 ± 0.049	RC
5113041	1.36 ± 0.11	9.576 ± 0.091	1.36 ± 0.12	9.550 ± 0.082	RC
5113061	1.43 ± 0.21	9.484 ± 0.188	1.43 ± 0.22	9.519 ± 0.191	RGB
5023889	1.30 ± 0.10	9.647 ± 0.104	1.30 ± 0.10	9.648 ± 0.105	RGB
5023953	1.67 ± 0.07	9.320 ± 0.047	1.69 ± 0.06	9.335 ± 0.044	RC
5112786	1.65 ± 0.20	9.345 ± 0.132	1.67 ± 0.19	9.343 ± 0.134	RGB
5112481	1.37 ± 0.20	9.518 ± 0.192	1.37 ± 0.20	9.569 ± 0.197	RGB
5112880	1.69 ± 0.15	9.230 ± 0.119	1.69 ± 0.14	9.270 ± 0.113	RGB
5112467	1.32 ± 0.11	9.530 ± 0.132	1.25 ± 0.10	9.678 ± 0.121	RGB
5112744	1.58 ± 0.08	9.420 ± 0.053	1.57 ± 0.08	9.422 ± 0.050	RC

Table 3.7: Detected radial ($\ell = 0$) oscillation modes for red giants in NGC 6791. Frequencies, linewidths, and amplitudes were derived by using a maximum-likelihood estimation method (Sec. 3.4.2.1). For the star marked with an asterisks, the modes were fitted with sinc functions. Thus, no linewidths are given in that case. As a further note, a full set of frequencies for all detected $\ell = 0, 1, 2$, and 3 modes are available upon request from the first author.

KIC	n	ℓ	Frequency [μHz]	Linewidth [μHz]	Amplitude [a.u.]	Height [a.u.]	AIC
2297793*	5	0	3.665 ± 0.002	–	0.727 ± 0.341	21.23	24
	6	0	4.447 ± 0.002	–	0.841 ± 0.421	28.38	28
2297825	5	0	18.871 ± 0.094	0.249 ± 0.126	0.830 ± 0.135	0.88	18
	7	0	22.635 ± 0.021	0.076 ± 0.034	0.990 ± 0.119	4.09	77
	8	0	26.155 ± 0.023	0.108 ± 0.037	1.631 ± 0.150	7.86	192
	9	0	29.903 ± 0.011	0.045 ± 0.013	1.893 ± 0.183	25.57	375
	10	0	33.790 ± 0.020	0.113 ± 0.025	2.265 ± 0.154	14.49	525
	11	0	37.576 ± 0.024	0.113 ± 0.030	1.621 ± 0.133	7.38	204
	12	0	41.556 ± 0.049	0.259 ± 0.081	1.467 ± 0.132	2.65	133
2435987	6	0	25.574 ± 0.005	0.009 ± 0.008	0.580 ± 0.148	12.02	19
	7	0	29.617 ± 0.019	0.077 ± 0.023	1.499 ± 0.141	9.27	164
	8	0	33.564 ± 0.008	0.030 ± 0.009	2.082 ± 0.229	45.46	484
	10	0	37.814 ± 0.008	0.031 ± 0.009	2.784 ± 0.294	79.98	925
	11	0	41.989 ± 0.011	0.051 ± 0.013	2.487 ± 0.218	38.49	565

	12	0	46.337 ± 0.018	0.066 ± 0.021	1.338 ± 0.140	8.64	120
	13	0	50.639 ± 0.025	0.069 ± 0.030	0.829 ± 0.116	3.16	38
2436209	8	0	41.022 ± 0.018	0.048 ± 0.019	0.929 ± 0.123	5.70	51
	9	0	46.409 ± 0.018	0.076 ± 0.023	1.314 ± 0.122	7.28	166
	10	0	51.984 ± 0.013	0.056 ± 0.015	1.543 ± 0.141	13.60	285
	11	0	57.774 ± 0.012	0.053 ± 0.014	2.027 ± 0.175	24.54	551
	12	0	63.447 ± 0.024	0.118 ± 0.033	1.537 ± 0.126	6.34	185
	13	0	69.368 ± 0.021	0.077 ± 0.024	1.148 ± 0.116	5.43	110
2436417	6	0	20.287 ± 0.025	0.082 ± 0.041	0.889 ± 0.120	3.08	23
	7	0	23.447 ± 0.014	0.054 ± 0.019	1.256 ± 0.132	9.28	44
	8	0	26.827 ± 0.017	0.088 ± 0.021	2.001 ± 0.151	14.50	331
	10	0	30.312 ± 0.014	0.062 ± 0.017	1.867 ± 0.162	17.99	323
	11	0	33.738 ± 0.036	0.175 ± 0.053	1.681 ± 0.147	5.13	81
	12	0	37.349 ± 0.039	0.135 ± 0.057	1.016 ± 0.128	2.43	30
2436688	9	0	59.368 ± 0.043	0.087 ± 0.033	0.679 ± 0.101	1.69	22
	10	0	66.203 ± 0.024	0.075 ± 0.024	0.919 ± 0.103	3.58	69
	11	0	73.465 ± 0.013	0.034 ± 0.023	1.019 ± 0.177	9.86	37
	12	0	80.665 ± 0.013	0.051 ± 0.014	1.298 ± 0.127	10.55	215
	13	0	87.933 ± 0.072	0.186 ± 0.072	0.821 ± 0.113	1.15	23
	14	0	95.538 ± 0.009	0.016 ± 0.015	0.481 ± 0.117	4.70	17
2436900	6	0	24.576 ± 0.006	0.008 ± 0.010	0.426 ± 0.132	7.30	16
	7	0	28.461 ± 0.010	0.026 ± 0.009	0.996 ± 0.131	12.12	131
	8	0	32.305 ± 0.007	0.024 ± 0.008	1.458 ± 0.181	28.12	342
	9	0	36.396 ± 0.007	0.023 ± 0.007	1.792 ± 0.223	45.13	532
	10	0	40.380 ± 0.013	0.047 ± 0.013	1.359 ± 0.135	12.41	226
	11	0	44.557 ± 0.037	0.086 ± 0.038	0.749 ± 0.114	2.08	25
2437040	6	0	18.398 ± 0.005	0.008 ± 0.006	0.520 ± 0.127	10.84	32
	7	0	21.225 ± 0.009	0.028 ± 0.011	1.040 ± 0.135	12.35	134
	8	0	24.275 ± 0.008	0.030 ± 0.010	1.768 ± 0.198	33.19	459
	9	0	27.342 ± 0.010	0.038 ± 0.011	1.892 ± 0.190	29.67	453
	10	0	30.420 ± 0.015	0.049 ± 0.018	1.166 ± 0.134	8.79	108
	11	0	33.585 ± 0.031	0.068 ± 0.026	0.881 ± 0.127	3.65	33
2437340	6	0	7.735 ± 0.007	0.016 ± 0.007	0.980 ± 0.163	19.68	106
	7	0	9.119 ± 0.006	0.013 ± 0.006	0.979 ± 0.171	23.67	124
	8	0	10.463 ± 0.009	0.020 ± 0.008	0.854 ± 0.135	11.51	72
	9	0	11.911 ± 0.015	0.020 ± 0.018	0.451 ± 0.125	3.26	5
2437353	7	0	26.308 ± 0.024	0.093 ± 0.029	1.159 ± 0.114	4.61	107
	8	0	30.042 ± 0.012	0.046 ± 0.013	1.589 ± 0.158	17.44	270
	9	0	33.927 ± 0.014	0.069 ± 0.017	1.890 ± 0.152	16.37	455
	11	0	37.689 ± 0.024	0.108 ± 0.026	1.721 ± 0.137	8.73	228
	12	0	41.666 ± 0.036	0.138 ± 0.050	1.085 ± 0.119	2.72	70
2437496	4	0	3.160 ± 0.008	0.008 ± 0.008	0.345 ± 0.105	4.50	5
	5	0	3.992 ± 0.005	0.009 ± 0.005	0.709 ± 0.151	17.81	68
	6	0	4.796 ± 0.011	0.018 ± 0.010	0.564 ± 0.115	5.72	22
	7	0	5.666 ± 0.012	0.025 ± 0.013	0.719 ± 0.123	6.64	42
	8	0	6.475 ± 0.031	0.067 ± 0.026	0.678 ± 0.101	2.17	25
2437507	6	0	15.525 ± 0.010	0.023 ± 0.013	0.701 ± 0.118	6.79	50

	7	0	17.902 ± 0.010	0.036 ± 0.012	1.260 ± 0.143	14.07	200
	8	0	20.548 ± 0.008	0.029 ± 0.009	2.112 ± 0.233	48.49	656
	9	0	23.118 ± 0.013	0.054 ± 0.016	1.742 ± 0.162	17.93	317
	10	0	25.821 ± 0.020	0.071 ± 0.023	1.145 ± 0.121	5.85	103
	11	0	28.570 ± 0.032	0.078 ± 0.035	0.826 ± 0.124	2.79	31
2437564	6	0	22.812 ± 0.026	0.071 ± 0.032	0.767 ± 0.106	2.64	39
	7	0	26.470 ± 0.017	0.052 ± 0.023	0.904 ± 0.117	5.01	66
	8	0	30.212 ± 0.021	0.101 ± 0.024	1.595 ± 0.124	8.04	254
	9	0	34.128 ± 0.017	0.073 ± 0.019	1.640 ± 0.145	11.80	218
	10	0	37.914 ± 0.018	0.056 ± 0.023	1.076 ± 0.135	6.63	72
	12	0	41.995 ± 0.013	0.031 ± 0.015	0.809 ± 0.130	6.81	46
2437804	6	0	19.854 ± 0.023	0.057 ± 0.024	0.708 ± 0.104	2.82	32
	7	0	22.968 ± 0.013	0.043 ± 0.015	1.137 ± 0.129	9.59	133
	8	0	26.348 ± 0.018	0.066 ± 0.016	1.382 ± 0.127	9.27	191
	10	0	29.739 ± 0.013	0.046 ± 0.014	1.302 ± 0.138	11.66	178
	11	0	33.140 ± 0.026	0.083 ± 0.029	1.081 ± 0.118	4.46	84
2437816	6	0	13.934 ± 0.007	0.017 ± 0.009	0.790 ± 0.132	11.50	77
	7	0	16.081 ± 0.006	0.016 ± 0.007	1.376 ± 0.204	36.64	306
	8	0	18.498 ± 0.005	0.015 ± 0.005	1.855 ± 0.282	75.26	531
	9	0	20.817 ± 0.007	0.018 ± 0.007	1.299 ± 0.193	30.28	187
	10	0	23.223 ± 0.021	0.063 ± 0.024	0.983 ± 0.124	4.92	56
2437965	6	0	7.242 ± 0.008	0.021 ± 0.008	1.060 ± 0.150	16.65	145
	7	0	8.581 ± 0.009	0.024 ± 0.010	0.996 ± 0.141	13.20	110
2438051	5	0	18.409 ± 0.026	0.074 ± 0.043	0.807 ± 0.120	2.79	38
	7	0	21.918 ± 0.036	0.121 ± 0.061	0.900 ± 0.126	2.13	26
	8	0	25.339 ± 0.012	0.046 ± 0.017	1.284 ± 0.139	11.39	149
	9	0	28.963 ± 0.012	0.055 ± 0.014	1.811 ± 0.159	18.83	385
	10	0	32.734 ± 0.036	0.156 ± 0.043	1.614 ± 0.143	5.30	75
	11	0	36.422 ± 0.035	0.153 ± 0.056	1.265 ± 0.133	3.33	80
	12	0	40.313 ± 0.054	0.215 ± 0.077	1.266 ± 0.137	2.38	58
	13	0	44.045 ± 0.093	0.312 ± 0.174	0.993 ± 0.165	1.01	19
	14	0	48.091 ± 0.027	0.050 ± 0.049	0.479 ± 0.130	1.47	4
2438333	7	0	37.762 ± 0.123	0.222 ± 0.226	0.725 ± 0.194	0.75	10
	8	0	43.665 ± 0.044	0.117 ± 0.089	0.763 ± 0.150	1.59	20
	9	0	49.407 ± 0.017	0.049 ± 0.030	0.844 ± 0.128	4.59	53
	10	0	55.278 ± 0.009	0.032 ± 0.010	1.614 ± 0.176	25.75	394
	11	0	61.387 ± 0.009	0.034 ± 0.009	2.077 ± 0.212	40.56	729
	12	0	67.437 ± 0.020	0.106 ± 0.024	1.645 ± 0.121	8.12	305
	13	0	73.610 ± 0.078	0.217 ± 0.089	0.836 ± 0.119	1.03	24
	14	0	80.050 ± 0.056	0.110 ± 0.058	0.604 ± 0.114	1.06	10
2568654	6	0	12.139 ± 0.008	0.024 ± 0.009	1.009 ± 0.138	13.71	136
	7	0	14.132 ± 0.009	0.030 ± 0.010	1.208 ± 0.147	15.71	184
	8	0	16.231 ± 0.006	0.014 ± 0.006	1.333 ± 0.217	39.55	181
	9	0	18.391 ± 0.026	0.069 ± 0.028	0.817 ± 0.114	3.08	37
	10	0	20.417 ± 0.041	0.088 ± 0.042	0.728 ± 0.115	1.92	22
2569055	6	0	18.651 ± 0.059	0.163 ± 0.085	0.796 ± 0.132	1.24	16
	7	0	22.152 ± 0.025	0.089 ± 0.029	1.146 ± 0.122	4.72	73

	8	0	25.560 ± 0.034	0.186 ± 0.049	1.948 ± 0.150	6.48	207
	9	0	29.218 ± 0.013	0.060 ± 0.016	1.898 ± 0.166	19.26	335
	10	0	33.071 ± 0.019	0.089 ± 0.025	1.892 ± 0.159	12.83	259
	11	0	36.762 ± 0.031	0.206 ± 0.038	2.501 ± 0.143	9.68	569
	12	0	40.594 ± 0.034	0.167 ± 0.040	1.570 ± 0.123	4.70	161
2569078	7	0	20.188 ± 0.015	0.045 ± 0.019	1.266 ± 0.172	11.42	122
	8	0	23.125 ± 0.007	0.016 ± 0.008	1.872 ± 0.352	67.87	343
	9	0	26.010 ± 0.015	0.043 ± 0.016	1.782 ± 0.234	23.54	174
	10	0	28.981 ± 0.025	0.090 ± 0.031	1.515 ± 0.163	8.11	142
2569137	6	0	4.826 ± 0.031	0.054 ± 0.027	0.764 ± 0.137	3.47	21
	7	0	5.601 ± 0.048	0.049 ± 0.029	0.547 ± 0.139	1.96	3
2569360	6	0	16.414 ± 0.013	0.032 ± 0.014	0.719 ± 0.108	5.15	47
	7	0	18.920 ± 0.009	0.031 ± 0.011	1.260 ± 0.148	16.37	222
	8	0	21.700 ± 0.006	0.018 ± 0.006	2.173 ± 0.297	83.55	797
	9	0	24.404 ± 0.016	0.066 ± 0.020	1.562 ± 0.144	11.73	230
	10	0	27.218 ± 0.022	0.088 ± 0.029	1.239 ± 0.125	5.53	118
	11	0	30.070 ± 0.042	0.106 ± 0.043	0.766 ± 0.110	1.76	27
2569618	8	0	40.586 ± 0.018	0.046 ± 0.030	0.687 ± 0.119	3.23	28
	9	0	45.884 ± 0.018	0.083 ± 0.025	1.436 ± 0.126	7.90	203
	10	0	51.482 ± 0.009	0.035 ± 0.011	1.794 ± 0.188	29.66	404
	11	0	57.159 ± 0.010	0.044 ± 0.012	2.083 ± 0.194	31.42	588
	12	0	62.760 ± 0.012	0.047 ± 0.015	1.469 ± 0.148	14.56	238
	13	0	68.591 ± 0.053	0.135 ± 0.065	0.844 ± 0.124	1.68	27
	14	0	74.445 ± 0.018	0.031 ± 0.029	0.461 ± 0.122	2.19	6
2569935	5	0	4.688 ± 0.006	0.011 ± 0.008	0.664 ± 0.137	12.50	53
	6	0	5.610 ± 0.008	0.021 ± 0.011	0.879 ± 0.135	11.56	92
	7	0	6.665 ± 0.007	0.016 ± 0.008	0.877 ± 0.150	15.44	81
2569945	6	0	22.607 ± 0.031	0.086 ± 0.071	0.714 ± 0.144	1.89	9
	8	0	26.191 ± 0.018	0.092 ± 0.029	1.598 ± 0.133	8.85	106
	9	0	29.869 ± 0.021	0.130 ± 0.035	2.051 ± 0.142	10.27	29
	10	0	33.797 ± 0.022	0.115 ± 0.034	1.751 ± 0.141	8.50	89
	11	0	37.609 ± 0.044	0.259 ± 0.071	1.921 ± 0.150	4.54	4
	12	0	41.545 ± 0.036	0.126 ± 0.048	1.099 ± 0.126	3.06	4
2570172	9	0	64.427 ± 0.011	0.026 ± 0.014	0.658 ± 0.110	5.25	40
	10	0	71.543 ± 0.011	0.037 ± 0.013	1.151 ± 0.131	11.31	176
	11	0	78.545 ± 0.018	0.079 ± 0.021	1.374 ± 0.117	7.56	223
	12	0	85.669 ± 0.034	0.088 ± 0.039	0.806 ± 0.109	2.35	41
2570214	7	0	24.428 ± 0.032	0.131 ± 0.041	1.175 ± 0.111	3.37	59
	8	0	27.951 ± 0.026	0.116 ± 0.027	1.403 ± 0.110	5.40	192
	9	0	31.617 ± 0.031	0.176 ± 0.038	1.701 ± 0.113	5.24	264
	10	0	35.142 ± 0.046	0.235 ± 0.056	1.596 ± 0.113	3.44	126
	12	0	38.922 ± 0.044	0.184 ± 0.051	1.196 ± 0.108	2.47	78

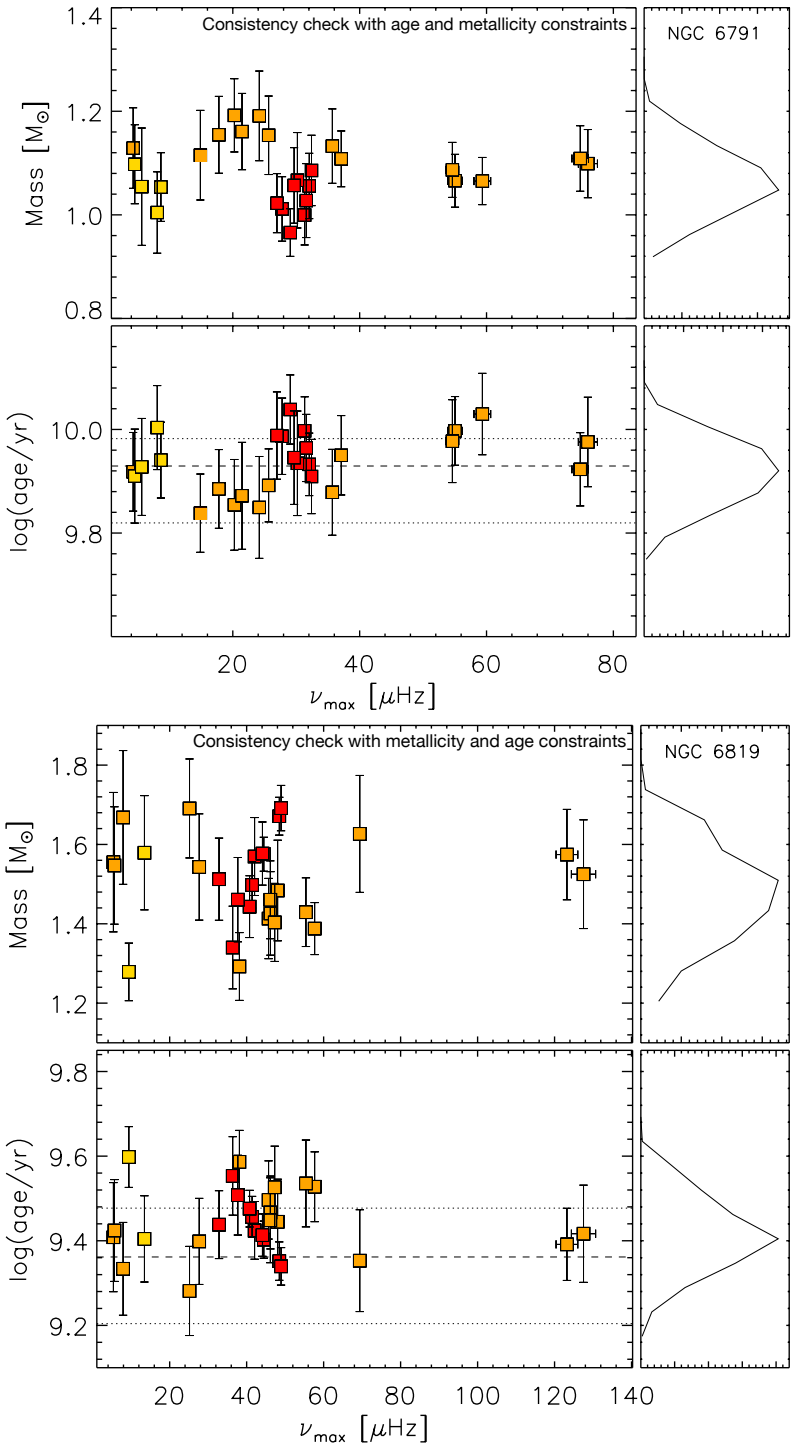

Figure 3.6: Stellar masses and logarithmic ages derived from GBM by using models with $\eta = 0.2$ and by adopting the clusters' metallicities and ages as additional constraints for NGC 6791 (top) and NGC 6819 (bottom). The dashed lines indicate computed cluster ages from isochrone fitting (including their 3σ uncertainties; dotted lines). The right panels provide the histograms of the calculated masses and ages for the red giants shown in the left panels.

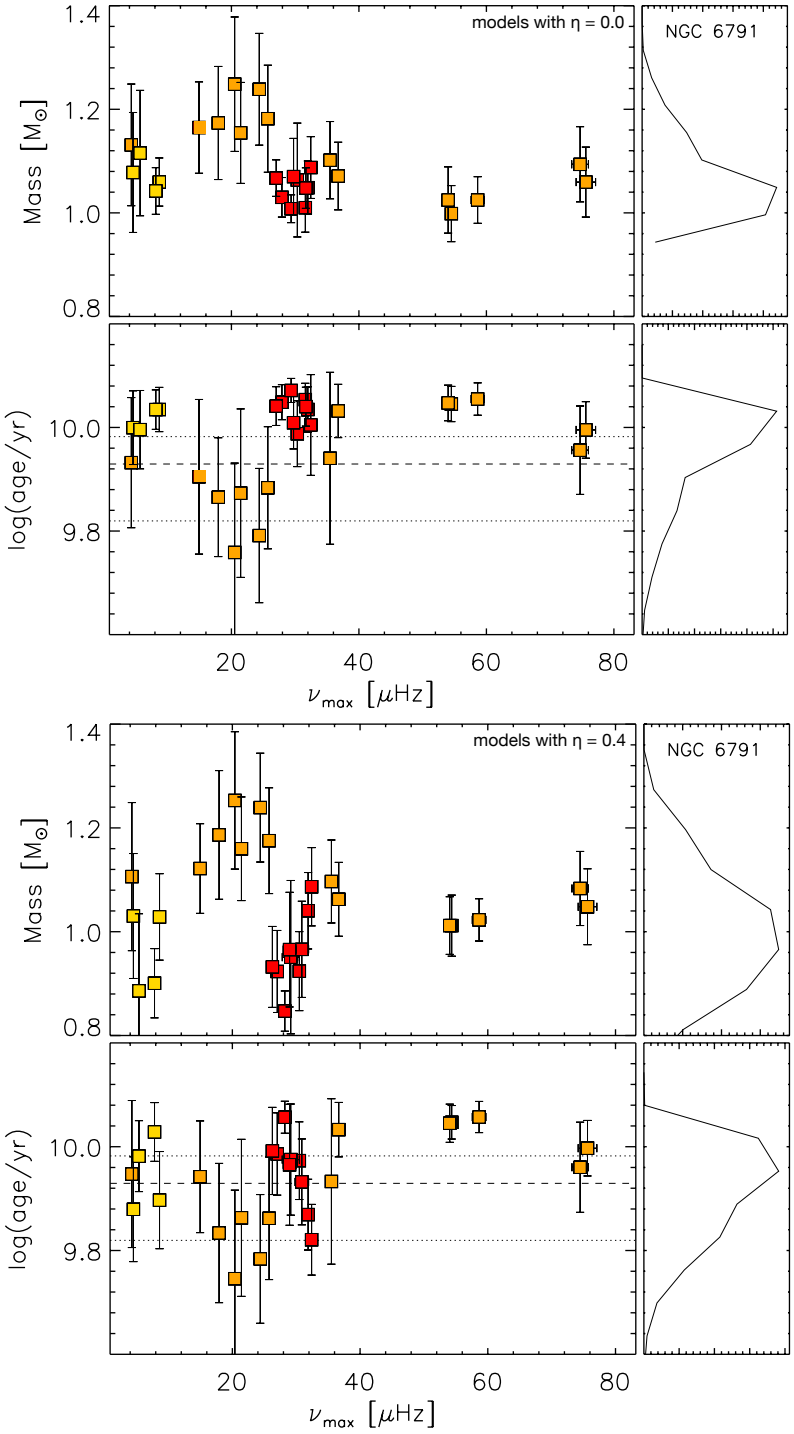

Figure 3.7: Stellar masses and logarithmic ages for stars in NGC 6791 derived from GBM with metallicity constraints from the cluster isochrones by using stellar models with $\eta = 0.0$ (top) and 0.4 (bottom). The dashed lines indicate computed cluster ages from isochrone fitting (including their 3σ uncertainties; dotted lines). The right panels provide the histograms of the calculated masses and ages for the red giants shown in the left panels.

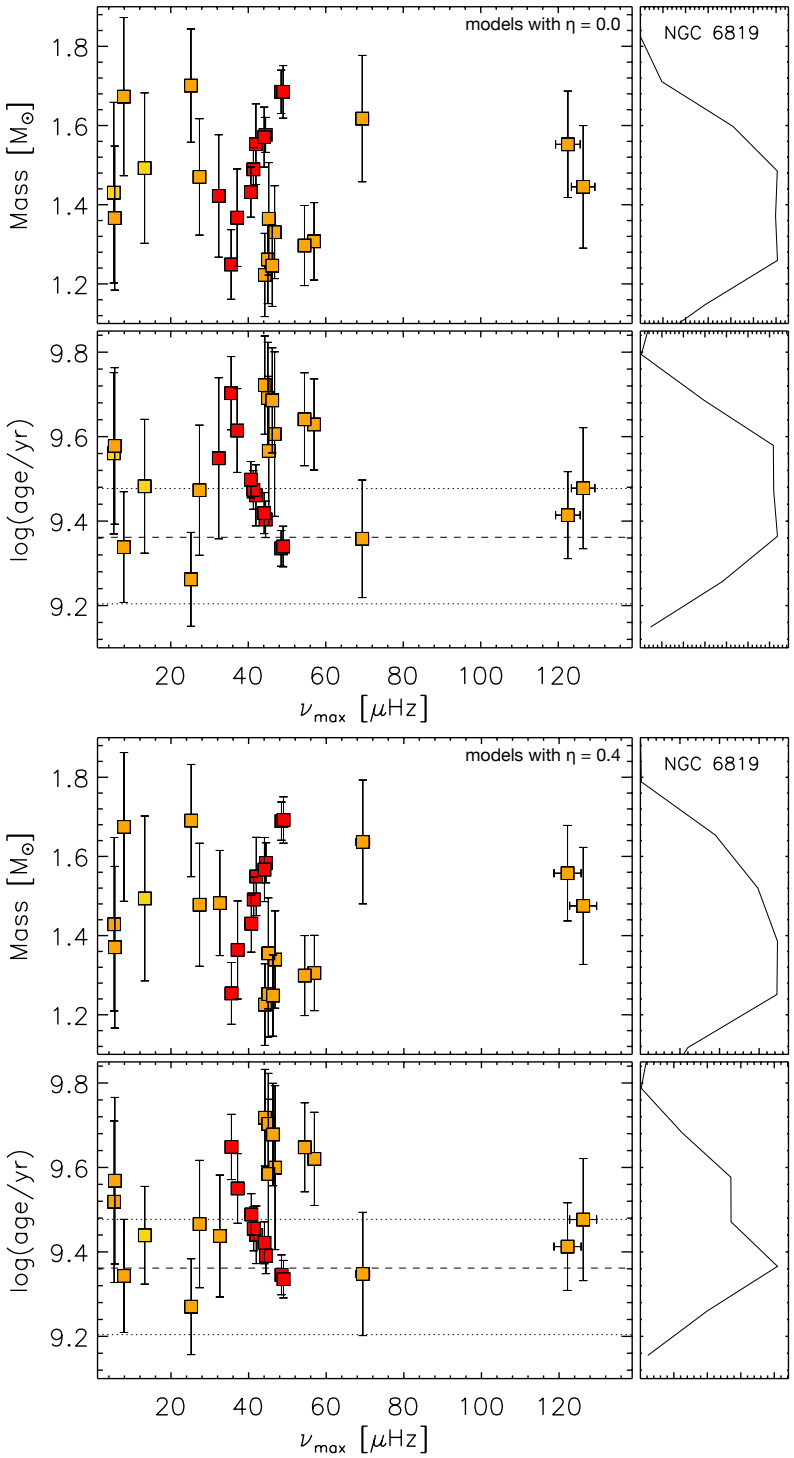

Figure 3.8: Same as Figure 3.7, now for red giants in NGC 6819.

Table 3.8: Same as Table 3.7 but for red giants in NGC 6819.

KIC	n	ℓ	Frequency [μHz]	Linewidth [μHz]	Amplitude [a.u.]	Height [a.u.]	AIC
4936335	5	0	6.980 ± 0.008	0.018 ± 0.009	0.987 ± 0.169	17.44	107
	7	0	8.349 ± 0.011	0.027 ± 0.010	1.091 ± 0.157	14.23	117
	8	0	9.881 ± 0.015	0.040 ± 0.018	0.982 ± 0.140	7.68	61
4937257	7	0	28.810 ± 0.087	0.500 ± 0.264	1.743 ± 0.231	1.93	3
	8	0	32.816 ± 0.024	0.138 ± 0.033	2.151 ± 0.152	10.67	303
	10	0	37.057 ± 0.016	0.074 ± 0.020	2.072 ± 0.178	18.51	364
	11	0	41.163 ± 0.022	0.099 ± 0.023	1.895 ± 0.154	11.61	253
	12	0	45.469 ± 0.043	0.153 ± 0.053	1.189 ± 0.133	2.95	56
	13	0	49.673 ± 0.119	0.336 ± 0.261	0.897 ± 0.200	0.76	1
4937576	8	0	28.207 ± 0.010	0.037 ± 0.012	1.975 ± 0.222	33.36	388
	9	0	31.764 ± 0.017	0.078 ± 0.022	2.186 ± 0.191	19.50	342
	10	0	35.289 ± 0.013	0.053 ± 0.014	2.554 ± 0.245	39.09	473
	11	0	38.916 ± 0.014	0.048 ± 0.018	1.591 ± 0.189	16.91	134
	12	0	42.488 ± 0.029	0.101 ± 0.039	1.299 ± 0.152	5.33	81
5023732	7	0	21.670 ± 0.016	0.036 ± 0.020	0.738 ± 0.124	4.87	36
	8	0	24.562 ± 0.014	0.043 ± 0.015	1.250 ± 0.150	11.65	139
	9	0	27.711 ± 0.011	0.041 ± 0.014	1.773 ± 0.197	24.33	307
	10	0	30.795 ± 0.018	0.061 ± 0.020	1.478 ± 0.161	11.40	128
	11	0	33.996 ± 0.021	0.077 ± 0.024	1.349 ± 0.138	7.49	123
	12	0	37.215 ± 0.039	0.064 ± 0.034	0.672 ± 0.136	2.26	9
5023889	7	0	38.398 ± 0.018	0.032 ± 0.022	0.561 ± 0.118	3.15	15
	8	0	43.451 ± 0.013	0.035 ± 0.017	0.871 ± 0.129	6.84	64
	9	0	48.751 ± 0.014	0.055 ± 0.015	1.702 ± 0.166	16.71	323
	10	0	54.082 ± 0.013	0.058 ± 0.014	2.599 ± 0.231	36.97	716
	11	0	59.436 ± 0.011	0.045 ± 0.012	2.453 ± 0.243	42.30	653
	12	0	64.934 ± 0.023	0.098 ± 0.024	1.648 ± 0.141	8.87	205
	13	0	70.403 ± 0.038	0.176 ± 0.050	1.499 ± 0.131	4.06	109
	14	0	75.879 ± 0.014	0.027 ± 0.031	0.569 ± 0.147	3.86	17
5023953	9	0	42.492 ± 0.021	0.088 ± 0.025	1.488 ± 0.134	8.01	202
	9	0	47.295 ± 0.017	0.074 ± 0.020	1.777 ± 0.157	13.61	321
	10	0	52.075 ± 0.016	0.068 ± 0.017	2.107 ± 0.184	20.73	441
	11	0	56.815 ± 0.020	0.081 ± 0.025	1.552 ± 0.146	9.44	215
	12	0	61.484 ± 0.053	0.275 ± 0.059	1.665 ± 0.118	3.22	181
5024043	8	0	45.350 ± 0.024	0.067 ± 0.028	0.981 ± 0.125	4.59	65
	9	0	50.906 ± 0.013	0.051 ± 0.014	1.832 ± 0.181	20.99	392
	10	0	56.492 ± 0.009	0.035 ± 0.010	2.786 ± 0.305	70.42	969
	11	0	62.099 ± 0.016	0.067 ± 0.017	1.917 ± 0.173	17.48	332
	12	0	67.846 ± 0.024	0.088 ± 0.026	1.357 ± 0.136	6.67	122
5024143	10	0	98.684 ± 0.032	0.073 ± 0.033	0.734 ± 0.114	2.35	25
	11	0	108.180 ± 0.017	0.057 ± 0.017	1.271 ± 0.134	9.02	162
	12	0	117.875 ± 0.015	0.059 ± 0.018	1.486 ± 0.149	12.00	229
	13	0	127.470 ± 0.014	0.054 ± 0.016	1.556 ± 0.158	14.35	265
	14	0	137.239 ± 0.017	0.034 ± 0.026	0.658 ± 0.130	4.01	21
	15	0	147.187 ± 0.049	0.093 ± 0.059	0.598 ± 0.127	1.23	8

5024750	6	0	10.457 ± 0.017	0.043 ± 0.022	0.909 ± 0.130	6.16	66
	7	0	12.140 ± 0.011	0.025 ± 0.015	0.864 ± 0.146	9.39	59
	8	0	13.981 ± 0.015	0.055 ± 0.017	1.456 ± 0.154	12.29	196
	9	0	15.760 ± 0.023	0.087 ± 0.025	1.558 ± 0.153	8.92	158
5111949	7	0	33.884 ± 0.027	0.047 ± 0.022	0.640 ± 0.112	2.76	18
	8	0	38.481 ± 0.028	0.124 ± 0.043	1.401 ± 0.133	5.02	89
	9	0	43.145 ± 0.014	0.055 ± 0.018	1.608 ± 0.164	14.85	235
	10	0	48.038 ± 0.018	0.084 ± 0.020	2.106 ± 0.169	16.90	441
	11	0	52.896 ± 0.024	0.124 ± 0.034	1.886 ± 0.149	9.17	281
	12	0	57.772 ± 0.030	0.147 ± 0.036	1.712 ± 0.133	6.35	190
5112072	10	0	102.761 ± 0.016	0.042 ± 0.017	1.008 ± 0.132	7.74	92
	11	0	112.653 ± 0.017	0.057 ± 0.017	1.234 ± 0.133	8.54	143
	12	0	122.729 ± 0.017	0.070 ± 0.017	1.625 ± 0.148	12.02	275
	13	0	132.732 ± 0.015	0.064 ± 0.020	1.595 ± 0.154	12.68	253
	14	0	142.878 ± 0.032	0.098 ± 0.044	0.999 ± 0.125	3.23	61
5112288	8	0	38.263 ± 0.021	0.046 ± 0.021	0.743 ± 0.122	3.80	26
	9	0	42.774 ± 0.016	0.071 ± 0.018	1.887 ± 0.164	15.95	351
	10	0	47.658 ± 0.015	0.070 ± 0.018	2.160 ± 0.184	21.08	446
	11	0	52.374 ± 0.020	0.085 ± 0.022	1.690 ± 0.150	10.66	240
	12	0	57.201 ± 0.026	0.120 ± 0.030	1.665 ± 0.136	7.35	194
5112361	9	0	56.179 ± 0.021	0.062 ± 0.024	0.936 ± 0.119	4.52	60
	10	0	62.216 ± 0.013	0.052 ± 0.016	1.638 ± 0.167	16.50	279
	10	0	68.425 ± 0.012	0.050 ± 0.013	2.073 ± 0.201	27.41	519
	11	0	74.549 ± 0.023	0.121 ± 0.028	2.021 ± 0.149	10.79	370
	12	0	80.793 ± 0.017	0.061 ± 0.019	1.354 ± 0.141	9.60	161
	13	0	87.055 ± 0.032	0.108 ± 0.036	1.126 ± 0.124	3.73	58
5112373	8	0	36.732 ± 0.045	0.253 ± 0.057	1.781 ± 0.122	3.98	224
	9	0	41.357 ± 0.012	0.050 ± 0.013	2.373 ± 0.226	35.80	683
	10	0	46.096 ± 0.014	0.052 ± 0.016	1.961 ± 0.198	23.42	316
	11	0	50.658 ± 0.019	0.093 ± 0.026	1.921 ± 0.161	12.67	320
	12	0	55.354 ± 0.029	0.119 ± 0.042	1.277 ± 0.129	4.37	112
	13	0	60.214 ± 0.030	0.060 ± 0.034	0.661 ± 0.125	2.33	14
5112387	8	0	37.549 ± 0.025	0.105 ± 0.035	1.415 ± 0.138	6.04	134
	9	0	42.163 ± 0.016	0.076 ± 0.019	2.131 ± 0.176	19.07	524
	10	0	46.911 ± 0.017	0.070 ± 0.019	1.786 ± 0.164	14.49	285
	11	0	51.588 ± 0.019	0.084 ± 0.025	1.837 ± 0.163	12.77	268
	12	0	56.375 ± 0.033	0.169 ± 0.045	1.783 ± 0.139	5.97	211
	13	0	61.293 ± 0.057	0.133 ± 0.057	0.875 ± 0.134	1.83	24
5112401	7	0	28.144 ± 0.019	0.065 ± 0.021	1.203 ± 0.131	7.11	105
	8	0	31.833 ± 0.039	0.145 ± 0.051	1.685 ± 0.171	6.24	84
	9	0	35.988 ± 0.018	0.081 ± 0.025	2.142 ± 0.189	18.13	297
	10	0	40.081 ± 0.028	0.161 ± 0.037	2.324 ± 0.163	10.69	468
	11	0	44.125 ± 0.029	0.130 ± 0.040	1.666 ± 0.153	6.79	197
5112467	9	0	42.569 ± 0.017	0.060 ± 0.018	1.366 ± 0.145	9.93	148
	10	0	47.466 ± 0.024	0.090 ± 0.039	1.201 ± 0.142	5.11	84
	11	0	52.212 ± 0.011	0.017 ± 0.025	0.580 ± 0.194	6.32	7

5112481	5	0	5.107 ± 0.012	0.025 ± 0.013	0.759 ± 0.133	7.44	42
	6	0	6.028 ± 0.016	0.035 ± 0.017	0.866 ± 0.144	6.85	42
	7	0	6.945 ± 0.018	0.029 ± 0.017	0.582 ± 0.123	3.70	14
5112730	7	0	32.078 ± 0.018	0.036 ± 0.023	0.766 ± 0.129	5.13	43
	8	0	36.384 ± 0.034	0.150 ± 0.050	1.329 ± 0.129	3.75	96
	9	0	40.817 ± 0.015	0.066 ± 0.017	2.030 ± 0.179	19.88	382
	10	0	45.484 ± 0.015	0.072 ± 0.020	2.017 ± 0.174	17.92	421
	11	0	49.975 ± 0.028	0.145 ± 0.035	1.989 ± 0.147	8.68	232
	12	0	54.689 ± 0.027	0.132 ± 0.034	1.656 ± 0.132	6.63	170
5112744	8	0	35.485 ± 0.011	0.031 ± 0.012	1.075 ± 0.146	11.81	118
	9	0	39.775 ± 0.012	0.040 ± 0.012	1.571 ± 0.176	19.57	272
	10	0	44.218 ± 0.016	0.063 ± 0.017	1.790 ± 0.168	16.14	301
	10	0	48.629 ± 0.017	0.068 ± 0.019	1.739 ± 0.165	14.16	240
	11	0	53.191 ± 0.019	0.061 ± 0.023	1.190 ± 0.141	7.33	92
	13	0	62.247 ± 0.051	0.086 ± 0.036	0.660 ± 0.114	1.62	13
5112786	5	0	6.613 ± 0.007	0.010 ± 0.006	0.685 ± 0.158	14.49	38
	6	0	7.767 ± 0.008	0.014 ± 0.008	0.797 ± 0.162	14.69	55
	7	0	8.916 ± 0.012	0.025 ± 0.019	0.863 ± 0.171	9.52	32
5112880	7	0	22.077 ± 0.021	0.082 ± 0.026	1.513 ± 0.153	8.92	152
	8	0	24.930 ± 0.009	0.023 ± 0.012	1.327 ± 0.214	24.40	90
	9	0	27.718 ± 0.012	0.044 ± 0.015	2.053 ± 0.227	30.57	281
5112938	7	0	33.302 ± 0.012	0.031 ± 0.017	0.839 ± 0.134	7.34	59
	8	0	37.828 ± 0.016	0.055 ± 0.019	1.299 ± 0.146	9.84	140
	9	0	42.409 ± 0.013	0.049 ± 0.014	1.861 ± 0.191	22.65	335
	10	0	47.217 ± 0.016	0.072 ± 0.017	2.175 ± 0.187	21.01	416
	11	0	52.005 ± 0.031	0.173 ± 0.039	2.006 ± 0.141	7.40	301
	12	0	56.817 ± 0.036	0.095 ± 0.041	0.967 ± 0.142	3.14	32
5112948	8	0	34.455 ± 0.012	0.030 ± 0.015	0.864 ± 0.135	7.94	63
	9	0	38.628 ± 0.015	0.054 ± 0.016	1.452 ± 0.152	12.43	201
	10	0	42.956 ± 0.012	0.049 ± 0.012	2.256 ± 0.219	32.99	597
	10	0	47.222 ± 0.009	0.028 ± 0.010	1.756 ± 0.225	34.69	342
5112950	7	0	30.564 ± 0.017	0.057 ± 0.023	1.097 ± 0.131	6.67	104
	8	0	34.641 ± 0.029	0.120 ± 0.050	1.331 ± 0.146	4.70	92
	9	0	38.874 ± 0.022	0.086 ± 0.025	1.469 ± 0.142	8.01	158
	10	0	43.384 ± 0.020	0.096 ± 0.025	2.067 ± 0.166	14.13	371
	11	0	47.683 ± 0.011	0.037 ± 0.013	1.615 ± 0.192	22.39	241
	12	0	52.189 ± 0.048	0.176 ± 0.052	1.243 ± 0.125	2.79	78
5112974	7	0	30.286 ± 0.016	0.041 ± 0.017	0.893 ± 0.126	6.18	59
	8	0	34.354 ± 0.016	0.064 ± 0.020	1.570 ± 0.153	12.21	220
	9	0	38.635 ± 0.016	0.072 ± 0.021	2.047 ± 0.180	18.65	355
	10	0	43.043 ± 0.023	0.123 ± 0.029	2.278 ± 0.168	13.42	444
	11	0	47.416 ± 0.021	0.084 ± 0.025	1.514 ± 0.143	8.73	176
	12	0	51.807 ± 0.047	0.181 ± 0.066	1.333 ± 0.143	3.13	48
5113041	7	0	28.111 ± 0.039	0.067 ± 0.030	0.647 ± 0.111	1.99	15
	8	0	31.864 ± 0.027	0.099 ± 0.030	1.208 ± 0.123	4.71	100
	9	0	35.805 ± 0.011	0.045 ± 0.012	2.184 ± 0.219	33.71	598

	10	0	39.779 ± 0.015	0.060 ± 0.016	1.950 ± 0.185	20.27	326
	11	0	43.708 ± 0.057	0.201 ± 0.051	1.599 ± 0.150	4.04	71
	12	0	47.935 ± 0.021	0.070 ± 0.025	1.166 ± 0.130	6.15	105
5113061	5	0	4.590 ± 0.029	0.076 ± 0.027	0.857 ± 0.112	3.09	43
	6	0	5.452 ± 0.023	0.044 ± 0.018	0.713 ± 0.113	3.65	28
	7	0	6.350 ± 0.017	0.040 ± 0.019	0.748 ± 0.120	4.50	36

4 KIC 2568888: To be or not to be a binary

This chapter reproduces the article *KIC 2568888: To be or not to be a binary* by N. Themeßl, S. Hekker, A. Mints, R. A. García, A. García Saravia Ortiz de Montellano, P. B. Stetson and J. De Ridder, published in the Astrophysical Journal, Volume 868, Issue 2, article id. 103, 10 pp. (2018), DOI: 10.3847/1538-4357/aae846[1].

4.1 Summary

In cases where both components of a binary system show oscillations, asteroseismology has been proposed as a method to identify the system. For KIC 2568888, observed with *Kepler*, we detect oscillation modes for two red giants in a single power density spectrum. Through an asteroseismic study we investigate if the stars have similar properties, which could be an indication that they are physically bound into a binary system. While one star lies on the red-giant branch (RGB), the other, more evolved star, is either a RGB or asymptotic giant branch star. We found similar ages for the red giants and a mass ratio close to 1. Based on these asteroseismic results we propose KIC 2568888 as a rare candidate binary system ($\sim$ 0.1% chance). However, when combining the asteroseismic data with ground-based *BVI* photometry we estimated different distances for the stars, which we cross-checked with *Gaia* DR2. From *Gaia* we obtained for one object a distance between and broadly consistent with the distances from *BVI* photometry. For the other object we have a negative parallax with a not yet reliable *Gaia* distance solution. The derived distances challenge a binary interpretation and may either point to a triple system, which could explain the visible magnitudes, or, to a rare chance alignment ($\sim$ 0.05% chance based on stellar magnitudes). This probability would even be smaller, if calculated for close pairs of stars with a mass ratio close to unity in addition to similar magnitudes, which may indeed indicate that a binary scenario is more favourable.

[1]Contribution statement: NT performed research, analyzed data, and wrote the paper. SH carried out grid-based modelling and provided useful advice and comments on the research and the manuscript. AM generated grids of ischrones and performed the UniDAM analysis. RAG checked the light curve with an independent code. AGSOM developed automated peakbagging algorithm. PBS provided ground-based *BVI* measurements. JDR contributed Bayesian distance measurements from *Gaia*.

4.2 Introduction

The *Kepler* space mission (Borucki et al. 2010) obtained high-precision photometric time series data for thousands of red giants that show solar-like oscillations. In many *Kepler* light curves eclipses were present due to the passage or occultation of a companion star or planet. These data have led to the detection of a number of eclipsing binary systems with an oscillating red-giant component (e.g. Hekker et al. 2010c, Gaulme et al. 2013). From theoretical predictions we expect more red giants with observable oscillation modes to belong to binary star systems (Miglio et al. 2014). The detection of these non-eclipsing binary systems requires different measures because they lack the distinct dips in flux in the light curves. A new class of eccentric non-eclipsing binary systems has already been detected with *Kepler* data (e.g. Beck et al. 2014, 2015). These binaries show ellipsoidal modulations due to strong gravitational distortions and heating that take place during periastron passage, which become visible as 'heartbeat' effects in their light curves. Their detection offered a new way of studying binary interactions, as well as the evolution of such eccentric systems.

Moreover, Miglio et al. (2014) suggested using asteroseismology to find potential binary systems that consist of two oscillating solar-type and/or red-giant stars. This method is applicable to high-precision long-term photometric data and independent of the inclination, separation, and velocities of the binary components. Based on simulations of binary populations in the *Kepler* field of view, Miglio et al. performed a study to predict the asteroseismic detectability of two solar-like oscillators that are gravitationally bound in a single light curve. According to their predictions there should be 200 or more so-called asteroseismic binaries detectable in *Kepler* long-cadence data. When considering a total number of about 200 000 long-cadence targets, we obtain a ~ 0.1 % chance of finding an asteroseismic binary. Additionally, the components should have a mass ratio near unity, which favours oscillations that overlap in frequency.

So far, there are only three published cases of asteroseismic binaries that are not in eclipsing systems, and that were detected in a single *Kepler* light curve. Appourchaux et al. (2015) reported the double-star system KIC 7510397 (or HIP 93511, or HD 177412), which shows two separated oscillation-mode envelopes of two solar-like stars with typical frequencies of the oscillations at about 1 200 and 2 200 μHz. Using speckle interferometry, Appourchaux et al. constrained the binary orbit and determined the stellar properties of both components from asteroseismic methods. More recently, White et al. (2017) presented an asteroseismic study of the binary system HD 176465, including the detection of individual mode frequencies for two solar-like oscillating stars that are on the main sequence. The stellar oscillations of both components cover the same range in frequency from $\sim 2\,000$ to $\sim 4\,500\,\mu$Hz. Based on the derived stellar parameters, White et al. classified them as two young physically-similar solar analogues. Furthermore, Beck et al. (2018) reported the detection of an eccentric binary system that consists of a sub-Nyquist and a super-Nyquist oscillating red-giant star with stellar oscillations present at around $120 - 250\,\mu$Hz. The two binary components were found to be low-luminosity red giants of similar mass that are in the early and advanced stages of the first dredge-up event on the red-giant branch. Another interesting system was found by Rawls et al. (2016). KIC 9246715 is a double red giant eclipsing binary, where both components have very

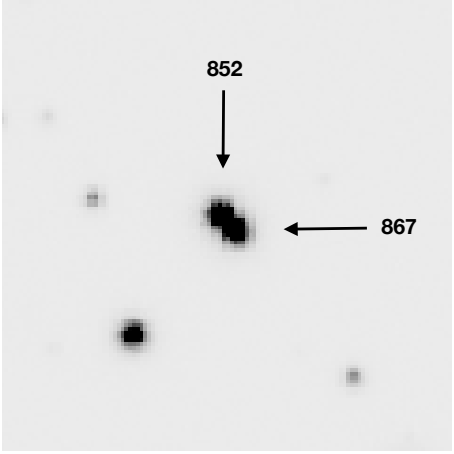

Figure 4.1: A 30 × 30 arcsecond postage stamp (stack of 10 images with 0.″69 < seeing < 0.″82) from Stetson et al. (2003, 2005) centred on our pair of red-giant stars, which have a spatial separation of ∼ 1.″6. The numbers are the sequential catalogue identifications for the two stars as listed in Table 4.1.

similar masses and radii. They measured one main set of solar-like oscillations with lower amplitudes and larger oscillation mode linewidths than expected, while a second set of oscillations was only marginally detectable. Rawls et al. interpreted this as being due to stellar activity and tidal forces weakening the oscillations of both stars.

These recent studies show the great potential of asteroseismology for binary systems where oscillations of the components can be detected. Here, we analyze the *Kepler* target KIC 2568888, which was originally proposed to be observed in the framework of a study of the open cluster NGC 6791. Based on asteroseismic stellar properties, *Gaia* parallaxes and supplementary ground- and space-based photometric measurements, we investigate if KIC 2568888 is a rare candidate binary system with two oscillating red-giant stars.

4.3 Data

In the following, we provide an overview of the data that we used for the analysis of KIC 2568888.

4.3.1 *Kepler* light curve

The basis for our asteroseismic analysis is the *Kepler* photometric time series of the respective stars. During each *Kepler* observation, pixel files were acquired for any given target star. The pixels contained within a predefined mask were then added up to create light curves (Thompson et al. 2016). When two stars are spatially coincident, as is the case here, they are observed as a single *Kepler* time series. To check if an optimal aperture mask was applied to derive this light curve, we inspected the individual target pixels of KIC 2568888. We found that all pixels with stellar signals include the flux of both stars, which makes the extraction of individual light curves impossible. We also performed the aperture photometry with the KADACS software (García et al. 2011) with the

same result.

For the asteroseismic study we used the concatenated corrected light curve (Handberg and Lund 2014) that was created from 860 days of observations during the nominal *Kepler* space mission with one exposure taken every $\sim$ 29.4 min (long-cadence mode). From these light-curve data we determined the asteroseismic stellar parameters for both red-giant stars, which we describe in Section 4.5.

4.3.2 APOGEE spectra

As further constraints we took the effective temperature and metallicity that were published by the 14$^{\rm th}$ data release of the Sloan Digital Sky Survey (SDSS; e.g. Blanton et al. 2017, Abolfathi et al. 2018): $T_{\rm eff}$ = 4378 ± 76 K and [M/H] = −0.005 ± 0.023 dex. These atmospheric parameters were derived from APOGEE spectra by using an automated pipeline and under the assumption that KIC 2568888 is a single stellar object with coordinates α = 290°.09354 ± 0°.00460 and δ = 37°.86151 ± 0°.00440. APOGEE visited the system twice, with the observations being 16 days apart. The mean measured radial velocity with respect to the barycentre is $-58.90\,{\rm km\,s^{-1}}$, with a radial velocity scatter of $0.18\,{\rm km\,s^{-1}}$. Only the spectral lines of a single component were visible in the spectra. Whenever we used $T_{\rm eff}$ and [M/H] in the asteroseismic stellar parameter determination (Sec. 4.5), we adopted uncertainties of ± 200 K and ± 0.3 dex, respectively. The impact of the unknown individual temperatures in particular is marginal, since red giants cover a very narrow range in $T_{\rm eff}$, which lies within the adopted uncertainties.

4.3.3 Ground-based *BVI* photometry

One of the photometric measurements in which the candidate binary is resolved is shown in Figure 4.1, where we see two stars with similar visual magnitudes in the region around KIC 2568888. These data were obtained during the original photometric survey of the open cluster NGC 6791 (Stetson et al. 2003, 2005) with additional measurements that were acquired more recently. We analyzed the *BVI* photometry of the two stars by using the methodology discussed in Stetson (2000) and Stetson et al. (2003, 2005). The positional and photometric measurements for both stars are given in Table 4.1. We used these magnitudes to estimate the distances in Section 4.5.3.

4.3.4 (Near-)infrared photometry

In the Two Micron All Sky Survey (2MASS; e.g. Skrutskie et al. 2006), the two stars are unresolved and thus observed as a single source. We report the combined $J-$band, $H-$band, and $K_{\rm s}-$band magnitude in Table 4.1, which we used to investigate the distances (see Sec. 4.5.3).

We further note that the *Wide-field Infrared Survey Explorer* (*WISE*; e.g. Wright et al. 2010) provides combined fluxes for the pair of stars in four bands, which are all similar. We do not find any noticeable features such as infrared excess emission, which in the case of a binary star would be the circumbinary dust that is commonly observed in post-asymptotic giant branch systems (e.g. Dermine et al. 2013). However, in case of a pole-on

system, the dust disk may be outside the photometric mask that was selected for obtaining the photometry.

4.3.5 *Gaia* DR2 parameters

The second *Gaia* data release (DR2; Gaia Collaboration et al. 2018) provided new data on the two stars that are identified as KIC 2568888, which we report in Table 4.1. The astrometric and photometric measurements were derived from a 22 month time span of observations. With an effective angular resolution of about 0.″5, *Gaia* could resolve the two sources. Due to the astrometric precision of 4×10^{-5} arcsec, we can update their angular separation to be $\sim 1.''5765$ (Fig. 4.2).

For both red giants parallaxes are provided, although for one of the stars the parallax value is negative. This is a result of the measurement process in cases where a model is fitted to noisy observations. About one-quarter of all published parallaxes in *Gaia* DR2 are negative (Bailer-Jones et al. 2018). If a negative parallax is used to estimate the distance, it is important to treat its derivation as an inference problem by using a full Bayesian analysis, because the likelihood is not informative enough and the influence of the prior is significant. Following this approach, we found different distances for the two red giants with ~ 5.6 kpc and ~ 14.7 kpc, respectively. It is worth noting that binarity was not taken into account in *Gaia* DR2. The source model that was used to derive the astrometric parameters is representative of a single star with the assumption of a uniform and rectilinear space motion relative to the solar system barycentre (Luri et al. 2018). This model describes the typical helix movement for the apparent motion of a star on the sky. Binarity can disrupt this movement and may alter the distance estimates and proper motions of the binary components significantly. Moreover, the pair of stars that we study is very close and they have similar visible magnitudes (see Tab. 4.1). This can lead to some further confusion during the analysis process, in which blending and decontamination from nearby sources are not included.

In Table 4.1 we also provide the 'astrometric_excess_noise' (ϵ), which quantifies how well the astrometric five-parameter model fits the observations. A large value of ϵ would show that the astrometric fitting was problematic. In order to evaluate the statistical significance of this parameter, we can use the dimensionless 'astrometric_excess_noise_sig' quantity (D). In cases where $D \leq 2$, the astrometric excess noise is considered statistically insignificant. For both stars investigated here, the provided D values are larger. This indicates that the *Gaia* astrometric pipeline did indeed encounter some problems when fitting the astrometric model, in particular for the source 2051291674955780992, in which case a negative parallax measurement was provided. Due to these possible complications we are not able to make any firm conclusions on the physical relation between the two stars based on the recently published *Gaia* data.

We further note that the resolution of the *Gaia* $G-$band is of the order of $\sim 0.''3 - 0.''5$, thus individual values for each star could be retrieved and they are of the same order of magnitude as the ground-based V measurements. The mean red- ($G_{\rm RP}$) and blue-band ($G_{\rm BP}$) magnitudes are given for one object only. As these bands have a lower resolution of $\sim 2.''$, which exceeds the angular separation of our pair of stars, it is likely that the published $G_{\rm BP}$ and $G_{\rm RP}$ values represent the combined flux of both sources.

Table 4.1: Ground-based *BVI* photometric measurements (Sec. 4.3.3) and *Gaia* DR2 parameters (Sec. 4.3.5) for the two stars as well as the combined 2MASS JHK_s magnitudes (Sec. 4.3.4). We note that the uncertainties in the *Gaia* distance estimates are represented by the lower and upper boundary of the 68 % credibility intervals.

Ground-based *BVI* photometry from Stetson et al. (2003, 2005)		
Sequential catalogue number	867	852
α (J2000.0) [deg]	290.09375	290.09333
δ (J2000.0) [deg]	+37.86144	+37.86178
B [mag]	16.001 ± 0.004	16.016 ± 0.003
V [mag]	14.689 ± 0.004	14.621 ± 0.004
I [mag]	13.258 ± 0.012	13.176 ± 0.006
Gaia data release 2 parameters		
Source name	2051291674950663808	2051291674955780992
α (J2000.0) [deg]	290.0937534437 ± 0.0000000058	290.0933600817 ± 0.0000000067
δ (J2000.0) [deg]	37.8613104547 ± 0.0000000078	37.8616192123 ± 0.0000000089
Parallax [mas]	0.137 ± 0.029	−0.145 ± 0.035
Proper motions (α^*) [mas yr^{-1}]	−2.123 ± 0.045	−3.833 ± 0.053
Proper motions (δ) [mas yr^{-1}]	−4.675 ± 0.051	−7.189 ± 0.053
G [mag]	14.25	14.15
G_{BP} [mag]	–	14.70
G_{RP} [mag]	–	13.04
ϵ [mas]	0.11	0.22
D	2.4	10.8
Distance [pc]	5585^{+1026}_{-772}	14737^{+3285}_{-2639}
2MASS all-sky data release		
Source name	2MASS J19202244+3751414	
α (J2000.0) [deg]	290.093536 ± 0.0075	
δ (J2000.0) [deg]	+37.861511 ± 0.0075	
J [mag]	11.503 ± 0.019	
H [mag]	10.759 ± 0.017	
K_s [mag]	10.629 ± 0.016	

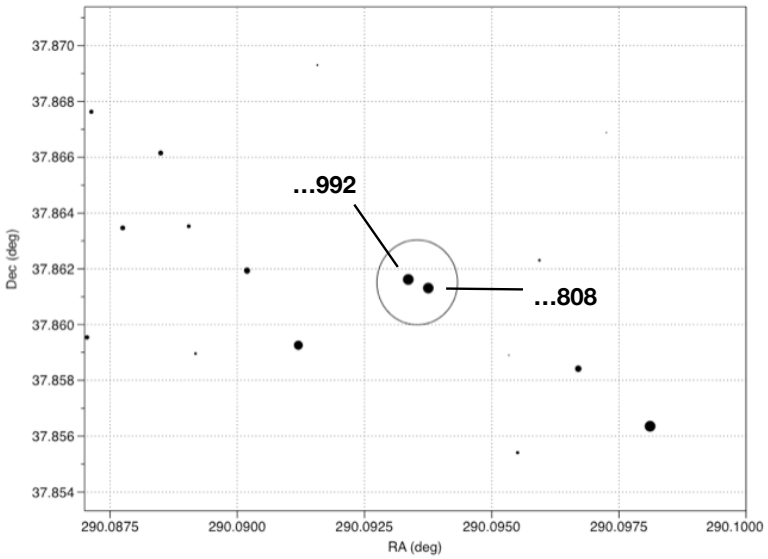

Figure 4.2: Position of the two stars in the *Gaia* view, with the numbers indicating the last three digits of their source names, as listed in Table 4.1.

At this moment no radial velocity data are provided by *Gaia* for our pair of stars.

4.4 Fourier spectrum analysis

The typical feature of a star showing solar-like oscillations is a well-defined power excess that is visible in the Fourier power density spectrum (PDS). For KIC 2568888 we observe excess power at $\sim 7\,\mu$Hz (star A) and $\sim 16\,\mu$Hz (star B), respectively, which can be attributed to two different red-giant stars. Through the analysis of individual oscillation modes we aim to get a picture of the interior structure of both stars.

4.4.1 The global background model

The oscillation modes are superimposed on a granulation background, which we need to define before studying the oscillations. We chose a model similar to the descriptions used by Kallinger et al. (2014), with the contribution of three granulation background components:

$$P_{\mathrm{bg}}(\nu) = n_{\mathrm{wh}} + \eta(\nu)^2 \left(\sum_{\mathrm{i}=1}^{3} \frac{A_{\mathrm{i}}}{1 + (\nu/b_{\mathrm{i}})^4} \right). \tag{4.1}$$

Here, n_{wh} represents the white noise. Each granulation component is defined by a Lorentzian-like function with a characteristic amplitude A_{i}, frequency b_{i}, and a fixed exponent of 4. The stellar granulation is further influenced by an attenuation η, which arises due to discrete time sampling of the flux measurements.

As a parameter estimation method we employed a Bayesian Markov Chain Monte Carlo (MCMC) framework with affine-invariant ensemble sampling, as implemented in the EM-

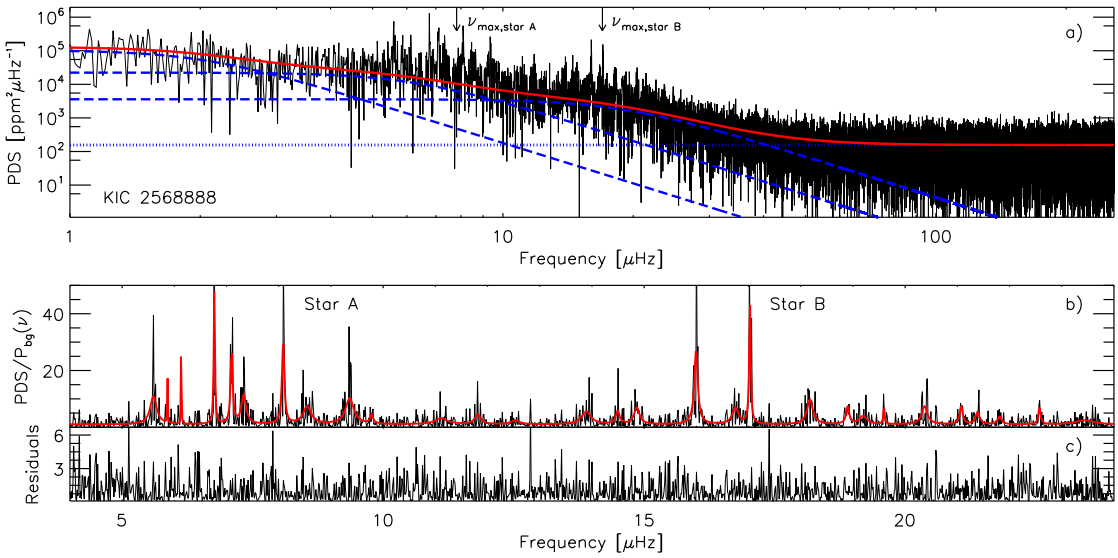

Figure 4.3: (a) Power density spectrum (PDS; in black) of KIC 2568888 showing three granulation components (blue dashed lines), one noise component (blue dotted line), and the global background fit (in red). The $\nu_{\max}$ values for stars A and B are indicated by arrows. (b) Background-normalized PDS covering the oscillation modes of the two red-giant stars with the final fit to the detected oscillation modes in red and the residuals in panel (c).

CEE[2] routine (Foreman-Mackey et al. 2013), to explore the parameter space of the granulation background components (eq. 4.1). After convergence, we used the MCMC chains to estimate the posterior probability density functions for each parameter. We adopted the medians of these distributions as an estimate of the expectation values for the parameters and their 16th and 84th percentiles as standard uncertainties. In panel (a) of Figure 4.3 we show the PDS of KIC 2568888 and the global background fit. The oscillation regions of the two red-giant stars are marginally overlapping at the edges. The parameter $\nu_{\max}$ represents the frequency of maximum oscillation power, which we define as the centre of the oscillation power envelope. In order to determine $\nu_{\max}$ for each red giant, we first corrected the PDS by the global background and then we fitted a model with two Gaussian functions to the normalized PDS. The global background parameters and $\nu_{\max}$ values are listed in Table 4.2. We further note that the amplitudes of the power excesses are on the lower edge of the empirical $\nu_{\max}$-amplitude relation (e.g. Huber et al. 2011, Kjeldsen and Bedding 2011, Stello et al. 2011, Mosser et al. 2012a). Although that does not provide decisive information about our pair of stars, it shows that the presence of two stars provides a 'diluted' light curve, which results in the observation of decreased amplitudes of the oscillations.

4.4.2 Oscillations

Another asteroseismic parameter of interest is the mean large frequency separation $\Delta\nu$, i.e. the frequency spacing between pressure (p) modes of the same spherical degree ℓ and

[2] EMCEE: The MCMC Hammer, http://dfm.io/emcee/

consecutive radial order n. Here, we used the continuous wavelet transform-based peak detection method developed by García Saravia Ortiz de Montellano et al. (2018) to search for all significant Lorentzian-like peaks in the background-normalized PDS. In the current analysis, we applied this automated peak detection algorithm with a signal-to-noise threshold of 1.5. As a measure of the statistical significance of each peak we compared the Akaike Information Criterion (AIC; Akaike 1998) of a PDS model including the peak and a model without it. The AIC difference between the two models is similar to a log-likelihood difference with a penalisation for the number of degrees of freedom. The model with a lower AIC value is preferred. For more details about the peak detection we refer the interested reader to García Saravia Ortiz de Montellano et al. (2018). In addition to the frequencies of the peaks, the algorithm provided initial values for their amplitudes and linewidths. Based on these estimates we used a maximum-likelihood method (MLE) to optimize all variable parameters simultaneously. From this final MLE fit we estimated the values for the frequencies, amplitudes, and linewidths of the oscillation modes, as well as their uncertainties, which we report in Table 4.4. We note that the mode amplitudes are given in units of the background-normalized power density spectrum. In panel (b) of Figure 4.3 we present the background-normalized PDS, including the model fit. The residuals in panel (c) show that only noise is left in the PDS after the fit. In the following, we assigned the spherical degree and the acoustic radial order to the set of detected frequencies by using the asymptotic relation (Tassoul 1980). For both stars in KIC 2568888 we detected several radial orders of $\ell = 0$, 1, and 2 modes and two $\ell = 3$ modes (Tab. 4.4) that are visible as vertical ridges in the échelle diagrams (Grec et al. 1983) in Figure 4.4. As a further note, no clear evidence of mixed modes was present in the power density spectrum. Therefore, no evolutionary stage determination based on period spacings was possible for either red-giant star (e.g. Mosser et al. 2011, Stello et al. 2013). A preliminary study by Themeßl et al. (2017) showed that about 50 % of red giants in detached eclipsing binaries show only p-dominated mixed modes compared to about 4 % of red giants not known to be in binary systems. This may hint at a binary scenario for KIC 2568888.

For each red giant, we computed the mean large frequency spacing $\Delta\nu$ from a linear fit through the set of four central $\ell = 0$ modes (marked with asterisks in Tab. 4.4 and with filled symbols in Fig. 4.4) that were unambiguously assigned to the respective star. According to the asymptotic relation for $\ell = 0$ modes, the slope parameter of each fit represents $\Delta\nu$ and the intercept is related to the phase term ϵ. We report the mean large frequency spacings for stars A and B in Table 4.2. In addition, we derived local values ($\Delta\nu_c$, ϵ_c) as these are proposed to provide information about the evolutionary stage of red giants (Kallinger et al. 2012). Based on $\Delta\nu_{c,\mathrm{star\,B}} = 2.168 \pm 0.021\,\mu$Hz and $\epsilon_{c,\mathrm{star\,B}} = 0.85 \pm 0.01$, star B is a red-giant branch (RGB) star. Star A is a more evolved red giant that may be in the asymptotic giant (AGB) phase of stellar evolution with measured $\Delta\nu_{c,\mathrm{star\,A}} = 1.202 \pm 0.012\,\mu$Hz and $\epsilon_{c,\mathrm{star\,A}} = 0.10 \pm 0.02$.

4.5 Determination of stellar parameters

We measured the global seismic parameters ($\nu_{\max}$ and $\Delta\nu$) to derive the stellar properties of stars A and B by using different asteroseismic methods. Here, we use the stellar parameters to investigate if the two red giants under study could potentially be physically

Table 4.2: Global background, and asteroseismic, and stellar parameters from scaling relations (sr) for both stars present in the light curve of KIC 2568888.

Parameter	Star A	Star B
$n_{\rm wh}$ [ppm$^2\mu$Hz^{-1}]	$156\ ^{+1}_{-1}$	
A_1 [ppm$^2\mu$Hz^{-1}]	$103\,617\ ^{+16\,732}_{-15\,981}$	
b_1 [μHz]	$2.0\ ^{+0.3}_{-0.2}$	
A_2 [ppm$^2\mu$Hz^{-1}]	$22\,301\ ^{+13\,405}_{-12\,446}$	
b_2 [μHz]	$6.2\ ^{+1.9}_{-2.6}$	
A_3 [ppm$^2\mu$Hz^{-1}]	$3\,590\ ^{+1\,684}_{-1\,235}$	
b_3 [μHz]	$18.8\ ^{+1.9}_{-1.7}$	
$\nu_{\rm max}$ [μHz]	7.82 ± 0.23	16.98 ± 0.41
$\Delta\nu$ [μHz]	1.210 ± 0.008	2.177 ± 0.011
Evolutionary state	AGB/RGB	RGB
$M_{\rm sr}$ [M$_\odot$]	1.36 ± 0.09	1.32 ± 0.09
$R_{\rm sr}$ [R$_\odot$]	25.11 ± 0.68	16.84 ± 0.45
$\bar{\rho}_{\rm sr}$ [$\bar{\rho}_\odot \times 10^{-3}$]	0.086 ± 0.002	0.277 ± 0.005
$\log g_{\rm sr}$ (cgs)	1.770 ± 0.008	2.107 ± 0.009

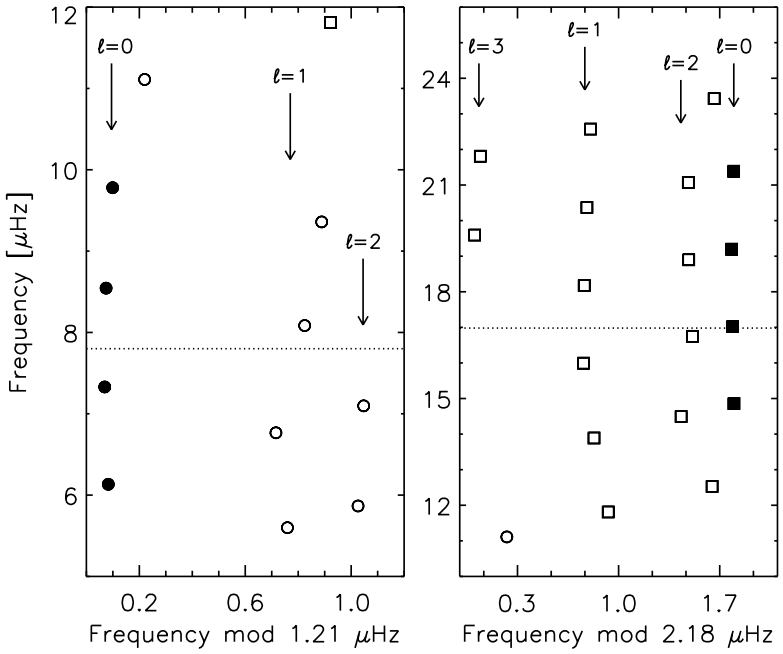

Figure 4.4: Échelle diagrams for stars A (left) and B (right) with extracted mode frequencies (A: circles; B: squares) that form vertical ridges corresponding to different spherical degrees ℓ. The filled symbols show frequencies that were used to determine $\Delta\nu$ and horizontal dotted lines represent $\nu_{\rm max}$ values.

Table 4.3: Stellar parameters from grid-based modelling (gbm) by using PARSEC isochrones for both stars. We note that for star A we also find a matching RGB model, which is less likely than the AGB model.

Parameter	Star A		Star B
$M_{\rm gbm}$ [$M_\odot$]	1.35 ± 0.20	1.37 ± 0.18	1.37 ± 0.21
$R_{\rm gbm}$ [$R_\odot$]	25.07 ± 1.26	25.20 ± 1.24	17.05 ± 1.01
$\bar{\rho}_{\rm gbm}$ [$\bar{\rho}_\odot \times 10^{-3}$]	0.086 ± 0.004	0.086 ± 0.004	0.277 ± 0.010
$\log g_{\rm gbm}$ (cgs)	1.770 ± 0.019	1.770 ± 0.019	2.112 ± 0.026
$\log(L/L_\odot)_{\rm gbm}$	2.30 ± 0.12	2.29 ± 0.10	1.99 ± 0.11
$T_{\rm eff,gbm}$ [K]	4324 ± 188	4301 ± 161	4419 ± 182
$\rm age_{gbm}$ [Gyr]	3.6 ± 1.5	3.2 ± 1.2	3.7 ± 1.7
Evolutionary state	AGB	RGB	RGB

bound in a binary system.

4.5.1 Asteroseismic scaling relations

One method to determine the stellar parameters of red giants is based on the asteroseismic scaling relations (SR; Ulrich 1986, Brown et al. 1991, Kjeldsen and Bedding 1995). These equations require reference values often taken from the Sun and thus it is implicitly assumed that the internal stellar structure is similar for all stars of different masses, metallicities, and evolutionary stages. From observations and theoretical predictions we know that this is not the case. Different studies have pointed out discrepancies in the derived asteroseismic stellar parameters of red-giant stars (e.g. Huber et al. 2010, Gaulme et al. 2016, Themeßl et al. 2018) even though several modifications to the scaling relations were proposed in order to improve the precision of these parameter estimates (e.g. White et al. 2011, Miglio et al. 2012, Hekker et al. 2013b, Mosser et al. 2013, Guggenberger et al. 2016, Sharma et al. 2016, Guggenberger et al. 2017, Rodrigues et al. 2017, Viani et al. 2017, Themeßl et al. 2018).

In the current study, we employ empirical reference values ($\nu_{\rm max,ref} = 3137 \pm 45\,\mu$Hz, $\Delta\nu_{\rm ref} = 130.8 \pm 0.9\,\mu$Hz) that were derived from a combined asteroseismic and binary analysis of three RGB stars (Themeßl et al. 2018). By using these reference values the metallicity, temperature, and mass dependence of stars, as well as surface effects, are incorporated in the SR. Based on the global seismic parameters, the spectroscopic effective temperature and metallicity from APOGEE spectra, and the empirical reference values, we computed the asteroseismic stellar parameters for both stars. We note that the formal uncertainties in the derived stellar parameters are larger due to our adopted uncertainty of ±200 K in temperature since we lack individual $T_{\rm eff}$ values for stars A and B. The stellar parameters are reported in Table 4.2.

4.5.2 Grid-based modelling

In addition to the determination of stellar parameters through SR, one can also use a precomputed grid of stellar isochrones to find the best-fit model to the observational data. For our grid-based modelling (GBM; Gai et al. 2011) approach we computed a

set of stellar isochrones with the PAdova and TRieste Stellar Evolution Code (PARSEC; Bressan et al. 2012). These isochrones extend from the lower main sequence up to the asymptotic giant branch for stars between $0.1\,M_\odot$ and $12\,M_\odot$ with ages ranging from ~ 4 Myr to 13.2 Gyr and metallicities in the range $0.0005 \leq Z \leq 0.07$ (corresponding to $-1.49 \leq [M/H] \leq +0.78$). For low-mass stars, mass loss due to stellar winds is incorporated during the RGB phase according to the empirical formula by Reimers (1975), with an efficiency factor of 0.2. We obtained this grid of stellar models through the CMD web interface at OAPD[3].

The stellar parameters were extracted from this grid using an independent implementation of the likelihood method described by Basu et al. (2010), where the likelihood of each model was computed from a given set of observed parameters. In this case, we used ν_{max} and $\Delta\nu$ from the asteroseismic analysis and atmospheric parameters (T_{eff}, [M/H]) provided by APOGEE to search for matching stellar models. For the computation of $\Delta\nu$ and ν_{max} for the models, we employed the scaling relations with the empirical reference values as stated in the previous section. Based on a Monte Carlo method, we obtained the stellar parameters and their uncertainties for each star from the centre and width of a Gaussian fit through the total likelihood distribution of 1 000 perturbations, which we report in Table 4.3. We note that the uncertainties of the GBM results are larger due to the lack of individual T_{eff} and [M/H] measurements for our pair of stars.

In addition to the individual ages of the two red-giant stars, the GBM approach provides an indication of which evolutionary state is favoured (Hekker et al. 2017). For star A we found two solutions in different evolutionary stages that matched the observations, a red-giant branch and a more evolved AGB model (Tab. 4.3). Based on our optimization method, we obtained a marginally higher statistical significance for the solution on the asymptotic giant branch. For both stars, we found the same evolutionary stages from stellar models and from the study of the local phase terms (Sec. 4.4.2). To check the results from PARSEC, we repeated the GBM analysis with stellar isochrones from the BaSTI[4] (Pietrinferni et al. 2004) code and obtained consistent results.

4.5.3 UniDAM

UniDAM (Mints and Hekker 2017, 2018) is a Bayesian isochrone fitting tool that can use different combinations of measured physical parameters (e.g. $R, T_{eff}, \log g$, [M/H]) as well as *Gaia* parallaxes as inputs to determine stellar masses, ages, and distances. We used this tool for a further test to constrain the age and the distance of each star independently by comparing our final R and $\log g$ values from SR (Tab. 4.2) together with the BVI photometry (Tab. 4.1) with PARSEC models (the same set of isochrones as described in Sec. 4.5.2). Since it is not known which photometric component corresponds to which asteroseismic signal (stars A and B), we employed both possible combinations of magnitudes with rather similar results. As a reference, we chose the result with the better fit to the photometry with a χ^2 probability close to 1. Based on this approach, we derived age estimates for both stars that were consistent with those derived from the asteroseismic analysis, while the apparent distance moduli turned out to be different with

[3] http://stev.oapd.inaf.it/cmd/
[4] http://albione.oa-teramo.inaf.it/

$\mu_{\rm d,A} = 14^m.63 \pm 0.12$ and $\mu_{\rm d,B} = 13^m.96 \pm 0.15$.

In Figure 4.5 we show the *Gaia* DR2 parallax probability distribution function (PDF) for the star with the positive *Gaia* parallax measurement and the parallax PDFs as derived by UniDAM from *BVI* photometry for both stars. From UniDAM, we computed a lower parallax value for star A and a higher parallax value for star B, while the positive *Gaia* parallax value lies in between, with its uncertainties covering the individual PDFs of both stars.

The discrepancies in the distance estimates is not surprising due to the fact that the apparent magnitudes are very similar, while we detected two power excesses with different $\nu_{\rm max}$ values and thus expect the two stars to have different radii (see Tab. 4.2 and 4.3). With similar effective temperatures, which can be assumed given the similar observed colors, different radii should lead to different absolute luminosities and thus absolute magnitudes. In our analysis, this difference is on the order of $0^m.65$ which can only partly be explained by the uncertainties in the models, the photometric calibration, and the extinction model that were used.

In addition, we can test if we find solutions for the two stars, assuming that they are in a binary system. In this case, we took as a constraint the combined apparent magnitude for KIC 2568888 from 2MASS (Tab. 4.1), where the pair of stars could not be spatially resolved. The combined magnitude should then match the predicted magnitudes from the best-fitting models for both stars. We selected a pair of models such that the following conditions are fulfilled: (1) metallicity and age (as computed from GBM) are the same within the uncertainties for both models; (2) R and $\log g$ are within the $4\,\sigma$ uncertainties from values derived from the asteroseismic analysis; and (3) *BVI* photometry for each model and combined *JHK* photometry match the observed values. Based on these criteria, we found solutions that give an age of ~ 3.4 Gyr, a metallicity of ~ -0.06 dex, and a distance modulus of $\sim 14^{\rm m}.4$ or ~ 7.5 kpc. We note, however, that the χ^2 probability for this model pair is rather low, on the order of 10^{-9}.

4.6 Discussion and conclusions

In the *Kepler* light curve of KIC 2568888 we detected the asteroseismic signals of two red giants. An asteroseismic analysis leads us to the following conclusions:

1. The similar ages ($\sim$ 3.6 and $\sim$ 3.7 Gyr) for stars A and B, and a mass ratio close to unity, support a possible binary scenario, where KIC 2568888 is comprised of either two RGB components or an RGB/AGB combination.

2. If KIC 2568888 is indeed an asteroseismic binary system, then this would be a very interesting and rare candidate binary according to Miglio et al. (2014), who pointed out that the detection of a binary system in this configuration is possible, yet not that common. According to their study, the overall probability of detecting two solar-like oscillating binaries in a single *Kepler* time series is of the order of 0.1 %.

3. If the derived ages of stars A and B are accurate, then it is unlikely that the two stars belong to the old ($\sim$ 8 Gyr) open cluster NGC 6791 (e.g. Martinez-Medina

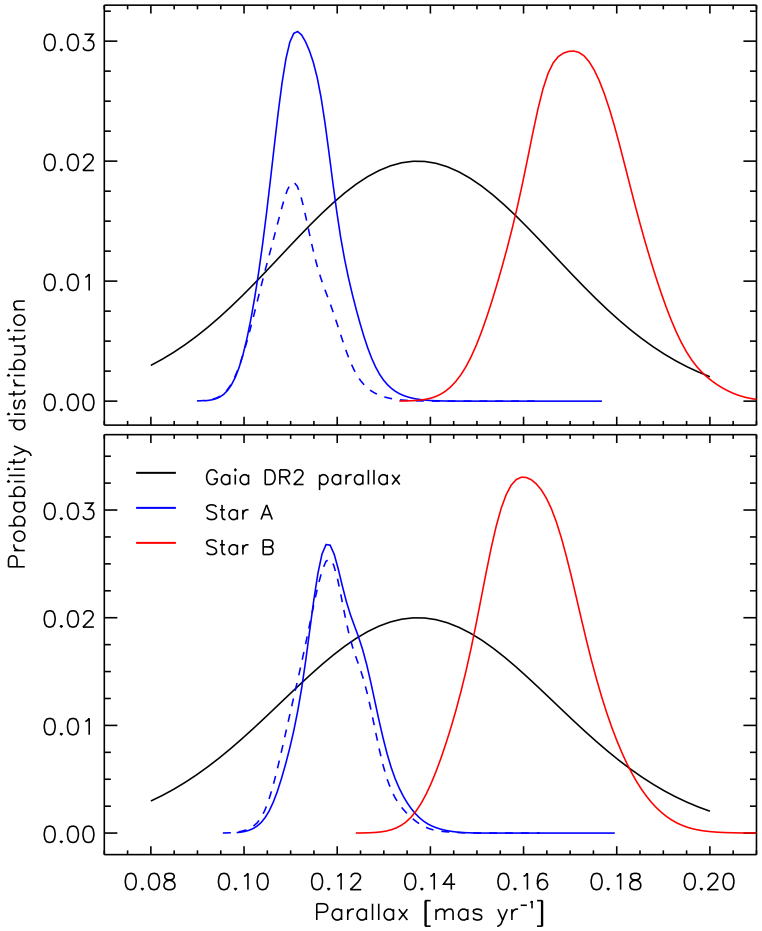

Figure 4.5: Parallax probability distribution functions (PDFs) for the observed parallax measurement for source 2051291674950663808 from *Gaia* DR2 (in black) and asteroseismic stars A (in blue) and B (in red) as derived from UniDAM (Sec. 4.5.3). For star A we show the PDFs for models in both evolutionary stages (RGB: solid, AGB: dashed). The upper and lower panels represent different combinations of asteroseismic R and $\log g$ values and ground-based *BVI* photometry, since we are not able to match the asteroseismic components with their photometric counterparts. In both cases the results are similar.

et al. 2018), as a member of which KIC 2568888 was proposed for observations. Moreover, the provided APOGEE radial velocity for the system (about $-58\,\mathrm{km\,s^{-1}}$) is not in line with either the radial velocity of the cluster ($-47.40 \pm 0.13\,\mathrm{km\,s^{-1}}$; Tofflemire et al. 2014) or published APOGEE radial velocities of known red-giant cluster members ranging from about −43 to about $-50\,\mathrm{km\,s^{-1}}$.

In addition, we computed distance estimates for the two stars that challenge a binary interpretation. From ground-based *BVI* photometry that we combined with the asteroseismic radii and logarithmic surface gravities, we obtained different distance moduli for both stars with $\mu_{\mathrm{d,A}} = 14^m.63 \pm 0.12$ and $\mu_{\mathrm{d,B}} = 13^m.96 \pm 0.15$, respectively. Comparing this with recently published *Gaia* data, we found a consistent distance estimate for the star with the positive *Gaia* parallax measurement, while for the other star a negative parallax is provided that results in a different distance measurement. Even though this distance may be correct, we do not consider it reliable due to the strong influence of the chosen prior in the Bayesian analysis, as well as the *Gaia* 'astrometric_excess_noise' flag, which indicates that the astrometric fitting of this source in particular was ambiguous. This leads us to the conclusion that:

1. If the discrepancy in the distances is true, then this could indicate that the pair of stars is not gravitationally bound and a chance alignment.

To calculate the probability (p_{chance}) of such a close pair happening as a chance alignment, we selected all stars in the observed region of NGC 6791 with $m_{\mathrm{B}} > 16^m.1$, which corresponds to the apparent magnitude of the fainter of the two components. We found 164 stars that are spread over 0.07 square degrees. The probability of having a chance companion for a star at an angular separation of $s \approx 1''.6 \approx 0^\circ.00044$, as derived from the coordinates of the two components of KIC 2568888, is given by $p_{\mathrm{chance}} = s^2\rho$, where ρ is the number density of stars on the sky. We have $\rho = 164/0.07 \approx 2\,300$ stars per square degree, thus we calculated p_{chance} to be 4.6×10^{-4} or about 0.05 %. This value marks the upper limit of the chance alignment probability, which would decrease further if we use a mass ratio close to 1 as an additional constraint for the pairs of stars that are considered in the calculation. We also note that we obtained a similar result when computing ρ from 2MASS stars in the same area. This brings us to the final conclusions that:

1. If the stars of KIC 2568888 are not components of a binary system, then it would be a very rare case of an optical double system. Based on the observed magnitudes, there is a $\sim 0.05\,\%$ chance that this is the case.

2. If the stellar radii of stars A and B are accurate and these stars are gravitationally bound, then there might be a third star to account for the excess flux. Additional radial velocity measurements from APOGEE and *Gaia* could potentially provide a test if either of the two stars is itself a binary. This would explain the visual magnitudes of the two observed oscillating red-giant stars, and thus the discrepancies in the distance estimates.

In any case, it will be interesting to see the *Gaia* end of mission products for this pair of stars. With a more complete set of astrometric and photometric parameters at hand, e.g. reliable proper motions and parallaxes for each component, the *Gaia* final data release

may provide the only possibility of solving this issue in the near future. Since binarity will be taken into account in the prospective *Gaia* data analysis, we propose KIC 2568888 as a strong candidate for further binary investigation.

4.7 Appendix: List of detected frequencies for KIC 2568888

We provide a list of extracted frequencies of oscillation modes, and their amplitudes, and linewidths in Table 4.4.

Table 4.4: Extracted frequencies, amplitudes, and linewidths of modes that were fitted with Lorentzian (resolved peaks) or sinc functions (unresolved peaks). In the latter case, the linewidth is not given. Modes marked with asterisks were used to determine $\Delta\nu$ (Sec. 4.4.2). We indicate more than one spherical degree ℓ and radial order n in cases where two modes are overlapping such that they could not be fitted individually.

Star	n	ℓ	Frequency [μHz]	Amplitude [a.u.]	Linewidth [μHz]	AIC
A	5	1	5.60 ± 0.02	1.53 ± 0.23	0.08 ± 0.06	158.56
	5	2	5.87 ± 0.01	0.99 ± 0.48	-	6.09
	6	0*	6.13 ± 0.01	1.30 ± 0.53	-	22.66
	6	1	6.77 ± 0.01	1.43 ± 0.31	0.01 ± 0.01	162.13
	6	2	7.10 ± 0.01	1.39 ± 0.25	0.02 ± 0.02	90.58
	7	0*	7.33 ± 0.02	1.31 ± 0.20	0.05 ± 0.03	78.16
	7	1	8.08 ± 0.01	1.59 ± 0.25	0.03 ± 0.02	162.95
	8	0*	8.54 ± 0.03	1.35 ± 0.16	0.09 ± 0.04	75.73
	8	1/2	9.36 ± 0.02	1.65 ± 0.17	0.10 ± 0.03	156.83
	9	0*	9.78 ± 0.03	0.57 ± 0.20	0.03 ± 0.03	10.14
	9/10	2/0	11.11 ± 0.06	0.97 ± 0.17	0.15 ± 0.08	22.81
B	5	1	11.81 ± 0.03	0.86 ± 0.15	0.07 ± 0.05	21.16
	5/6	2/0	12.53 ± 0.06	0.63 ± 0.18	0.09 ± 0.07	2.71
	6	1	13.89 ± 0.03	1.24 ± 0.15	0.11 ± 0.05	71.53
	6	2	14.49 ± 0.02	0.79 ± 0.16	0.04 ± 0.03	15.35
	7	0*	14.86 ± 0.02	1.07 ± 0.16	0.06 ± 0.03	51.34
	7	1	15.99 ± 0.01	1.83 ± 0.23	0.04 ± 0.02	281.66
	7	2	16.75 ± 0.03	1.13 ± 0.17	0.07 ± 0.03	50.88
	8	0*	17.03 ± 0.01	1.55 ± 0.29	0.02 ± 0.01	157.77
	8	1	18.18 ± 0.02	1.37 ± 0.16	0.07 ± 0.02	118.12
	8	2	18.90 ± 0.02	0.83 ± 0.16	0.04 ± 0.02	21.82
	9	0*	19.20 ± 0.04	0.89 ± 0.15	0.09 ± 0.04	22.34
	8	3	19.59 ± 0.01	0.52 ± 0.17	0.01 ± 0.01	9.87
	9	1	20.37 ± 0.02	1.15 ± 0.15	0.07 ± 0.03	74.80
	9	2	21.07 ± 0.02	0.83 ± 0.15	0.03 ± 0.02	29.84
	10	0*	21.39 ± 0.02	0.78 ± 0.15	0.05 ± 0.03	21.51
	9	3	21.81 ± 0.03	0.61 ± 0.15	0.04 ± 0.03	8.16
	10	1	22.57 ± 0.01	0.70 ± 0.16	0.03 ± 0.02	20.60
	10/11	2/0	23.43 ± 0.09	0.98 ± 0.14	0.21 ± 0.08	24.70

5 Discussion and future prospects

Stars are the building blocks of the universe. By studying stars with a wide range of stellar properties and stars in different stages of stellar evolution one can explore the past, present, and future of the universe. The astrophysical potential of stars is very large due to the great number and diversity of stellar objects that have been discovered, analyzed, and modelled so far. This thesis shows that asteroseismology is a powerful analysis method for the study of oscillating stars with the ability to derive reliable stellar parameters for red giants in eclipsing binary systems and open clusters. Due to stringent constraints on age, chemical composition, and distance, stars in these associations are ideal candidates for validating asteroseismic methods and for testing the accuracy of the asteroseismic results. The scientific breakthroughs in red-giant asteroseismology have been facilitated by the unprecedented quality and quantity of photometric data that were provided by space-borne missions over the past $\sim$ 15 years. Further advances in data analysis techniques have led to a new era of the interpretation of asteroseismic signals. The analysis of 4 years of *Kepler* data showed that it is possible to derive accurate asteroseismic stellar parameters for red-giant stars in eclipsing binary systems and open clusters. To achieve this, additional knowledge about the effective temperature and the metallicity of the stars is important, since these parameters provide useful constraints for asteroseismic analysis methods. In the larger context, obtaining accurate stellar parameter estimates does not only play a crucial role for stellar studies. It is also contributing to the understanding of extra-solar planetary systems, in which case the accuracy of planet parameters depends on the proper characterization of their host stars. Another powerful application of asteroseismology is Galactic archaeology, which focuses on studying the structure and evolution of our own Galaxy, the Milky Way, including its formation history and chemical evolution.

5.1 Importance for current and future space missions

Testing the accuracy of stellar parameters determined through asteroseismology is of importance because of the wealth of data that is already available and will become available in the (near) future. The recently launched *Transiting Exoplanet Survey Satellite* (TESS) and the upcoming *Planetary Transits and Oscillations of stars* (PLATO 2.0) mission are referred to as legacy missions for stellar and galactic physics. They will monitor an unprecedented number of stars, which will increase the field of asteroseismology even more. Major breakthroughs are expected in terms of asteroseismic characterization of stellar ensembles including the detection of a significant number of binary systems. Along with distances, effective temperatures, and absolute luminosities provided by *Gaia* (e.g. Gaia Collaboration et al. 2016b, 2018), the analysis of the new data will provide a unique

database for Galactic structure studies, which will comprise accurate stellar parameters, including ages, for an unprecedented number of stars of various masses and chemical compositions in many galactic directions.

The Transiting Exoplanet Survey Satellite (TESS) was launched on April 18th, 2018 for its 2-year prime mission and started its science operation on July 25th, 2018. TESS aims at searching for exoplanets outside of our solar system that may support life. One of the key features of the mission is that it is a near all-sky survey, which will monitor the brightest ($\sim 4-13$ mag) nearby stars in different directions of the Galaxy. TESS will provide 2 min cadence observations for $\sim$ 200 000 – 400 000 selected stars and 30 min cadence observations for all objects in the fields of view adding up to $\sim$ 423 000 000 observed stars as reported in the TESS input catalogue (Stassun et al. 2018). The photometric precision of the brightness measurements will be very suitable for asteroseismic studies of red giants. Depending on the location of the target on the sky, continuous observations will be taken for 27 (around ecliptic equator), 70, and 351 (around ecliptic poles) days with the frequency resolution of the measurements increasing with longer observation periods. TESS will be very important for investigating the history of the Milky Way by providing reliable estimates of the stellar mass, age, radius, and thus distance, for many thousands of stars at different distances in many galactic directions. More information about the mission design and the science program can be found in Ricker et al. (2016) and references therein.

The PLAnetary Transits and Oscillations of stars (PLATO 2.0) mission is targeted for launch in $\sim$ 2026 with a nominal science operation of 6 years. PLATO will be dedicated to detecting and characterizing terrestrial planets in the habitable zone in extra-solar planetary systems around bright ($\sim 4-16$ mag) solar-type stars. The mission will provide observations for about 1 000 000 stars in different galactic directions covering about 50 % of the sky with a cadence of 25 and 2.5 seconds. The planned observing strategy will comprise two long continuous pointings (first one with 2 – 3 years and second one with 2 years) and a 'step-and-stare' phase of different fields (1 – 2 years in total with observations between 2 to 5 months). The former is useful for exploring small planets out to the habitable zone, while the latter is useful for the detection of planets with shorter periods. The primary aim of the mission is to determine precise planetary radii with $\sim$ 3 % accuracy as well as planetary masses with $\sim$ 10 % accuracy by using complementary spectroscopic ground-based follow-up observations. Asteroseismology is also among the core science of PLATO. To support the exoplanet science, asteroseismology is expected to provide stellar masses, radii, and ages for about 85 000 stars with an accuracy of better than 10 %, 1-2 %, and 10 %, respectively. Thus, PLATO will provide ages for many planetary systems through asteroseismology. Since planet formation occurs on short time scales, the age of the exoplanet and the host star can be assumed to be similar. More about the PLATO 2.0 mission is provided by Rauer et al. (2016) and references therein.

5.2 Additional aspects of asteroseismic stellar parameter determination

For the study of oscillating red-giant stars in eclipsing binary systems and open clusters I used powerful asteroseismic diagnostics to derive their stellar parameters. In the following, I will discuss some further aspects that play an important role for the asteroseismic parameter determination and I will point out future science prospects with regard to each topic.

5.2.1 Presence of mixed modes in red giants in binaries

For the three red-giant stars in eclipsing binary systems (Chapter 2) we found that the g-dominated mixed modes are not pronounced (see Sec. 1.2.4). These modes are key to understanding the physical conditions in the stellar core and are thus important for the determination of the evolutionary state of red-giant stars. To investigate if the presence of only p-dominated mixed modes is specific for binary systems, we compared the fraction of stars with only p-dominated mixed modes in binaries and in a larger set of stars from the APOKASC sample. The work presented in this Section was originally published in Themeßl et al. (2017).

For a sample of 18 confirmed red giants in binary or triple-star systems (Gaulme et al. 2013, Beck et al. 2014, Gaulme et al. 2014, 2016), we used the unweighted power density spectra of the corrected and concatenated time series based on *Kepler* long-cadence observations provided by KASOC (Handberg and Lund 2014). In addition, we used the corrected light curves for 6 604 red giants from the APOKASC (Pinsonneault et al. 2014) sample that are available as a data bundle. For those APOKASC stars that could not be classified by Elsworth et al. (2017), we performed a visual inspection of the dipole $\ell = 1$ modes in the oscillation region around the frequency of maximum oscillation power in the range $\nu_{\max} \pm 2.5\,\Delta\nu$. Each dipole mode comprises a central most p-dominated mode and several mixed modes that have a more g-dominated character. Based on the computed power density spectra we classified the red giants into three different classes: (a) stars where g-dominated mixed modes are clearly present, (b) stars that show only p-dominated dipole modes, and (c) stars exhibiting non-radial mode suppression. An example of the three categories is shown in Figure 5.1. For 284 APOKASC stars a categorization was not possible due to either very low signal-to-noise spectra, oscillation regions that were too close to the Nyquist frequency or the absence of solar-like oscillations. In Table 5.1 we present the results with the percentage of red giants according to the three different types that we defined.

About 50 % of the red giants in known detached binary systems show mainly p-dominated dipole modes compared to about 4 % in the larger APOKASC sample. This could indicate that this phenomenon is tightly related to binarity and that the binary fraction in the APOKASC sample is about 8 %. For the latter case, Elsworth et al. (2017) detected distinct mixed modes in a large fraction of these stars, while we inspected the remaining 4 % to either have suppressed or only p-dominated dipole modes. The fraction of stars that show suppressed dipole modes is of the same order of magnitude for both samples. As we used a statistically insignificant number of known binaries, we were not able to

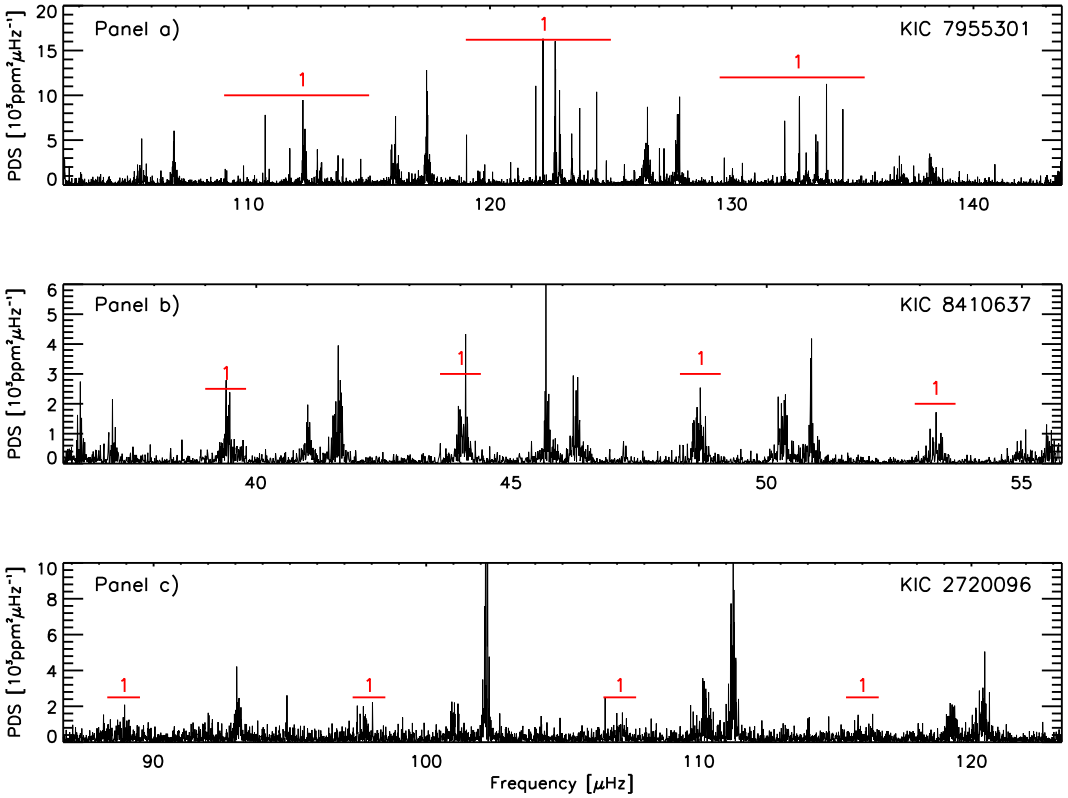

Figure 5.1: The frequency range of oscillations around the frequency of maximum oscillation power. Panel a) shows KIC 7955301 which exhibits clear mixed modes. Panel b) shows KIC 8410637 where only the p-dominated non-radial modes are distinct. Panel c) shows KIC 2720096, a red-giant star with suppressed dipole modes. This Figure was originally published in Themeßl et al. (2017).

Table 5.1: The percentage of stars in the different categories. This Table was originally published in Themeßl et al. (2017).

	Number of stars	Mixed modes	P-dominated modes	Suppressed modes	Unidentified
Binaries	18	~ 39 %	~ 50 %	~ 11 %	0 %
APOKASC	6 604	~ 85 %	~ 4 %	~ 7 %	~ 4 %

draw any firm conclusions from this. We could however speculate that the binary nature does not seem to be the cause for mode suppression. Yet, binarity appears to have some influence on the g-dominated mixed modes. If we take this one step further, saying that the presence of mainly p-dominated mixed modes only appears in about half the binaries, this would mean that the binary fraction in the APOKASC sample would be ~ 8 %.

Future prospects: To further investigate the presence of g-dominated mixed modes of red-giant components in multiple star systems, it is necessary to extend the stellar sample size. Only about two dozens of systems could be detected based on *Kepler* data. Long

and continuous photometric observations are required for mixed modes to be resolved in the Fourier power density spectrum. These requirements can be achieved by TESS, in particular for targets that are located in the continuous viewing zone, as well as by the upcoming PLATO mission. They are both expected to detect many more binary and multiple star systems that contain oscillating components.

5.2.2 Expected oscillation parameters from dynamical masses and radii

Chapter 2 was dedicated to the determination of stellar parameters of red-giant components in eclipsing binary systems. Based on the measured oscillation features ($\nu_{\rm max}$ and $\Delta\nu$) and effective temperatures, their masses and radii could be determined by using the well-known asteroseismic scaling relations (Brown et al. 1991, Kjeldsen and Bedding 1995) that were introduced in Section 1.3.8.

In a pilot study originally published in Themeßl and Hekker (2017), we performed a test to predict the oscillation parameters for a sample of known double-lined spectroscopic binaries with red-giant components (Gaulme et al. 2016, Themeßl et al. 2018). For these binary systems, dynamical masses and radii were measured from binary analyses using Kepler's laws. We used these measurements together with effective temperatures in equations 1.24 and 1.26 to compute the oscillation parameters of a sample of 11 stars. For the calculations we varied the solar reference values in the ranges $134.9 \leq \Delta\nu_{\odot} \leq 135.2\ \mu$Hz and $3025 \leq \nu_{\rm max,\odot} \leq 3175\ \mu$Hz, with step sizes of 0.1 μHz and 25 μHz, respectively. Based on this approach, we derived a set of $\Delta\nu$ and $\nu_{\rm max}$ values for each star. Figure 5.2 shows how $\nu_{\rm max}$ varies for one of the red-giant stars under study. The ratios between the oscillation parameters determined from the scaling relations and those directly measured from the asteroseismic signal are shown in the left panel of Figure 5.3. We found that the predicted $\nu_{\rm max}$ ($\Delta\nu$) values are lower (higher) than the asteroseismically determined values, with a clear correlation. The right panel of Figure 5.3 shows the $\Delta\nu$ ratio as a function of temperature with the metallicity colour-coded. By using only 11 red-giant stars we did not recover the trend in effective temperature and global metallicity that was found in stellar models (Guggenberger et al. 2016).

In this study, we showed that the use of the solar reference values in the asteroseismic scaling relations introduces biases in the mass and radius estimates of red-giant stars. We found that the $\Delta\nu$ and $\nu_{\rm max}$ scaling relations both add to the observed discrepancies between the dynamical and asteroseismic masses and radii, when the Sun is used as the reference star. This issue can be solved by using a corrected reference value as shown by the work presented in Chapter 2.

Future prospects: A study that can probe the applicability of the asteroseismic scaling relations and find possible corrections to the reference values requires a larger sample of binary star systems with oscillating red-giant components. The stars should cover a wide range of stellar parameters and different evolutionary stages. With *Kepler* data, only 11 systems were reported so far, where the global oscillation parameters and dynamical masses and radii were derived with sufficient precision in order to perform this study. The TESS and PLATO missions are expected to increase the sample size of known red-

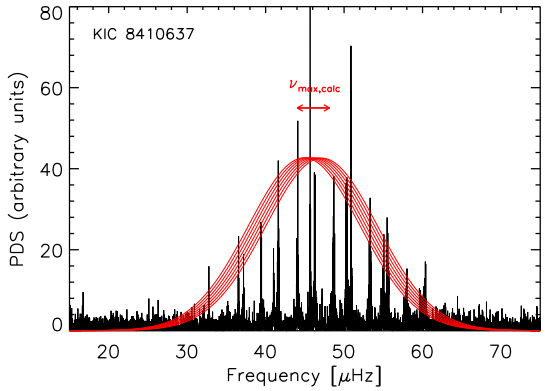

Figure 5.2: Power density spectrum (in black) of KIC 8410637 centred around ν_{max}. The range of predicted ν_{max} ($\nu_{max,calc}$) values for this red giant is indicated by the red arrow. The corresponding Gaussian fits (multiplied by a factor for visual purposes) are shown in red. No inconsistencies between the predicted and measured values for ν_{max} are apparent. This Figure and caption were originally published in Themeßl and Hekker (2017).

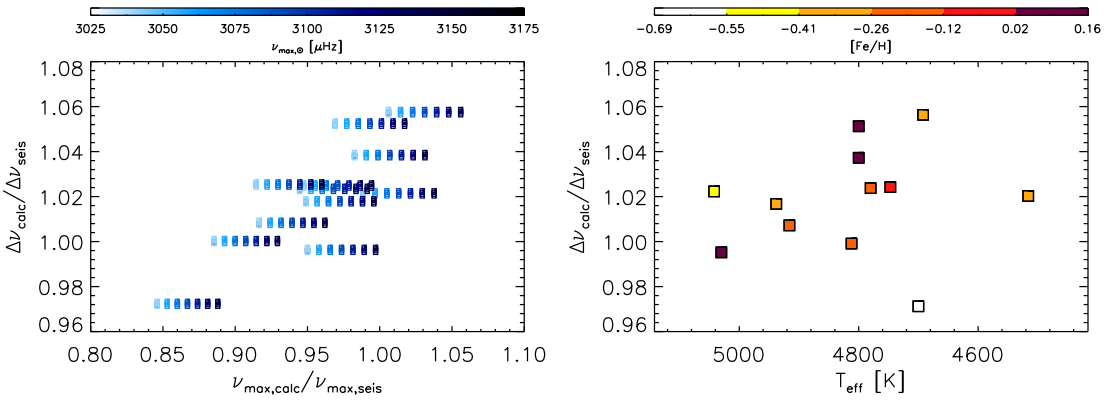

Figure 5.3: The ratio of predicted $\Delta\nu$ ($\Delta\nu_{calc}$) to the seismically determined $\Delta\nu$ ($\Delta\nu_{seis}$) as a function of the ratio of predicted ν_{max} ($\nu_{max,calc}$) over observed ν_{max} ($\nu_{max,seis}$), left, and as a function of effective temperature T_{eff}, right. The left panel shows all results for the different solar values (see colourbar) and the right panel shows results using a single solar value ($\Delta\nu_{\odot}$ = 135.1 μHz) with the points colour-coded for metallicity (see colourbar). This Figure and caption were originally published in Themeßl and Hekker (2017).

giant components in binary systems in the future. The analysis of their data will then provide observables with the level of accuracy that is required to compare asteroseismic and dynamical stellar parameters for a statistically significant number of red-giant stars.

5.2.3 Surface effects on the red-giant branch

For the three red-giant branch stars in double-lined eclipsing binaries (Chapter 2) several orders of $\ell = 0, 1$, and 2 modes could be extracted. We used the observed oscillation frequencies to study the magnitude of the surface effect in these evolved stars, which was published in Ball et al. (2018).

Fitting stellar models to observed oscillation frequencies is a challenging task partly because of the influence of the surface effect (see Sec. 1.3.8 for an introduction). This effect causes a systematic frequency difference between modelled and observed frequencies, and needs to be accounted for. So far, corrections of the surface effect were developed and tested for main-sequence and subgiant stars. We extended this work to more evolved stars to probe if the same formulations hold for red giants.

The observed frequencies of the red-giant branch stars under study contained one mode per acoustic radial order and per angular degree without the presence of g-dominated mixed modes. Thus in our approach, we suppressed g modes in the core in order for the stellar model to comprise pure p modes. In addition, for all non-radial modes that have a mixed character, we only considered the most p-dominated modes. As initial input parameters for stellar modelling, we used the effective temperature, the surface metallicity, and the individual mode frequencies of the three stars, which were determined by Themeßl et al. (2018) (see Chapter 2). The stars coincidently fall all at roughly the red giant bump. For each star, we searched for the best-fitting models before and after the red-giant branch bump by applying once the one-term (cubic) surface correction and then the two-term surface correction, which were both proposed by Ball and Gizon (2014). Besides the fiducial fit, the model-fitting procedure was carried out using the dynamical masses and radii of the stars as further constraints for the models and by fixing the mixing-length parameter to a solar-calibrated value of 1.66. Each model fit provided a set of derived parameters for each star including mass, initial helium abundance, initial metallicity, mixing length parameter, age, and surface term coefficients.

For most choices of initial model parameters we found equally good models before and after the red-giant branch bump. For KIC 8410637 and KIC 9540226 the pre- and post-bump models were of the same quality, which is not surprising, since stars before and after the bump have similar p-mode spectra, surface gravities, and mean densities. In addition, with our approach we lack any information of the g modes and thus the core of the stars. In the case of KIC 5640750 the post-bump model seemed to fit the data better, which could be an indication that this star has evolved past the red-giant branch bump.

The scale of the surface corrections was consistent for all the models before and after the red-giant branch bump that used the one-term (cubic) fit and also similar to predictions reported by Sonoi et al. (2015). The two-term (combined) fit provided a larger surface correction for all three stars. The scale was the same for the pre- and post-bump models for the two stars, while for the one star with the preferred post-bump model the scale dif-

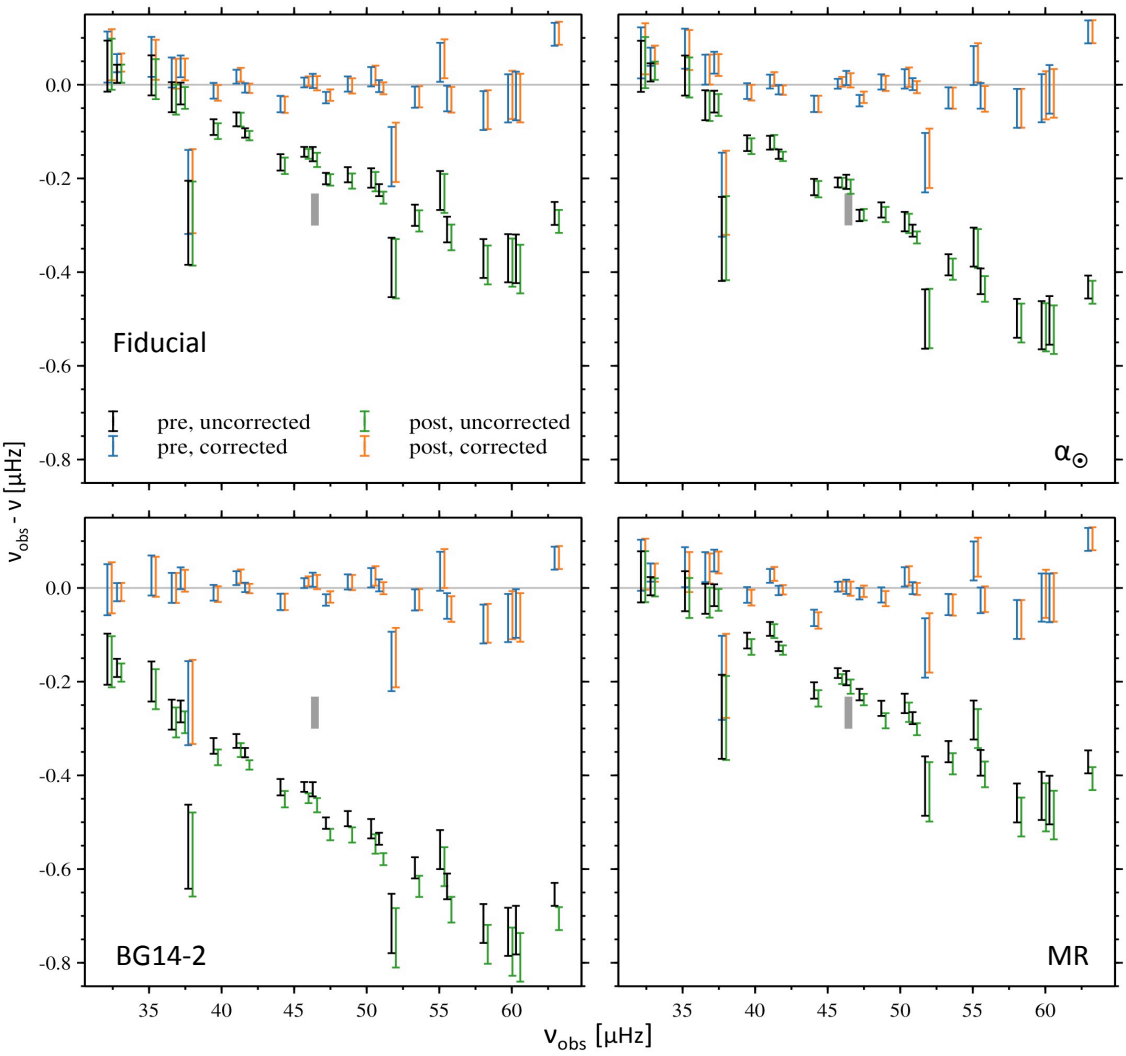

Figure 5.4: Frequency differences before and after applying a surface correction as a function of observed frequency for best-fitting models of KIC 8410637. The four panels are for the fiducial fit (top left), the fit with solar-calibrated mixing-length (top right), the fit using the two-term surface correction (bottom left), and the fit using the orbital mass and radius as observable constraints (bottom right). For each fit, we have plotted the frequency difference before (uncorrected) and after correction (corrected) for both the pre- and post-RGB bump models. The post-RGB bump frequencies are shifted right by 0.3 μHz for clarity. The solid grey bars indicate the surface correction predicted by eq. (10) of Sonoi et al. (2015). The error bars represent the observed uncertainties. This Figure and caption were originally published in Ball et al. (2018).

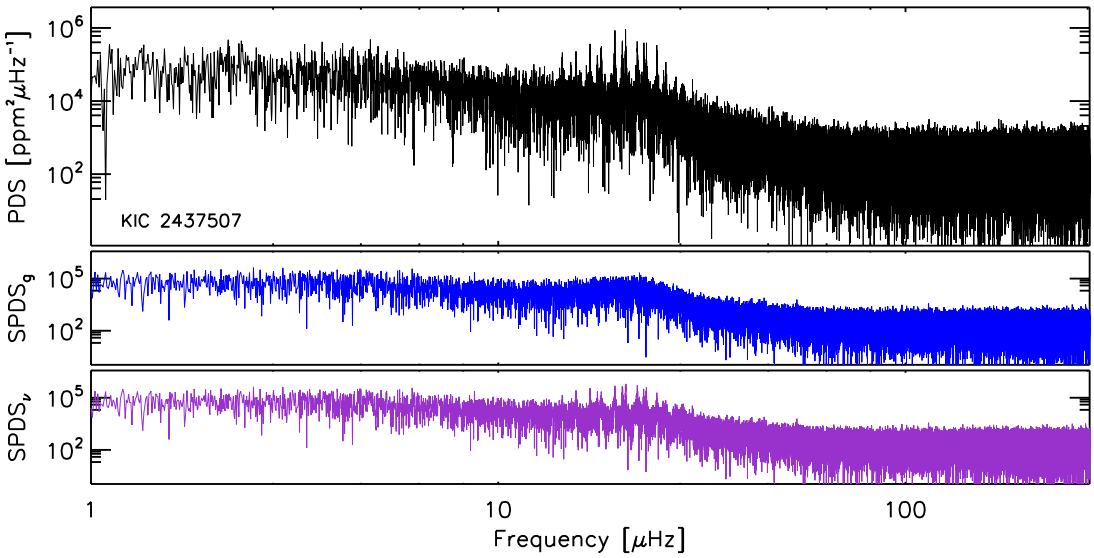

Figure 5.5: Top: Fourier power density of the red-giant star KIC 2437507. Middle: Simulated power density spectrum by using a Gaussian fit (eq. 1.11) to approximate the power excess. Bottom: Simulated power density spectrum based on the results from fitting of individual oscillation peaks (eq. 1.19).

fered.

For all three red-giant branch stars, the inferred masses and radii from the best-fitting stellar models were more massive and larger than the dynamical masses and radii derived from the binary analysis, when the models were not constrained and when the mixing-length parameter was fixed to the solar-calibrated value. The discrepancy was about 15 and 5 % in mass and radius, which is of the same order as reported by Gaulme et al. (2016) and Themeßl et al. (2018) in cases where the asteroseismic scaling relations were not corrected for the mass, effective temperature, metallicity dependence, and the surface effect of the stars. For KIC 8410637, KIC 5640226, and KIC 9540750 the modelled frequencies showed a decrease of $\sim 0.1 - 0.3\ \mu$Hz around the frequency of maximum oscillation power due to the surface effect. Figure 5.4 shows the differences between observed and modelled frequencies for one of the red giants under study before and after the surface effect was corrected. This study shows that the surface effect for p modes in red-giant branch stars is of the same order of magnitude as in main-sequence and subgiant stars and that the same formulations can be used to describe it.

Future prospects: The red-giant branch stars investigated here cover a very narrow range in stellar evolution close to the RGB bump. For further investigations of the scale of the surface effect this study should be extended to other parts of the RGB (e.g. above the bump) as well as more evolved clump stars. To perform this analysis a set of individual frequencies must be available for the stars, which requires dedicated peakbagging efforts. An additional challenge is the increasing number of mixed modes that are detectable for more evolved stars. This makes the comparison between observed and modelled frequencies even more challenging.

5.2.4 Definition of the typical frequency of the oscillations

Accurate estimates of the global oscillation parameters are important for the determination of asteroseismic masses and radii of red-giant stars. While the large frequency separation $\Delta\nu$ represents the frequency difference between p modes of the same spherical degree ℓ and consecutive radial order n, there is no distinct definition for the frequency of maximum oscillation power $\nu_{\rm max}$. The latter is commonly measured as the centre of a Gaussian fit to the power excess, the peak of the power excess in the smoothed Fourier power spectrum, or the first moment of the area under the smoothed power envelope (see Hekker and Christensen-Dalsgaard 2017, and references therein). Comparisons between $\nu_{\rm max}$ values derived from these slightly different methods showed that the spread in the results is of the order of a few per cent by using 4 months (Hekker et al. 2011a) and 7 months (Verner et al. 2011) of *Kepler* data. However, with 4-years worth of *Kepler* observations, the oscillation parameters can be determined more precisely and thus it is important to investigate the influence of different $\nu_{\rm max}$ estimates on the asteroseismic stellar parameter determinations.

The basis of this study are simulated Fourier power density spectra of oscillating red-giant stars, which were generated by using the global background fitting results for the cluster giants that were analyzed in Chapter 3. Each global model fit comprised three granulation background components, one white noise component and a Gaussian fit to approximate the oscillation power excess. Following the formulations presented by Gizon and Solanki (2003), the theoretical power density spectra $P_{\rm sim}(\nu)$ can be calculated according to:

$$P_{\rm sim}(\nu) = -\ln(U_{\rm j}) \times P_{\rm PDS}(\nu). \tag{5.1}$$

Here, $U_{\rm j}$ represents a uniform distribution in the interval [0,1] and $P_{\rm PDS}(\nu)$ is the global model fit (eq. 1.9) that can be used for fitting the red-giant Fourier power density spectrum. Red-giant stars in the sample under study oscillate in a broad range of frequency covering a range of stellar properties and two distinct metallicities. For this sample, two different sets of theoretical power density spectra were created. The first one used the global model with the Gaussian parameters as input values (eq. 1.9), while the second one substituted the Gaussian fit $P_{\rm gauss}(\nu)$ with the peakbagging parameters $P_{\rm peaks}(\nu)$ described by equation 1.19. Figure 5.5 shows the observed Fourier power density spectrum (top panel) of a red-giant star together with the simulated power density spectrum based on the Gaussian fit (middle panel) and by using the peak-bagged frequencies (bottom panel). Additionally, for each model star the theoretical power density spectra were produced for varying slope parameters (c) of the granulation background components in the range $3.5 \leq c \leq 4.5$ with a step size of 0.1 (see eq. 1.10). This slope parameter defines the curvature of the granulation background component and thus can influence the determination of $\nu_{\rm max}$.

In the next step, the global model (eq. 1.9 with $c = 4$) was fitted to the theoretical power density spectra in order to recover $\nu_{\rm max,sim}$ for the sample of modelled red-giant stars. During the fitting process, the frequency data points were arranged in a total number of 300 bins in order to reduce the computation time for the background fitting, which was described in Chapter 3. The derived $\nu_{\rm max,sim}$ values are shown in Figure 5.6. While for many stars the spread is of the order of a few per cents, there are some red giants that show a

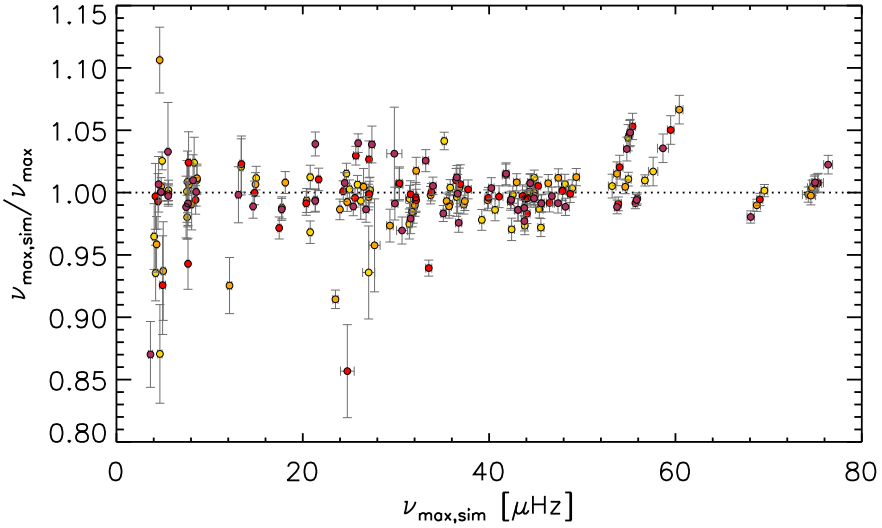

Figure 5.6: Ratio between simulated $\nu_{\mathrm{max,sim}}$ and observed ν_{max} as a function of $\nu_{\mathrm{max,sim}}$. Different colours represent different slope parameters that were used for describing the granulation background components.

difference of up to about 15 % in $\nu_{\mathrm{max,sim}}$. The latter case will lead to large discrepancies in the stellar mass and radius estimates based on the asteroseismic scaling relations and from grid-based modelling.

Future prospects: A next step is to use a larger sample of red giants with a wider range of stellar properties than the $\sim$ 60 model stars with two distinct metallicities that are currently used. A suitable stellar ensemble would be the APOKASC sample, which contains about 6 660 red-giant stars. With a larger number of model stars, influences on the ν_{max} determinations due to potential differences in the slope parameters in the observations and fitting, as well as different binnings that are applied during the fitting procedures can be investigated.

Bibliography

Abolfathi, B., Aguado, D. S., Aguilar, G., Allende Prieto, C., Almeida, A., Tasnim Ananna, T., Anders, F., Anderson, S. F., Andrews, B. H., Anguiano, B., and et al.: 2018, *ApJS* **235**, 42

Aerts, C., Christensen-Dalsgaard, J., and Kurtz, D. W.: 2010, *Asteroseismology*

Ak, T., Bostancı, Z. F., Yontan, T., Bilir, S., Güver, T., Ak, S., Ürgüp, H., and Paunzen, E.: 2016, *Ap&SS* **361**, 126

Akaike, H.: 1998, *Information Theory and an Extension of the Maximum Likelihood Principle*, pp 199–213, Springer New York, New York, NY

An, D., Terndrup, D. M., Pinsonneault, M. H., and Lee, J.-W.: 2015, *ApJ* **811**, 46

Anderson, E. R., Duvall, Jr., T. L., and Jefferies, S. M.: 1990, *ApJ* **364**, 699

Appourchaux, T.: 2003, *A&A* **412**, 903

Appourchaux, T., Antia, H. M., Ball, W., Creevey, O., Lebreton, Y., Verma, K., Vorontsov, S., Campante, T. L., Davies, G. R., Gaulme, P., Régulo, C., Horch, E., Howell, S., Everett, M., Ciardi, D., Fossati, L., Miglio, A., Montalbán, J., Chaplin, W. J., García, R. A., and Gizon, L.: 2015, *A&A* **582**, A25

Baglin, A., Auvergne, M., Barge, P., Deleuil, M., Catala, C., Michel, E., Weiss, W., and COROT Team: 2006, in M. Fridlund, A. Baglin, J. Lochard, and L. Conroy (eds.), *The CoRoT Mission Pre-Launch Status - Stellar Seismology and Planet Finding*, Vol. 1306 of *ESA Special Publication*, p. 33

Baglin, A., Auvergne, M., Barge, P., Michel, E., Catala, C., Deleuil, M., and Weiss, W.: 2007, in C. Dumitrache, N. A. Popescu, M. D. Suran, and V. Mioc (eds.), *Fifty Years of Romanian Astrophysics*, Vol. 895 of *American Institute of Physics Conference Series*, pp 201–209

Bailer-Jones, C. A. L., Rybizki, J., Fouesneau, M., Mantelet, G., and Andrae, R.: 2018, *AJ* **156**, 58

Ball, W. H.: 2017, in *European Physical Journal Web of Conferences*, Vol. 160 of *European Physical Journal Web of Conferences*, p. 02001

Ball, W. H., Beeck, B., Cameron, R. H., and Gizon, L.: 2016, *A&A* **592**, A159

Ball, W. H. and Gizon, L.: 2014, *A&A* **568**, A123

Ball, W. H. and Gizon, L.: 2017, *A&A* **600**, A128

Ball, W. H., Themeßl, N., and Hekker, S.: 2018, *MNRAS* **478**, 4697

Barban, C., Matthews, J. M., De Ridder, J., Baudin, F., Kuschnig, R., Mazumdar, A., Samadi, R., Guenther, D. B., Moffat, A. F. J., Rucinski, S. M., Sasselov, D., Walker, G. A. H., and Weiss, W. W.: 2007, *A&A* **468**, 1033

Basu, S. and Chaplin, W.: 2017, *Asteroseismic Data Analysis: Foundations and Techniques*, PRINCETON SERIES IN MODERN OBS, Princeton University Press

Basu, S., Chaplin, W. J., and Elsworth, Y.: 2010, *ApJ* **710**, 1596

Basu, S., Grundahl, F., Stello, D., Kallinger, T., Hekker, S., Mosser, B., García, R. A., Mathur, S., Brogaard, K., Bruntt, H., Chaplin, W. J., Gai, N., Elsworth, Y., Esch, L., Ballot, J., Bedding, T. R., Gruberbauer, M., Huber, D., Miglio, A., Yildiz, M., Kjeldsen, H., Christensen-Dalsgaard, J., Gilliland, R. L., Fanelli, M. M., Ibrahim, K. A., and Smith, J. C.: 2011, *ApJ* **729**, L10

Batalha, N. M.: 2014, *Proceedings of the National Academy of Science* **111**, 12647

Bate, M. R., Tricco, T. S., and Price, D. J.: 2014, *MNRAS* **437**, 77

Batten, A. H.: 1973, *Binary and multiple systems of stars*

Beck, P. G., Bedding, T. R., Mosser, B., Stello, D., Garcia, R. A., Kallinger, T., Hekker, S., Elsworth, Y., Frandsen, S., Carrier, F., De Ridder, J., Aerts, C., White, T. R., Huber, D., Dupret, M.-A., Montalbán, J., Miglio, A., Noels, A., Chaplin, W. J., Kjeldsen, H., Christensen-Dalsgaard, J., Gilliland, R. L., Brown, T. M., Kawaler, S. D., Mathur, S., and Jenkins, J. M.: 2011, *Science* **332**, 205

Beck, P. G., Hambleton, K., Vos, J., Kallinger, T., Bloemen, S., Tkachenko, A., García, R. A., Østensen, R. H., Aerts, C., Kurtz, D. W., De Ridder, J., Hekker, S., Pavlovski, K., Mathur, S., De Smedt, K., Derekas, A., Corsaro, E., Mosser, B., Van Winckel, H., Huber, D., Degroote, P., Davies, G. R., Prša, A., Debosscher, J., Elsworth, Y., Nemeth, P., Siess, L., Schmid, V. S., Pápics, P. I., de Vries, B. L., van Marle, A. J., Marcos-Arenal, P., and Lobel, A.: 2014, *A&A* **564**, A36

Beck, P. G., Hambleton, K., Vos, J., Kallinger, T., Garcia, R. A., Mathur, S., and Houmani, K.: 2015, in *European Physical Journal Web of Conferences*, Vol. 101 of *European Physical Journal Web of Conferences*, p. 06004

Beck, P. G., Kallinger, T., Pavlovski, K., Palacios, A., Tkachenko, A., Mathis, S., García, R. A., Corsaro, E., Johnston, C., Mosser, B., Ceillier, T., do Nascimento, J.-D., and Raskin, G.: 2018, *A&A* **612**, A22

Beck, P. G., Montalban, J., Kallinger, T., De Ridder, J., Aerts, C., García, R. A., Hekker, S., Dupret, M.-A., Mosser, B., Eggenberger, P., Stello, D., Elsworth, Y., Frandsen, S., Carrier, F., Hillen, M., Gruberbauer, M., Christensen-Dalsgaard, J., Miglio, A., Valentini, M., Bedding, T. R., Kjeldsen, H., Girouard, F. R., Hall, J. R., and Ibrahim, K. A.: 2012, *Nature* **481**, 55

Bedding, T. R. and Kjeldsen, H.: 2008, in G. van Belle (ed.), *14th Cambridge Workshop on Cool Stars, Stellar Systems, and the Sun*, Vol. 384 of *Astronomical Society of the Pacific Conference Series*, p. 21

Bedding, T. R., Mosser, B., Huber, D., Montalbán, J., Beck, P., Christensen-Dalsgaard, J., Elsworth, Y. P., García, R. A., Miglio, A., Stello, D., White, T. R., De Ridder, J.,

Hekker, S., Aerts, C., Barban, C., Belkacem, K., Broomhall, A.-M., Brown, T. M., Buzasi, D. L., Carrier, F., Chaplin, W. J., di Mauro, M. P., Dupret, M.-A., Frandsen, S., Gilliland, R. L., Goupil, M.-J., Jenkins, J. M., Kallinger, T., Kawaler, S., Kjeldsen, H., Mathur, S., Noels, A., Aguirre, S. V., and Ventura, P.: 2011, *Nature* **471**, 608

Belkacem, K., Goupil, M. J., Dupret, M. A., Samadi, R., Baudin, F., Noels, A., and Mosser, B.: 2011, *A&A* **530**, A142

Belkacem, K., Samadi, R., Mosser, B., Goupil, M.-J., and Ludwig, H.-G.: 2013, in H. Shibahashi and A. E. Lynas-Gray (eds.), *Progress in Physics of the Sun and Stars: A New Era in Helio- and Asteroseismology*, Vol. 479 of *Astronomical Society of the Pacific Conference Series*, p. 61

Benomar, O., Belkacem, K., Bedding, T. R., Stello, D., Di Mauro, M. P., Ventura, R., Mosser, B., Goupil, M. J., Samadi, R., and Garcia, R. A.: 2014, *The Astrophysical Journal Letters* **781**, L29

Blanton, M. R., Bershady, M. A., Abolfathi, B., Albareti, F. D., Allende Prieto, C., Almeida, A., Alonso-García, J., Anders, F., Anderson, S. F., Andrews, B., and et al.: 2017, *AJ* **154**, 28

Blomme, J., Debosscher, J., De Ridder, J., Aerts, C., Gilliland, R. L., Christensen-Dalsgaard, J., Kjeldsen, H., Brown, T. M., Borucki, W. J., Koch, D., Jenkins, J. M., Kurtz, D. W., Stello, D., Stevens, I. R., Suran, M. D., and Derekas, A.: 2010, *ApJ* **713**, L204

Böhm-Vitense, E.: 1958, *ZAp* **46**, 108

Borucki, W. J., Koch, D., Basri, G., Batalha, N., Brown, T., Caldwell, D., Caldwell, J., Christensen-Dalsgaard, J., Cochran, W. D., DeVore, E., Dunham, E. W., Dupree, A. K., Gautier, T. N., Geary, J. C., Gilliland, R., Gould, A., Howell, S. B., Jenkins, J. M., Kondo, Y., Latham, D. W., Marcy, G. W., Meibom, S., Kjeldsen, H., Lissauer, J. J., Monet, D. G., Morrison, D., Sasselov, D., Tarter, J., Boss, A., Brownlee, D., Owen, T., Buzasi, D., Charbonneau, D., Doyle, L., Fortney, J., Ford, E. B., Holman, M. J., Seager, S., Steffen, J. H., Welsh, W. F., Rowe, J., Anderson, H., Buchhave, L., Ciardi, D., Walkowicz, L., Sherry, W., Horch, E., Isaacson, H., Everett, M. E., Fischer, D., Torres, G., Johnson, J. A., Endl, M., MacQueen, P., Bryson, S. T., Dotson, J., Haas, M., Kolodziejczak, J., Van Cleve, J., Chandrasekaran, H., Twicken, J. D., Quintana, E. V., Clarke, B. D., Allen, C., Li, J., Wu, H., Tenenbaum, P., Verner, E., Bruhweiler, F., Barnes, J., and Prsa, A.: 2010, *Science* **327**, 977

Borucki, W. J., Koch, D., Basri, G., Brown, T., Caldwell, D., Devore, E., Dunham, E., Gautier, T., Geary, J., Gilliland, R., Gould, A., Howell, S., Jenkins, J., and Latham, D.: 2008, in M. Livio, K. Sahu, and J. Valenti (eds.), *A Decade of Extrasolar Planets around Normal Stars Proceedings of the Space Telescope Science Institute Symposium, held in Baltimore, Maryland May 2-5, 2005. Edited by Mario Livio, Kailash Sahu and Jeff Valenti, Space Telescope Science Institute, Baltimore Series: Space Telescope Science Institute Symposium Series (No. 19) ISBN: 9780521897846 Publication date: June 2008, 196 pages, pp.36-49*, Vol. 19, pp 36–49

Bressan, A., Marigo, P., Girardi, L., Salasnich, B., Dal Cero, C., Rubele, S., and Nanni, A.: 2012, *MNRAS* **427**, 127

Brogaard, K., Hansen, C. J., Miglio, A., Slumstrup, D., Frandsen, S., Jessen-Hansen, J., Lund, M. N., Bossini, D., Thygesen, A., Davies, G. R., Chaplin, W. J., Arentoft, T., Bruntt, H., Grundahl, F., and Handberg, R.: 2018, *MNRAS* **476**, 3729

Brogaard, K., Jessen-Hansen, J., Handberg, R., Arentoft, T., Frandsen, S., Grundahl, F., Bruntt, H., Sandquist, E. L., Miglio, A., Beck, P. G., Thygesen, A. O., Kjærgaard, K. L., and Haugaard, N. A.: 2016, *Astronomische Nachrichten* **337**, 793

Broomhall, A.-M., Miglio, A., Montalbán, J., Eggenberger, P., Chaplin, W. J., Elsworth, Y., Scuflaire, R., Ventura, P., and Verner, G. A.: 2014, *MNRAS* **440**, 1828

Brown, T. M., Gilliland, R. L., Noyes, R. W., and Ramsey, L. W.: 1991, *ApJ* **368**, 599

Brown, T. M., Latham, D. W., Everett, M. E., and Esquerdo, G. A.: 2011, *AJ* **142**, 112

Bruntt, H., Bikmaev, I. F., Catala, C., Solano, E., Gillon, M., Magain, P., Van't Veer-Menneret, C., Stütz, C., Weiss, W. W., Ballereau, D., Bouret, J. C., Charpinet, S., Hua, T., Katz, D., Lignières, F., and Lueftinger, T.: 2004, *A&A* **425**, 683

Burkhead, M. S.: 1971, *AJ* **76**, 251

Buzasi, D., Catanzarite, J., Laher, R., Conrow, T., Shupe, D., Gautier, III, T. N., Kreidl, T., and Everett, D.: 2000, *ApJ* **532**, L133

Carraro, G., Villanova, S., Demarque, P., McSwain, M. V., Piotto, G., and Bedin, L. R.: 2006, *ApJ* **643**, 1151

Carter, J. A., Yee, J. C., Eastman, J., Gaudi, B. S., and Winn, J. N.: 2008, *ApJ* **689**, 499

Casagrande, L., Silva Aguirre, V., Schlesinger, K. J., Stello, D., Huber, D., Serenelli, A. M., Schönrich, R., Cassisi, S., Pietrinferni, A., Hodgkin, S., Milone, A. P., Feltzing, S., and Asplund, M.: 2016, *MNRAS* **455**, 987

Cassisi, S. and Salaris, M.: 1997, *MNRAS* **285**, 593

Chaplin, W. J., Houdek, G., Elsworth, Y., Gough, D. O., Isaak, G. R., and New, R.: 2005, *MNRAS* **360**, 859

Chaplin, W. J. and Miglio, A.: 2013, *ARA&A* **51**, 353

Choi, J., Conroy, C., Ting, Y.-S., Cargile, P. A., Dotter, A., and Johnson, B. D.: 2018, *ApJ* **863**, 65

Christensen-Dalsgaard, J.: 1984, in A. Mangeney and F. Praderie (eds.), *Space Research in Stellar Activity and Variability*, p. 11

Christensen-Dalsgaard, J.: 2008, *Lecture notes, Sixth Edition, Fourth Printing* pp 1–236

Christensen-Dalsgaard, J.: 2012, *Astronomische Nachrichten* **333**, 914

Christensen-Dalsgaard, J.: 2014, *Lecture notes, Fifth Edition* pp 1–268

Christensen-Dalsgaard, J., Silva Aguirre, V., Elsworth, Y., and Hekker, S.: 2014, *MNRAS* **445**, 3685

Corsaro, E. and De Ridder, J.: 2014, *A&A* **571**, A71

Corsaro, E., De Ridder, J., and García, R. A.: 2015a, *A&A* **579**, A83

Corsaro, E., De Ridder, J., and García, R. A.: 2015b, *A&A* **578**, A76

Corsaro, E., Mathur, S., García, R. A., Gaulme, P., Pinsonneault, M., Stassun, K., Stello, D., Tayar, J., Trampedach, R., Jiang, C., Nitschelm, C., and Salabert, D.: 2017, *A&A* **605**, A3

Corsaro, E., Stello, D., Huber, D., Bedding, T. R., Bonanno, A., Brogaard, K., Kallinger, T., Benomar, O., White, T. R., Mosser, B., Basu, S., Chaplin, W. J., Christensen-Dalsgaard, J., Elsworth, Y. P., García, R. A., Hekker, S., Kjeldsen, H., Mathur, S., Meibom, S., Hall, J. R., Ibrahim, K. A., and Klaus, T. C.: 2012, *ApJ* **757**, 190

Cowling, T. G.: 1941, *MNRAS* **101**, 367

Cox, J. P.: 1980, *Theory of stellar pulsation*

Datta, A., Mazumdar, A., Gupta, U., and Hekker, S.: 2015, *MNRAS* **447**, 1935

Davies, G. R., Silva Aguirre, V., Bedding, T. R., Handberg, R., Lund, M. N., Chaplin, W. J., Huber, D., White, T. R., Benomar, O., Hekker, S., Basu, S., Campante, T. L., Christensen-Dalsgaard, J., Elsworth, Y., Karoff, C., Kjeldsen, H., Lundkvist, M. S., Metcalfe, T. S., and Stello, D.: 2016, *MNRAS* **456**, 2183

De Ridder, J., Barban, C., Baudin, F., Carrier, F., Hatzes, A. P., Hekker, S., Kallinger, T., Weiss, W. W., Baglin, A., Auvergne, M., Samadi, R., Barge, P., and Deleuil, M.: 2009, *Nature* **459**, 398

Dermine, T., Izzard, R. G., Jorissen, A., and Van Winckel, H.: 2013, *A&A* **551**, A50

Duvall, Jr., T. L. and Harvey, J. W.: 1986, in D. O. Gough (ed.), *NATO Advanced Science Institutes (ASI) Series C*, Vol. 169 of *NATO Advanced Science Institutes (ASI) Series C*, pp 105–116

Edmonds, P. D. and Gilliland, R. L.: 1996, *ApJ* **464**, L157

Elmegreen, B. G., Efremov, Y., Pudritz, R. E., and Zinnecker, H.: 2000, *Protostars and Planets IV* p. 179

Elsworth, Y., Hekker, S., Basu, S., and Davies, G. R.: 2017, *MNRAS* **466**, 3344

Flannery, B. P. and Johnson, B. C.: 1982, *ApJ* **263**, 166

Foreman-Mackey, D., Hogg, D. W., Lang, D., and Goodman, J.: 2013, *PASP* **125**, 306

Frandsen, S., Lehmann, H., Hekker, S., Southworth, J., Debosscher, J., Beck, P., Hartmann, M., Pigulski, A., Kopacki, G., Kołaczkowski, Z., Stęślicki, M., Thygesen, A. O., Brogaard, K., and Elsworth, Y.: 2013, *A&A* **556**, A138

Frayn, C. M. and Gilmore, G. F.: 2003, *MNRAS* **339**, 887

Friel, E. D.: 1995, *ARA&A* **33**, 381

Fröhlich, C., Andersen, B. N., Appourchaux, T., Berthomieu, G., Crommelynck, D. A., Domingo, V., Fichot, A., Finsterle, W., Gomez, M. F., Gough, D., Jimenez, A., Leifsen, T., Lombaerts, M., Pap, J. M., Provost, J., Cortes, T. R., Romero, J., Roth, H., Sekii, T., Telljohann, U., Toutain, T., and Wehrli, C.: 1997, *Sol. Phys.* **170**, 1

Fröhlich, C., Romero, J., Roth, H., Wehrli, C., Andersen, B. N., Appourchaux, T., Domingo, V., Telljohann, U., Berthomieu, G., Delache, P., Provost, J., Toutain, T., Crommelynck, D. A., Chevalier, A., Fichot, A., Däppen, W., Gough, D., Hoeksema, T., Jiménez, A., Gómez, M. F., Herreros, J. M., Cortés, T. R., Jones, A. R., Pap, J. M., and Willson, R. C.: 1995, *Sol. Phys.* **162**, 101

Gai, N., Basu, S., Chaplin, W. J., and Elsworth, Y.: 2011, *ApJ* **730**, 63

Gaia Collaboration, Brown, A. G. A., Vallenari, A., Prusti, T., de Bruijne, J. H. J., Babusiaux, C., Bailer-Jones, C. A. L., Biermann, M., Evans, D. W., Eyer, L., and et al.: 2018, *A&A* **616**, A1

Gaia Collaboration, Brown, A. G. A., Vallenari, A., Prusti, T., de Bruijne, J. H. J., Mignard, F., Drimmel, R., Babusiaux, C., Bailer-Jones, C. A. L., Bastian, U., and et al.: 2016a, *A&A* **595**, A2

Gaia Collaboration, Prusti, T., de Bruijne, J. H. J., Brown, A. G. A., Vallenari, A., Babusiaux, C., Bailer-Jones, C. A. L., Bastian, U., Biermann, M., Evans, D. W., and et al.: 2016b, *A&A* **595**, A1

García, R. A., Hekker, S., Stello, D., Gutiérrez-Soto, J., Handberg, R., Huber, D., Karoff, C., Uytterhoeven, K., Appourchaux, T., Chaplin, W. J., Elsworth, Y., Mathur, S., Ballot, J., Christensen-Dalsgaard, J., Gilliland, R. L., Houdek, G., Jenkins, J. M., Kjeldsen, H., McCauliff, S., Metcalfe, T., Middour, C. K., Molenda-Zakowicz, J., Monteiro, M. J. P. F. G., Smith, J. C., and Thompson, M. J.: 2011, *MNRAS* **414**, L6

García Saravia Ortiz de Montellano, A., Hekker, S., and Themeßl, N.: 2018, *MNRAS* **476**, 1470

Gaulme, P., Jackiewicz, J., Appourchaux, T., and Mosser, B.: 2014, *ApJ* **785**, 5

Gaulme, P., McKeever, J., Jackiewicz, J., Rawls, M. L., Corsaro, E., Mosser, B., Southworth, J., Mahadevan, S., Bender, C., and Deshpande, R.: 2016, *ApJ* **832**, 121

Gaulme, P., McKeever, J., Rawls, M. L., Jackiewicz, J., Mosser, B., and Guzik, J. A.: 2013, *ApJ* **767**, 82

Girardi, L., Bertelli, G., Bressan, A., Chiosi, C., Groenewegen, M. A. T., Marigo, P., Salasnich, B., and Weiss, A.: 2002, *A&A* **391**, 195

Gizon, L. and Solanki, S. K.: 2003, *ApJ* **589**, 1009

Gough, D. O.: 1990, in Y. Osaki and H. Shibahashi (eds.), *Progress of Seismology of the Sun and Stars*, Vol. 367 of *Lecture Notes in Physics, Berlin Springer Verlag*, p. 283

Grec, G., Fossat, E., and Pomerantz, M. A.: 1983, *International Astronomical Union and Akademiia Nauk SSSR, Colloquium on Problems of Solar and Stellar Oscillations* **82**, 55

Grundahl, F., Clausen, J. V., Frandsen, S., Arentoft, T., Bruntt, H., and Jensen, H. R.: 2008, *Mem. Soc. Astron. Italiana* **79**, 476

Guggenberger, E., Hekker, S., Angelou, G. C., Basu, S., and Bellinger, E. P.: 2017, *MNRAS* **470**, 2069

Guggenberger, E., Hekker, S., Basu, S., and Bellinger, E.: 2016, *MNRAS*

Hadrava, P.: 1995, *A&AS* **114**, 393

Handberg, R., Brogaard, K., Miglio, A., Bossini, D., Elsworth, Y., Slumstrup, D., Davies, G. R., and Chaplin, W. J.: 2017, *MNRAS* **472**, 979

Handberg, R. and Campante, T. L.: 2011, *A&A* **527**, A56

Handberg, R. and Lund, M. N.: 2014, *MNRAS* **445**, 2698

Harvey, J.: 1985, in E. Rolfe and B. Battrick (eds.), *Future Missions in Solar, Heliospheric & Space Plasma Physics*, Vol. 235 of *ESA Special Publication*

Hastings, W. K.: 1970, *Biometrika* **57(1)**, 97

Hekker, S.: 2013, *Advances in Space Research* **52**, 1581

Hekker, S., Barban, C., Baudin, F., De Ridder, J., Kallinger, T., Morel, T., Chaplin, W. J., and Elsworth, Y.: 2010a, *A&A* **520**, A60

Hekker, S., Basu, S., Elsworth, Y., and Chaplin, W. J.: 2013a, in J. C. Suárez, R. Garrido, L. A. Balona, and J. Christensen-Dalsgaard (eds.), *Stellar Pulsations: Impact of New Instrumentation and New Insights*, Vol. 31 of *Astrophysics and Space Science Proceedings*, p. 73

Hekker, S., Basu, S., Stello, D., Kallinger, T., Grundahl, F., Mathur, S., García, R. A., Mosser, B., Huber, D., Bedding, T. R., Szabó, R., De Ridder, J., Chaplin, W. J., Elsworth, Y., Hale, S. J., Christensen-Dalsgaard, J., Gilliland, R. L., Still, M., McCauliff, S., and Quintana, E. V.: 2011a, *A&A* **530**, A100

Hekker, S., Broomhall, A.-M., Chaplin, W. J., Elsworth, Y. P., Fletcher, S. T., New, R., Arentoft, T., Quirion, P.-O., and Kjeldsen, H.: 2010b, *MNRAS* **402**, 2049

Hekker, S. and Christensen-Dalsgaard, J.: 2017, *A&A Rev.* **25**, 1

Hekker, S., Debosscher, J., Huber, D., Hidas, M. G., De Ridder, J., Aerts, C., Stello, D., Bedding, T. R., Gilliland, R. L., Christensen-Dalsgaard, J., Brown, T. M., Kjeldsen, H., Borucki, W. J., Koch, D., Jenkins, J. M., Van Winckel, H., Beck, P. G., Blomme, J., Southworth, J., Pigulski, A., Chaplin, W. J., Elsworth, Y. P., Stevens, I. R., Dreizler, S., Kurtz, D. W., Maceroni, C., Cardini, D., Derekas, A., and Suran, M. D.: 2010c, *ApJ* **713**, L187

Hekker, S., Elsworth, Y., and Angelou, G. C.: 2018, *A&A* **610**, A80

Hekker, S., Elsworth, Y., Basu, S., and Bellinger, E.: 2017, in *European Physical Journal Web of Conferences*, Vol. 160 of *European Physical Journal Web of Conferences*, p. 04006

Hekker, S., Elsworth, Y., De Ridder, J., Mosser, B., García, R. A., Kallinger, T., Mathur, S., Huber, D., Buzasi, D. L., Preston, H. L., Hale, S. J., Ballot, J., Chaplin, W. J., Régulo, C., Bedding, T. R., Stello, D., Borucki, W. J., Koch, D. G., Jenkins, J., Allen, C., Gilliland, R. L., Kjeldsen, H., and Christensen-Dalsgaard, J.: 2011b, *A&A* **525**, A131

Hekker, S., Elsworth, Y., Mosser, B., Kallinger, T., Basu, S., Chaplin, W. J., and Stello, D.: 2013b, *A&A* **556**, A59

Hekker, S., Elsworth, Y., Mosser, B., Kallinger, T., Chaplin, W. J., De Ridder, J., García, R. A., Stello, D., Clarke, B. D., Hall, J. R., and Ibrahim, K. A.: 2012, *A&A* **544**, A90

Hekker, S., Kallinger, T., Baudin, F., De Ridder, J., Barban, C., Carrier, F., Hatzes, A. P., Weiss, W. W., and Baglin, A.: 2009, *A&A* **506**, 465

Henden, A. A., Levine, S. E., Terrell, D., Smith, T. C., and Welch, D.: 2012, *Journal of the American Association of Variable Star Observers (JAAVSO)* **40**, 430

Hensberge, H., Ilijić, S., and Torres, K. B. V.: 2008, *A&A* **482**, 1031

Hensberge, H. and Pavlovski, K.: 2007, in W. I. Hartkopf, P. Harmanec, and E. F. Guinan (eds.), *Binary Stars as Critical Tools & Tests in Contemporary Astrophysics*, Vol. 240 of *IAU Symposium*, pp 136–147

Hilditch, R. W.: 2001, *An Introduction to Close Binary Stars*

Hole, K. T., Geller, A. M., Mathieu, R. D., Platais, I., Meibom, S., and Latham, D. W.: 2009, *AJ* **138**, 159

Houdek, G. and Gough, D. O.: 2007, *MNRAS* **375**, 861

Huber, D.: 2014, *ArXiv e-prints*

Huber, D., Bedding, T. R., Stello, D., Hekker, S., Mathur, S., Mosser, B., Verner, G. A., Bonanno, A., Buzasi, D. L., Campante, T. L., Elsworth, Y. P., Hale, S. J., Kallinger, T., Silva Aguirre, V., Chaplin, W. J., De Ridder, J., García, R. A., Appourchaux, T.,

Frandsen, S., Houdek, G., Molenda-Żakowicz, J., Monteiro, M. J. P. F. G., Christensen-Dalsgaard, J., Gilliland, R. L., Kawaler, S. D., Kjeldsen, H., Broomhall, A. M., Corsaro, E., Salabert, D., Sanderfer, D. T., Seader, S. E., and Smith, J. C.: 2011, *ApJ* **743**, 143

Huber, D., Bedding, T. R., Stello, D., Mosser, B., Mathur, S., Kallinger, T., Hekker, S., Elsworth, Y. P., Buzasi, D. L., De Ridder, J., Gilliland, R. L., Kjeldsen, H., Chaplin, W. J., García, R. A., Hale, S. J., Preston, H. L., White, T. R., Borucki, W. J., Christensen-Dalsgaard, J., Clarke, B. D., Jenkins, J. M., and Koch, D.: 2010, *ApJ* **723**, 1607

Huber, D., Silva Aguirre, V., Matthews, J. M., Pinsonneault, M. H., Gaidos, E., García, R. A., Hekker, S., Mathur, S., Mosser, B., Torres, G., Bastien, F. A., Basu, S., Bedding, T. R., Chaplin, W. J., Demory, B.-O., Fleming, S. W., Guo, Z., Mann, A. W., Rowe, J. F., Serenelli, A. M., Smith, M. A., and Stello, D.: 2014, *ApJS* **211**, 2

Iben, Jr., I.: 2013, *Stellar Evolution Physics, Volume 1: Physical Processes in Stellar Interiors*

Ilijic, S., Hensberge, H., Pavlovski, K., and Freyhammer, L. M.: 2004, in R. W. Hilditch, H. Hensberge, and K. Pavlovski (eds.), *Spectroscopically and Spatially Resolving the Components of the Close Binary Stars*, Vol. 318 of *Astronomical Society of the Pacific Conference Series*, pp 111–113

Jeffries, Jr., M. W., Sandquist, E. L., Mathieu, R. D., Geller, A. M., Orosz, J. A., Milliman, K. E., Brewer, L. N., Platais, I., Brogaard, K., Grundahl, F., Frandsen, S., Dotter, A., and Stello, D.: 2013, *AJ* **146**, 58

Jiménez, A., Roca Cortés, T., and Jiménez-Reyes, S. J.: 2002, *Sol. Phys.* **209**, 247

Kalirai, J. S., Richer, H. B., Fahlman, G. G., Cuillandre, J.-C., Ventura, P., D'Antona, F., Bertin, E., Marconi, G., and Durrell, P. R.: 2001, *AJ* **122**, 266

Kallinger, T., Beck, P. G., Stello, D., and Garcia, R. A.: 2018, *A&A* **616**, A104

Kallinger, T., De Ridder, J., Hekker, S., Mathur, S., Mosser, B., Gruberbauer, M., García, R. A., Karoff, C., and Ballot, J.: 2014, *A&A* **570**, A41

Kallinger, T., Guenther, D. B., Matthews, J. M., Weiss, W. W., Huber, D., Kuschnig, R., Moffat, A. F. J., Rucinski, S. M., and Sasselov, D.: 2008, *A&A* **478**, 497

Kallinger, T., Hekker, S., Mosser, B., De Ridder, J., Bedding, T. R., Elsworth, Y. P., Gruberbauer, M., Guenther, D. B., Stello, D., Basu, S., García, R. A., Chaplin, W. J., Mullally, F., Still, M., and Thompson, S. E.: 2012, *A&A* **541**, A51

Kallinger, T., Mosser, B., Hekker, S., Huber, D., Stello, D., Mathur, S., Basu, S., Bedding, T. R., Chaplin, W. J., De Ridder, J., Elsworth, Y. P., Frandsen, S., García, R. A., Gruberbauer, M., Matthews, J. M., Borucki, W. J., Bruntt, H., Christensen-Dalsgaard, J., Gilliland, R. L., Kjeldsen, H., and Koch, D. G.: 2010, *A&A* **522**, A1

Kane, S. R., Hill, M. L., Kasting, J. F., Kopparapu, R. K., Quintana, E. V., Barclay, T., Batalha, N. M., Borucki, W. J., Ciardi, D. R., Haghighipour, N., Hinkel, N. R., Kaltenegger, L., Selsis, F., and Torres, G.: 2016, *ApJ* **830**, 1

Kinman, T. D.: 1965, *ApJ* **142**, 655

Kippenhahn, R. and Weigert, A.: 1990, *Stellar Structure and Evolution*

Kirk, B., Conroy, K., Prša, A., Abdul-Masih, M., Kochoska, A., Matijevič, G., Hambleton, K., Barclay, T., Bloemen, S., Boyajian, T., Doyle, L. R., Fulton, B. J., Hoekstra, A. J., Jek, K., Kane, S. R., Kostov, V., Latham, D., Mazeh, T., Orosz, J. A., Pepper, J., Quarles, B., Ragozzine, D., Shporer, A., Southworth, J., Stassun, K., Thompson, S. E., Welsh, W. F., Agol, E., Derekas, A., Devor, J., Fischer, D., Green, G., Gropp, J., Jacobs, T., Johnston, C., LaCourse, D. M., Saetre, K., Schwengeler, H., Toczyski, J., Werner, G., Garrett, M., Gore, J., Martinez, A. O., Spitzer, I., Stevick, J., Thomadis, P. C., Vrijmoet, E. H., Yenawine, M., Batalha, N., and Borucki, W.: 2016, *AJ* **151**, 68

Kjeldsen, H. and Bedding, T. R.: 1995, *A&A* 293

Kjeldsen, H. and Bedding, T. R.: 2011, *A&A* **529**, L8

Kjeldsen, H., Bedding, T. R., and Christensen-Dalsgaard, J.: 2008, *ApJ* **683**, L175

Koch, D. G., Borucki, W. J., Basri, G., Batalha, N. M., Brown, T. M., Caldwell, D., Christensen-Dalsgaard, J., Cochran, W. D., DeVore, E., Dunham, E. W., Gautier, III, T. N., Geary, J. C., Gilliland, R. L., Gould, A., Jenkins, J., Kondo, Y., Latham, D. W., Lissauer, J. J., Marcy, G., Monet, D., Sasselov, D., Boss, A., Brownlee, D., Caldwell, J., Dupree, A. K., Howell, S. B., Kjeldsen, H., Meibom, S., Morrison, D., Owen, T., Reitsema, H., Tarter, J., Bryson, S. T., Dotson, J. L., Gazis, P., Haas, M. R., Kolodziejczak, J., Rowe, J. F., Van Cleve, J. E., Allen, C., Chandrasekaran, H., Clarke, B. D., Li, J., Quintana, E. V., Tenenbaum, P., Twicken, J. D., and Wu, H.: 2010, *ApJ* **713**, L79

Kolbas, V., Pavlovski, K., Southworth, J., Lee, C.-U., Lee, D.-J., Lee, J. W., Kim, S.-L., Kim, H.-I., Smalley, B., and Tkachenko, A.: 2015, *MNRAS* **451**, 4150

Kopal, Z.: 1950, *Harvard College Observatory Circular* **454**, 1

Kumar, P., Ao, C. O., and Quataert, E. J.: 1995, *ApJ* **449**, 294

Kupka, F. G., Ryabchikova, T. A., Piskunov, N. E., Stempels, H. C., and Weiss, W. W.: 2000, *Baltic Astronomy* **9**, 590

Kurtz, D. W.: 1982, *MNRAS* **200**, 807

Kurucz, R.: 1993, *ATLAS9 Stellar Atmosphere Programs and 2 km/s grid. Kurucz CD-ROM No. 13. Cambridge, Mass.: Smithsonian Astrophysical Observatory, 1993.* 13

Lada, C. J.: 2010, *Philosophical Transactions of the Royal Society of London Series A* **368**, 713

Lada, C. J. and Lada, E. A.: 1991, in K. Janes (ed.), *The Formation and Evolution of Star Clusters*, Vol. 13 of *Astronomical Society of the Pacific Conference Series*, pp 3–22

Lamb, H.: 1932, *Hydrodynamics*

Lattanzio, J. C.: 1986, *ApJ* **311**, 708

Libbrecht, K. G.: 1988, *ApJ* **334**, 510

Libbrecht, K. G. and Woodard, M. F.: 1990, *Nature* **345**, 779

Luri, X., Brown, A. G. A., Sarro, L. M., Arenou, F., Bailer-Jones, C. A. L., Castro-Ginard, A., de Bruijne, J., Prusti, T., Babusiaux, C., and Delgado, H. E.: 2018, *A&A* **616**, A9

Maeder, A. and Renzini, A. (eds.): 1984, *Observational tests of the stellar evolution theory; Proceedings of the Symposium, Geneva, Switzerland, September 12-16, 1983*, Vol. 105 of *IAU Symposium*

Majewski, S. R., Schiavon, R. P., Frinchaboy, P. M., Allende Prieto, C., Barkhouser, R., Bizyaev, D., Blank, B., Brunner, S., Burton, A., Carrera, R., Chojnowski, S. D., Cunha, K., Epstein, C., Fitzgerald, G., García Pérez, A. E., Hearty, F. R., Henderson, C., Holtzman, J. A., Johnson, J. A., Lam, C. R., Lawler, J. E., Maseman, P., Mészáros, S., Nelson, M., Nguyen, D. C., Nidever, D. L., Pinsonneault, M., Shetrone, M., Smee, S., Smith, V. V., Stolberg, T., Skrutskie, M. F., Walker, E., Wilson, J. C., Zasowski, G., Anders, F., Basu, S., Beland, S., Blanton, M. R., Bovy, J., Brownstein, J. R., Carlberg, J., Chaplin, W., Chiappini, C., Eisenstein, D. J., Elsworth, Y., Feuillet, D., Fleming, S. W., Galbraith-Frew, J., García, R. A., García-Hernández, D. A., Gillespie, B. A., Girardi, L., Gunn, J. E., Hasselquist, S., Hayden, M. R., Hekker, S., Ivans, I., Kinemuchi, K., Klaene, M., Mahadevan, S., Mathur, S., Mosser, B., Muna, D., Munn, J. A., Nichol, R. C., O'Connell, R. W., Parejko, J. K., Robin, A. C., Rocha-Pinto, H., Schultheis, M., Serenelli, A. M., Shane, N., Silva Aguirre, V., Sobeck, J. S., Thompson, B., Troup, N. W., Weinberg, D. H., and Zamora, O.: 2017, *AJ* **154**, 94

Mamajek, E. E., Prsa, A., Torres, G., Harmanec, P., Asplund, M., Bennett, P. D., Capitaine, N., Christensen-Dalsgaard, J., Depagne, E., Folkner, W. M., Haberreiter, M., Hekker, S., Hilton, J. L., Kostov, V., Kurtz, D. W., Laskar, J., Mason, B. D., Milone, E. F., Montgomery, M. M., Richards, M. T., Schou, J., and Stewart, S. G.: 2015, *arXiv e-prints*

Marigo, P., Girardi, L., Bressan, A., Rosenfield, P., Aringer, B., Chen, Y., Dussin, M., Nanni, A., Pastorelli, G., Rodrigues, T. S., Trabucchi, M., Bladh, S., Dalcanton, J., Groenewegen, M. A. T., Montalbán, J., and Wood, P. R.: 2017, *ApJ* **835**, 77

Martinez-Medina, L. A., Gieles, M., Pichardo, B., and Peimbert, A.: 2018, *MNRAS* **474**, 32

Matthews, J. M., Kuschnig, R., Walker, G. A. H., Pazder, J., Johnson, R., Skaret, K., Shkolnik, E., Lanting, T., Morgan, J. P., and Sidhu, S.: 2000, in L. Szabados and D. Kurtz (eds.), *IAU Colloq. 176: The Impact of Large-Scale Surveys on Pulsating Star Research*, Vol. 203 of *Astronomical Society of the Pacific Conference Series*, pp 74–75

Mayer, P., Harmanec, P., and Pavlovski, K.: 2013, *A&A* **550**, A2

Mazumdar, A., Monteiro, M. J. P. F. G., Ballot, J., Antia, H. M., Basu, S., Houdek, G., Mathur, S., Cunha, M. S., Silva Aguirre, V., García, R. A., Salabert, D., Verner, G. A., Christensen-Dalsgaard, J., Metcalfe, T. S., Sanderfer, D. T., Seader, S. E., Smith, J. C., and Chaplin, W. J.: 2014, *ApJ* **782**, 18

Metropolis, N., Rosenbluth, A. W., Rosenbluth, M. N., Teller, A. H., and Teller, E.: 1953, *The Journal of Chemical Physics* **21**, 1087

Miglio, A., Brogaard, K., Stello, D., Chaplin, W. J., D'Antona, F., Montalbán, J., Basu, S., Bressan, A., Grundahl, F., Pinsonneault, M., Serenelli, A. M., Elsworth, Y., Hekker, S., Kallinger, T., Mosser, B., Ventura, P., Bonanno, A., Noels, A., Silva Aguirre, V., Szabo, R., Li, J., McCauliff, S., Middour, C. K., and Kjeldsen, H.: 2012, *MNRAS* **419**, 2077

Miglio, A., Chaplin, W. J., Farmer, R., Kolb, U., Girardi, L., Elsworth, Y., Appourchaux, T., and Handberg, R.: 2014, *ApJ* **784**, L3

Miglio, A., Chiappini, C., Morel, T., Barbieri, M., Chaplin, W. J., Girardi, L., Montalbán, J., Valentini, M., Mosser, B., Baudin, F., Casagrande, L., Fossati, L., Silva Aguirre, V., and Baglin, A.: 2013, *MNRAS* **429**, 423

Miglio, A., Montalbán, J., Carrier, F., De Ridder, J., Mosser, B., Eggenberger, P., Scuflaire, R., Ventura, P., D'Antona, F., Noels, A., and Baglin, A.: 2010, *A&A* **520**, L6

Mints, A. and Hekker, S.: 2017, *A&A* **604**, A108

Mints, A. and Hekker, S.: 2018, *A&A* **618**, A54

Montgomery, K. A., Janes, K. A., and Phelps, R. L.: 1994, *AJ* **108**, 585

Mosser, B. and Appourchaux, T.: 2009, *A&A* **508**, 877

Mosser, B., Belkacem, K., Goupil, M. J., Michel, E., Elsworth, Y., Barban, C., Kallinger, T., Hekker, S., De Ridder, J., Samadi, R., Baudin, F., Pinheiro, F. J. G., Auvergne, M., Baglin, A., and Catala, C.: 2011, *A&A* **525**, L9

Mosser, B., Belkacem, K., Goupil, M.-J., Miglio, A., Morel, T., Barban, C., Baudin, F., Hekker, S., Samadi, R., De Ridder, J., Weiss, W., Auvergne, M., and Baglin, A.: 2010, *A&A* **517**, A22

Mosser, B., Benomar, O., Belkacem, K., Goupil, M. J., Lagarde, N., Michel, E., Lebreton, Y., Stello, D., Vrard, M., Barban, C., Bedding, T. R., Deheuvels, S., Chaplin, W. J., De Ridder, J., Elsworth, Y., Montalban, J., Noels, A., Ouazzani, R. M., Samadi, R., White, T. R., and Kjeldsen, H.: 2014, *A&A* **572**, L5

Mosser, B., Goupil, M. J., Belkacem, K., Marques, J. P., Beck, P. G., Bloemen, S., De Ridder, J., Barban, C., Deheuvels, S., Elsworth, Y., Hekker, S., Kallinger, T., Ouazzani, R. M., Pinsonneault, M., Samadi, R., Stello, D., García, R. A., Klaus, T. C., Li, J., Mathur, S., and Morris, R. L.: 2012a, *A&A* **548**, A10

Mosser, B., Goupil, M. J., Belkacem, K., Michel, E., Stello, D., Marques, J. P., Elsworth, Y., Barban, C., Beck, P. G., Bedding, T. R., De Ridder, J., García, R. A., Hekker, S., Kallinger, T., Samadi, R., Stumpe, M. C., Barclay, T., and Burke, C. J.: 2012b, *A&A* **540**, A143

Mosser, B., Michel, E., Belkacem, K., Goupil, M. J., Baglin, A., Barban, C., Provost, J., Samadi, R., Auvergne, M., and Catala, C.: 2013, *A&A* **550**, A126

Mosser, B., Vrard, M., Belkacem, K., Deheuvels, S., and Goupil, M. J.: 2015, *A&A* **584**, A50

Mullally, F., Coughlin, J. L., Thompson, S. E., Rowe, J., Burke, C., Latham, D. W., Batalha, N. M., Bryson, S. T., Christiansen, J., Henze, C. E., Ofir, A., Quarles, B., Shporer, A., Van Eylen, V., Van Laerhoven, C., Shah, Y., Wolfgang, A., Chaplin, W. J., Xie, J.-W., Akeson, R., Argabright, V., Bachtell, E., Barclay, T., Borucki, W. J., Caldwell, D. A., Campbell, J. R., Catanzarite, J. H., Cochran, W. D., Duren, R. M., Fleming, S. W., Fraquelli, D., Girouard, F. R., Haas, M. R., Hełminiak, K. G., Howell, S. B., Huber, D., Larson, K., Gautier, III, T. N., Jenkins, J. M., Li, J., Lissauer, J. J., McArthur, S., Miller, C., Morris, R. L., Patil-Sabale, A., Plavchan, P., Putnam, D., Quintana, E. V., Ramirez, S., Silva Aguirre, V., Seader, S., Smith, J. C., Steffen, J. H., Stewart, C., Stober, J., Still, M., Tenenbaum, P., Troeltzsch, J., Twicken, J. D., and Zamudio, K. A.: 2015, *ApJS* **217**, 31

Murray, N.: 2011, *ApJ* **729**, 133

Pavlovski, K. and Hensberge, H.: 2005, *A&A* **439**, 309

Pavlovski, K. and Hensberge, H.: 2010, in A. Prša and M. Zejda (eds.), *Binaries - Key to Comprehension of the Universe*, Vol. 435 of *Astronomical Society of the Pacific Conference Series*, p. 207

Paxton, B., Bildsten, L., Dotter, A., Herwig, F., Lesaffre, P., and Timmes, F.: 2011, *ApJS* **192**, 3

Paxton, B., Schwab, J., Bauer, E. B., Bildsten, L., Blinnikov, S., Duffell, P., Farmer, R., Goldberg, J. A., Marchant, P., Sorokina, E., Thoul, A., Townsend, R. H. D., and Timmes, F. X.: 2018, *ApJS* **234**, 34

Pérez Hernández, F., García, R. A., Corsaro, E., Triana, S. A., and De Ridder, J.: 2016, *A&A* **591**, A99

Pietrinferni, A., Cassisi, S., Salaris, M., and Castelli, F.: 2004, *ApJ* **612**, 168

Pietrinferni, A., Molinaro, M., Cassisi, S., Pasian, F., Salaris, M., Pelusi, D., Manzato, P., and Vuerli, C.: 2014, *Astronomy and Computing* **7**, 95

Pinsonneault, M. H., Elsworth, Y., Epstein, C., Hekker, S., Mészáros, S., Chaplin, W. J., Johnson, J. A., García, R. A., Holtzman, J., Mathur, S., García Pérez, A., Silva Aguirre, V., Girardi, L., Basu, S., Shetrone, M., Stello, D., Allende Prieto, C., An, D., Beck, P., Beers, T. C., Bizyaev, D., Bloemen, S., Bovy, J., Cunha, K., De Ridder, J., Frinchaboy,

P. M., García-Hernández, D. A., Gilliland, R., Harding, P., Hearty, F. R., Huber, D., Ivans, I., Kallinger, T., Majewski, S. R., Metcalfe, T. S., Miglio, A., Mosser, B., Muna, D., Nidever, D. L., Schneider, D. P., Serenelli, A., Smith, V. V., Tayar, J., Zamora, O., and Zasowski, G.: 2014, *ApJS* **215**, 19

Platais, I., Cudworth, K. M., Kozhurina-Platais, V., McLaughlin, D. E., Meibom, S., and Veillet, C.: 2011, *ApJ* **733**, L1

Press, W. H., Flannery, B. P., Teukolsky, S. A., and Vetterling, W. T.: 1989, *Numerical recipes in Pascal. The art of scientific computing*

Prša, A., Harmanec, P., Torres, G., Mamajek, E., Asplund, M., Capitaine, N., Christensen-Dalsgaard, J., Depagne, É., Haberreiter, M., Hekker, S., Hilton, J., Kopp, G., Kostov, V., Kurtz, D. W., Laskar, J., Mason, B. D., Milone, E. F., Montgomery, M., Richards, M., Schmutz, W., Schou, J., and Stewart, S. G.: 2016, *AJ* **152**, 41

Raskin, G.: 2011, *Ph.D. thesis*, Institute of Astronomy, Katholieke Universiteit Leuven, Belgium

Raskin, G., van Winckel, H., Hensberge, H., Jorissen, A., Lehmann, H., Waelkens, C., Avila, G., de Cuyper, J.-P., Degroote, P., Dubosson, R., Dumortier, L., Frémat, Y., Laux, U., Michaud, B., Morren, J., Perez Padilla, J., Pessemier, W., Prins, S., Smolders, K., van Eck, S., and Winkler, J.: 2011, *A&A* **526**, A69

Rauer, H., Aerts, C., Cabrera, J., and PLATO Team: 2016, *Astronomische Nachrichten* **337**, 961

Rawls, M. L., Gaulme, P., McKeever, J., Jackiewicz, J., Orosz, J. A., Corsaro, E., Beck, P. G., Mosser, B., Latham, D. W., and Latham, C. A.: 2016, *ApJ* **818**, 108

Reimers, D.: 1975, *Memoires of the Societe Royale des Sciences de Liege* **8**, 369

Remus, F., Mathis, S., and Zahn, J.-P.: 2012, *A&A* **544**, A132

Ricker, G. R., Vanderspek, R., Winn, J., Seager, S., Berta-Thompson, Z., Levine, A., Villasenor, J., Latham, D., Charbonneau, D., Holman, M., Johnson, J., Sasselov, D., Szentgyorgyi, A., Torres, G., Bakos, G., Brown, T., Christensen-Dalsgaard, J., Kjeldsen, H., Clampin, M., Rinehart, S., Deming, D., Doty, J., Dunham, E., Ida, S., Kawai, N., Sato, B., Jenkins, J., Lissauer, J., Jernigan, G., Kaltenegger, L., Laughlin, G., Lin, D., McCullough, P., Narita, N., Pepper, J., Stassun, K., and Udry, S.: 2016, in *Space Telescopes and Instrumentation 2016: Optical, Infrared, and Millimeter Wave*, Vol. 9904 of *Proceedings of the SPIE*, p. 99042B

Robert, C. P.: 2015, *arXiv e-prints*

Rodrigues, T. S., Bossini, D., Miglio, A., Girardi, L., Montalbán, J., Noels, A., Trabucchi, M., Coelho, H. R., and Marigo, P.: 2017, *MNRAS* **467**, 1433

Rucinski, S. M.: 2002, *AJ* **124**, 1746

Salaris, M. and Cassisi, S.: 1998, *MNRAS* **298**, 166

Salaris, M. and Cassisi, S.: 2005, *Evolution of Stars and Stellar Populations*

Sharma, S., Stello, D., Bland-Hawthorn, J., Huber, D., and Bedding, T. R.: 2016, *ApJ* **822**, 15

Shu, F. H., Adams, F. C., and Lizano, S.: 1987, *ARA&A* **25**, 23

Shulyak, D., Tsymbal, V., Ryabchikova, T., Stütz, C., and Weiss, W. W.: 2004, *A&A* **428**, 993

Simon, K. P. and Sturm, E.: 1994, *A&A* **281**, 286

Sing, D. K.: 2010, *A&A* **510**, A21

Skrutskie, M. F., Cutri, R. M., Stiening, R., Weinberg, M. D., Schneider, S., Carpenter, J. M., Beichman, C., Capps, R., Chester, T., Elias, J., Huchra, J., Liebert, J., Lonsdale, C., Monet, D. G., Price, S., Seitzer, P., Jarrett, T., Kirkpatrick, J. D., Gizis, J. E., Howard, E., Evans, T., Fowler, J., Fullmer, L., Hurt, R., Light, R., Kopan, E. L., Marsh, K. A., McCallon, H. L., Tam, R., Van Dyk, S., and Wheelock, S.: 2006, *AJ* **131**, 1163

Smith, P. H., McMillan, R. S., and Merline, W. J.: 1987, *ApJ* **317**, L79

Sneden, C., Bean, J., Ivans, I., Lucatello, S., and Sobeck, J.: 2012, *MOOG: LTE line analysis and spectrum synthesis*, Astrophysics Source Code Library

Soderblom, D. R.: 2010, *Annual Review of Astronomy and Astrophysics* **48**, 581

Sonoi, T., Samadi, R., Belkacem, K., Ludwig, H.-G., Caffau, E., and Mosser, B.: 2015, *A&A* **583**, A112

Southworth, J.: 2008, *MNRAS* **386**, 1644

Southworth, J.: 2012, *MNRAS* **426**, 1291

Southworth, J.: 2013, *A&A* **557**, A119

Southworth, J., Bruntt, H., and Buzasi, D. L.: 2007, *A&A* **467**, 1215

Southworth, J., Maxted, P. F. L., and Smalley, B.: 2005, *A&A* **429**, 645

Stassun, K. G., Oelkers, R. J., Pepper, J., Paegert, M., De Lee, N., Torres, G., Latham, D. W., Charpinet, S., Dressing, C. D., Huber, D., Kane, S. R., Lépine, S., Mann, A., Muirhead, P. S., Rojas-Ayala, B., Silvotti, R., Fleming, S. W., Levine, A., and Plavchan, P.: 2018, *AJ* **156**, 102

Stello, D., Basu, S., Bruntt, H., Mosser, B., Stevens, I. R., Brown, T. M., Christensen-Dalsgaard, J., Gilliland, R. L., Kjeldsen, H., Arentoft, T., Ballot, J., Barban, C., Bedding, T. R., Chaplin, W. J., Elsworth, Y. P., García, R. A., Goupil, M.-J., Hekker, S., Huber, D., Mathur, S., Meibom, S., Sangaralingam, V., Baldner, C. S., Belkacem, K., Biazzo, K., Brogaard, K., Suárez, J. C., D'Antona, F., Demarque, P., Esch, L., Gai, N., Grundahl, F., Lebreton, Y., Jiang, B., Jevtic, N., Karoff, C., Miglio, A., Molenda-Żakowicz, J., Montalbán, J., Noels, A., Roca Cortés, T., Roxburgh, I. W., Serenelli,

A. M., Silva Aguirre, V., Sterken, C., Stine, P., Szabó, R., Weiss, A., Borucki, W. J., Koch, D., and Jenkins, J. M.: 2010, *ApJ* **713**, L182

Stello, D., Chaplin, W. J., Basu, S., Elsworth, Y., and Bedding, T. R.: 2009, *MNRAS* **400**, L80

Stello, D., Huber, D., Bedding, T. R., Benomar, O., Bildsten, L., Elsworth, Y. P., Gilliland, R. L., Mosser, B., Paxton, B., and White, T. R.: 2013, *ApJ* **765**, L41

Stello, D., Huber, D., Kallinger, T., Basu, S., Mosser, B., Hekker, S., Mathur, S., García, R. A., Bedding, T. R., Kjeldsen, H., Gilliland, R. L., Verner, G. A., Chaplin, W. J., Benomar, O., Meibom, S., Grundahl, F., Elsworth, Y. P., Molenda-Żakowicz, J., Szabó, R., Christensen-Dalsgaard, J., Tenenbaum, P., Twicken, J. D., and Uddin, K.: 2011, *ApJ* **737**, L10

Stetson, P. B.: 2000, *PASP* **112**, 925

Stetson, P. B., Bruntt, H., and Grundahl, F.: 2003, *PASP* **115**, 413

Stetson, P. B., Bruntt, H., and Grundahl, F.: 2005, *VizieR Online Data Catalog* 611

Tassoul, M.: 1980, *ApJS* **43**, 469

Tayar, J., Somers, G., Pinsonneault, M. H., Stello, D., Mints, A., Johnson, J. A., Zamora, O., García-Hernández, D. A., Maraston, C., Serenelli, A., Allende Prieto, C., Bastien, F. A., Basu, S., Bird, J. C., Cohen, R. E., Cunha, K., Elsworth, Y., García, R. A., Girardi, L., Hekker, S., Holtzman, J., Huber, D., Mathur, S., Mészáros, S., Mosser, B., Shetrone, M., Silva Aguirre, V., Stassun, K., Stringfellow, G. S., Zasowski, G., and Roman-Lopes, A.: 2017, *ApJ* **840**, 17

Themeßl, N. and Hekker, S.: 2017, in *European Physical Journal Web of Conferences*, Vol. 152 of *European Physical Journal Web of Conferences*, p. 05012

Themeßl, N., Hekker, S., and Elsworth, Y.: 2017, in *European Physical Journal Web of Conferences*, Vol. 160 of *European Physical Journal Web of Conferences*, p. 05009

Themeßl, N., Hekker, S., Southworth, J., Beck, P. G., Pavlovski, K., Tkachenko, A., Angelou, G. C., Ball, W. H., Barban, C., Corsaro, E., Elsworth, Y., Handberg, R., and Kallinger, T.: 2018, *MNRAS*

Thompson, S. E., Everett, M., Mullally, F., Barclay, T., Howell, S. B., Still, M., Rowe, J., Christiansen, J. L., Kurtz, D. W., Hambleton, K., Twicken, J. D., Ibrahim, K. A., and Clarke, B. D.: 2012, *ApJ* **753**, 86

Thompson, S. E., Fraquelli, D., Van Cleve, J. E., and Caldwell, D. A.: 2016, *Kepler Archive Manual*, Technical report

Tkachenko, A.: 2015, *A&A* **581**, A129

Tkachenko, A., Van Reeth, T., Tsymbal, V., Aerts, C., Kochukhov, O., and Debosscher, J.: 2013, *A&A* **560**, A37

Tofflemire, B. M., Gosnell, N. M., Mathieu, R. D., and Platais, I.: 2014, *AJ* **148**, 61

Tonry, J. and Davis, M.: 1979, *AJ* **84**, 1511

Torres, G., Sandberg Lacy, C. H., Pavlovski, K., Feiden, G. A., Sabby, J. A., Bruntt, H., and Viggo Clausen, J.: 2014, *ApJ* **797**, 31

Toutain, T. and Appourchaux, T.: 1994, *A&A* **289**, 649

Tsymbal, V.: 1996, in S. J. Adelman, F. Kupka, and W. W. Weiss (eds.), *M.A.S.S., Model Atmospheres and Spectrum Synthesis*, Vol. 108 of *Astronomical Society of the Pacific Conference Series*, p. 198

Ulrich, R. K.: 1986, *ApJ* **306**, L37

Valls-Gabaud, D.: 2014, in *EAS Publications Series*, Vol. 65 of *EAS Publications Series*, pp 225–265

Verner, G. A., Elsworth, Y., Chaplin, W. J., Campante, T. L., Corsaro, E., Gaulme, P., Hekker, S., Huber, D., Karoff, C., Mathur, S., Mosser, B., Appourchaux, T., Ballot, J., Bedding, T. R., Bonanno, A., Broomhall, A.-M., García, R. A., Handberg, R., New, R., Stello, D., Régulo, C., Roxburgh, I. W., Salabert, D., White, T. R., Caldwell, D. A., Christiansen, J. L., and Fanelli, M. N.: 2011, *MNRAS* **415**, 3539

Viani, L. S., Basu, S., Chaplin, W. J., Davies, G. R., and Elsworth, Y.: 2017, *ApJ* **843**, 11

Vorontsov, S. V.: 1988, in J. Christensen-Dalsgaard and S. Frandsen (eds.), *Advances in Helio- and Asteroseismology*, Vol. 123 of *IAU Symposium*, p. 151

Vrard, M., Mosser, B., Barban, C., Belkacem, K., Elsworth, Y., Kallinger, T., Hekker, S., Samadi, R., and Beck, P. G.: 2015, *A&A* **579**, A84

Vrard, M., Mosser, B., and Samadi, R.: 2016, *A&A* **588**, A87

White, R. J. and Ghez, A. M.: 2001, *ApJ* **556**, 265

White, T. R., Bedding, T. R., Stello, D., Christensen-Dalsgaard, J., Huber, D., and Kjeldsen, H.: 2011, *ApJ* **743**, 161

White, T. R., Benomar, O., Silva Aguirre, V., Ball, W. H., Bedding, T. R., Chaplin, W. J., Christensen-Dalsgaard, J., Garcia, R. A., Gizon, L., Stello, D., Aigrain, S., Antia, H. M., Appourchaux, T., Bazot, M., Campante, T. L., Creevey, O. L., Davies, G. R., Elsworth, Y. P., Gaulme, P., Handberg, R., Hekker, S., Houdek, G., Howe, R., Huber, D., Karoff, C., Marques, J. P., Mathur, S., McQuillan, A., Metcalfe, T. S., Mosser, B., Nielsen, M. B., Régulo, C., Salabert, D., and Stahn, T.: 2017, *A&A* **601**, A82

Wright, E. L., Eisenhardt, P. R. M., Mainzer, A. K., Ressler, M. E., Cutri, R. M., Jarrett, T., Kirkpatrick, J. D., Padgett, D., McMillan, R. S., Skrutskie, M., Stanford, S. A., Cohen, M., Walker, R. G., Mather, J. C., Leisawitz, D., Gautier, III, T. N., McLean, I., Benford, D., Lonsdale, C. J., Blain, A., Mendez, B., Irace, W. R., Duval, V., Liu, F., Royer, D., Heinrichsen, I., Howard, J., Shannon, M., Kendall, M., Walsh, A. L.,

Larsen, M., Cardon, J. G., Schick, S., Schwalm, M., Abid, M., Fabinsky, B., Naes, L., and Tsai, C.-W.: 2010, *AJ* **140**, 1868

Wu, T., Li, Y., and Hekker, S.: 2014a, *ApJ* **786**, 10

Wu, T., Li, Y., and Hekker, S.: 2014b, *ApJ* **781**, 44

Wurster, J., Bate, M. R., and Price, D. J.: 2018, *MNRAS* **475**, 1859

Zucker, S. and Mazeh, T.: 1994, *ApJ* **420**, 806

Publications

Refereed publications

★ **Themeßl, N.**; S. Hekker; A. Mints; R. A. García; A. García Saravia Ortiz de Montellano; P. B. Stetson; J. De Ridder: *KIC 2568888: To be or not to be a binary*, The Astrophysical Journal, Volume 868, Issue 2, article id. 103, 10 pp., 12/2018

★ **Themeßl, N.**; Hekker, S.; Southworth, J.; Beck, P. G.; Pavlovski, K.; Tkachenko, A.; Angelou, G. C.; Ball, W. H.; Barban, C.; Corsaro, E.; Elsworth, Y.; Handberg, R.; Kallinger, T.: *Oscillating red giants in eclipsing binary systems: empirical reference value for asteroseismic scaling relation*, Monthly Notices of the Royal Astronomical Society, Volume 478, Issue 4, p.4669–4696, 08/2018

★ Ball, W. H.; **Themeßl, N.**; Hekker, S.: *Surface effects on the red giant branch, Monthly Notices of the Royal Astronomical Society, Volume 478, Issue 4, p.4697–4709, 08/2018*

★ García Saravia Ortiz de Montellano, Andrés; Hekker, S.; **Themeßl, N.**: *Automated asteroseismic peak detections*, Monthly Notices of the Royal Astronomical Society, Volume 476, Issue 2, p.1470–1496, 05/2018

★ Zwintz, K.; Moravveji, E.; Pápics, P. I.; Tkachenko, A.; Przybilla, N.; Nieva, M.-F.; Kuschnig, R.; Antoci, V.; Lorenz, D.; **Themeßl, N.**; Fossati, L.; Barnes, T. G.: *A comprehensive study of young B stars in NGC 2264. I. Space photometry and asteroseismology*, Astronomy & Astrophysics, Volume 601, id.A101, 19 pp., 05/2017

★ Anders, F.; Chiappini, C.; Rodrigues, T. S.; Miglio, A.; Montalbán, J.; Mosser, B.; Girardi, L.; Valentini, M.; Noels, A.; Morel, T.; Johnson, J. A.; Schultheis, M.; Baudin, F.; de Assis Peralta, R.; Hekker, S.; **Themeßl, N.** et al.: *Galactic archaeology with asteroseismology and spectroscopy: Red giants observed by CoRoT and APOGEE*, Astronomy & Astrophysics, Volume 597, id.A30, 27 pp., 01/2017

★ Chiappini, C.; Anders, F.; Rodrigues, T. S.; Miglio, A.; Montalbán, J.; Mosser, B.; Girardi, L.; Valentini, M.; Noels, A.; Morel, T.; Minchev, I.; Steinmetz, M.; Santiago, B. X.; Schultheis, M.; Martig, M.; da Costa, L. N.; Maia, M. A. G.; Allende Prieto, C.; de Assis Peralta, R.; Hekker, S.; **Themeßl, N.** et al.: *Young [α/Fe]–enhanced stars discovered by CoRoT and APOGEE: What is their origin?*, Astronomy & Astrophysics, Volume 576, id.L12, 7 pp., 04/2015

★ Schmid, V. S.; **Themeßl, N.**; Breger, M.; Degroote, P.; Aerts, C.; Beck, P. G.; Tkachenko, A.; Van Reeth, T.; Bloemen, S.; Debosscher, J.; Castanheira, B. G.; McArthur, B. E.; Pápics, P. I.; Fritz, V.; Falcon, R. E.: *Discovery of binarity, spectroscopic frequency analysis, and mode identification of the δ Scuti star 4 CVn*, Astronomy & Astrophysics, Volume 570, id.A33, 17 pp., 10/2014

Conference proceedings

- ⋆ **Themeßl, Nathalie**; Hekker, Saskia; Elsworth, Yvonne: *Presence of mixed modes in red giants in binary systems*, Seismology of the Sun and the Distant Stars – Using Today's Successes to Prepare the Future – TASC2 & KASC9 Workshop – SPACEINN & HELAS8 Conference, Azores Islands, Portugal, Edited by Monteiro, M.J.P.F.G.; Cunha, M.S.; Ferreira, J.M.T.S.; EPJ Web of Conferences, Volume 160, id.05009, 10/2017

- ⋆ **Themeßl, Nathalie**; Hekker, Saskia: *Expected oscillation parameters for red giants from dynamical masses and radii*, Wide–Field Variability Surveys: A 21st Century Perspective – 22nd Los Alamos Stellar Pulsation – Conference Series Meeting, San Pedro de Atacama, Chile, Edited by Catelan, M.; Gieren, W.; EPJ Web of Conferences, Volume 152, id.05012, 09/2017

- ⋆ **Themeßl, N.**; Kallinger, T.; Montalbán, J.; García, R. A.: *Oscillation parameters of red giants observed in the CoRoT exofield*, Precision Asteroseismology, Proceedings of the International Astronomical Union, IAU Symposium, Volume 301, pp. 501-502, 02/2014

- ⋆ **Themeßl, Nathalie**; Fritz, Veronique; Breger, Michel; Karrer, Sabine; Castanheira, Barbara G., *The fast rotating δ Scuti pulsator V376 Per: Frequency analysis and mode identification*, Precision Asteroseismology, Proceedings of the International Astronomical Union, IAU Symposium, Volume 301, pp. 499-500, 02/2014

Conference contributions

- ⋆ **Talk**, *Red-giant workshop series*, Vienna, Austria, September 2017

- ⋆ **Talk**, *Ages^2: Taking Stellar Ages to the Next Power*, Isola d'Elba, Italy, September 2017

- ⋆ **Talk**, *SIfA seminar*, Sydney Institute for Astronomy - The University of Sydney, Sydney, Australia, December 2016

- ⋆ **Poster**, *Wide-field Variability Surveys: a 21st–century perspective*, San Pedro de Atacama, Chile, November 2016

- ⋆ **Poster**, *Seismology of the Sun and the Distant Stars*, Angra do Heroísmo, Terceira-Açores, Portugal, July 2016

- ⋆ **Poster**, *Cambridge Workshop on Cool Stars, Stellar Systems, and the Sun (Cool Stars 19)*, Uppsala, Sweden, June 2016

- ⋆ **Talk**, *Red-giant workshop series*, Meudon, France, November 2015

- ⋆ **Talk**, *Space Asteroseismology: The next generation (KASC8/TASC1 workshop)*, Aarhus, Denmark, June 2015
- ⋆ **Joint project**, *Stars, Planets and Life in the Universe Stellar Astrophysics Centre Summer School*, Aarhus, Denmark, July–August 2014
- ⋆ **Poster**, *The Space Photometry Revolution*, Toulouse, France, July 2014

Acknowledgements

First of all, I would like to thank my daily supervisor Saskia Hekker for her mentoring, patience, and advice during the course of my PhD. I am very grateful to my TAC committee as well as the coordinator of the International Max Planck Research School for Solar System Science at the University of Göttingen for their support and guidance.

I would like to thank the members of my defence committee for agreeing to be part of it and for taking the time to read my thesis. In addition, I thank all SAGE members for the great working atmosphere, countless scientific discussions, and times spent outside of MPS during the past years.

I would like to thank all the IMPRS students for the great activities, get-togethers, and laughs that we shared. In addition, I want to thank all the people that I met at MPS. I feel very fortunate to have got to know you.

A special thanks to Emanuele, George, and Thomas for reading parts of the thesis and for providing me with very useful suggestions as well as discussions about red-giant stars.

Moreover, I would like to thank the people involved in administrative tasks at MPS as well as the IT department, who were always there when help was needed.

Last but not least, I would like to say thank you to my family and closest friends for their invaluable support!